**The Promise and Challenges of Inverted Perovskite Solar Cells**

Peng Chen[a§], Yun Xiao[a,b§], Shunde Li[a§], Xiaohan Jia[a§#], Deying Luo[c], Wei Zhang[d,e*], Henry J. Snaith[b*], Qihuang Gong[a,f,g*], and Rui Zhu[a,f,g*]

[a]State Key Laboratory for Artificial Microstructure and Mesoscopic Physics, School of Physics, Frontiers Science Center for Nano-optoelectronics & Collaborative Innovation Center of Quantum Matter, Peking University, Beijing 100871, China

[b]Clarendon Laboratory, Department of Physics, University of Oxford, Oxford OX1 3PU, UK

[c]School of Integrated Circuits, Beijing Advanced Innovation Center for Integrated Circuits, Peking University, Beijing 100871, China

[d]Advanced Technology Institute, Department of Electrical and Electronic Engineering, University of Surrey, Guildford, Surrey GU2 7XH, UK

[e]State Centre for International Cooperation on Designer Low-carbon & Environmental Materials (CDLCEM), School of Materials Science and Engineering, Zhengzhou University, Zhengzhou 450001, P. R. China

[f]Peking University Yangtze Delta Institute of Optoelectronics, Nantong, Jiangsu 226010, China

[g]Collaborative Innovation Center of Extreme Optics, Shanxi University, Taiyuan, Shanxi 030006, China

*E-mail: wz0003@surrey.ac.uk, henry.snaith@physics.ox.ac.uk, qhgong@pku.edu.cn, zhurui3@pku.edu.cn

§P.C., Y.X., S.L., and X.J. contributed equally to this work.

**ABSTRACT:** Recently, there has been an extensive focus on inverted perovskite

solar cells (PSCs) with a p-i-n architecture due to their attractive advantages, such as exceptional stability, high efficiency, low cost, low-temperature processing, and compatibility with tandem architectures, leading to a surge in their development. Single-junction and perovskite-silicon tandem solar cells (TSCs) with an inverted architecture have achieved certified PCEs of 26.1% and 33.9% respectively, showing great promise for commercial applications. To expedite real-world applications, it is crucial to investigate the key challenges for further performance enhancement. We first introduce representative methods, such as composition engineering, additive engineering, solvent engineering, processing engineering, innovation of charge transporting layers, and interface engineering, for fabricating high-efficiency and stable inverted PSCs. We then delve into the reasons behind the excellent stability of inverted PSCs. Subsequently, we review recent advances in TSCs with inverted PSCs, including perovskite-Si TSCs, all-perovskite TSCs, and perovskite-organic TSCs. To achieve final commercial deployment, we present efforts related to scaling up and economic assessment. Lastly, we discuss the potential and challenges of inverted PSCs in the future.

**Table of Contents:**

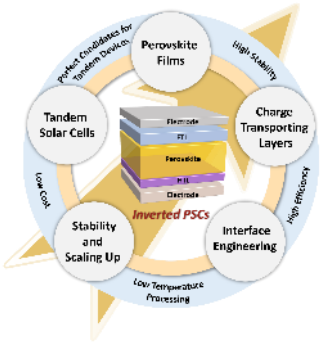
Perovskite Films
Charge Transporting Layers
Interface Engineering
Stability and Scaling Up
Tandem Solar Cells
Inverted PSCs
High Stability
High Efficiency
Low Temperature Processing
Low Cost
Perfect Candidates for Tandem Devices

## CONTENTS

1. Introduction ..... 5

2. Perovskite films ..... 8

2.1 Composition Engineering ..... 8

2.2 Additive Engineering ..... 16

2.3 Solvent Engineering ..... 29

2.4 Processing Engineering ..... 34

3. Charge trasnporting layers ..... 37

3.1 Conventional charge transporting layers ..... 37

3.2 Emerging charge transporting layers - SAMs ..... 45

4. Interface engineering ..... 61

4.1 Top Interface Engineering ..... 66

4.2 Buried Interface Engineering ..... 79

5. Stability of inverted PSCs ..... 86

6. Tanddem devices with inverted PSCs ..... 97

6.1 2T Perovskite-Si TSCs ..... 99

6.2 2T All-Perovskite TSCs ..... 111

6.3 2T Perovskite-Organic TSCs ..... 119

7. Scaling up inverted PSCs ..... 124

8. Economic accessment of inverted PSCs ..... 134

9. Summary and perspectives ..... 139

Author inforamation ..... 153

Corresponding Authors ..... 153

Authors ..... 153

Author Contributions ..... 154

Notes ..... 154

Acknowledgements ..... 157

References ..... 164

## 1. INTRODUCTION

Metal halide perovskites with excellent optoelectronic properties including long charge-carrier diffusion lengths, tunable bandgaps, high absorption coefficient have become a game-changer in the research of optoelectronics (e.g., solar cells, light-emitting diodes).[1-4] Metal halide perovskites generally form an $ABX_3$ structure, in which A represents monocations like methylammonium ($MA^+$), formamidium, ($FA^+$), or caesium ($Cs^+$), B is divalent metal cations such as $Pb^{2+}$ or $Sn^{2+}$ and X denotes halide anions like $I^-$, $Br^-$, or less-frequent $Cl^-$ (Figure 1a). Due to their remarkable properties, harvesting solar energy by metal halide perovskites has attracted enormous research interest. The initiation work of using metal halide perovskites as light-absorbing materials started in 2009 with a comparably low power conversion efficiency (PCE) of 3.8%.[5] At the initial stage, the development of PSCs learns lessons from dye-sensitized solar cells (DSSCs) with perovskites as sensitizers.[5-7] However, since perovskites can be easily degraded by the liquid electrolyte, it is imperative to obtain a tailored device architecture for PSCs. It was found that solid-state charge transporting layers (CTLs) are compatible with the fabrication of high-performance PSCs. After dedicated efforts over the last decade, presently a typical PSC typically consists of an intrinsic light-absorbing perovskite layer (i), a solid n-type electron transporting layer (ETL), a solid p-type hole transporting layer (HTL), a front electrode, and a back electrode. The main-stream device structures can be classified into two categories: n-i-p (regular) and p-i-n (inverted) structures (Figure 1b,c).

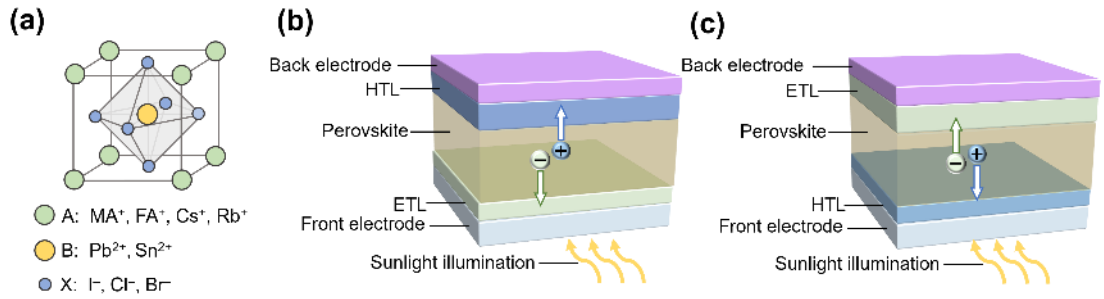


**Figure 1.** (a) The crystal structure of perovskite semiconductors. Schematic

illustration of the architecture of regular (b) and inverted (c) perovskite solar cells (PSCs).

In 2016, we systematically reviewed the progress of inverted PSCs.[8] At that stage, inverted PSCs due to the small hysteresis and easy fabrication attracted enormous research interest.[9-12] However, the limited device performance and especially poor device stability challenged further development. In the years following 2016, there have been notable advancements in the PCEs and device stability for this type of device, with the efficiency records for this type of device being frequently updated (as shown in Figure 2). Nowadays, a certified value of 26.14% was realized for inverted PSCs in 2023,[13-14] for the first time, surpassing the certified PCE of regular PSCs (26.0%).[15] Furthermore, several groups reported that the optimized inverted PSCs exhibited excellent stability, which is capable of passing the international standards for evaluating photovoltaic stability.[16-18] Moreover, recently, a certified PCE of 33.9% was achieved for a monolithic perovskite-silicon tandem solar cell based on inverted PSCs, which surpasses the theoretical performance limit for single-junction silicon solar cells.[19] Additionally, the inverted structure has shown great advantages for large-scale deployment.[20] The elevated PCEs for the inverted PSCs originate from dedicated efforts including defect passivation, interface engineering, morphology control, and innovations of CTLs. These thrilling results indicate that the inverted PSCs are promising candidates for commercial applications. Therefore, a timely review of the recent development of inverted PSCs is meaningful.

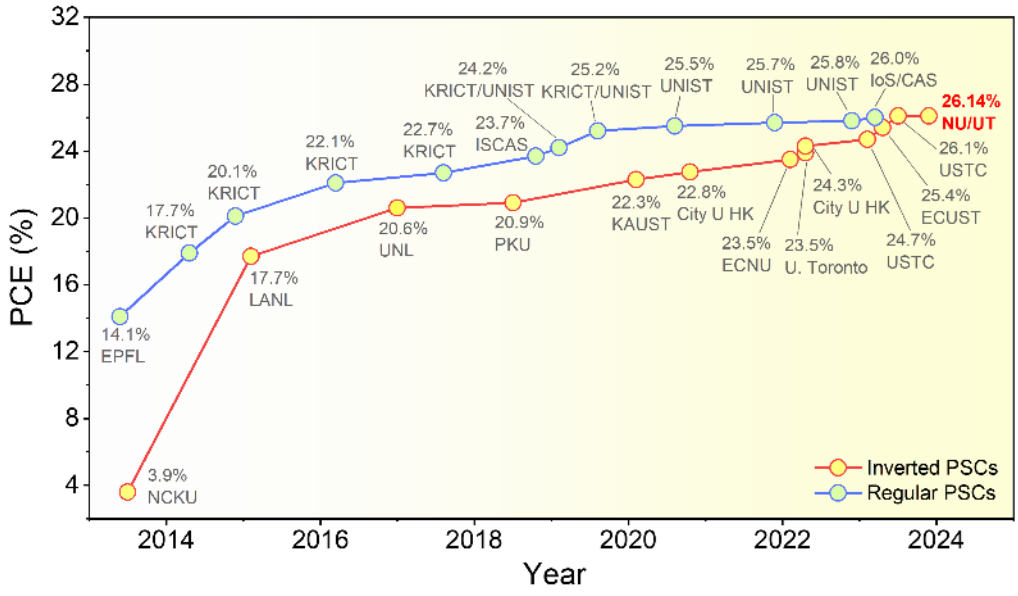


**Figure 2**. Chronological evolution of the power conversion efficiency (PCE) of single-junction inverted and regular PSCs. Data extracted from National Renewable Energy Laboratory data sheet.[19]

In this review, we provide an overview of the recent exciting progress in inverted PSCs. To construct state-of-the-art inverted PSCs, it is crucial to begin by enhancing the quality of the perovskite film. We will start by discussing the latest efforts dedicated to this improvement. Additionally, the inclusion of CTLs, such as electron and hole transporting layers, is vital for efficient charge extraction and contributes to achieving higher open-circuit voltage ($V_{OC}$), short-circuit current density ($J_{SC}$), and fill factor (FF). Therefore, we will systematically summarize the recent developments in CTLs. It is widely recognized that perovskite film interfaces often accumulate a high density of defects and may display band misalignment. Consequently, the selection of suitable interface engineering materials to create tailored interfaces is equally crucial. As such, we will discuss the representative interface engineering techniques, including those applied to both the top and bottom (buried) interfaces of the perovskite layer, as reported recently. Furthermore, we will highlight the factors contributing to the remarkable long-term stability of inverted PSCs. We will also provide a comprehensive summary of tandem devices based on inverted PSCs, which

hold great promise for commercial applications. Furthermore, we will discuss key issues related to scalable fabrication and commercialization, including challenges in upscaling, outdoor applications, and economic assessment. Finally, we will offer a summary and present our insights on future research focus aimed at further enhancing the performance of inverted PSCs for real-life applications.

## 2. PEROVSKITE FILMS

To fabricate high-performance PSCs, it is of critical importance to obtain high-quality perovskite films. A high-quality perovskite film generally requires highly crystalline perovskite crystals, a compact or even monolithic grain structure, excellent film morphology, and ideally should be defect-free, which can reduce shunt paths and suppress notorious non-radiative recombination. Previous works denote that composition engineering, additive engineering, solvent engineering, and processing engineering are closely related to the final perovskite film quality.

### 2.1 Composition Engineering

In metal halide perovskites with a stoichiometry formula of $ABX_3$, the A-cation does not directly impact the band-edge construction, whereas the engineering of A cation would induce the change of bond length and angle of B-site cation and C-site halide, altering the crystal structure of perovskite.[21] Early research on the perovskites generally used single-A cation perovskites. However, single A-cation perovskites such as $MAPbI_3$, $FAPbI_3$, and $CsPbI_3$ show problems that limit their widespread deployment. For $MAPbI_3$ perovskites, the $MA^+$ cation with a volatile nature has a weak secondary hydrogen bonding with the $BX_6^{4-}$ octahedra, which would easily escape from the perovskite crystals and impair device stability, especially under elevated temperature. For $FAPbI_3$ perovskites, compared to the $MA^+$ cation, the $FA^+$ cation has a larger ionic radius (0.253 nm for $FA^+$ and 0.217 nm for $MA^+$, respectively.), and ideal-$FAPbI_3$ perovskite exhibits a narrow bandgap of 1.48 eV corresponding to a higher theoretical performance limit. Nevertheless, the large size

of $FA^+$ cation results in intrinsic lattice strain. As a result, the $FAPbI_3$ perovskite film would transform to the non-perovskite hexagonal phase at room temperature. For inorganic $CsPbI_3$ perovskites, the small size of $Cs^+$ cation (0.188 nm) induces a small tolerance factor (0.81), which greatly undermines thermodynamic stability at room temperature. To address the above issues, mixed A-cation perovskites including double-($FA_{1-x}MA_x^+$, $Cs_{1-x}FA_x^+$),[22-23] triple-($Cs_{1-x-y}FA_xMA_y^+$),[24] and even quadruple ($Rb_{1-x-y-z}Cs_xFA_yMA_z^+$)-cation perovskites[25] have been developed. Taking FA/MA mixed cations perovskites for example, introducing smaller $MA^+$ cations into the $FA^+$ cation-based composition systems could help stabilize the cubic phase at room temperature.[22-23] Furthermore, the inorganic $Cs^+$ and $Rb^+$ cations could form strong chemical bonds with the $BX_6^{4-}$ octahedra, thus stabilizing the cubic phase at room temperature. Moreover, introducing these inorganic cations enabled highly crystalline FA-based perovskites.[25-26] Sargent and coworkers' recent research involved the addition of $Rb^+$ cations to Cs-based perovskites, resulting in a greater degree of lattice distortion. The increment of lattice distortion raised the ion migration energy barrier, thereby suppressing light-induced phase segregation and ultimately improving stability (Figure 3a).[27]

As for metal ions in B-site, most high-performance PSCs are Pb-based perovskite PSCs. Nonetheless, due to the environmental concerns and potential health risks to human beings, tin (Sn) halide perovskite, and mixed tin-lead perovskites have emerged as a hot research topic because of their lower toxicity versus lead halide perovskites. Sn perovskites are known to have higher charge carrier mobility and smaller diffusion lengths.[28] Partly or totally substituting Pb with Sn is able to realize a more ideal bandgap which is about 1.34 eV based on Shockley–Queisser (S–Q) theory prediction (Figure 3b).[28-30] Furthermore, narrow-bandgap perovskites typically below 1.4 eV are fundamental elements for constructing all-perovskite tandem solar cells as rear cells. Nevertheless, the introduction of Sn in the B-site would induce excessive self-doping because of the fast oxidation of Sn (II) to Sn (IV), decreasing the charges

diffusion length and adversely influencing the device performance.[31-32] To stabilize the Sn perovskites, various methods have been developed such as introducing reducing additives (e.g., Sn powder,[33-34] $SnF_2$[35]) and surface passivation.[36-37] It is interesting to note that the majority of Sn PSCs are based on the inverted structure at present.

The modification of X-site anions including halide ions (e.g., $Cl^-$, $Br^-$, and $I^-$) or pseudohalide ions (e.g., $SCN^-$, $HCOO^-$) directly impacts the band edge states of perovskite materials, and thus influencing the device performance. Since $Cl^-$ in perovskite precursors is prone to volatile as the form of MACl during the annealing process,[15] I or Br/I mixed perovskite films would be formed (Table 1) in the end. Nevertheless, Cl alloys in the final perovskite film are still ambiguous and need further research. It should be noted that the addition of $Cl^-$ in the perovskite precursor plays a decisive role in meditating the perovskite crystallization process and stabilizing the photoactive black phase of α-$FAPbI_3$. Replacing $I^-$ with $Br^-$ widens the bandgap,[38] leading to a higher $V_{OC}$ in devices (Figure 3c).[39] However, an excessive amount of Br in Br/I mixed perovskites results in the blue shift of absorption spectra, leading to the loss of $J_{SC}$ in devices. Additionally, the phase homogeneity would be impaired in the presence of Br especially under light illumination due to the formation of I-rich and Br-rich regions. The I-rich regions with a low bandgap tend to trap the charge carrier, decreasing the device performance (Figure 3d). Such light-induced phase separation in Br/I mixed perovskites, especially in wide-bandgap perovskites (typically with Br fraction over 20%), greatly restricts the commercial application of all-perovskite tandem devices.[40]

Currently, the high-performance PSCs, regardless of regular or inverted configuration, are based on the $FAPbI_3$-dominant composition with bandgaps around 1.5 eV (Table 1). There is a clear transition trend of perovskite compositions from $MAPbI_3$-dominant to $FAPbI_3$-dominant compositions during recent years for inverted PSCs.[41] We summarize the composition of the typical inverted PSCs with state-of-the-art

PCEs over 23% in Table 1. Since the perovskite composition is closely related to the final device performance, choosing a desirable perovskite composition is the prerequisite for the construction of stable and efficient PSCs. For instance, recently, Zang et al. reported MA- and Br-free perovskites show advantages of enhancing device longevity.[23]

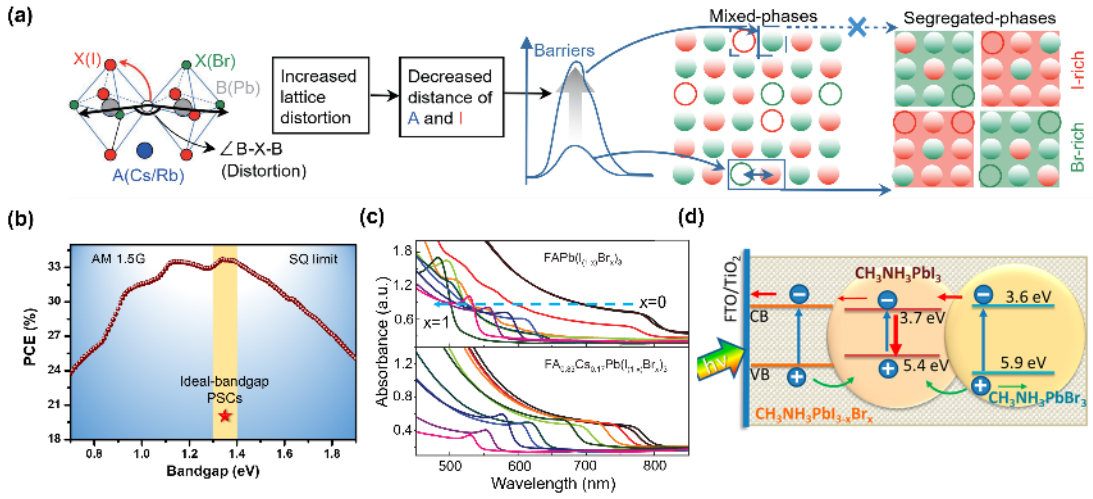


**Figure 3**. (a) Schematic illustration of the suppression mechanism of light-induced phase segregation (LIPS). Vacancies are represented by hollow circles. Reproduced with permission from ref [27]. Copyright 2023 Springer Nature. (b) PCE limit versus bandgap for single-junction solar cells according to the Shockley–Queisser (S-Q) theory. Reproduced with permission from ref [29]. Copyright 2021 Elsevier. (c) Ultraviolet-visible absorbance spectra of $FAPb(I_{1-x}Br_x)_3$ and $FA_{0.83}Cs_{0.17}Pb(I_{1-x}Br_x)_3$ perovskite films. Reproduced with permission from ref [38]. Copyright 2016 American Association for the Advancement of Science. (d) Schematic illustration of charge carrier recombination at the iodide-rich phase due to LIPS. Reproduced with permission from ref [42]. Copyright 2018 Royal Society of Chemistry.

It is noteworthy that the incorporation of a proper amount of excess $PbI_2$ (typically 5-10 mol% with respect to the stoichiometric composition) in the processing solvent could exert a huge influence on the device performance.[43] Excess $PbI_2$ has been shown to be conducive to enlarged grain sizes, reduced halide vacancies, and promoting more oriented α-phase perovskite crystals. Moderate reaction-residual or

heating-induced $PbI_2$ in polycrytalline perovskites can passivate defects at grain boundaries.[44-45] For instance, Zhang et al. introduced excess $PbI_2$ into the precursor solvent with a series of molar ratios of 3 mol%, 5 mol%, and 7 mol%. It was found that the inverted PSCs containing 5 mol% excess $PbI_2$ showed an optimal performance of 22.13% with decent device stability.[46] Recently, a remarkable PCE of 25% was realized for inverted PSCs and the precursor solvent contains a 5 mol% excess $PbI_2$. The optimized PSCs exhibited excellent device stability under continuous light illumination or harsh damp-heat (85 °C and 85% relative humidity) ageing conditions.[17] Nevertheless, there is still a hot debate on the utilization of excess $PbI_2$. Stranks et al. reported that even though the addition of a small amount of excess $PbI_2$ delivered better device performance compared to PSCs with a strict stoichiometric composition, the photolysis of $PbI_2$ would create non-radiative recombination centers and hamper efficient charge extraction.[47] Additionally, Guo et al. claimed that the excessive $PbI_2$ would migrate to the interface, creating the shunting pathways and compromising device longevity under a vacuum or nitrogen atmosphere.[48] We recently came up with a chemical polishing technique to decouple the double-edged effect of excess $PbI_2$, simultaneously realizing both higher PCEs and stability in regular PSCs.[49] So, in-depth and thorough studies are required to uncover the effects of the excess $PbI_2$ on the photovoltaic performance of the films.

**Table 1. A summary of representative perovskites with state-of-the-art performance in inverted PSCs. The device performance and key parameters are provided.**

| Perovskite composition | $E_g$ (eV) | Device configuration | Solvent[c] | Anti -solvent[c] | $V_{OC}$ (V) | $J_{SC}$ (mA cm$^{-2}$) | FF | PCE (%) | Year | Ref. |
|---|---|---|---|---|---|---|---|---|---|---|
| $Cs_{0.05}MA_{0.1}FA_{0.85}PbI_3$ | 1.53 | FTO/Me-4PACz:2PACz/ perovskite/$C_{60}$/$SnO_2$/Ag | DMF:DMSO (745:155/v:v) | ANS | 1.18 | 26.4 | 0.86 | 26.9 (26.1)[d] | 2024 | 50 |
| $Cs_{0.05}MA_{0.05}FA_{0.90}PbI_3$ | - | FTO/$NiO_x$/4PACz/perovskite/ $C_{60}$/BCP/Ag | DMF:DMSO (4:1/v:v) | ANS | 1.17 | 26.2 | 0.86 | 26.4 (25.9)[d] | 2023 | 51 |
| $Cs_{0.05}(FA_{0.98}MA_{0.02})_{0.95}PbI_3$ | 1.55 | FTO/Me-4PACz/perovskite/ $C_{60}$/BCP/Cu | DMF:DMSO (4:1/v:v) | CB | 1.18 | 25.7 | 0.86 | 26.2 (25.9) | 2023 | 52 |
| $Cs_{0.05}(FA_{0.98}MA_{0.02})_{0.95}Pb(I_{0.98}Br_{0.02})_3$ | - | ITO/PTAA/perovskite /$C_{60}$/BCP/Ag | DMF:DMSO (5:1/v:v) | CB | 1.19 | 25.9 | 0.84 | 26.1 (25.8)[d] | 2024 | 53 |
| $Cs_{0.05}FA_{0.95}PbI_3$ | 1.51 | ITO/PTAA/perovskite /$C_{60}$/BCP/Ag | DMF:DMSO (8:1/v:v) | CB | 1.16 | 26.1 | 0.86 | 26.1 (25.2)[d] | 2023 | 54 |
| - | - | ITO/DMAcPA/perovskite/ PCBM/BCP/Ag | DMF:DMSO (4:1/v:v) | CB | 1.19 | 25.7 | 0.85 | 25.9 (25.4)[d] | 2023 | 13 |
| $Cs_{0.1}FA_{0.9}PbI_3$ | | FTO/$ATO_x$/Me-4PACz/perovskite/ $C_{60}$/BCP/Ag | DMF:NMP (960:150/v:v) | CB | 1.17 | 25.7 | 0.80 | 25.7 (25.1)[d] | 2024 | 55 |
| $Cs_{0.05}FA_{0.85}MA_{0.1}PbI_3$ | 1.53 | ITO/$NiO_x$/MeO-4PADBC/ perovskite/$C_{60}$/BCP/Ag | DMF:DMSO (4:1/v:v) | CB | 1.19 | 25.4 | 0.85 | 25.6[d] | 2023 | 56 |
| $Cs_{0.05}(FA_{0.95}MA_{0.05})_{0.95}Pb(I_{0.95}Br_{0.05})_3$ | 1.55 | ITO/Me-4PACz/perovskite/ LiF/$C_{60}$/BCP/Ag | DMF:DMSO (4:1/v:v) | DE | 1.21 | 25.1 | 0.84 | 25.6 (24.7)[d] | 2023 | 57 |
| $FAPbI_3$ | 1.52 | ITO/$NiO_x$/Me-4PACz/perovskite/ /PCBM/$SnO_2$/Cu | DMF:DMSO (4:1/v:v) | CB | 1.16 | 26.2 | 0.84 | 25.6 | 2023 | 58 |
| $Rb_{0.05}Cs_{0.05}MA_{0.05}FA_{0.85}Pb(I_{0.95}Br_{0.05})_3$ | 1.53 | ITO/MeO-2PACz/perovskite/ LiF/$C_{60}$/BCP/Ag | DMF:DMSO (4:1/v:v) | CB | 1.15 | 26.2 | 0.84 | 25.5 (24.05)[d] | 2022 | 59 |
| $(FAPbI_3)_{0.967}(CsPbI_3)_{0.025}(MAPbBr_3)_{0.008}$ | 1.54 | ITO/PTAA/perovskite /$C_{60}$/BCP/Ag | DMF:DMSO (8:1/v:v) | CB | 1.16 | 25.6 | 0.86 | 25.5 (24.9)[d] | 2023 | 60 |
| $Cs_{0.05}MA_{0.1}FA_{0.85}PbI_3$ | - | FTO/2PACz:3-MPA/ perovskite/$C_{60}$/BCP/Ag | DMF:DMSO (4:1/v:v) | ANS | 1.16 | 25.9 | 0.84 | 25.3 (24.8)[d] | 2023 | 61 |
| $Cs_{0.05}(FA_{0.95}MA_{0.05})_{0.95}Pb(I_{0.95}Br_{0.05})_3$ | 1.56 | ITO/MPA-CPA/perovskite/ $C_{60}$/BCP/Ag | DMF:DMSO (4:1/v:v) | CB:IPA (9:1/v:v) | 1.20 | 24.8 | 0.85 | 25.2 (25.4)[d] | 2023 | 14 |

| | | | | | | | | | | |
|---|---|---|---|---|---|---|---|---|---|---|
| $Cs_{0.05}FA_{0.95}PbI_3$ | - | ITO/$NiO_x$/PTAA/$Al_2O_3$/perovskite /PCBM/BCP/Ag | DMF:DMSO (4:1/v:v) | CB | 1.17 | 26.2 | 0.82 | 25.1 (24.6)[d] | 2023 | 23 |
| $(FA_{0.98}MA_{0.02})_{0.95}Cs_{0.05}Pb(I_{0.95}Br_{0.02})_3$ | 1.55[a] | ITO/PTAA/perovskite/ $C_{60}$/BCP/Ag | DMF:DMSO (8:1/v:v) | CB | 1.18 | 25.7 | 0.82 | 25.0 (24.3)[d] | 2022 | 17 |
| $Cs_{0.1}FA_{0.9}PbI_3$ | - | ITO/PTAA:BCP/perovskite/ $C_{60}$/BCP/Cu | 2ME:DMSO | w/o | 1.17 | 25.5 | 0.83 | 24.6 | 2023 | 62 |
| $Cs_{0.05}(FA_{0.98}MA_{0.02})_{0.95}Pb(I_{0.98}Br_{0.02})_3$ | 1.55[a] | ITO/MeO-2PACz/perovskite/ PCBM/BCP/Ag | DMF:DMSO (4:1/v:v) | CB | 1.18 | 24.8 | 0.84 | 24.6 | 2023 | 63 |
| $Cs_{0.05}(FA_{0.98}MA_{0.02})_{0.95}(I_{0.98}Br_{0.02})_3$ | 1.55 | ITO/Me-4PACz/perovskite/ LiF/$C_{60}$/BCP/Ag | DMF:DMSO (4:1/v:v) | CB | 1.19 | 24.9 | 0.84 | 24.5 | 2023 | 64 |
| $Cs_{0.05}FA_{0.95}PbI_3$ | - | FTO/$NiO_x$/Me-4PACz/perovskite/ $C_{60}$/$SnO_2$/Ag | DMF:DMSO (5:1/v:v) | CB | 1.16 | 25.7 | 0.83 | 24.5 | 2023 | 65 |
| $Cs_{0.03}(FA_{0.90}MA_{0.10})_{0.97}PbI_3$ | 1.55[b] | ITO/2PACz/perovskite/ $C_{60}$/BCP/Ag | DMF:DMSO (4:1/v:v) | ANS | 1.21 | 24.5 | 0.82 | 24.3 | 2022 | 16 |
| $(FAPbI_3)_{0.95}(MAPbBr_3)_{0.05}$ | - | ITO/P3CT-N/perovskite/ $C_{60}$/TPBi/Cu | DMF:DMSO (8:1/v:v) | CB | 1.19 | 24.8 | 0.83 | 24.3 (23.5)[d] | 2022 | 66 |
| $Cs_{0.05}FA_{0.85}MA_{0.1}PbI_3$ | 1.53[a] | ITO/$NiO_x$/perovskite/PCBM/ BCP/Ag | DMF:DMSO (4:1/v:v) | ANS | 1.15 | 24.9 | 0.83 | 23.9[d] | 2022 | 67 |
| $MA_{0.6}FA_{0.4}PbI_3$ | 1.49[a] | ITO/PTAA/perovskite/ $C_{60}$/BCP/Cu | - | w/o | 1.17 | 24.1 | 0.84 | 23.8 | 2021 | 68 |
| $Cs_{0.05}(FA_{0.92}MA_{0.08})_{0.95}Pb(I_{0.92}Br_{0.08})_3$ | - | FTO/$NiO_x$/PTAA/perovskite/ PCBM/BCP/Ag | DMF:DMSO (4:1/v:v) | CB | - | - | - | 23.7 | 2022 | 69 |
| $Cs_{0.05}(FA_{5/6}MA_{1/6})_{0.95}Pb(I_{0.85}Br_{0.15})_3$ | - | ITO/PTAA/F-PEAI/perovskite/ PCBM/BCP/Ag | DMF:DMSO (4:1/v:v) | CB:IPA (9:1/v:v) | 1.16 | 24.1 | 0.85 | 23.7 | 2021 | 70 |
| $FAMAPbI_3$ | 1.55[b] | ITO/2PACz/perovskite/ $C_{60}$/BCP/Ag | DMF:DMSO (8:1/v:v) | w/o | - | - | - | 23.6 | 2022 | 16 |
| $Cs_{0.1}FA_{0.6}MA_{0.3}Sn_{0.5}Pb_{0.5}I_3$ | ~1.25[b] | FTO/PEDOT:PSS/perovskite/ $C_{60}$/BCP/Ag | DMF:DMSO (3:1/v:v) | CB | 0.89 | 32.5 | 0.82 | 23.6 (23.1)[d] | 2022 | 71 |
| $Cs_{0.05}MA_{0.15}FA_{0.80}PbI_3$ | 1.49 | ITO/Co-SAM/perovskite/ PI/$C_{60}$/BCP/Ag | DMF:DMSO (4:1/v:v) | CB | 1.16 | 24.7 | 0.82 | 23.6 | 2022 | 72 |
| $Cs_{0.05}FA_{0.95}PbI_3$ | - | ITO/P3CT-N/perovskite/ $C_{60}$/TPBi/Cu | DMF:DMSO (8:1/v:v) | CB | 1.14 | 26.3 | 0.79 | 23.5 (23.4)[d] | 2022 | 66 |
| $Cs_{0.03}FA_{0.97}PbI_3$ | - | ITO/$NiO_x$/$Al_2O_3$/PTAA/perovskite PCBM/BCP/Ag | DMF:DMSO (4:1/v:v) | CB | 1.14 | 25.4 | 0.81 | 23.5 | 2022 | 73 |

| | | | | | | | | | | |
|---|---|---|---|---|---|---|---|---|---|---|
| GACsFAMAPb($I_xBr_{3-x}$)$_3$ | 1.59[b] | ITO/$NiO_x$/PTAA/perovskite/ PCBM+$C_{60}$/BCP/Cr/Au | DMF:DMSO (4:1/v:v) | CB | 1.17 | 23.9 | 0.84 | 23.5 | 2022 | 74 |
| $Cs_{0.05}(FA_{0.95}MA_{0.05})_{0.95}Pb(I_{0.95}Br_{0.05})_3$ | 1.50[b] | ITO/PTAA/perovskite/ $C_{60}$/BCP/Ag | DMF:DMSO (4:1/v:v) | CB | 1.17 | 24.9 | 0.80 | 23.4 (22.8)[d] | 2020 | 75 |
| $Cs_{0.025}FA_{0.475}MA_{0.5}Sn_{0.5}Pb_{0.5}I_{2.925}Br_{0.075}$ | 1.25[b] | FTO/2PACZ-MPA/perovskite/ $C_{60}$/BCP/Ag | DMF:DMSO (4:1/v:v) | TL | 0.88 | 33.1 | 0.80 | 23.2 | 2022 | 76 |
| $Cs_{0.05}(FA_{0.92}MA_{0.08})_{0.95}Pb(I_{0.92}Br_{0.08})_3$ | 1.56[b] | ITO/PTAA/perovskite/ $C_{60}$/BCP/Cu | DMF:DMSO (4:1/v:v) | CB | 1.17 | 24.1 | 0.82 | 23.0 (22.3)[d] | 2020 | 77 |

[a]The optical bandgap ($E_g$) was determined from external quantum efficiency (EQE) spectra; [b]The $E_g$ was calculated from the Tauc plot; [c]DMF, dimethyl formamide; DMSO, dimethyl sulfoxide; 2ME, 2-methoxy-ethanol; ANS, anisole; CB, chlorobenzene; DE, diethyl ether, IPA: isopropanol; TL, toluene. [d]Certified values.

## 2.2 Additive Engineering

Due to the solution processing method and quick crystal growth of perovskite films with thermal-annealing treatment, it is inevitable to generate a wide range of defects and high defect densities in the perovskite thin films.[78] These defects are mainly accumulated at grain boundaries and surfaces of the perovskite films. Based on first-principle calculations, taking typical $MAPbI_3$ as an example, there are 12 possible origins of intrinsic point defects including interstitials ($MA_i$, $Pb_i$, $I_i$), vacancies ($V_{MA}$, $V_{Pb}$, $V_I$), and antisites ($MA_{Pb}$, $MA_I$, $Pb_{MA}$, $Pb_I$, $I_{MA}$, $I_{Pb}$) (Figure 4a). Despite most of these defects are shallow traps due to antibonding coupling between the Pb s orbitals and I p orbitals, several deep-level defects (e.g., undercoordinated $Pb^{2+}$ and Pb–I antisite defects) would act as Shockley–Read–Hall centers for non-radiative recombination, impairing the device performance (Figure 4b).[1, 79-81] Apart from point defects, extended defects with a higher dimensional order such as surfaces, grain boundaries, large voids, and second-phase domains are defective regions, which are also closely tied to defect-promoted performance losses.[82-83] The introduction of additives has been proven to be beneficial to passivate these defects in the films through coordination bonds, hydrogen bonds, ionic bonds, and conversion of impurity phases.[36, 73, 83-84] Furthermore, the interaction between additives and perovskites or processing solvents can modulate perovskite crystallization, forming phase-pure, large-grain, and void-free perovskite films.[13, 85-86] In general, the additive can be directly added into the perovskite precursor or the antisolvent like CB. Note that the materials in post-treatment for the obtained perovskite film or pre-treatment for the underlying substrate before spin-coating the perovskite precursor may also function as the additive and penetrate into the perovskite film,[87-88] and this part will be discussed in the following section. A variety of additive-assisted strategies have been proposed during the last few years and greatly boosted the PCE and device stability of the inverted PSCs. The representative additives used in the preparation of perovskite films include inorganic salts, small organic molecules, polymers, alkylammonium

salts, and ionic liquids.[83]

Alkali halide salts like KI and KBr as an important category of inorganic salts are effective passivating agents for the Frenkel defects and have demonstrated great efficacy in addressing the hysteresis problem in the PSCs regardless of the device configuration.[89] Apart from the defect passivation effect of alkali halides, it was discovered that this kind of additive could produce the dielectric screening effect as indicated by higher dielectric response for perovskite films with KI (Figure 4c), endowing the PSCs with mitigated charged defects, suppressed non-radiative recombination and lower electron-phonon coupling strength. Moreover, it was observed that target perovskite films with KI exhibited a larger grain size and smoother surface. The resulting PSCs with the inverted structure showed a PCE of 22.3% with a high $V_{OC}$ of 1.25 V corresponding to a small $V_{OC}$ deficit of 0.37 V.[90]

Another popular type of additive is small organic molecules. Osman and coworkers added a series of small organic molecules, including phenethylamine (PEA), octylamine (OA), n-butylamine (BA), and oleylamine (OAm), into the perovskite precursor, and investigated its influence on perovskite crystallinity and optoelectronic properties. The grazing-incidence wide-angle X-ray scattering (GIWAXS) test results denoted that promoted (100) grain orientation was formed for the optimized perovskite films with the OAm treatment. The authors speculated that OAm with a long alkyl chain was accumulated at the grain boundary, and could prevent the perovskite grains from tilting during the crystal growth, contributing to a (100)-orientation-dominant film and reduced defect density. As a result, the inverted PSC based on OAm realized a PCE of 23.0%.[77] The addition of small organic molecules-based additives is also able to reduce the interfacial voids. Dimethyl sulfoxide (DMSO) entrapped in the buried interface between the perovskite film and the HTLs could induce the formation of interfacial voids and hasten the device degradation. To solve this problem, Chen et al. introduced a certain amount of carbohydrazide combined with N-and O-donors into the perovskite precursor. According to focused

ion beam–secondary electron microscopy (SEM) images, the interfacial voids disappeared after adding the carbohydrazide (Figure 4d). Due to its high boiling point and minimal evaporation during thermal annealing, the use of this additive helped prevent the volume collapse that can occur when DMSO escapes. As a result, a void-free perovskite film was obtained, leading to a PCE of 23.8%. Moreover, the optimized device based on carbohydrazide treatment showed improved operational stability.[68]

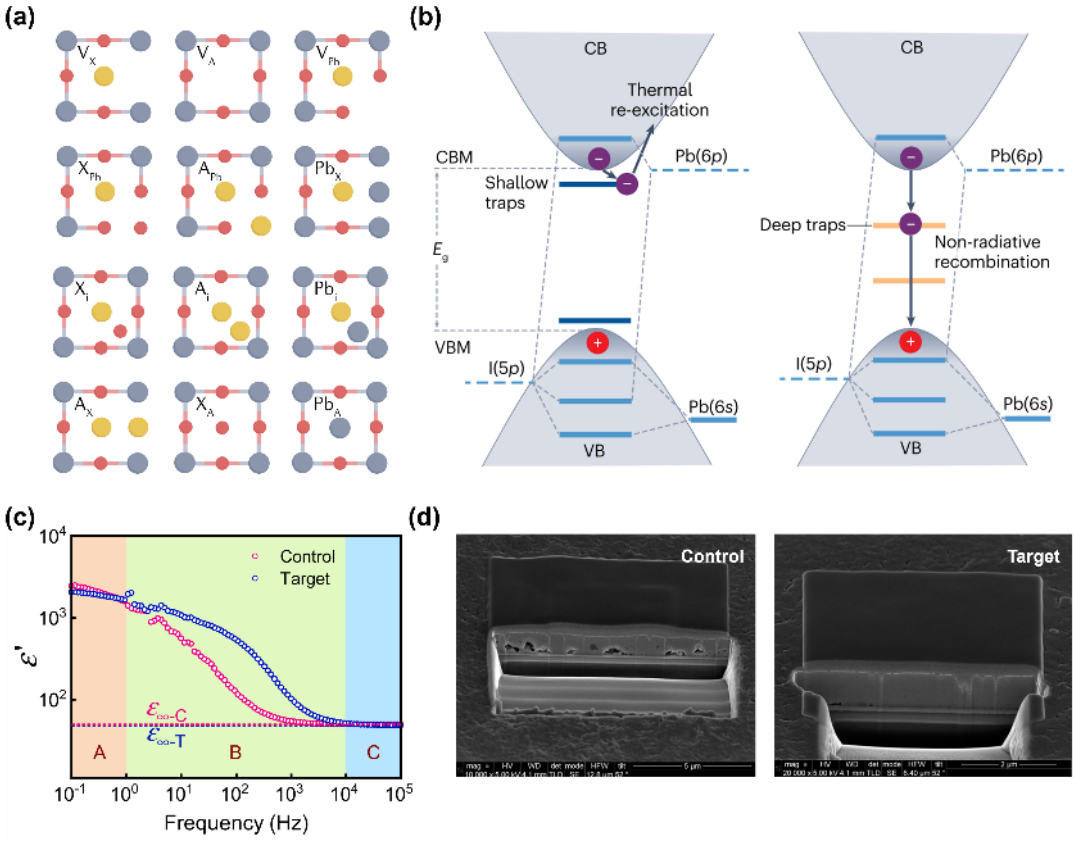


**Figure 4**. (a) Intrinsic point defects in metal-halide perovskite. Reproduced with permission from ref [91]. Copyright 2023 Springer Nature. (b) Schematic illustration of deep and shallow charge carrier traps in perovskites. Reproduced with permission from ref [83]. Copyright 2023 Springer Nature. (c) The real part of dielectric constant for the control and target perovskite films treated by KI versus frequency: region A (low frequency), region B (moderate frequency), and region C (high frequency). Reproduced with permission [90]. Copyright 2021. Springer Nature. (d) Focus ion beam

(FIB)-Secondary electron microscopy (SEM) images of pristine perovskite films (Control) and perovskite films treated by carbohydrazide (Target). Reproduced with permission from ref [68]. Copyright 2021 American Association for the Advancement of Science.

A dimethylacridine-based molecular doping strategy reported by He et al. is also capable of reducing interfacial voids for perovskite films grown on hydrophobic surfaces. Moreover, the dimethylacridine-based molecular could coordinate with $PbI_2$ and form amorphous chelates. Interestingly, these chelates were extruded to the bottom surface as suggested by time-of-flight secondary ions mass spectroscopy (ToF-SIMS) measurements due to the weaker dative bonds of dimethylacridine-based molecular with $PbI_2$ compared to Pb-I bonding of $[PbI_6]^{4-}$ cages (Figure 5a). Furthermore, the upward band bending and reduced energy offset ($\Delta E_h$) at the bottom interface with the aid of dimethylacridine enhanced the hole-extraction rate (Figure 5b). The PCE of the inverted PSC was as high as 25.85% via introducing this additive.[13] Apart from modulating the film morphology, Pan and coworkers reported that employing small organic molecule (phenylsulfonyl)pyrrole (PSP) as an additive to the perovskite films could reduce the compositional inhomogeneity within perovskites, and such compositional inhomogeneity is detrimental to the device performance. According to the TEM images, a decreasing trend of lattice interplanar spacing (*d*) was observed for the reference perovskite film, indicating lattice mismatch at the buried interface due to the accumulation of small Cs atoms. While the PSP-treated film showed negligible variation of *d* values, suggesting reduced lattice stress (Figure 5c). In addition, the use of PSP fastened both crystallization and δ- to α-phase transition rates as evidenced by *in-situ* GIWAXS results, thus inhibiting FA-Cs phase segregation and leading to higher compositional homogeneity. As a consequence, the PCE of the single-junction inverted PSCs for the first time surpassed 26%.[54] Very recently, Chen and coworker reported the orientation of passivating additives greatly impacted the device performance. 4-chlorobenzenesulfonate (4Cl-

BZS), whose structure and electronic potential are depicted in Figure 5d, is more favorable to form perpendicular ligand-surface orientations compared to parallel orientations due to the additional $Pb^{2+}$ surface binding through Cl functional group in 4Cl-BZS. This contributed to a dual-site $Pb^{2+}$ passivation. Through further interface modification, the 4Cl-BZS-based inverted PSCs realized a remarkable PCE of 26.9% with certified quasi–steady state PCEs of 26.15 and 24.74% for 0.05– and 1.04–$cm^2$ devices, respectively (Figure 5g-i). This marks the first instance where the PCE of single-junction inverted PSCs has exceeded that of their traditional counterparts, signifying a groundbreaking advancement in perovskite photovoltaics.[50]

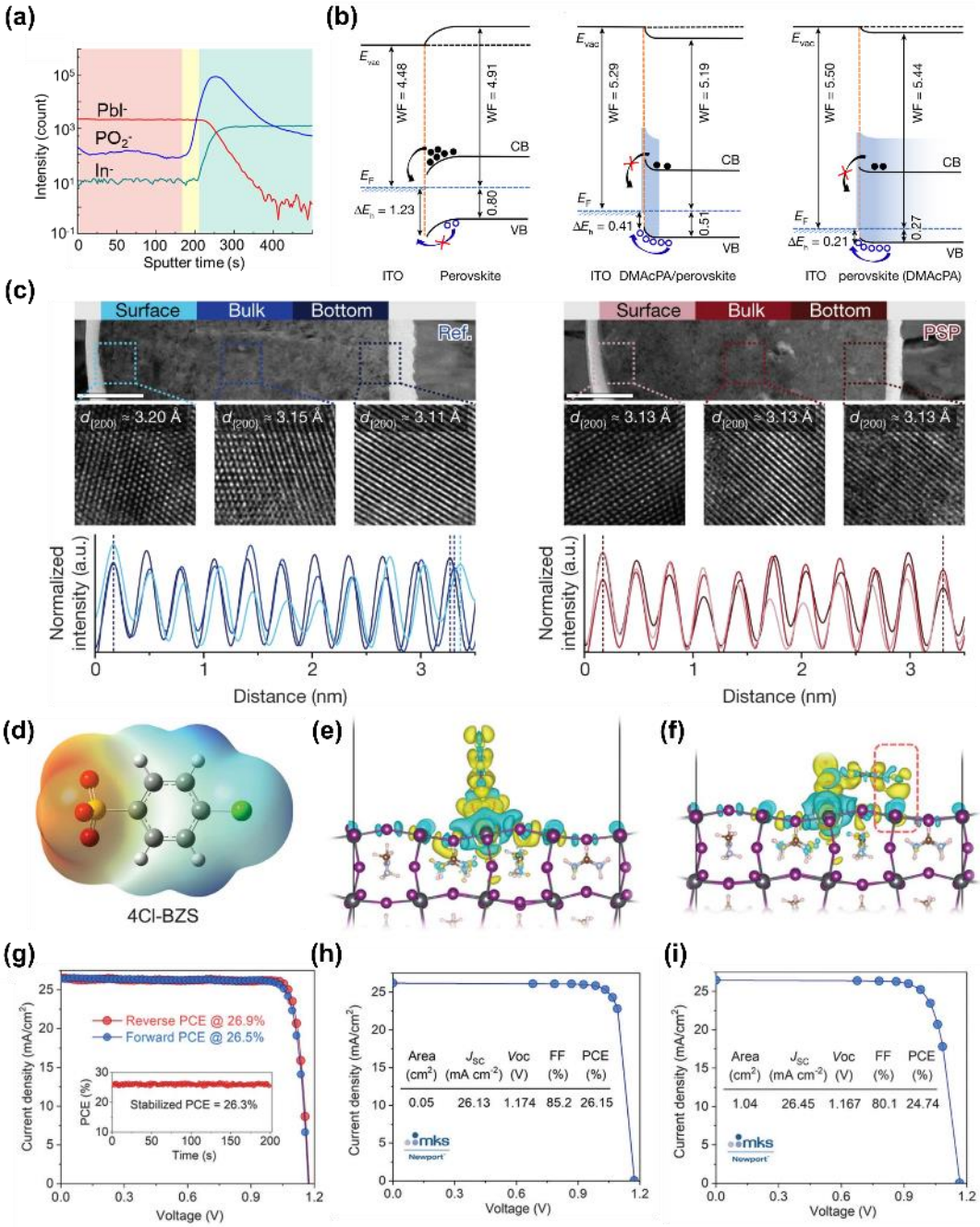


**Figure 5**. (a) Time-of-flight secondary ions mass spectroscopy (ToF-SIMS) profiles of samples with the architecture of ITO/Perovskite (DMAcPA). (b) Energy-level alignmnet for ITO/perovskite (d), ITO/DMAcPA/perovskite (e) and ITO/perovskite (DMAcPA) (f). a.u., arbitrary units, $W_F$, work function; $E_F$, Fermi level; CB, conduction band; VB, valence band. Reproduced with permission from ref [13]. Copyright 2023 Springer Nature. (c) High-angle annular dark field (HAADF) transmission electron microscopy images of the reference sample and the PSP-based

sample. The scale bar refers to 200 nm. Reproduced with permission from ref [54]. Copyright 2023 Springer Nature. (d) Structure and electrostatic potential of sodium 4-chlorobenzenesulfonate (4Cl-BZS) ligand. Atomic structures of ligand adsorbed in a perpendicular (e) and parallel (f) orientation on the perovskite surface. (g) J-V curves of the champion inverted PSC under forward and reverse scans. Insert: the stabilized PCE. Newport-certified quasi–steady state J-V curve of the champion 0.05-$cm^2$ (h) and 1.04-$cm^2$ (i) devices. Reproduced with permission from ref [50]. Copyright 2024 American Association for the Advancement of Science.

Even though the small organic molecule-based additives have greatly boosted the performance of inverted PSCs, these additives tend to have high volatility and high diffusion coefficients, making them challenging to realize long-term stability. While, polymeric additives with lower volatility and diffusion coefficient, as well as hydrophobic aliphatic chains, are good for device stability.[85, 92] In addition, polymeric additives with long alkyl chains are less likely to be integrated into the crystalline structure and primarily reside in grain boundaries. The multiple functional groups of the polymers can effectively passivate the defects at grain boundaries. Hu et al. have shown that adding 3D star-shaped polyhedral oligomeric silsesquioxane-poly(trifluoroethyl methacrylate)-b-poly(methyl methacrylate) (PPP) polymer into the perovskite precursor solution could effectively regulate perovskite crystallization (Figure 5a). In comparison to the control perovskite films, the PPP-modified perovskite films exhibited a larger grain size and almost monolithic grain structure based on the top-view and cross-sectional SEM images. Moreover, the functional groups like carbonyl (C=O) and $–CF_3$ in PPP could passivate under-coordinated $Pb^{2+}$ defects at grain boundaries and interfaces of perovskite films through forming Lewis adducts as indicated by Fourier transform infrared (FTIR) and X-ray photoelectron spectroscopy (XPS) spectra (Figure 5b).[93] Abate et al. reported the use of polymer dipole β-poly(1,1-difluoroethylene) (β-pV2F) as the additive for perovskite films in inverted PSCs. It was found that β-pV2F not only enabled a more compact perovskite

film with a larger grain size but also increased the surface work function by 300 mV versus the control perovskite films. According to the GIWAXS patterns, β-pV2F could increase the phase conversion rate, leading to a more well-crystalline perovskite film (Figure 5c). As a consequence, the inverted PSCs with β-pV2F showed a champion PCE of 24.6% for small-area devices (working area: 0.18 $cm^2$) and a certified PCE of 23.1% for devices with a larger working area of 1 $cm^2$. More importantly, the β-pV2F-based devices exhibited stable power output at temperatures as high as 75°C, and devices subjected to rapid thermal cycling between temperatures ranging from −60°C to +80°C exhibited no symptoms of fatigue.[63]

Alkylammonium salt-based additives like phenethylammonium iodide (PEAI), guanidinium iodide (GAI), butylammonium iodide (BAI), and methylammonium chloride (MACl) have been widely used in perovskite optoelectronics such as PSCs and perovskite light-emitting diodes (PLEDs). This kind of molecule shows great efficacy in defect passivation through molecular interactions with various kinds of defects in perovskites.[94] Additionally, alkylammonium cations with an appropriate size have a strong tendency to form two-dimensional (2D) perovskites with a general formula $A'_mA_{n-1}B_nX_{3n+1}$, where A′ represents divalent or monovalent organic cations. Figure 5d displays the chemical structure of the ammonium cations that are commonly employed at the A′-site.[95-96] 2D perovskites with bulky organic cations are thermally robust leading to improved stability. However, the existence of bulky organic cations in 2D perovskites induces lower conductivity compared to their 3D counterparts. Thereafter, the amount of 2D perovskite in the 3D perovskite film should be carefully optimized to reach the balance between device stability and performance. Wang et al. incorporated a trace amount of fluorinated alkylammonium salts (2-(2,3,4,5,6-pentafluorophenyl) ethylammonium iodide (FEAI) into the perovskite precursor. It was expected that the addition of FEAI would induce the formation of 2D/3D structure perovskites. However, there were no observable 2D perovskites as evidenced by GIWAXS measurement possibly due to the extremally

small amount or the crystalline structure. Compared to the control samples, the perovskite films based on FEAI were more hydrophobic owing to the surface accumulation of fluorine atoms, leading to enhanced device stability under humidity. Moreover, the authors remarked that a proper amount of additives that could form unobservable reduced dimensional perovskites were pleasurable to fabricate devices with good stability and performance.[97] Similarly, Vaynzof et al. added PEAI into the antisolvent. The PEAI-doped perovskite films showed no 2D perovskite-related diffraction patterns possibly due to the formed 2D perovskite below the detection limit of XRD.[70] Recently, Zang et al. added 2-aminoindan hydrochloride (AICl) into the MA-free perovskite precursor inks. According to ToF-SIMS characterization results, the AICl was spontaneously enriched at the bottom interface, and AICl-related 2D perovskites signals were detected through GIWAXS with a high incidence angle (Figure 5e). Furthermore, high-resolution transmission electron microscopy (HRTEM) together with damage-free cryogenic focused ion beam measurements was conducted to study the distribution AICl-related 2D perovskites (Figure 5f). A thin layer of 2D perovskites ($(AI)_2(FA)_{n-1}Pb_nI_{3n-1}Cl_2$) was found at the buried interface, in good agreement with the ToF-SIMS and GIWAXS results. This bottom-up 2D/3D heterojunction structure is conducive to improving hole extraction according to time-resolved photoluminescence (TRPL) spectra, contributing to a high PCE of 25.12% and excellent stability.[23] Furthermore, it is worth noting that excess of MACl would enlarge the grain size, improve film surface coverage, endow a preferred orientation, and passivate defective grain boundaries. This is because MACl-based intermediate mixtures slowed down the crystallization rate. These intermediate mixtures quickly vanished owing to the facile volatilization of MACl through decomposing into MA ion and FACl during thermal annealing.[98-99] Plenty of previous research on inverted PSCs with decent PCEs also incorporated excess MACl into the perovskite precursor inks.[54, 56-57, 65]

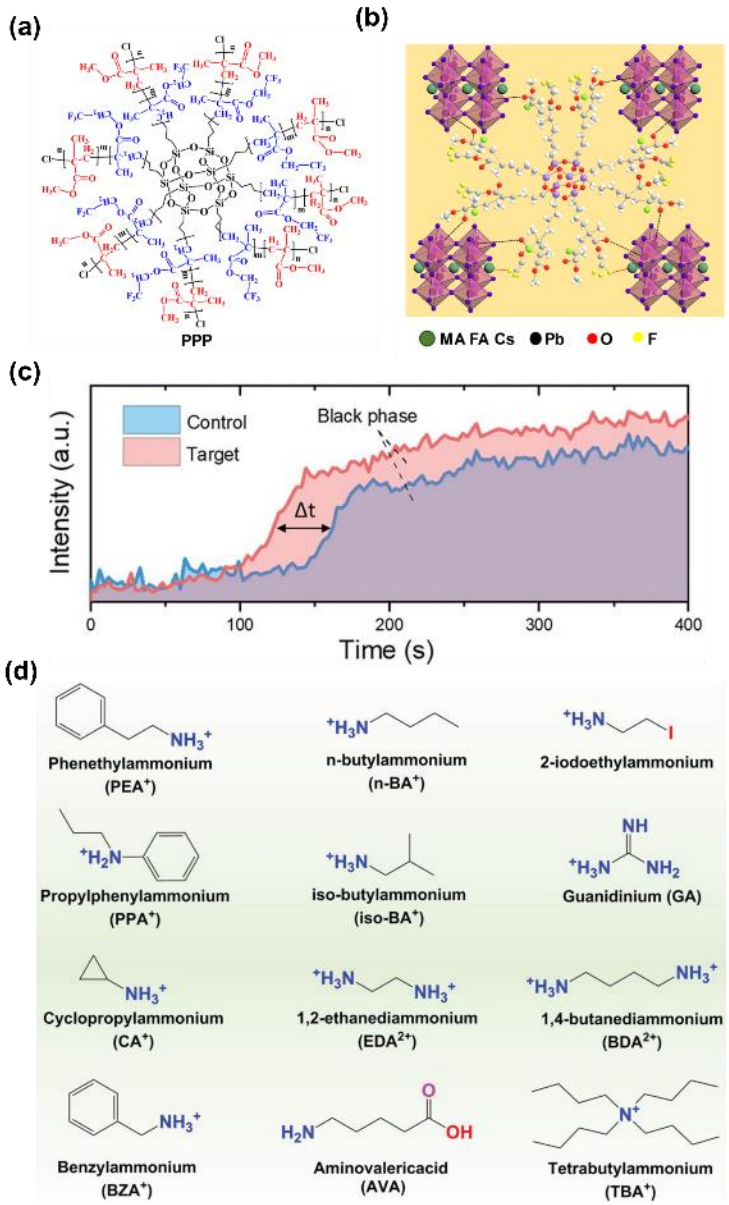


**Figure 6.** (a) The chemical structure of polyhedral oligomeric silsesquioxane-poly(trifluoroethyl methacrylate)-b-poly(methyl methacrylate) (PPP). (b) Schematic illustration of the interaction between PPP and perovskite. The interaction includes chelation between C=O and noncoordinating $Pb^{2+}$ and hydrogen bonding between -$CF_3$ and organic cations. Reproduced with permission from ref [93]. Copyright 2021 American Association for the Advancement of Science. (c) Time-resolved integrated peak area intensity for black phases of control and target perovskites based on *in situ* grazing incidence wide-angle X-ray scattering (GIWAXS) spectra. Reproduced with permission from ref [63]. Copyright 2023 American Association for the Advancement of Science. (d) Chemical structure of the typical ammonium cations which are capable of

forming two-dimensional (2D) perovskites. Reproduced with permission from ref [95]. Copyright 2019 John Wiley and Sons.

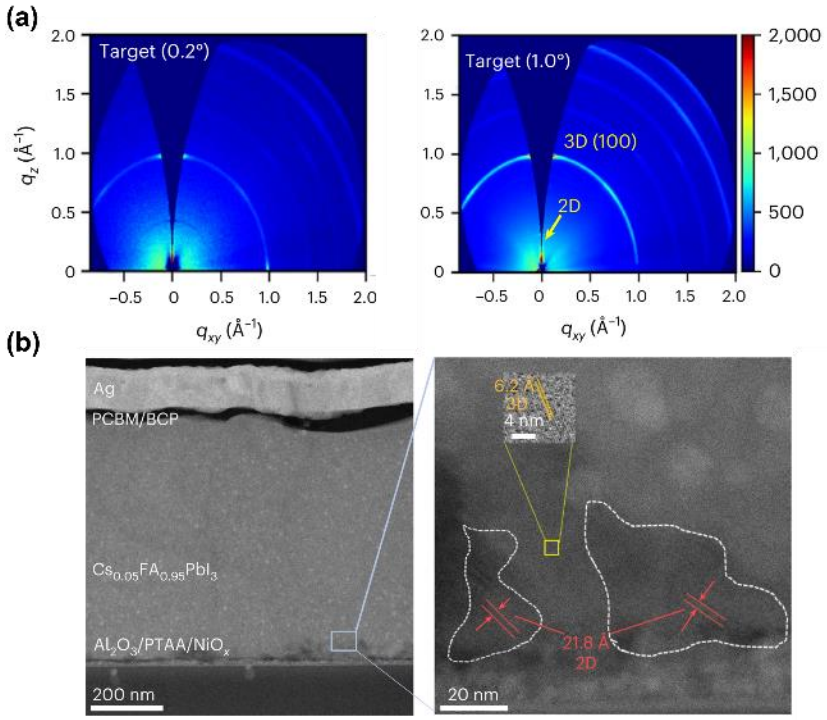


**Figure 7.** (a) 2D GIWAXS mappings of the target perovskite films with different incidence angles. (b) Cross-sectional HRTEM images of the target PSC. The inset shows the magnified TEM image of the yellow squared area. The areas enclosed by the dashed white lines are the formed 2D perovskite. Reproduced with permission from ref [23]. Copyright 2023. Springer Nature.

As we discussed, ammonium cations such as $PEA^+$ and $BA^+$ are commonly incorporated into 3D perovskites to form 2D perovskite structures, which assists in defect passivation and thereby enhances device performance. Nevertheless, Huang and colleagues discovered that the currently used PEACl additive was prone to cation deprotonation reactions under light soaking at high temperatures, leading to the formation of pinholes in perovskite films (Figure 6a-d).[100] This phenomenon undermined the operational stability of PSCs, even though it might enhance the performance of fresh devices. Both $BA^+$ and $PEA^+$ tended to lose their proton and transform into amines, which subsequently reacted with $FA^+$ to form

(butylamino)methaniminium ($BAMA^+$) and (phenethylamino)methaniminium ($PEAMA^+$), respectively (Figure 6e). Notably, ammonium cations with higher acid dissociation constants ($pK_a$), such as $BAMA^+$ ($pK_a$ = 12.0) and $PEAMA^+$ ($pK_a$ = 12.0), could be used instead of $BA^+$ or $PEA^+$ for effective passivation. These cations, $BAMA^+$ or $PEAMA^+$, demonstrated enhanced stability with FA-based perovskites due to their lower propensity for deprotonation. The $PEAMA^+$ treated films gave higher PL intensity, longer charge carrier lifetime, higher crystallinity, and better film quality, and gave a significantly lowered defect density of $n = 1.33 \times 10^{16}$ $cm^{-3}$ compared to untreated film ($n = 4.89 \times 10^{16}$ $cm^{-3}$). The best-performing device achieved a PCE of 24.1%, whereas the control device only showed a PCE of 21.2%. Control devices with no ammonium cations retained 90% of their original efficiency after approximately 800 hours. By contrast, the devices containing $PEAMA^+$ preserved 90% of their initial efficiency for about 1,500 hours.

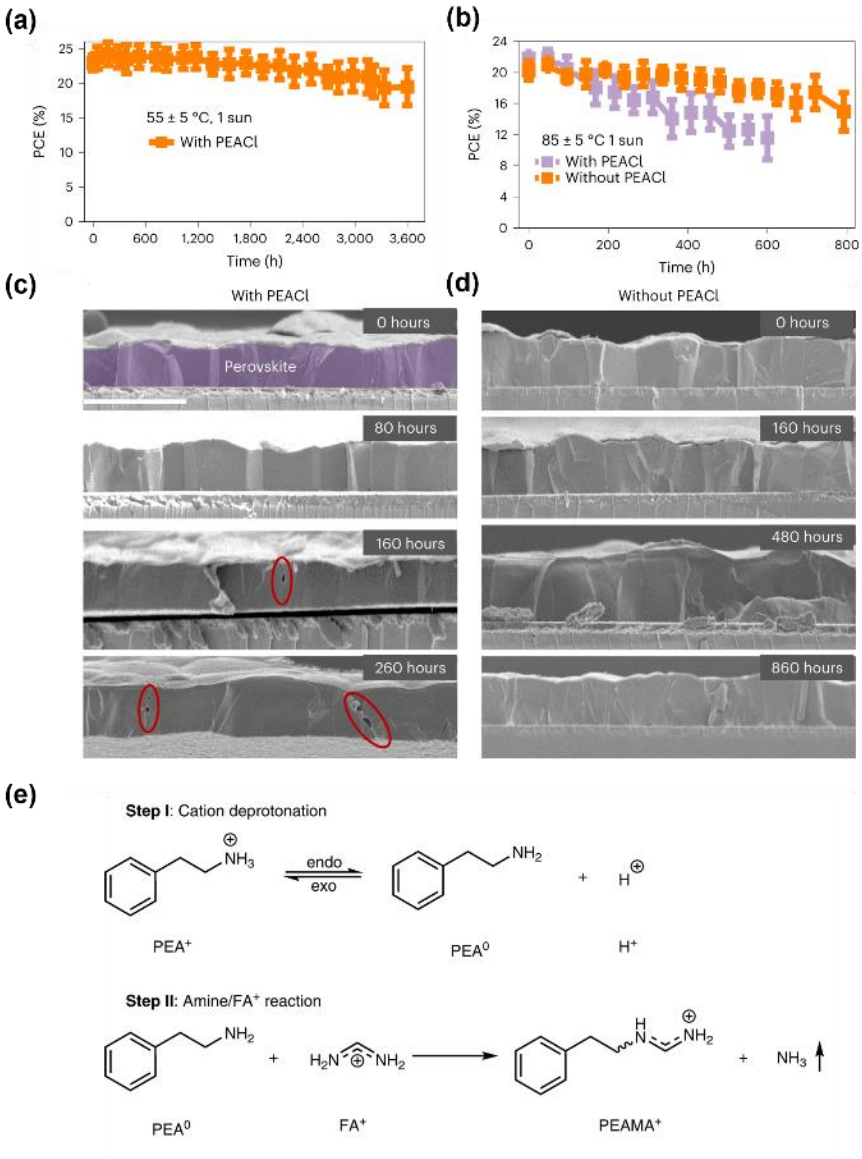


**Figure 8.** (a) The PCE of encapsulated devices with PEACl treatment was measured over time under approximately 55°C and 1 sun illumination at $V_{OC}$ conditions in a nitrogen atmosphere. (b) For unencapsulated devices, the PCE was compared between those treated with PEACl (five devices) and those without PEACl (eight devices), over a period under approximately 85°C and 1 sun illumination at $V_{OC}$ condition in nitrogen. (c) Cross-sectional SEM images illustrate PEACl-treated PSCs after undergoing stability tests under 85°C at 1 sun illumination $V_{OC}$ conditions for 0, 80, 160, and 250 hours, respectively. The voids formed along grain boundaries are highlighted by red circles. (d) Cross-sectional SEM images depict PSCs not treated with PEACl following stability tests under 1 sun illumination at 85°C and open circuit

conditions at intervals of 0, 160, 480, and 860 hours, respectively. A scale bar indicating 3 μm is included in the SEM images. (e) Reaction mechanism of $PEA^+$ with $FA^+$. Reproduced with permission from ref [100]. Copyright 2023 Springer Nature.

The stability of the fabricated PSCs is an important parameter for commercial application. Ionic liquids, which is a type of molten salts and remains in a liquid state at room temperature, have recently been as the additive in the fabrication of inverted PSCs, and demonstrate great efficacy in enhancing the device stability.[70, 101-104] In 2019, Snaith's group thoroughly investigated the effect of ionic liquid additives on the improvement of performance for the inverted PSCs. Morphology characterization results demonstrated enhanced texturing or crystallinity of perovskite films with the addition of ionic liquid 1-butyl-3-methylimidazolium tetrafluoroborate ($BMIMBF_4$). $BMIMBF_4$-containing perovskite films showed significantly suppressed ion migration according to photoluminescence measurement under the applied bias. $[BMIM]^+$ cation would be accumulated at the surface, protecting the perovskite layer from the invasion of oxygen and moisture. As a results, the $BMIMBF_4$-containing device exhibited excellent long-term stability under various ageing conditions.[101] Even though the effectiveness of ionic liquid additives in improving device stability and charge-carrier transportation has been verified by lots of works, the ionic liquid-modified PSCs only show moderate efficiencies in most cases, which calls for more efforts to fully tap the potential of ionic liquid additives. Furthermore, the ionic liquid can also be used as the sole solvent for the preparation perovskite film, and the detailed discussion is given in the following section.

### 2.3 Solvent Engineering

Since the first development of PSCs, researchers have been striving to find a solvent or solvent blend with a suitable set of characteristics. These characteristics, including boiling point, vapor pressure, viscosity, and coordination ability towards perovskite precursors, directly influence the quality of a solution-processed perovskite layer[105].

For a solution-processed perovskite film, the transition from a precursor solution to a perovskite film is usually observed to not directly proceed into the perovskite phase. This process often occurs through the formation of intermediates such as non-photoactive perovskite phases and intermediate adducts (e.g., MAI-$PbI_2$-DMF, MAI-$PbI_2$-DMSO, and $PbI_2$-2DMSO). These solvent-based intermediates formed through Lewis acid−base interaction generally contain high-boiling point solvents like DMSO or N-methyl-2-pyrrolidone (NMP). During the spin-coating process, the antisolvent like chlorobenzene (CB) helps extract dimethyl formamide (DMF), and the formed wet film containing intermediate adducts contributes to dominant crystal growth and high crystallinity of perovskite through reducing the nucleation rate of the perovskite.[4, 106-108] However, film formation with excess solvent that strongly coordinates with the precursor results in the predominance of crystal growth over nucleation, leading to the formation of dendritic or island-like films with large grains but inadequate film coverage.[108] To date, the mixed solvent of DMF/DMSO with proper volume ratio according to the perovskite composition has shown great success in fabricating high-performance PSCs. The majority of inverted PSCs with PCEs over 23% utilize the DMF/DMSO mixed solvent, and volume ratios between DMF and DMSO are 4:1 and 8:1 in most cases (Table 1). Nevertheless, the commonly used solvents like DMF are highly toxic, which would hinder the practical application of PSCs.[109-110] Such issues can be addressed by using environmentally friendly solvents.[111] In regular n-i-p PSCs, Zhao et al. used eco-friendly biomass-derived green solvents γ-valerolactone (GVL) and n-butyl acetate as host solvent and antisolvent, respectively. The strong interaction between GVL and $FA^+$ cation greatly increased the perovskite precursor stability and delivered a high PCE of 25.09%.[111] Seok reported a similar efficiency of 25.1% using mixed green solvents of ethanol and N-dimethylacetamide without the antisolvent extraction process.[112] Another type of eco-friendly solvent is known as ionic liquids.[113] When used in the preparation of perovskite films, the ionic liquid solvent offers several advantages. Not only does it reduce toxicity, but the strong

chemical interactions between the solute and the ionic liquid, including coordinate bonds and hydrogen bonds, aid in the complete dissolution of the perovskite precursor powders, regulating the crystallization process of the perovskite film, and the formation of high-quality perovskite films.[113] Early in 2015, the ionic liquid methylammonium formate (MAFa) was used as the single solvent for the $MAPbI_3$ precursor solutions. The resulting perovskite films have excellent coverage, uniformity, as well as highly oriented and large crystal domains. Furthermore, it was found that there was no intermediate crystalline phase during the annealing process, which may be beneficial for the better control of the perovskite film structure.[114] Afterward, Huang and Chen et al. used MAFa to synthesize $FAPbI_3$ perovskite films. A stable black-phase α-$FAPbI_3$ perovskites was obtained in the air insensitive to the temperature and humidity. The use of ionic liquid MAFa led to vertically aligned $PbI_2$ thin films, due to the strong interactions between $PbI_2$ and MAFa containing C=O···Pb chelation and N-H···I hydrogen bonds. This is desirable for the formation of nanoscale ion channels that facilitate the permeation of FAI into the $PbI_2$ thin films. As a result, the energy barrier to formation of α-$FAPbI_3$ was greatly reduced, and the resulting PSCs with a regular n-i-p architecture realized a high PCE of 24.1% with outstanding stability.[115] This works demonstrate the huge potential of ionic solvent for the development of efficient and stable PSCs in the air regardless of temperature and humidity, which would greatly promote the development large-scale PSCs production. Furthermore, employing ionic liquid solution would help form phase-pure quantum well films so that improved charge carrier transportation and improved device performance were achieved.[116] While there have been limited studies on the application of ionic liquid solvents or other types of environmentally-friendly solvents in inverted PSCs, the PCE of these cells using such solvents is much lower compared to regular PSCs. The previous research conducted on their regular counterparts could offer valuable insights for future studies on inverted PSCs processed by green solvents. We believe that the green-solvent especially the ionic liquid processed

inverted PSCs are more desirable for industrial application and will attract more and more research attention. Moreover, despite the wide-employment of DMF/DMSO mixed solvents, it may not be the ideal choice especially for the preparation of large-area perovskite films considering the prolonged coating time, which will be discussed in detail in Section 7.

For perovskite films deposited by the one-step spin-coating procedure (The detailed discussion is given in the following section), antisolvents, such as CB, diethyl ether (DE), anisole (ANS), and toluene (TL), are needed to selectively dissolve one solvent in perovskite precursor solution typically DMF, and the perovskite is slightly soluble in the antisolvent.[105] However, most of these antisolvents are highly toxic. It is imperative to develop green antisolvents or antisolvent-free process. Wei and coworkers chose ethanol as the antisolvent, and MABr was doped into the antisolvent. When the concentration of MABr in ethanol is 2 mg $mL^{-1}$, a PCE approaching 21% was realized.[117] Furthermore, the antisolvent process is not adapted to the mature industrial processes like the roll-to-roll process and fabricate large perovskite solar modules. To solve this problem, several methods have been reported such as solvent engineering,[118] vacuum-controlled growth,[119] and $N_2$ gas knife drying.[120] Among these methods, solvent engineering without the need to employ additional equipment shows unique advantages. Deng et al. combined volatile noncoordinating solvents 2-methoxyethanol (2ME) and low-volatile coordinating solvents DMSO, achieving both fast deposition and high crystallinity. They compared the Gutmann donor number ($D_N$) of the solvent, which can help compare the coordinating ability between Lewis-basic solvents and the Lewis-acidic $Pb^{2+}$ center.[121] Further study by Huang et al. revealed that the solvents with higher $D_N$ like DMF and DMSO could dissolve $PbI_2$ because of their strong coordination strength to $Pb^{2+}$ ions, while the solvents with lower $D_N$ like 2ME could not dissolve $PbI_2$ alone unless in the presence of MAI.[118] Kim compared solvents with different $D_N$ as additives to find alternatives to DMSO-induced precipitation in the antisolvent-free process. Lower $D_N$ values in the additives result in

decreased precipitation levels in the precursor solution. Adjusting the NMP concentration, which has a relatively low $D_N$, controlled the intermediate phase in the deposited film without precipitation. A 2ME-based solution containing an optimized NMP concentration obtained a PCE of 20.29% via an antisolvent-free process.[108] Furthermore, phase-pure 2D halide perovskite stacks could be achieved by selecting solvents with appropriate dielectric constant and $D_N$.[122] Based on the works mentioned earlier, the solvent properties such as $D_N$ are closely linked to the crystallization kinetics of the perovskite films. When developing new solvent systems, these properties should be carefully considered. We have summarized some fundamental properties of commonly used solvents and antisolvents in Table 2.

**Table 2. Characteristics of commonly used solvents (S) and antisolvents (A/S) in perovskite film fabrication.**[122, 118, 123]

| Solvent[a] | Type | Boling point (°C) | Viscosity (cP) | Dielectric constant | Vapor pressure at 20°C (Torr) | Donor number (kcal $mol^{-1}$) |
|---|---|---|---|---|---|---|
| ACN | S | 82 | 0.44 | 37.5 | 72.8 | 14.1 |
| 2ME | S | 124 | 1.72 | 16.9 | 6 | 19.7 |
| DMF | S | 152 | 0.92 | 36.7 | 2.7 | 30.9 |
| DMSO | S | 189 | 2.00 | 46.7 | 0.42 | 29.8 |
| NMP | S | 202 | 1.65 | 33.0 | 0.29 | 27.3 |
| GBL | S | 204 | 1.90 | 39.1 | 1.5 | 18 |
| DMAc | S | 165 | 0.95 | 37.8 | 2.25 | 27.8 |
| PC | S | 242 | 2.50 | 64.9 | 0.59 | 15.1 |
| EA | A/S | 77.1 | 0.426 | 4.3 | 73 | 17.1 |
| CB | A/S | 131 | 0.8 | 5.62 | 9 | 3.3 |
| DE | A/S | 34.6 | 0.224 | 4.33 | 440 | 19.2 |
| ANS | A/S | 154 | 1.52 | 4.33 | 3.54 | 9.0 |
| TL | A/S | 110.6 | 0.59 | 2.38 | 21 | 0.1 |

[a]ACN, acetonitrile; 2ME, 2-methoxy-ethanol; DMF, dimethyl formamide; DMSO, dimethyl sulfoxide; NMP, N-methyl-2-pyrrolidone; GBL, γ-butyrolactone; DMAc,

dimethylacetamide; PC, propylene carbonate; EA, ethyl acetate; CB, chlorobenzene; DE, diethyl ether; ANS, anisole; TL, toluene.

### 2.4 Processing Engineering

There are two primary methods for coating perovskite films: the one-step procedure and the two-step procedure. During the one-step procedure, a perovskite film is formed by applying a solution containing all components including lead halide salts and ammonium halide salts for the formation of perovskites followed by solvent extraction to induce the nucleation and growth of perovskites. There are various ways to extract the solvents such as the antisolvent extraction method,[124] the hot-casting method,[125] the gas-quenching method,[126-127] and the vacuum flash-assisted method.[119, 128] Each of them has its advantages and challenges. Currently, most lab-scale inverted PSCs (typically <0.1 $cm^2$) are fabricated through the antisolvent extraction method. While, for the perovskite solar modules (typically > 10 $cm^2$)[129], gas-quenching and vacuum flash-assisted methods are more adaptable combining blade coating or slot-die coating methods, and this part will be further discussed in Section 7.

Conversely, in the two-step procedure, a perovskite film is formed by placing an ammonium halide salts solution onto a pre-deposited lead halide film followed by a thermal interdiffusion process to attain the final perovskite films[130] The two-step method shows attractive advantages including easy fabrication and decent performance reproducibility.[130] Moreover, lead halide films can be thermally evaporated on the substrate without using toxic DMF solvent. On a large area scale, the lead halide films prepared by vacuum evaporation exhibit remarkable uniformity and consistency. Though this method combined with the solution process, Yi et al. reported a high PCE of 24.0% (certified 23.7%) for the regular PSCs with an active area of 1 $cm^2$.[131] This method has also been used to fabricate inverted PSCs with wide bandgap perovskites on the pyramid structures, which can help realize highly uniform perovskite film.[132] Recently, regular-structured PSCs based on the two-step method

have achieved a remarkable PCE of 26.07% for a 0.08-$cm^2$ device (25.8% certified) and 24.63% for a 1-$cm^2$ device.[133] Nevertheless, the research on the inverted PSCs based on the two-step method has lagged behind that of its regular counterparts. Until now, only moderate PCEs have been realized for inverted PSCs employing the two-step method (Figure 7).[16] The origin of this result may be relevant to the substrate difference, leading to unfavorable perovskite nucleation and growth.

We postulate that through dedicated interface engineering and perovskite bulk engineering,[134] the PCE of inverted PSCs using the two-step deposition method would catch up with their regular counterpart in the near future.

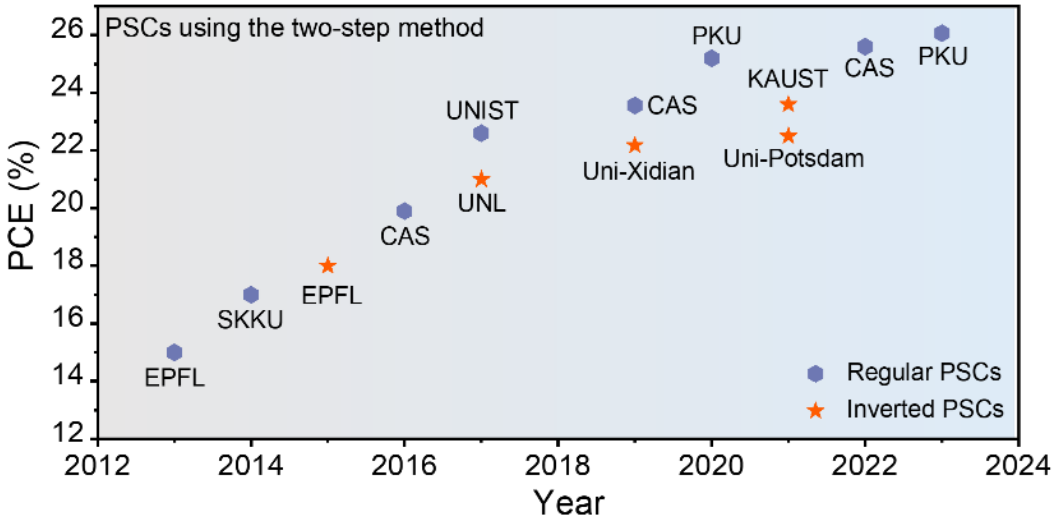


**Figure 9.** Development map of inverted and regular PSCs based on the two-step method.

Despite the huge success obtained by regular or inverted structure PSCs, these solar cells are primarily based on polycrystalline perovskite films, which inevitably possess high defect densities. To address this issue, recently, inverted PSCs with the single-crystal absorber have been developed and made huge progress.[135-136] Through interface engineering by incorporating poly(3-hexylthiophene) (P3HT) into the HTL, single-crystal $MAPbI_3$-based inverted PSCs showed an optimal PCE of 22.1%.[137] In 2021, Bakr et al. utilized a mixed-cation single-crystal perovskite to fabricate inverted PSCs with the structure of Glass/ITO/PTAA/perovskite/$C_{60}$/BCP/Cu (Figure 8a). The

single-crystal perovskite has a much lower defect density and longer carrier diffusion length compared to polycrystalline perovskite films, which makes it possible to fabricate thick light-absorbing layers. As shown in Figure 8b, the single-crystal (SC) perovskite films utilizing the space-limited inverse temperature crystallization method show film thickness ~15 μm, and the corresponding inverted PSCs delivered a champion efficiency of 22.8% with an outstanding $J_{SC}$ of 26.2 mA cm$^{-2}$ (Figure 8c).[135] Recently, in the same group, through composition engineering *via* Cs doping and modulating crystallization kinetics, the SC PSCs with an MA-free composition ($Cs_{0.05}FA_{0.95}PbI_3$) displayed a remarkable PCE of 24.29% with a $T_{90}$ of 900 h at 53°C (Figure 8d). Additionally, compared to the polycrystalline perovskite films, SC $Cs_{0.05}FA_{0.95}PbI_3$ perovskite films demonstrated enhanced stability under the damp–heat (85°C/65% RH) tests (Figure 8e).[138] Even though SC inverted PSCs have great potential, there are far fewer reports on this type of device compared to devices based on polycrystalline perovskite films.

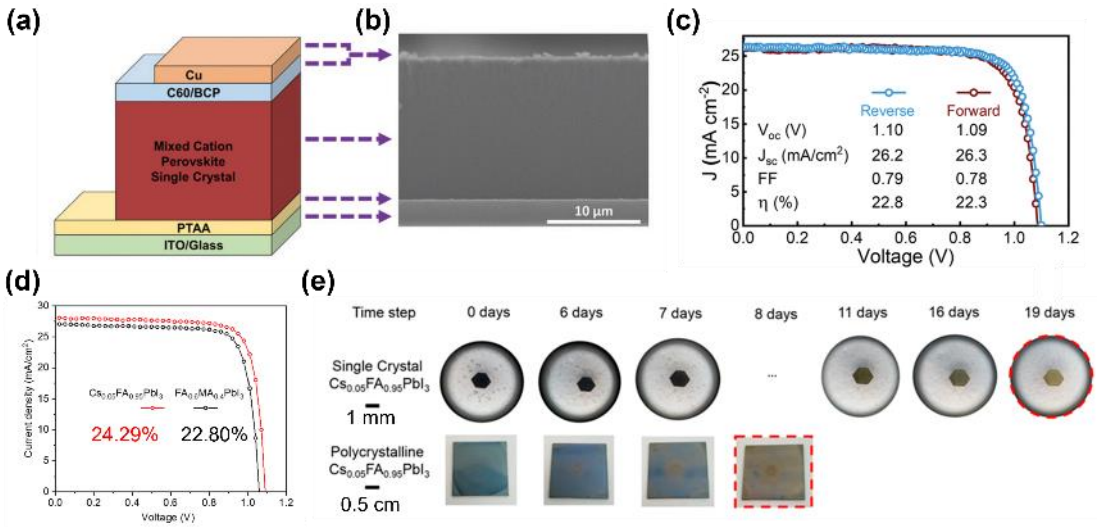


**Figure 10.** (a) Device structure of the single-crystal PSCs with the inverted structure. (b) The cross-sectional SEM image of the PSCs. (c) *J*–*V* characteristics of the best-performance devices under different scan directions. Reproduced with permission from ref [135]. Copyright 2021 Royal Society of Chemistry. (d) *J*–*V* characteristics of the champion $Cs_{0.05}FA_{0.95}PbI_3$ and $FA_{0.6}MA_{0.4}PbI_3$ inverted PSCs. (e) Photographs of

$Cs_{0.05}FA_{0.95}PbI_3$ single crystals and polycrystalline film under damp–heat ageing conditions (85°C/65% RH). Reproduced with permission from ref [138]. Copyright 2023 Royal Society of Chemistry.

## 3. CHARGE TRANSPORTING LAYERS

In a typical PSC, the perovskite light-absorbing layer is sandwiched between an HTL and an ETL, and these CTLs can not only transport the photo-generated charge carriers to the electrode but also prevent the minority charge carrier from reaching the electrode to reduce charge recombination. Since the CTL is an indispensable part of PSCs, especially for high-performance devices, its basic properties including wettability, conductivity, transparency, energy level, intrinsic stability and trap-state density directly influence the performance of the fabricated PSCs. We summarize the device architecture of the state-of-the-art inverted PSCs in Table 1. As can be seen, fullerene $C_{60}$ and its derivatives such as [6,6]-phenyl-C61-butyric acid methyl ester (PCBM) are the most commonly utilized ETLs. While for HTLs, the poly[bis(4-phenyl)(2,4,6-trimethylphenyl)amine] (PTAA) and $NiO_x$ are among the most popular choices. It is noteworthy that the emerging self-assembled monolayers (SAMs) based HTLs have attracted enormous attention and achieved remarkable device performance for both single-junction inverted PSCs and tandem PSCs over the past few years. Herein, we briefly summarize the recent development of CTLs for the high-performance inverted PSCs with special attention to the promising SAMs-based HTLs.

### 3.1 Conventional charge transporting layers

Inorganic ETLs: Commercial photovoltaic technologies like silicon and GaAs solar cells generally employ inorganic CTLs due to their superior chemical and thermal stability. And n-type semiconducting materials, such as titanium dioxide ($TiO_2$) and tin(IV) dioxide ($SnO_2$) have been widely used in regular PSCs and achieved impressive PCEs approaching the best PCE of crystalline silicon solar cells. However, due to the technical difficulties (e.g., high-temperature annealing process,

incompatible solvents, etc.) and inferior band-alignment, it is challenging to construct inverted PSCs with such inorganic ETLs directly atop the perovskite layer. Recently, Zhang et al. reported that $SnO_2$ nanoparticles (NPs) in butanol solution could be directly deposited on the perovskite layer by a solution process without damaging the underlying perovskite layer. The additional PCBM layer atop the $SnO_2$ layer was desirable for passivating defects within $SnO_2$ (i.e., oxygen vacancies). Furthermore, the band mismatch between $SnO_2$ and perovskite could be minimized, resulting in an improved PCE of 23.5%.[139] Currently inserting an inorganic ETL between fullerene $C_{60}$ or its derivatives and cathode for the inverted PSCs is a popular choice, contributing to significantly improved long-term stability. To improve damp-heat (85°C/85% of relative humidity) stability, Wolf's group replaced organic SAM HTL with inorganic $NiO_x$. Additionally, a ~10 nm layer of $SnO_2$ and an 80 nm layer of indium zinc oxide (IZO) via atomic layer deposition (ALD) and sputtering techniques, respectively, were deposited atop the $C_{60}$ sequentially. The fabricated inverted PSCs, when combined with encapsulation, can effectively shield against the invasion of moisture and oxygen present in the ambient environment, thereby ensuring remarkable stability of the devices.[16]

Organic ETLs: At present, the ETL for inverted PSCs is largely dependent on the fullerene $C_{60}$ and its derivatives PCBM owing to their excellent electrical properties and physical softness. In addition, it was acknowledged that fullerenes are capable of filling pinholes in the perovskite layer and passivating defects,[140-141] eliminating the current−voltage hysteresis and giving rise to a higher PCE. Typically, the PCBM using nonpolar CB as the solvent, which is orthogonal to the processing solvent for the perovskite film, could protect the perovskite layer from erosion in the subsequent layer deposition. It is worth noting that in recent years indene-$C_{60}$ bisadduct (ICBA) has emerged as a promising ETL for Sn-based inverted PSCs due to improved energy level alignment, contributing to the unprecedented enhancement of $V_{OC}$.[142-143] However, due to the inappropriate energy alignment between fullerene and metal

cathode, charge accumulation would emerge, inducing the loss of FF. To reduce the carrier recombination and form an ideal ohmic contact at the ETL/electrode interface, an ultra-thin interfacial buffer layer is generally adopted such as bathocuproine (BCP), LiF, polyethyleneimine ethoxylated (PEIE), bathophenanthroline (Bphen), 1,3,5-Tris(1-phenyl-1H-benzimidazol-2-yl)benzene (TPBi). Nevertheless, it was reported that the utilization of such organic buffer layers would cause thermal instability, restricting real-life application.[144] Furthermore, it should be noted that $C_{60}$ and PCBM are pricy. Taking $C_{60}$ for an example, the price of $C_{60}$ is around 160,000 \$ $kg^{-1}$, and the material cost of fabricating 1-$m^2$ inverted perovskite modules is 4 \$ $m^{-2}$.[145] because of the additional synthetic process, the price of PCBM with the advantages of solution-processing is even higher than that of $C_{60}$. Therefore, constructing fullerene-free inverted PSCs is a promising research direction with the aim of further reducing the device cost.

Inorganic HTLs: Compared to organic HTLs, inorganic HTLs have higher intrinsic thermal and moisture stability, there are various types of inorganic p-type semiconducting materials which are suitable to be used in inverted PSCs including antimony-doped tin oxides (ATO), nickel oxide ($NiO_x$), copper compounds (e.g., $Cu_xO$, CuI, CuS, CuSCN).[11, 55] Moreover, some inorganic transition metal oxides, which are highly n-type semiconducting materials, can also be used to selectively transport holes like vanadium oxide ($VO_x$), molybdenum oxide ($MoO_x$), tungsten oxide ($WO_x$).[146]

Among them, $NiO_x$ is attracting the most research attention due to its advantages like low cost, high optical transmittance ($E_g$ over 3.4 eV), suitable work function ($W_F$) and excellent chemical stability.[147] The $NiO_x$ film can be deposited via various methods, such as sol-gel, sputtering, ALD, electrodeposition, e-beam evaporation, combustion, and indirect nanoparticle deposition, making it a readily accessible HTL.[148] Recently, Sargent and coworkers achieved an excellent quasi-steady-state certified PCE of 25.1% by employing the $NiO_x$ HTL, where the $NiO_x$ film was prepared by spin-coating the

$NiO_x$ nanoparticles. In addition, through further interface modification (The detailed discussion is given in the following section), the encapsulated inverted PSCs showed excellent long-term thermal stability following the ISOS-D-2 protocol.[51] Despite the huge success of p-type $NiO_x$ film, the $NiO_x$ film suffers from some limitation: 1) The $NiO_x$ displays a relatively low intrinsic conductivity of $10^{-4}$ S $cm^{-1}$; 2) The energy level mismatch between the $NiO_x$ and the perovskite tends to reduce the built-in field of PSCs due to the fact that valance band maximum (VBM) of $NiO_x$ is not deep enough (–5.4 eV) ; 3) There are too much surface defects on $NiO_x$ surface like $Ni^{3+}$, which would react with the $FA^+$ or $I^-$ presented in the perovskite layer, leading to the loss of the PCEs.[147, 149] Numerous approaches have been developed to improved conductivity, modify te work function, and passivate the surface defects of $NiO_x$, and these methods can be generally categorized into elemental doping, physical treatment, and chemical treatment.[148]

For the elemental doping method, the introduced dopants include alkali/alkaline metal (e.g., Li, Cs, Mg, Sr), rare-earth metal (e.g. Y, La, Ce, Nd, Eu, Tb, and Yb), transition metal (e.g., Cu, Ag, Co, Zn), and small molecule (e.g., F6TCNNQ).[148-149] An early work by Han et al. reported that doping 5 mol% Li and 15 mol% Mg into the $NiO_x$ lattice could improve the lattice stability and enhance film conductivity ($2.32 \times 10^{-3}$ S $cm^{-1}$). The resulting inverted PSCs with an aperture area greater than 1 $cm^2$ delivered a certified PCE exceeding 15%.[150]Another notable alkali metal dopant is Cs. In 2017, He et al. prepared Cs-doped $NiO_x$ to construct inverted PSCs. They observed that compared to the pristine $NiO_x$ film, the Cs-doped $NiO_x$ (Cs:$NiO_x$) film exhibited significantly improved hole extraction ability confirmed by the conductive atomic force microscopy (AFM) measurement (Figure 9a,b). Furthermore, incorporating Cs into the $NiO_x$ can elevate the work function, which corresponds to a reduction in the Highest Occupied Molecular Orbital (HOMO) energy level. This adjustment results in improved band alignment between the $NiO_x$ and the perovskite layer, facilitating more efficient charge transfer and overall device performance.[151] The transition metal Cu

own similar ionic radii, similar crystal structure (face-centered cubic), and similar electronegativity as Ni, which has also been successfully doped into $NiO_x$. Early in 2015, Jen and coworkers managed to obtain Cu-doped $NiO_x$ and observed an enhanced electrical conductivity ($8.4 \times 10^{-4}$ S $cm^{-1}$ for Cu-doped $NiO_x$ versus $2.2 \times 10^{-6}$ S $cm^{-1}$ for pristine $NiO_x$). This work demonstrates that incorporating Cu into $NiO_x$ is an efficient and simple strategy to enhance its properties as a HTL for high-performance inverted PSCs.[152] Later, He et al. thoroughly studied the Cu doping mechanism for the $NiO_x$, and the Cu-doped $NiO_x$ (Cu:$NiO_x$) film was attained by spin-coating the nanoparticle ink with the stoichiometric ratio of 5.3% relative to nickel. It was found that there was a clear increase in the conductivity from 0.12 $cm^2$ $V^{-1}$ $s^{-1}$ for un-doped $NiO_x$ to 2.53 $cm^2$ $V^{-1}$ $s^{-1}$ for Cu:$NiO_x$ according to Hall measurements. They suggest that the Cu:NiO films led to more efficient charge extraction due to a favorable shift in the work function and improved energy level alignment with the perovskite layer. When introduced into the fabrication of inverted PSCs on both rigid and flexible polyethylene naphthalate (PEN) substrates, high PCEs of 20.26% and 17.41% were achieved, respectively (Figure 9c,e).[153] Through further optimization of ETL and contact passivation, the Cu:$NiO_x$-based inverted PSCs recently gained a PCE of 22% (Figure 9f,g).[154]

Another effective way to modify the properties of $NiO_x$ films is by physical surface treatments including UV-ozone plasma treatment, oxygen, argon, and/or helium plasma treatment.[119, 148] The investigation of $NiO_x$ films subjected to UV-ozone treatment by Saraswat et al. reveals a significant reduction in film resistivity and an increase in ionization potential. Moreover, this treatment altered the film stoichiometry, creating Ni vacancies that contribute to the material's p-type semiconducting behavior. Angle-resolved XPS measurements confirmed that these changes occurred throughout the film's depth, not just at the surface.[155] Moreover, after the UV-ozone treatment, nickel oxyhydroxide (NiOOH) was formed on $NiO_x$ surface, creating a large surface dipole and increasing $W_F$ of the $NiO_x$ film.[156]

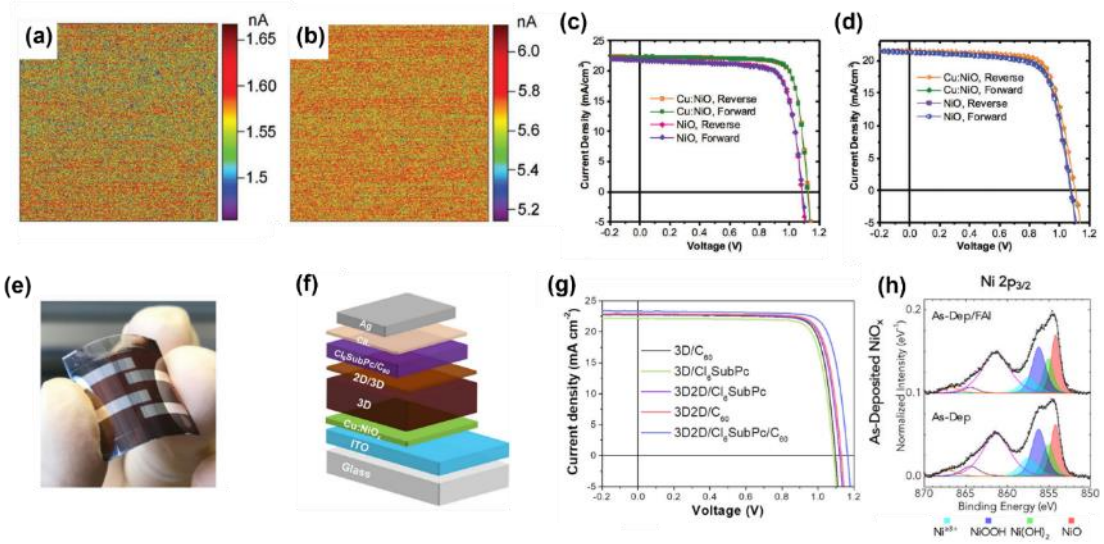


**Figure 11**. Conductive-atomic force microscopy (AFM) images of the $NiO_x$ (a) and Cs:$NiO_x$ (b) films coated on FTO glass. Reproduced with permission [151]. Copyright 2017 John Wiley and Sons. (c) *J*–*V* characteristics of $NiO_x$ and Cu: $NiO_x$ -based inverted PSCs at reverse and forward scan conditions on the rigid substrate (c) and flexible substrate (d). (e) Photograph of the Cu:$NiO_x$ HTL-based flexible inverted PSCs. Reproduced with permission from ref [153]. Copyright 2018 John Wiley and Sons. (f) Scheme for the device architecture with the inverted structure based on the Cu:$NiO_x$ HTL. (g) *J*–*V* characteristics of the PSCs based on various modifications. Reproduced with permission from ref [154]. Copyright 2021 Elsevier. (h) Ni 2p2/3 X-ray photoelectron spectroscopy (XPS) of $NiO_x$ films before (bottom) and after (top) being treated with FAI. Reproduced with permission from ref [157]. Copyright 2020 Elsevier.

The $NiO_x$ film tends to exist with abundant impurities/surface defects (e.g., surface hydroxyl groups ($OH^-$), $Ni^{\geq 3+}$), inducing notorious non-radiative recombination. Moreover, it was reported that the under-coordinated metal cation sites ($Ni^{\geq 3+}$) in $NiO_x$ could deprotonate cationic amines and oxidize iodide species in perovskites, forming a $PbI_2$-rich hole extraction barrier and leading to a severe interfacial charge recombination (Figure 9h).[157] In order to alleviate the surface defect states of $NiO_x$ and attain better contact at the perovskite buried interface, it is necessary to pretreat the $NiO_x$ thin film before depositing the perovskite film. A variety of tailored

materials such as SAM,[158-160] alkali halide, polymer, small molecular, have been developed to treat the $NiO_x$ film to reduce the trap states of both $NiO_x$ and buried interface of perovskite films, which exerts a significant influence on the device performance. A detailed discussion about the related works is given below).

Organic HTLs: Organic HTLs demonstrate advantages of low-temperature processability, tunable properties through chemical synthesis, and simple preparation, making them popular candidates as HTL to fabricate a variety of electronic devices (e.g., light-emitting diodes, photodetectors, organic thin-film transistors).[4, 140] Initially, in 2013, poly(3,4-ethylenedioxythiophene)−poly(styrenesulfonate) (PEDOT:PSS) which is a popular HTL for another thin-film technology (i.e., organic solar cells) was utilized as the HTL for the first inverted PSCs. This HTL exhibits many advantages like low-temperature processing, appropriate highest occupied molecular orbital (HOMO) energy level (−5.5 eV), excellent light transmission, and good conductivity. However, due to its acidic and hygroscopic nature, the PEDOT:PSS-based PSCs generally show unfavorable device stability, which limits their application. Nevertheless, it is worth noting that most inverted Sn or mixed Sn-Pb PSCs utilize PEDOT:PSS as the HTL.[161] This is primarily influenced by the following factors. Firstly, PEDOT:PSS is a well-established and extensively utilized conductive polymer blend and shows many advantages including high conductivity, transparency, compatibility, and ease of film deposition. Secondly, the PEDOT:PSS shows excellent wettability,[162] which provides sufficient nucleation sites for the rapid crystallization of Sn-containing perovskite films without any pinholes.[163] Thirdly, PEDOT:PSS exhibits redox-inactive properties under normal conditions, which helps to minimize the possibility of Sn(II) oxidation in Sn-containing perovskites.

Later, numerous organic semiconducting polymers and small organic molecules like PTAA and poly(N,N'-bis-4-butylphenyl-N,N'-bisphenyl)benzidine (poly-TPD) have been introduced into the inverted PSCs. Among these materials, PTAA has become a popular HTL candidate for high-performance inverted PSCs because of its ease of

fabrication, high transparency, mechanical flexibility, decent conductivity, and stability. In addition, hydrophobic PTAA is conductive to enlarge the grain size of perovskite.[162] Nonetheless, the non-wetting nature of PTAA is likely to induce solution processing difficulties. To address this issue, several methods such as oxygen plasma treatment,[164] DMF pre-wetting,[165] and introducing an interlayer on PTAA[166] have been reported. It should be noted that oxygen plasma treatment would damage the organic PTAA. In early studies on PTAA, doping like F4TCNQ is necessary to increase the conductivity of PTAA,[167] and the doped-PTAA HTL generally shows large thickness. However, the addition of hydrophilic dopant F4TCNQ could impair device stability. Therefore, dopant-free PTAA HTL is a promising choice for fabricating stable inverted PSCs, and the ultrasmooth surface of the commercial ITO-coated glass makes it possible to coat ultra-thin non-doped PTAA. Recently, with the assistance of perovskite surface modification, the non-doped PTAA-based inverted PSCs have achieved a champion PCE of 25.0% (with a certified PCE of 24.3%) and demonstrated excellent stability under the international standards for mature photovoltaics.[17] This result indicates the great potential of non-doped PTAA as the HTL. However, it is important to consider that PTAA, like other organic CTLs such as $C_{60}$ and PCBM, comes with a significant price tag (US$423.3 $g^{-1}$), which may partially offset the inherent cost advantages of inverted PSCs in terms of material expenses.[168] In addition, for polymeric HTLs, the batch-to-batch variation of polymers greatly restricts the performance reproducibility. Small-molecule HTLs (SM-HTLs), which are usually easy to be synthesized and purified, are known as promising alternatives to address this issue. For instance, Wang and coworkers designed and synthesized two imide-functionalized thiophene-based SM-HTMs named MPA-BTI and MPA-BTTI. When introduced into the construction of inverted PSCs, the MPA-BTTI-based solar cells delivered a champion efficiency exceeding 21% because of the decent hole-transporting ability and energy-level alignment with the perovskite layer. Furthermore, it was observed that the MPA-BTTI-based PSCs exhibited better long-

term stability compared to the PEDOT:PSS, $NiO_x$, and PTAA-based devices, which paves a new avenue for fabricating stable and efficient PSCs.[169] Recently, in the same group, they used a novel dendritic engineering strategy to design dopant-free SM-HTLs, namely MPA-Cz-BTI and MCz-Cz-BTI. The diphenylamine and/or carbazole were chosen as the building blocks for dendrons. Both MPA-Cz-BTI and MCz-Cz-BTI exhibited good thermal stability and highly smooth surfaces. Benefiting from these, the inverted PSCs based on MPA-Cz-BTI delivered an excellent FF of 85.2% and MPA-Cz-BTI-based devices showed an optimal PCE of 21.35%.[170]

### 3.2 Emerging charge transporting layers - SAMs

SAM-based HTLs are 2D nanomaterials with the thickness of one or few molecules formed by molecules with certain functional properties spontaneously adsorbed on solid/liquid or gas/solid interfaces through chemical bonding or supramolecular interactions.[171-173] In the past three years, the SAM HTLs have greatly improved the PCE of both single-junction and tandem inverted PSCs, attracting enormous research interest.[174] The SAM HTLs demonstrate some unique advantages: 1) in-situ and spontaneous formation; 2) thermodynamically stable; 3) high tolerance to the morphology of the substrates; 4) low material consumption; 5) ordered molecular arrangement; 6) tunable physical and chemical properties; 7) green-solvent processibility. Typically, SAMs consist of three key groups: anchor, linker, and tail. And Different groups exert different functions (Figure 10a)

Anchor: Thermodynamic adsorption process is the crux to molecular self-assembly on the surface, which is determined by the high-affinity anchor bonding with the substrate. In SAMs for inverted PSCs, phosphoryl acid (PA) and carboxyl acid (CA) are extensively utilized anchors that are bound tightly to inorganic oxide substrates such as ITO, FTO, and $NiO_x$. Monodentate, bidentate, and tridentate bonds to the substrate are formed 1) by recombination of a water molecule via protonation of a surface -OH group by PA or CA groups and 2) when a dissociated water molecule reassembles to provide an empty adsorption site for the oxygen atom from the PA or

CA molecules. Different combinations of anchor and substrate vary the binding energy between them, e.g., phosphonates are more strongly bound to aluminum oxide than carboxylates, so carboxylates can be replaced easily by phosphonates.[175]

Linker: The linker connects the SAMs' anchor to the tail and usually consists of aliphatic chains. The lateral self-assembly of individual molecules is governed by Van der Waals interaction among the linkers. It has been reported that the long linker length of 6 carbon atoms could contribute to current-voltage hysteresis of inverted PSCs.[176]

Tail: The tail of the SAMs, also known as the functional group, directly interacts with the perovskite layer, significantly influencing crystal growth, morphology, and the work function of the deposited perovskite layer.[171, 173, 177] Moreover, SAMs with carbazole-, phenothiazine-, or triphenylamine-based cores and passivating groups such as amines or thiols can effectively passivate defects at the bottom interface of perovskite films. Carbazole and its derivatives are the most widely used in SAMs' tails to regulate the interfacial interaction and have greatly boosted the device PCEs and longevity.[176, 178]

Early works on SAMs-based inverted PSCs only realized moderate PCEs below 20%. The breakthrough work that facilitates SAMs into wild application in inverted PSCs was reported by Getautis, Albrecht, and coworkers in 2018, who designed and synthesized a new SAM V1036. This is the first example of a carbazole-based SAM with phosphonic acid as the anchoring group (Figure 10b). The V1036 SAM had a weaker absorption in the visible range and negligible parasitic absorption, which was conducive to obtaining a higher $J_{SC}$ in comparison to PTAA-based devices (Figure 10c-e). Additionally, it was demonstrated that the introduction of butylphosphonic acid could modify the perovskite film morphology and ionization potential, contributing to an improved PCE. This work indicates the great promise of SAM-based HTLs.[179] Since then, SAMs containing phosphonic acid and carbazole derivate

groups have been extensively applied to the inverted PSCs as HTLs, achieving huge enhancement on PCEs together with excellent device stability as discussed below.[180]

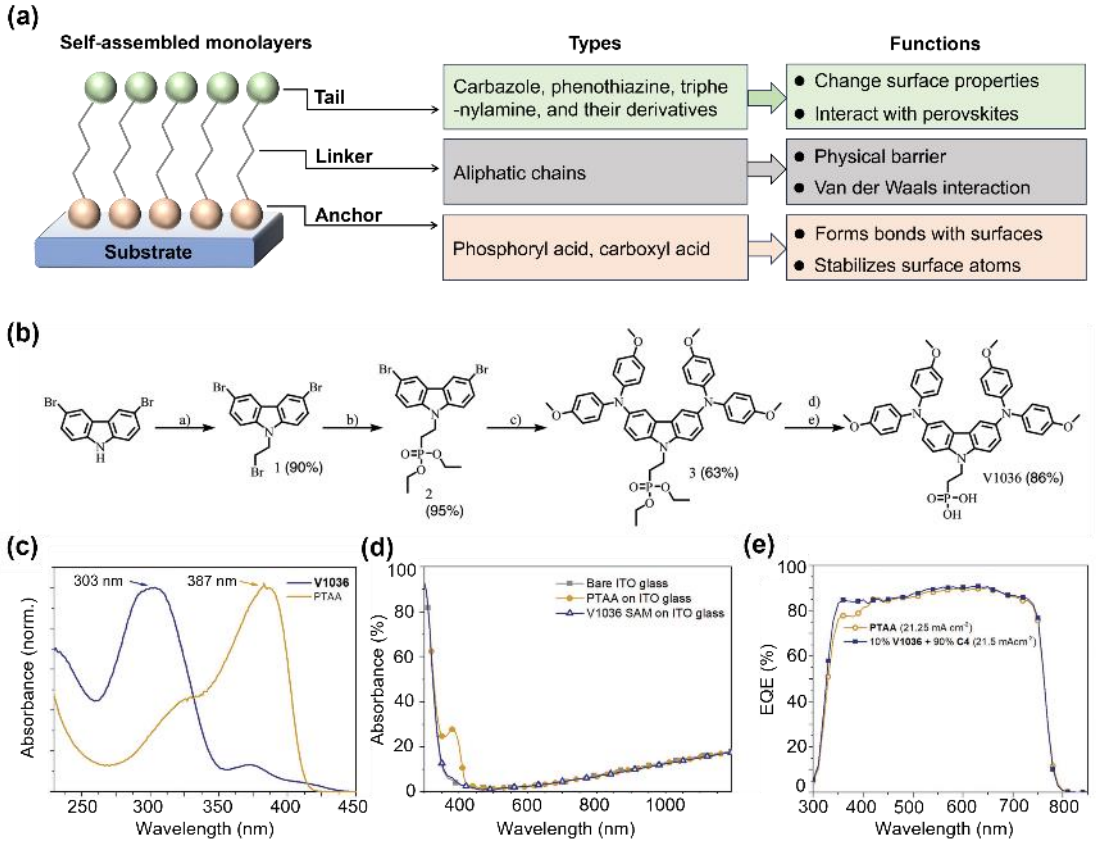


**Figure 12**. (a) Schematic illustration of the structure, types, and functions of SAMs.[181] (b) Synthetic route for SAM V1036. (c) UV–vis absorption spectra of PTAA and V1036. (d) UV–vis absorption spectra of the ITO-coated glass, ITO with PTAA, and ITO with V1036. (e) External quantum efficiency spectra of the inverted PSCs based on PTAA HTL and SAM containing 10% V1036 and 90% butylphosphonic acid (C4). Reproduced with permission from ref [179]. Copyright 2018 John Wiley and Sons.

Subsequently, following the pioneering work mentioned above, Albrecht and coworkers synthesized three molecules named 2-(9H-carbazol-9-yl)ethyl)phosphonic acid (2PACz), 2-(3,6-dimethoxy-9H-carbazol-9-yl)ethyl)phosphonic acid (MeO-2PACz), and 4-(3,6-dimethyl-9H-carbazol-9-yl)butyl)phosphonic acid (Me-4PACz), and then employed them in monolithic perovskite/Copper Indium Gallium Selenide

(CIGSe) or monolithic perovskite/silicon tandem devices.[177-178] The SAM 2PACz or MeO-2PACz was inserted into the ITO/perovskite interface to enable conformal coverage of oxide surfaces and create an energetically aligned interface.[178] The monolithic perovskite/CIGSe tandem device with MeO-2PACz was endowed with a higher $V_{OC}$ than PTAA-based PSCs, delivering a certified PCE of 23.26% on an active area of 1 $cm^2$. Moreover, the monolithic perovskite/silicon tandem device with a certified PCE of 29.15% was realized with the help of Me-4PACz.[176] The use of Me-4PACz was effective in promoting hole extraction, suppressing non-radiative recombination, and mitigating phase instability, resulting in an outstanding FF of 84%. Further discussion about the use of the SAM HTLs in perovskite-silicon and all-perovskite tandem devices is shown in Section 6. The above works by Albrecht et al. represent a milestone in promoting the application of SAMs in inverted PSCs and continuously enhancing the performance of inverted PSCs to catch up with their regular counterparts. Since then, inverted PSCs have extensively employed 2PACz, MeO-2PACz, and Me-4PACz as HTLs, and showcased their excellent efficacy in constructing high-performance inverted PSCs and compatibility with a broad range of perovskites, including Pb-based,[14, 160, 182] Sn-based,[183] and mixed Sn−Pb perovskites.[76] We summarize the performance parameters of the representative state-of-the-art inverted PSCs using SAMs in Table 3 and the molecular structures of these SAMs are displayed in Figure 11.

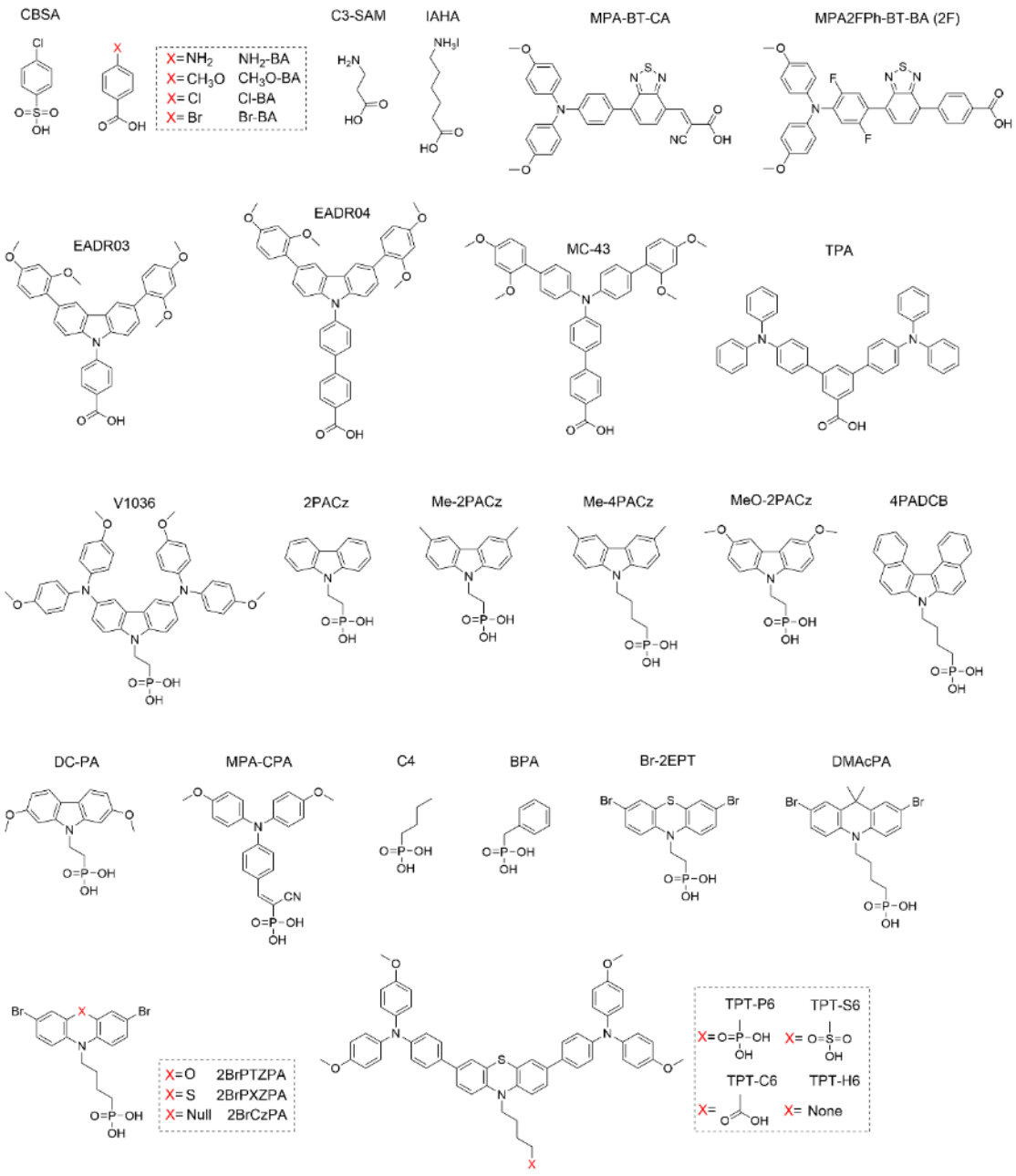


**Figure 13.** Chemical structure of the representative self-assembling monolayers (SAMs) for the fabrication of inverted PSCs.

**Table 3. A summary of representative inverted PSCs based on SAM HTLs. The device performance and key parameters are provided.**

| SAM | Anchor | Linker | Tail[b] | Device configuration | $V_{OC}$ (V) | $J_{SC}$ (mA cm$^{-2}$) | FF | PCE (%) | Year | Ref. |
|---|---|---|---|---|---|---|---|---|---|---|
| C3-SAM | Ammonium | Ethyl | Carboxylic acid | ITO/PEDOT:PSS/SAM/$CH_3NH_3PbI_{3-x}Cl_x$/ PCBM/ZnO NPs/Ag | 0.89 | 18.9 | 0.69 | 11.6 | 2015 | 184 |
| Br-BA | Carboxylic acid | - | Br-phenyl | FTO/$NiO_x$/SAM/$CH_3NH_3PbI_3$/PCBM/ Bis-$C_{60}$/Ag | 1.11 | 21.7 | 0.76 | 18.4 | 2017 | 185 |
| V1036 | Phosphonic acid | Ethyl | Carbazole# | ITO/SAM/$Cs_{0.05}(MA_{0.17}FA_{0.83})_{0.95}Pb(I_{0.83}Br_{0.17})_3$/$C_{60}$/BCP/Cu | 1.09 | 21.9 | 0.81 | 17.8 | 2018 | 179 |
| MC-43 | Carboxylic acid | Biphenyl | Amino# | ITO/SAM/$CH_3NH_3PbI_3$/PCBM/Ag | 1.07 | 20.3 | 0.80 | 17.3 | 2019 | 186 |
| MPA-BT-CA | Carboxylic acid | | | ITO/SAM/$(FA_{0.17}MA_{0.94}PbI_{3.01})_{0.95}(PbCl_2)_{0.05}$ /$C_{60}$/BCP/Ag | 1.11 | 22.4 | 0.82 | 20.5 | 2020 | 187 |
| 2PACz | Phosphonic acid | Ethyl | Carbazole | ITO/SAM/$Cs_{0.05}(MA_{0.17}FA_{0.83})_{0.95}Pb(I_{0.83}Br_{0.17})_3$/$C_{60}$/BCP/Cu | 1.19 | 21.9 | 0.80 | 20.9 | 2019 | 178 |
| | | | | ITO/SAM/$Cs_{0.18}FA_{0.82}PbI_3$/$C_{60}$/BCP/Ag | 1.16 | 23.5 | 0.83 | 22.7 | 2021 | 188 |
| | | | | ITO/SAM/$Cs_{0.03}(FA_{0.90}MA_{0.10})_{0.97}PbI_3$ /$C_{60}$/BCP/Ag | 1.21 | 24.5 | 0.82 | 24.3 | 2022 | 180 |
| | | | | ITO/SAM/$Cs_{0.1}FA_{0.9}PbI_3$/$C_{60}$/BCP/Ag | 1.16 | 25.8 | 0.82 | 24.5 | 2023 | 189 |
| MeO-2PACz | Phosphonic acid | Ethyl | Carbazole# | ITO/SAM/$Cs_{0.05}(FA_{0.98}MA_{0.02})_{0.95}Pb(I_{0.98}Br_{0.02})_3$/PCBM/BCP/Ag | 1.18 | 24.8 | 0.84 | 24.6 | 2023 | 63 |
| Me-4PACz | Phosphonic acid | Butyl | Carbazole# | ITO/SAM/$Cs_{0.05}(FA_{0.77}MA_{0.23})_{0.95}Pb(I_{0.77}Br_{0.23})_3$/LiF/$C_{60}$/$SnO_2$/Ag | 1.15 | 20.3 | 0.84 | 20.0 | 2020 | 176 |
| | | | | ITO/SAM/$(FA_{0.95}MA_{0.05})_{0.95}Cs_{0.05}Pb(I_{0.95}Br_{0.05})_3$/LiF/$C_{60}$/BCP/Ag | 1.21 | 25.1 | 0.84 | 25.6 | 2023 | 57 |
| | | | | ITO/$NiO_x$/SAM/$FAPbI_3$/ /PCBM/$SnO_2$/Cu | 1.16 | 26.2 | 0.84 | 25.6 | 2023 | 58 |
| | | | | FTO/$NiO_x$/SAM/$FA_{0.95}Cs_{0.05}PbI_3$ /$C_{60}$/$SnO_2$/Ag | 1.16 | 25.7 | 0.83 | 24.5 | 2023 | 65 |
| | | | | FTO/SAM/$Cs_{0.05}(FA_{0.98}MA_{0.02})_{0.95}PbI_3$/ $C_{60}$/BCP/Cu | 1.18 | 25.7 | 0.86 | 26.2 | 2023 | 52 |

| | | | | | | | | | | |
|---|---|---|---|---|---|---|---|---|---|---|
| EADR03<br>EADR04 | Carboxylic acid | Phenyl<br>Biphenyl | Carbazole# | ITO/SAM/($Cs_{0.05}FA_{0.79}MA_{0.16}Pb(I_{0.84}Br_{0.16})_3$ /$C_{60}$/BCP/Cu | 1.16<br>1.16 | 22.9<br>22.6 | 0.80<br>0.80 | 21.2<br>21.0 | 2021 | 190 |
| Br-2EPT | Phosphonic acid | Ethyl | Phenothiazine# | FTO/SAM/$Cs_{0.05}(FA_{0.92}MA_{0.08})_{0.95}Pb(I_{0.92}Br_{0.08})_3$/$C_{60}$/BCP/Ag | 1.09 | 25.1 | 0.82 | 22.4 | 2021 | 191 |
| BPA | Phosphonic acid | - | Benzyl | ITO/$NiO_x$/SAM/$Cs_{0.25}FA_{0.75}Pb(I_{0.6}Br_{0.4})_3$ /$C_{60}$/BCP/Ag | 1.26 | 17.9 | 0.79 | 17.8 | 2022 | 159 |
| DC-PA/ IAHA | Phosphonic acid/Carboxylic acid | Ethyl/ Pentyl | Carbazole#/ $NH_3^+$ | ITO/SAM/$Cs_{0.05}MA_{0.15}FA_{0.80}PbI_3$/ $C_{60}$/BCP/Ag | 1.16 | 24.7 | 0.83 | 23.6 | 2022 | 72 |
| 2PACz/ MPA | Phosphonic acid | Ethyl | Carbazole | FTO/SAM/$Cs_{0.025}FA_{0.475}MA_{0.5}Sn_{0.5}Pb_{0.5}I_{2.925}Br_{0.075}$/PCBM/$C_{60}$/BCP/Ag | 0.88 | 32.8 | 0.80 | 23.3 | 2022 | 76 |
| CBSA | Sulfonic acid | - | p-chlorobenzene | ITO/$NiO_x$/SAM/$Cs_{0.05}(FA_{0.92}MA_{0.08})_{0.95}(I_{0.92}Br_{0.08})_3$/PCBM/BCP/Ag | 1.11 | 24.0 | 0.81 | 21.8 | 2022 | 192 |
| 2BrPXZPA | Phosphonic acid | Butyl | Phenoxazine# | ITO/$NiO_x$/SAM/$Cs_{0.05}(FA_{0.85}MA_{0.15})_{0.95}Pb(I_{0.85}Br_{0.15})_3$/PCBM/BCP/Ag | 1.21 | 23.5 | 0.82 | 23.7 | 2023 | 193 |
| DMAcPA | Phosphonic acid | Butyl | Phenothiazine# | ITO/SAM/perovskite/PCBM/BCP/Ag | 1.19 | 25.7 | 0.85 | 25.9 | 2023 | 13 |

[a]The '#' represents its derivatives.

Despite the great success of these SAMs, creating a dense and uniform SAM coverage is still challenging, posing a threat to the device longevity and broadening performance distribution. To address this issue, a widely-used approach is to use mixed SAMs containing relatively small and large SAMs.[194] The co-adsorption of these SAMs on the substrate is beneficial for achieving a homogeneous distribution of SAMs. For example, Jen et al. treated the ITO electrode with co-assembled SAMs including 6-(iodo-$\lambda^5$-azanyl) hexanoic acid (IAHA) and a newly designed SAM, (2,7-dimethoxy-9H-carbazol-9-yl) methyl) phosphonic acid (DC-PA) (Figure 12a,b). In DC-PA, the 2,7-substituted methoxy groups were introduced in the terminal groups, instead of 3,6-substituted methoxy groups in MeO-2PACz, which helped form aligned energy levels and a favorable dipole moment. Through strategically adjusting the ratio of co-SAM components (i.e., DC-PA: IAHA), an excellent SAM coverage and good passivation effect for the top perovskite layer were simultaneously realized, leading to a champion PCE of 23.59%.[72] In a similar manner, Sargent and coworkers blended the 2PACz with 3-mercaptopropionic acid (3-MPA) to treat the textured FTO substrate. The use of 3-MPA as a co-adsorbent could break apart 2PACz clusters, which was beneficial for obtaining a more homogeneous distribution of phosphonic acid molecules. The FTO substrate with mixed SAMs exhibited a narrower contact potential difference distribution compared to the control sample as evidenced by kelvin probe force microscopy (KPFM) measurements (Figure 12c). The high-angle annular dark-field (HAADF) scanning transmission electron microscopy (STEM) further verified the improvement of SAM uniformity and coverage after introducing 3-MPA (Figure 12d). As a result, the inverted PSCs based on this co-adsorbent strategy yielded an impressive PCE of 25.3% (certified quasi-steady-state PCE of 24.8%) together with excellent stability under International Summit on Organic Photovoltaic Stability (ISOS)-L-3 protocols (Figure 12e,f). [61] This strategy is also applicable to fabricate efficient Sn-Pb PSCs. Hayase et al. found that the coabsorption of 2PACz and a small organic molecule methyl phosphonic acid (MPA) on FTO led to

reduced trap-assisted recombination compared to perovskite films coated on PEDOT:PSS. When incorporated into the construction of Sn-Pb PSCs, a champion PCE of 23.23% was obtained with a $V_{OC}$ of 0.88 V, an FF of 0.80, and a $J_{SC}$ of 33.13 mA $cm^{-2}$, which was much higher than PSCs based on 2PACz (21.39%) or PEDOT:PSS (21.37%) (Figure 12g). Additionally, the use of 2PACz/MPA HTL could suppress the oxidization of $Sn^{2+}$, contributing an enhanced device stability.[76] Another effective approach to obtaining dense and homogeneous SAM coverages is the rational design of the molecular structure. To enhance the uniform coating of SAMs on the substrate, it was advantageous to weaken the π-π intermolecular interaction of SAMs. To accomplish this objective, the introduction of benzene rings into the carbazole group was found to impede the aggregation of SAMs, leading to improvements in both SAM and perovskite coverage (A detailed discussion of these works is presented in Section 6).[195-196] According to reports, solutions of widely-used carbazole phosphonic acid (PACz)-containing SAMs are expected to initially fill the nano-size valley of transparent conductive oxides (TCO), leading to the stacking of multilayer SAMs. Due to the non-conjugated nature of commonly used SAMs' linker (i.e., non-conjugated alkyl chains), they exhibit insulating properties, and charge carriers need to tunnel through these insulating SAMs. Consequently, a thick PACz-based SAM would hamper charge transportation. To solve this problem, Chen et al. designed and synthesized a novel type SAM by polymerizing carbazole phosphonic acid small molecules. The resultant Poly-4PACz with a conjugated backbone that supports electron delocalization showed enhanced conductivity, contributing to a reduced sensitivity to layer thickness and surface roughness (Figure 12h). This was desirable for the scalable coating of perovskite films. As a consequence, the small-area PSC and perovskite solar module achieved impressive PCEs of 24.4% and 20.7% (aperture area 25.0 $cm^2$), respectively.[197] Very recently, Hou et al. reported that flattening the ITO surface by plasma treatment could also help obtain a conformally distributed 2PACz layer, suppressing the interface energy loss and enhancing the

PCEs from 22.7% to 24.5% (Figure 12i).[189]

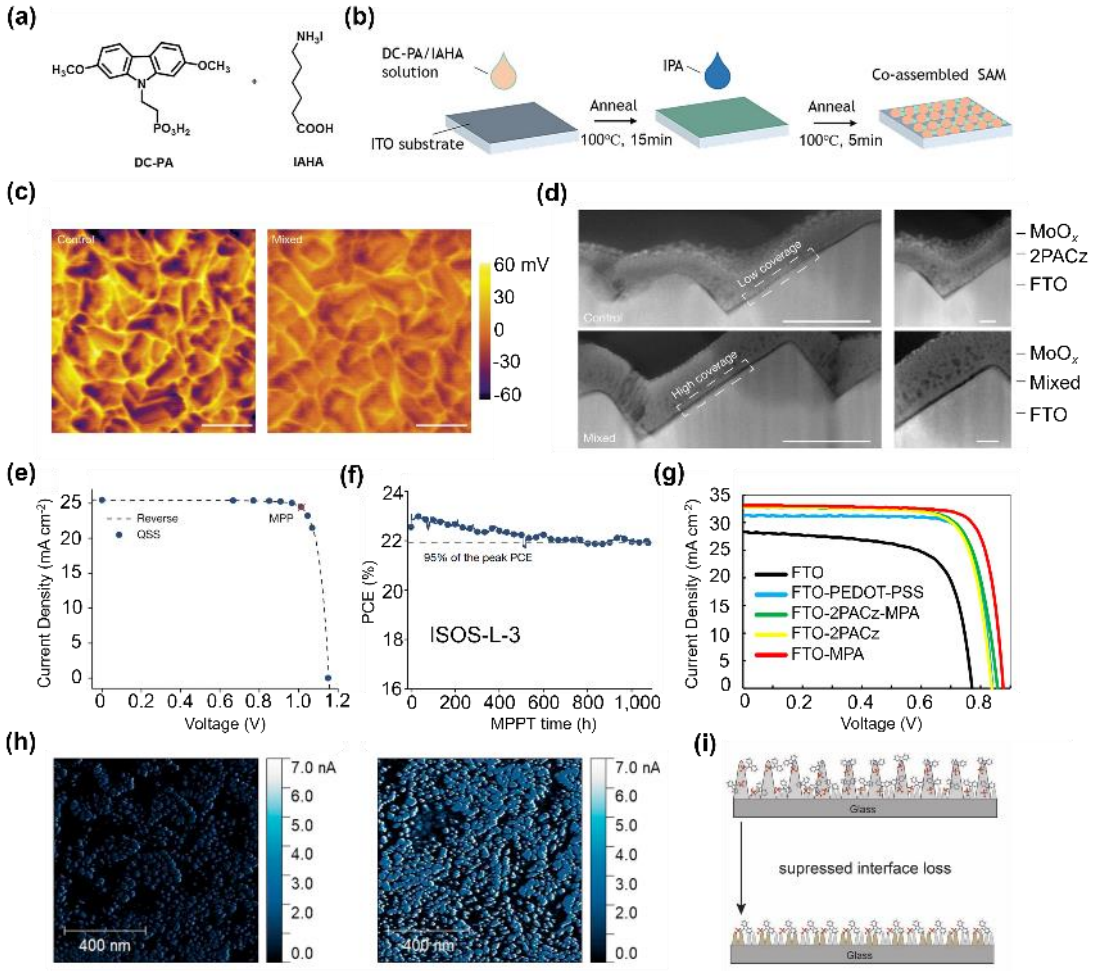


**Figure 14**. (a) Molecular structures of DC-PA and IAHA. (b) Schematic illustration of the process of depositing a co-assemble monolayer. Reproduced with permission from ref [72]. Copyright 2022 John Wiley and Sons. (c) KPFM images of control (left) and mixed (right) SAM-coated FTO substrates. (d) Cross-sectional HAADF-STEM images of control (top) and mixed (bottom) SAMs sandwiched between FTO and $MoO_x$. Scale bars, 500 nm (c); 100 nm (d, left); 20 nm (d, right). (e) QSS J–V characteristics of one representative mixed SAM-based inverted PSC. Inset: photovoltaic parameters of the device. (f) Device stability using ISOS-L-3 protocol. The device architecture used for the stability testing is FTO/SAM/perovskite/345FAn/$C_{60}$/ALD-$SnO_2$/Cu, with a PCE of 24.6% at room temperature. Reproduced with permission from ref [61]. Copyright 2023 Springer

Nature. (g) J–V characteristics of Sn-Pb PSCs using PEDOT:PSS, 2PACz, MPA, and mixed 2PACz-MPA HTLs. Reproduced with permission from ref [76]. Copyright 2022 American Chemical Society. (h) Conductive AFM images of Me-4PACz (left) and Poly-4PACz (right) -coated ITO substrates. Reproduced with permission from ref [197]. Copyright 2023 Elsevier. (i) Schematic illustration of substrate morphology modulation enabling a uniform growth of SAMs, resulting in suppressed the interface energy loss. Reproduced with permission from ref [189]. Copyright 2023 John Wiley and Sons.

As mentioned before, despite the advantages of the $NiO_x$ HTL, this HTL shows some interfacial issues including abundant surface traps, mismatch energy level, potential redox reaction between $Ni^{3+}$ and A-site cations in perovskites, and thermal expansion coefficient mismatch. The HTLs combining $NiO_x$ and SAMs are reported to be conducive to solving these problems and have achieved huge success in single-junction inverted PSCs,[51, 160] all-perovskite tandem solar cells,[51] and perovskite/organic tandem solar cells.[159] For example, a p-chlorobenzenesulfonic acid (CBSA)-based SAM was used to anchor $NiO_x$ and perovskite crystals, providing dual-passivation. This approach enabled strain release and surface defect passivation, while also preventing adverse interfacial reactions (Figure 13a-c).[192] Another study presents a thermally stable HTL for high-performance inverted PSCs by anchoring (4-(3,11-dimethoxy-7H-dibenzo[c,g]carbazol-7-yl)butyl)phosphonic acid (MeO-4PADBC) SAM molecules on $NiO_x$ films. The molecular structure of widely-used MeO-2PACz and MeO-4PADBC are shown in Figure 13d. The OMe substitution on the carbazole core resulted in a decrease in dipole moment from about 2.0 D for 2PACz to around 0.2 D for MeO-2PACz, when compared to MeO-2PACz. This contributed to a better energy level alignment with different perovskite absorbers (Figure 13e). The strong tridentate bond formed between the MeO-4PADBC and $NiO_x$ reduced voltage loss and maintained a strong fixation effect under thermal stress (Figure 13f). Impressively, the devices exhibited over 90% of their initial efficiency after 1,200 hours of

continuous operation at 65°C under 1-sun illumination.[160] Apart from introducing new SAMs, modifying the $NiO_x$ layer is another useful approach to forming higher-quality SAMs. You et al. showed that treating the $NiO_x$ nanoparticle solution with hydrogen peroxide resulted in a more uniform dispersion of nanoparticles with increased conductivity due to the formation of $Ni^{3+}$ (Figure 13g). A more condensed and uniform $NiO_x$ layer, possessing a higher amount of surface hydroxyl groups, offered an improved substrate for the formation of high-quality SAMs (Figure 13h). The resulting device achieved a certified PCE of 25.2% while maintaining 85.4% of the initial PCE after 1,000 hours of stabilized power output operation at ~50°C and 85.1% of the initial PCE after 500 hours of accelerated aging at 85°C.[58] Typically, the advancement of $NiO_x$ and SAMs is interconnected, as they collaborate to offset each other's deficiencies. The pairing of $NiO_x$ and SAMs aids in improving energy level alignment, mitigating the adverse interactions between $NiO_x$ and perovskite, along with the uneven and sparse coverage of the substrate by SAMs. As a result, their combined effect surpasses what each could achieve independently.

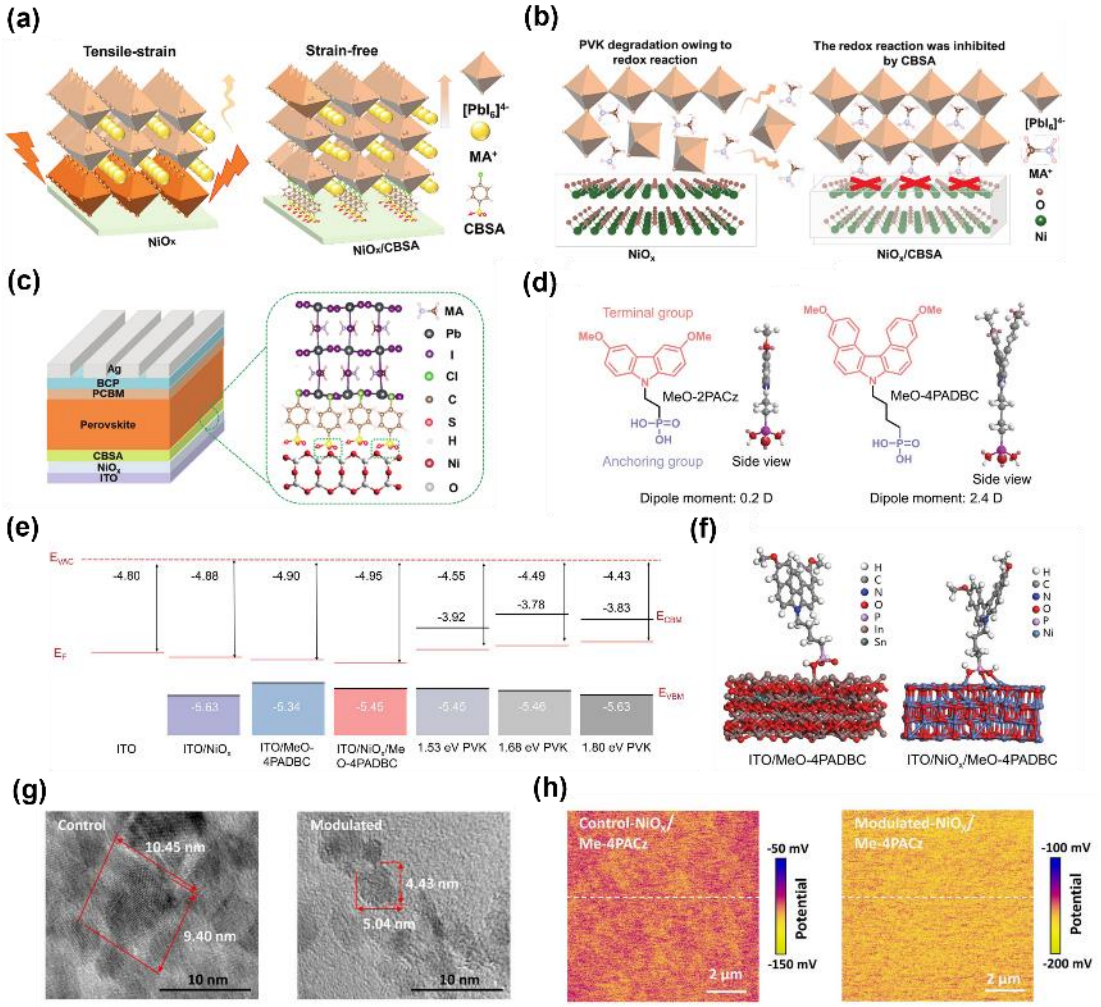


**Figure 15.** Schematic diagrams of strain release (a) and the inhibition of redox reaction (b) by introducing the CSBA SAM. (c) Schematic illustration of passivating the defects from perovskites and $NiO_x$ by introducing the CSBA SAM, where the chlorine (-Cl) atoms of CBSA can passivate iodine vacancies of perovskite crystals and the sulfonic acid ($-SO_3H$) groups can passivate the surface defects of $NiO_x$. Reproduced with permission from ref [192]. Copyright 2022 John Wiley and Sons. (d) Molecular structure and side view of MeO-2PACz (left) and MeO-4PADBC (right). (e) Energy levels of the studied HTLs and perovskite layers based on UPS measurements. Key parameters shown are $E_{VAC}$ (vacuum level), $E_{CBM}$ (conduction band minimum), $E_{VBM}$ (valence band maximum), and $E_F$ (Fermi level). (f) DFT calculation of the binding energy of MeO-4PADBC with ITO and $NiO_x$. Reproduced with permission from ref [160]. Copyright 2023 American Association for the Advancement of Science.

(g) HRTEM images of the $NiO_x$ nanoparticles without (left) and with (right) hydrogen peroxide treatment. (h) KPFM images of control-$NiO_x$/Me-4PACz (left) and modulated-$NiO_x$/Me-4PACz (right). Reproduced with permission from ref [58]. Copyright 2023 American Association for the Advancement of Science.

The above-mentioned SAMs are generally based on the carbazole terminal group. However, this core building block is relatively expensive (188 dollars per 500 g). Hong et al. replaced the carbazole terminal group with a cost-competitive phenothiazine group and synthesized a new SAM molecule, (2-(3,7-dibromo-10H-phenothiazin-10-yl)ethyl)phosphonic acid (Br-2EPT). The Br-2EPT SAM enables efficient charge collection, effective electron blocking, and surface passivation of the perovskite. When integrated as the HTL in inverted PSCs, the Br-2EPT SAM created an interface that was energetically well-suited to the top perovskite absorber. The PSCs incorporating the Br-2EPT SAM achieved a high PCE of 22.44%, with an average FF close to 81%.[191] Another problem of commonly used SAMs is the undesirable surface wetting, which would induce a high density of nanovoids at the buried interface of perovskite films. Wu et al presented that an amphiphilic molecular hole transporter, (2-(4-(bis(4-methoxyphenyl)amino)phenyl)-1-cyanovinyl)phosphonic acid (MPA-CPA) was able to address this issue by forming a superwetting underlayer for perovskite deposition. The origin of superwetting properties of MPA-CPA might originate from the cyano group of MPA-CPA and a unique bilayer stack containing an anchored SAM and an unabsorbed, disordered overlayer. The use of MPA-CPA helped form a more compact and homogeneous perovskite film without observable voids at the buried interface compared to PTAA- and 2PACz-based perovskite films. As a result, an outstanding certified PCE of 25.4%, with a $V_{OC}$ of 1.21 V and an FF 84.7%, was obtained. In the meantime, the corresponding devices demonstrated high stability under operational and damp-heat ageing conditions.[14] Furthermore, given that the linker group in the commonly used SAMs is nonconjugated. This structure tends to impede the continuous transfer of

charges through SAMs, leading to a thickness-sensitive issue.[174] Apart from the polymerization strategy reported by Chen and coworkers, designing and synthesizing small-molecule SAMs with π-conjugated backbone was also useful for addressing this issue. A notable work was reported by Wang et al, in which the MPA-BT-CA SAM derived from dyes was synthesized. The MPA-BT-CA containing a D-A type backbone was beneficial for strengthened hole extraction and reduced charge recombination. Inverted PSCs based on MPA-BT-CA demonstrated a PCE of 21.24% while exhibiting good long-term and thermal stabilities. Additionally, devices using MPA-BT-CA demonstrated minimal sensitivity to the thickness of MPA-BT-CA, ranging from less than 5 to approximately 23 nm, indicating that the tunneling transportation did not happen.[187]

Recently, Luther and coworkers reported that incorporating SAM molecules directly into the perovskite precursor allowed for simultaneous deposition of hole-transporting SAM and perovskite layers, addressing wetting issues and simplifying manufacturability while maintaining high efficiency. In addition, this approach is compatible with various SAM molecules, perovskite compositions, solvent systems, and coating methods. The inverted PSCs achieved a champion PCE of 24.5% when Me-4PACz-incorporated.[64] Similarly, He et al. designed and synthesized a new SAM molecule, (4-(2,7-dibromo-9,9-dimethylacridin-10(9H)yl)butyl)phosphonic acid (DMAcPA) and incorporated this molecule into the perovskite precursor. The methyl groups in DMAcPA could introduce a steric effect, hampering the unwanted aggregations at the grain boundaries. Additionally, according to UPS testing results, a favorable electronic structure of DMAcPA made it a possible candidate for HTL. Compared to the perovskite films grown on pristine ITO and DMAcPA modified-ITO, the perovskite films doped with DMAcPA showed fewer nanovoids at the buried interface. Moreover, a molecular-extrusion process was proposed to illustrate the distribution of DMACPA at grain boundaries and the buried interface. The p-type doping of the perovskite film resulted from the core coordination complex between

the DMACPA and lead polyiodide, leading to an outstanding PCE of 25.86% and excellent long-term stability.[13] The above works demonstrate a novel approach to fabricating the inverted PSCs without depositing the HTL before. This means a simple fabrication process, which is beneficial for the commercial application of PSCs. However, the universality of this approach should be further verified in the perovskite solar modules in the future study.

In the large-scale production of commercial PSCs, SAMs also demonstrate significant advantages as they can be prepared using large-area techniques such as dip coating and thermal evaporation, which offer high-throughput fabrication. For instance, thermal evaporation of SAM-HTL layers (2PACz, MeO-2PACz, and Me-4PACz) is presented to enhance the process flexibility.[198] The chemical properties of the SAMs are unchanged by the evaporation process, maintaining their monolayer formation at the ITO interface. The evaporation of these layers results in slightly improved implied $V_{OC}$ values and improved wettability of perovskite on Me-4PACz, enhancing the applicability of these materials without sacrificing their interfacial properties or device performance. This is greatly beneficial for the future commercial production of PSCs using SAMs. However, several nanometer-thick SAM may not fully cover the TCOs, and the large-scale preparation of perovskite layers may lead to the formation of pinholes (which has not yet been resolved in industrial-scale perovskite layers prepared by blade coating or slot die coating). This significantly affects the application of SAM in commercial PSCs. Although the use of mixed SAM[158] and bilayer deposition of SAMs[76] can improve the coverage of SAM, current research is limited to small-scale devices. In addition, adding a layer of nanoparticle $NiO_x$ between TCOs and SAM can help reduce the probability of device short-circuiting, and the small-area inverted PSCs based on $NiO_x$/SAM achieved certified efficiencies of over 25% and maintained MPPT for over 1,000 hours. Nevertheless, it is worth mentioning that due to the low material consumption of SAMs it is more-effective to use SAM monolayer compared to $NiO_x$- or $NiO_x$/SAM-mixed HTLs.

Another important aspect to consider is the stability of SAMs in the context of devices during operation. This includes the stability of SAM molecules bound to the substrate and the occurrence of buried interface delamination during thermal cycling. SAMs are anchored to the TCOs substrate through carboxylic or phosphonic acid groups, which form ester bonds with hydroxyl groups upon dehydration. However, carboxylic esters are prone to hydrolysis in the presence of water, and phosphonic esters can also undergo hydrolysis under acidic or alkaline conditions. These hydrolysis reactions may lead to the detachment of SAM molecules and have a detrimental effect on the long-term stability of the device.[199] Future developments in SAM molecules should aim to address these issues. Furthermore, while SAM molecules provide tight contact by covalently anchoring to the TCOs, they lack sufficient adhesion to the perovskite layer. This is because the thermal expansion coefficients of TCOs and perovskites do not match. Consequently, during prolonged thermal cycling, the perovskite absorbing layer may experience delamination. To overcome this, it would be beneficial to develop SAMs that exhibit strong adhesion to both perovskites and TCOs. This could be a promising direction for future research.

## 4. INTERFACE ENGINEERING

A standard PSC is typically composed of a series of stacked layers including the perovskite layer for light absorption, transporting layers for charge transport, and electrodes. The efficacy of PSCs hinges not just on the integrity of these layers but also on the quality of the interfaces that are crucial for charge transport. The development of 3D perovskite is often interrupted by the top and bottom surfaces, which results in irregular atomic structures and surface defects such as halide ions with insufficient coordination, clusters of lead, and $Pb^{2+}$ ions with inadequate bonds.[196, 200] The density of trap states on the surface of perovskite is significantly higher compared to its bulk, which is a well-established fact.[201] This defect build-up at the surface would prompt unwanted non-radiative recombination, thereby diminishing the efficiency of the device. Furthermore, improper alignment of energy bands at the

interface would induce additional recombination losses. In the realm of commercial solar cells, such as those made from silicon and Cu(In,Ga)Se2, perfecting the interface has become a crucial aspect of the manufacturing process. In the context of PSCs, refining the engineering of interfaces at both the top and bottom of perovskite films has been the focus of intense research, leading to significant advances in PCEs and stability.[202-203] In recent years, various interface engineering approaches have been developed to improve device efficiency and stability by applying a range of functional molecules such as organometallic compounds, inorganic salts, small organic molecules, polymers, alkylammonium salts, and meal oxides to the top and bottom of the perovskite layers (as detailed in Table 4).

**Table 4. A summary of the interface engineering strategies for recent representative inverted PSCs. The device performance and key parameters are provided.**

| Materials | Material Type | Engineering Type[a] | Device structure | $V_{OC}$ (V) | $J_{SC}$ (mA cm$^{-2}$) | FF | PCE (%) | Ref. |
|---|---|---|---|---|---|---|---|---|
| $FcTc_2$ | Organometallic compound | TIE | ITO/PTAA/$(FA_{0.98}MA_{0.02})_{0.95}Cs_{0.05}Pb(I_{0.95}Br_{0.02})_3$/$FcTc_2$ /$C_{60}$/BCP/Ag | 1.18 | 25.7 | 0.82 | 25.0 | 17 |
| OLAI | Alkylammonium salt | TIE | ITO/2PACz/$Cs_{0.03}(FA_{0.90}MA_{0.10})_{0.97}PbI_3$/OLAI/$C_{60}$/BCP/Ag | 1.21 | 24.5 | 0.82 | 24.3 | 16 |
| 3F-PEA | Alkylammonium salt | TIE | ITO/$NiO_x$/$Cs_{0.05}FA_{0.85}MA_{0.1}PbI_3$/3F-PEA/PCBM/BCP/Ag | 1.15 | 24.9 | 0.83 | 23.9 | 67 |
| PBAI | Alkylammonium salt | BIE | ITO/PTAA:F4TCNQ/PMMA/$FA_{0.91}Cs_{0.07}MA_{0.05}PbI_{2.88}Br_{0.15}$ /PBAI/PCBM:Bphen/Al | 1.16 | 24.6 | 0.82 | 23.3 | 204 |
| PEACl | Alkylammonium salt | BIE/TIE | FTO/$NiO_x$/Me-4PACz/PEACl/$FAPbI_3$/PEACl/PCBM/$SnO_2$/Cu | 1.16 | 26.2 | 0.84 | 25.6 | 58 |
| PEAI | Alkylammonium salt | BIE/TIE | ITO/PTAA/PEAI/$Cs_{0.05}(FA_{5/6}MA_{1/6})_{0.95}Pb(I_{0.85}Br_{0.15})_3$/PEAI/ PCBM/BCP/Ag | 1.15 | 23.7 | 0.81 | 22.0 | 70 |
| PEAMAI | Alkylammonium salt | TIE | ITO/PTAA/$FA_{0.9}Cs_{0.1}PbI_3$/PEAMAI/$C_{60}$/BCP/Cu | 1.14 | 25.8 | 0.82 | 24.1 | 100 |
| PEABr | Alkylammonium salt | TIE | ITO/DMAcPA/Perovskite/PEABr/PCBM/BCP/Ag | 1.19 | 25.7 | 0.85 | 25.9 | 13 |
| Cl-PEAI | Alkylammonium salt | BIE/TIE | ITO/PTAA/Cl-PEAI/$Cs_{0.05}(FA_{5/6}MA_{1/6})_{0.95}Pb(I_{0.85}Br_{0.15})_3$ /Cl-PEAI/PCBM/BCP/Ag | 1.15 | 23.7 | 0.85 | 23.1 | 70 |
| F-PEAI | Alkylammonium salt | BIE/TIE | ITO/PTAA/F-PEAI/$Cs_{0.05}(FA_{5/6}MA_{1/6})_{0.95}Pb_{1.01}(I_{0.85}Br_{0.15})_3$ /F-PEAI/PCBM/BCP/Ag | 1.16 | 24.1 | 0.85 | 23.7 | |
| BDAI | Alkylammonium salt | BIE | ITO/PTAA/BDAI/$(CsPbI_3)_{0.05}(FA_{0.85}MA_{0.15}Pb(I_{0.85}Br_{0.15})_3)_{0.95}$/ PCBM/BCP/Ag | 1.21 | 22.6 | 0.82 | 22.3 | 205 |
| GABr | Alkylammonium salt | BIE/TIE | ITO/PTAA/$(FA_{0.95}PbI_{2.95})_{0.85}(MAPbBr_3)_{0.15}$/GABr /PCBM/$C_{60}$/BCP/Cu | 1.21 | 22.5 | 0.79 | 21.5 | 165 |
| 3MTPAI-$PDAI_2$ | Alkylammonium salt | TIE | FTO/$NiO_x$/4PACz/$Cs_{0.05}MA_{0.05}FA_{0.90}PbI_3$/3MTPAI-$PDAI_2$/$C_{60}$/BCP/Ag | 1.17 | 26.3 | 0.86 | 26.4 | 51 |
| GlyHCl /$EDAI_2$ | Alkylammonium salt | BIE/TIE | FTO/PEDOT:PSS/GlyHCl/$Cs_{0.1}FA_{0.6}MA_{0.3}Sn_{0.5}Pb_{0.5}I_3$/$EDAI_2$ /$C_{60}$/BCP/Ag | 0.89 | 32.5 | 0.82 | 23.6 | 71 |

| | | | | | | | | |
|---|---|---|---|---|---|---|---|---|
| 345FAn | Alkylammonium salt | TIE | ITO/2PACz/$Cs_{0.05}MA_{0.05}FA_{0.9}Pb(I_{0.95}Br_{0.05})_3$/345FAn/$C_{60}$/BCP/Ag | 1.16 | 25.9 | 0.83 | 24.1 | 206 |
| PFN-I | Polymer | BIE/TIE | ITO/poly-TPD/PFN-I/$Cs_{0.05}FA_{0.79}MA_{0.16}PbI_{2.4}Br_{0.6}$/ PFN-I/PCBM/BCP/Ag | 1.13 | 22.5 | 0.81 | 20.5 | 207 |
| PFN-Br | Polymer | BIE | ITO/PTAA/PFN-Br/$FAMAPbI_3$/$C_{60}$/BCP/Cu | 1.10 | 24.7 | 0.83 | 22.5 | 208 |
| PTAA | Polymer | BIE | FTO/$NiO_x$/PTAA/$Cs_{0.05}MA_{0.15}FA_{0.80}PbI_3$/PCBM/BCP/Ag | - | - | - | 23.7 | 69 |
| PMMA | Polymer | BIE/TIE | ITO/PTAA/PMMA/perovskite/PBAI/PCBM/Bphen/Al | 1.16 | 24.6 | 0.82 | 23.3 | 204 |
| PMMA | Polymer | BIE | ITO/$NiO_x$/PMMA/$(MAPbI_3)_{0.95}(MAPbBr_2Cl)_{0.05}$/PCBM/BCP/Ag | 1.19 | 22.2 | 0.79 | 21.1 | 209 |
| PS | Polymer | BIE | ITO/$NiO_x$/PS/$(MAPbI_3)_{0.95}(MAPbBr_2Cl)_{0.05}$/PCBM/BCP/Ag | 1.17 | 22.4 | 0.79 | 20.8 | |
| PFN-Br/ PEAI | Polymer/ Alkylammonium salt | BIE/TIE | ITO/PTAA/poly-TPD/PFN-Br/$Cs_{0.05}FA_{0.79}MA_{0.16}PbI_{2.4}Br_{0.6}$/ PEAI/PCBM/BCP/Ag | 1.18 | 21.9 | 0.83 | 21.3 | 210 |
| 3MTPAI/ $PDAI_2$ | Small organic molecule/ Alkylammonium salt | TIE | FTO/Me-4PACz:2PACz/perovskite/3MTPAI/ $PDAI_2$/$C_{60}$/$SnO_2$/Ag | 1.18 | 26.4 | 0.86 | 26.9 | 50 |
| 3-APy | Small organic molecule | TIE | ITO/MeO-2PACz/perovskite/3-APy/LiF/$C_{60}$/BCP/Ag | 1.15 | 26.2 | 0.84 | 25.5 | 59 |
| Choline chloride | Small organic molecule | TIE | ITO/PTAA/$FA_{0.85}MA_{0.15}Pb(I_{0.85}Br_{0.15})_3$ /Choline chloride/$C_{60}$/BCP/Cu | 1.14 | 23.7 | 0.78 | 21.0 | 84 |
| PFDT | Small organic molecule | TIE | FTO/$NiO_x$/$Cs_{0.05}(FA_{0.85}MA_{0.15})_{0.95}Pb(I_{0.85}Br_{0.15})_3$/PFDT /PCBM/BCP/Ag/PFDT | 1.16 | 23.5 | 0.80 | 21.8 | 211 |
| PI | Small organic molecule | TIE | ITO/PTAA/$Cs_{0.05}(FA_{0.95}MA_{0.05})_{0.95}Pb(I_{0.95}Br_{0.05})_3$/PI/$C_{60}$/BCP/Ag | 1.17 | 24.9 | 0.80 | 23.4 | 75 |
| PCBB-3N-3I | Small organic molecule | TIE | ITO/PTAA/$MAPbI_3$/PCBB-3N-3I/PCBM/Al | 1.11 | 23.3 | 0.81 | 21.1 | 212 |
| $PbPyA_2$ | Small organic molecule | TIE | ITO/P3CT-N/$(FAPbI_3)_{0.95}(MAPbBr_3)_{0.05}$/$PbPyA_2$/$C_{60}$/TPBi/Cu | 1.19 | 24.8 | 0.83 | 24.3 | 66 |
| Y6 | Small organic molecule | TIE | ITO/PTAA/perovskite/Y6/PCBM/$C_{60}$/BCP/Ag | 1.12 | 23.7 | 0.79 | 21.0 | 87 |

| | | | | | | | | |
|---|---|---|---|---|---|---|---|---|
| BCP | Small organic molecule | BIE | ITO/PTAA:BCP/FACsPbI$_3$/C$_{60}$/BCP/Cu | 1.17 | 25.5 | 0.83 | 24.6 | 62 |
| DPPP | Small organic molecule | BIE | FTO/NiO$_x$/Me-4PACz/DPPP/FA$_{0.95}$Cs$_{0.05}$PbI$_3$/ C$_{60}$/SnO$_2$/Ag | 1.16 | 25.7 | 0.83 | 24.5 | 65 |
| KF | Inorganic salt | BIE/TIE | ITO/PTAA/KF/Cs$_{0.05}$(FA$_{0.88}$MA$_{0.12}$)$_{0.95}$PbI$_3$/KF/C$_{60}$/BCP/Ag | 1.15 | 23.4 | 0.82 | 22.0 | 213 |
| CdI$_2$ | Inorganic salt | TIE | ITO/PTAA/Rb$_{0.025}$Cs$_{0.025}$FA$_{0.70}$MA$_{0.25}$PbI$_3$/CdI$_2$/C$_{60}$/BCP/Cu | 1.20 | 23.5 | 0.78 | 21.9 | 214 |
| InBr$_3$ | Inorganic salt | TIE | ITO/PTAA/Cs$_{0.07}$FA$_{0.70}$MA$_{0.23}$PbI$_3$/InBr$_3$/C$_{60}$/BCP/Cu | 1.18 | 23.5 | 0.80 | 22.2 | 215 |
| KSCN | Inorganic salt | BIE | ITO/NiO$_x$/KSCN/MAPbI$_{3-x}$Cl$_x$/PCBM:C$_{60}$/ZrAcac/Ag | 1.14 | 23.3 | 0.80 | 21.2 | 216 |
| F-TiO$_2$ NSs | Metal oxide | TIE | ITO/PTAA/Cs$_{0.05}$(FA$_{0.95}$MA$_{0.05}$)$_{0.95}$Pb(I$_{0.95}$Br$_{0.05}$)$_3$ /F-TiO$_2$ NSs/C$_{60}$/BCP/Ag | 1.14 | 24.8 | 0.81 | 22.9 | 217 |
| Nanoplate Al$_2$O$_3$ | Metal oxide | BIE | ITO/Me-4PACz/Al$_2$O$_3$/(FA$_{0.95}$MA$_{0.05}$)$_{0.95}$Cs$_{0.05}$Pb(I$_{0.95}$Br$_{0.05}$)$_3$/ LiF/C$_{60}$/BCP/Ag | 1.21 | 25.1 | 0.84 | 25.6 | 57 |
| ALD-AlO$_x$ | Metal oxide | BIE | ITO/NiO$_x$/ALD-AlO$_x$/FA$_{0.79}$MA$_{0.16}$Cs$_{0.05}$PbI$_3$/C$_{60}$/BCP/Ag | 1.11 | 24.8 | 0.81 | 22.5 | 218 |

[a]Buried interface engineering (BIE); Top interface engineering (TIE).

### 4.1 Top Interface Engineering

Extensive research has been conducted on the surface properties of perovskite films due to their exposed nature. Surface engineering techniques involve treating the films with functional molecules, typically dissolved in polar solvents such as IPA, and subsequently subjecting them to thermal annealing to remove the solvents. Additionally, inorganic modification molecules like $MgF_x$ and LiF can be deposited onto the top surface of the perovskite films using physical vapor deposition.[18] It is worth noting that, as the surface engineering method is primarily a post-treatment approach, it does not have a huge impact on the film coverage, crystallinity, and grain size of the perovskite films. However, the use of polar solvents for perovskite precursors and post-treatment agents can lead to partial dissolution of the formed perovskite films and subsequent secondary growth during thermal annealing, altering the distribution of surface components.[165] Moreover, applying a thin layer of passivating material can effectively reduce trap-assisted recombination at the interface, while inherently hydrophobic materials can prevent moisture intrusion, thereby enhancing device stability.[219-220] This approach also minimizes the energy barriers at the interface between the perovskite film and ETL, facilitating efficient charge carrier transport.[196, 203] Subsequently, we will delve into some representative methods for fabricating high-performance inverted PSCs.

Unlike regular PSCs, where perovskites are grown on an n-type substrate like $SnO_2$ or $TiO_2$, the inverted PSCs involve perovskite growth on a p-type substrate, resulting in more p-type characteristics for the perovskites. Direct contact of the p-type perovskite with the n-type ETL could cause unfavorable charge recombination. To address this issue, Li et al. reported a surface sulfidation treatment (SST) by sulfurizing the Pb-rich interface, achieved by spin-coating pyridine-2-carboxylic lead ($PbPyA_2$) with hexamethyldisilathiane (Figure 14a). After SST, the perovskite layer exhibited a shallower Fermi level (more n-type in nature), which created an additional back-surface field at the interface that facilitated charge extraction (Figure 14b-c).[66] The

optimized device delivered a remarkable PCE of 24.3% with enhanced $V_{OC}$, $J_{SC}$, and FF (1.19 V, 24.8 mA $cm^{-2}$, and 82.9%, respectively). Furthermore, the strong Pb-S bonds effectively impeded unwanted charged-ion migration and preserved the PCBM layer in the device, greatly enhancing device stability. Similarly, early in 2018, we proposed a solution-processed secondary growth strategy with guanidinium bromide (SSG-G) for mixed-cation lead mixed-halide perovskite to control the semiconductor nature at the perovskite surface. The up-shifted Fermi level toward the conduction band minimum, possibly originating from composition variation at the interface, suggested a more n-type nature for the SSG-G perovskite film (Figure 14d). Moreover, it was observed that the bandgap near the top interface of the treated film was broadened due to the enrichment of the Br element. Such bandgap widening at the interface would be beneficial for achieving desirable Type-I or Type-II band alignment, reducing the accumulation of charge carriers at the interface. These improvements in the electronic nature between the perovskite and ETL led to an enhancement in $V_{OC}$ by up to 100 mV (1.21 V) without sacrificing the photocurrent, culminating in a champion PCE of 21.51%.[165] Recently, a 3-(Aminomethyl)pyridine (3-APy)-based top surface engineering method was developed by Jiang et al. The use of 3-APy was able to react with surface $FA^+$, forming N-(3-methylpyridine)formamidinium ($MPyFA^+$) and releasing $NH_3$. This reaction led to a "polishing" effect, contributing to a smoother perovskite surface. Furthermore, the 3-APy surface treatment exhibited a significant decrease in the work function, reducing it from approximately 4.77 eV to 4.21 eV. Additionally, it effectively shifted the VBM from around 0.80 eV to 1.51 eV, indicating an effective n-type doping in the perovskite film surface with 3-APy treatment (Figure 14e). This resulted in favorable surface energetics and band bending that promote electron extraction while blocking holes. With this method, the PCE increased from 23.39% to 25.49% with a certified stabilized PCE of 24.05 ± 0.48% (Figure 14f).[59]

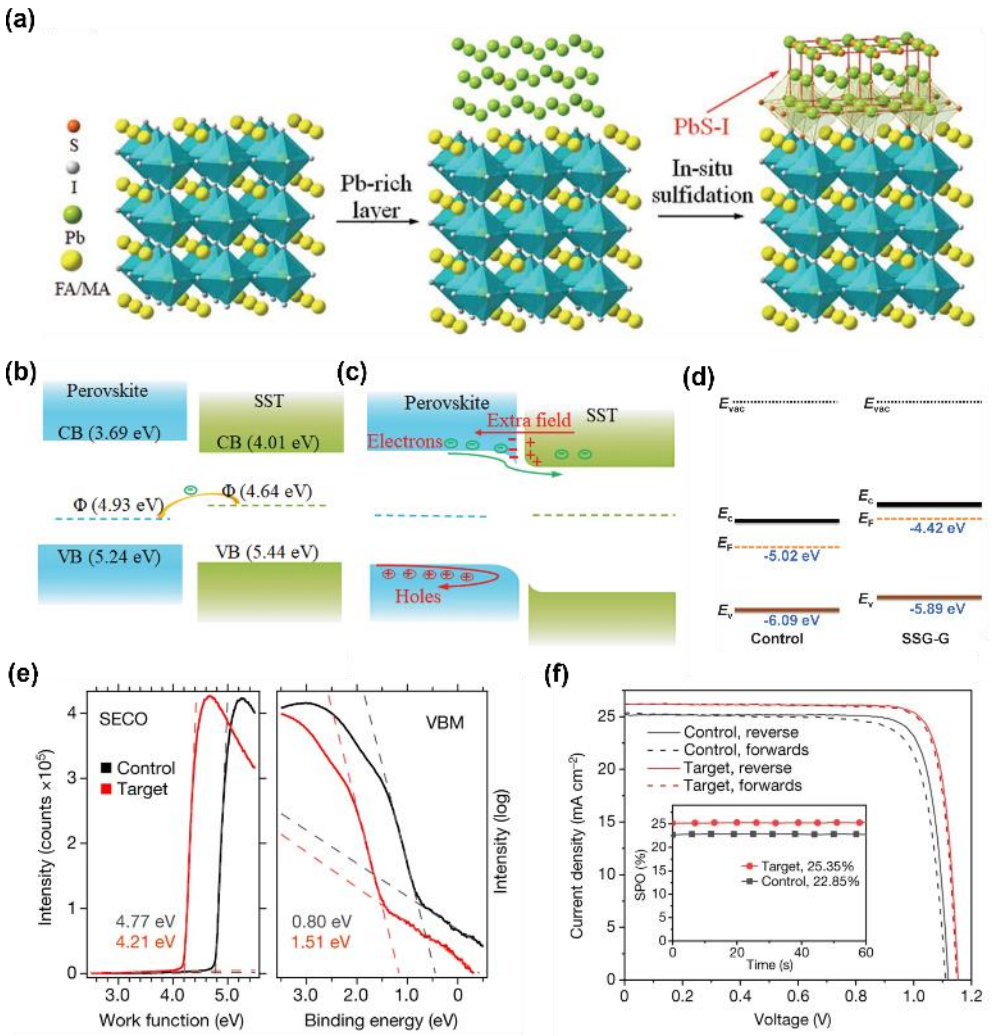


**Figure 16.** (a) Schematic illustrations of the SST process. (b) The energy level of the perovskite films, where Φ is the Fermi level. The yellow arrow shows a spontaneous electron-flow to bulk perovskite, (c) Formation of the back-surface field at the perovskite interface with SST. Reproduced with permission from ref [66]. Copyright 2022 American Association for the Advancement of Science. (d) Energy level alignment of control and SSG-G perovskite films. Reproduced with permission from ref [165]. Copyright 2018 American Association for the Advancement of Science. (e) UPS spectra of the control and target film. Left panel: secondary electron cutoff. Right panel: valence band spectrum. (f) J-V curves of the champion control and target PSCs under reverse and forward scans. Insert: The stabilized power output (SPO) of the control and target PSCs. Reproduced with permission from ref [59]. Copyright 2022 Springer Nature.

The presence of dangling bonds in polycrystalline films makes surfaces energetically unfavorable and more reactive. To address this issue, most advanced polycrystalline thin-film technologies like CdTe and CIGS solar cells passivate the absorber surface by coating it with a reduced-dimensional layer, typically a 2D layer. The 2D capping layer on top of the 3D light absorber has proven to be an effective way to enhance the device's $V_{OC}$ and stability.[221] This 3D/2D passivation strategy is also applicable to emerging PSCs and has significantly improved their performance.[16, 67, 222] Alkylammonium halides such as PEAI and OAI could passivate both cation and anion defects at interfaces, and an enhanced passivation effect was achievable through the formation of hydrogen or ionic bonds with the perovskite. The application of alkylammonium halides generated an interfacial dipole that counteracts band bending at the surface of the perovskite films. Moreover, the deposition of alkylammonium halide salts with short alkyl chains, like PEAI and BAI, tended to result in the formation of reduced-dimensional perovskites, typically 2D perovskites. A heterojunction interface comprising both 2D and 3D perovskites was advantageous for constructing stable and efficient solar cells,[221] as the 2D-dimensional perovskite layer was able to terminate the dangling bonds at perovskite surfaces, suppressing ion migration and passivating charged defects. Recently, Azmi and colleagues reported a versatile and universal strategy to passivate the 3D perovskite layer with a Ruddlesden-Popper (RP) phase 2D perovskite layer using oleylammonium iodide (OLAI) molecules.[16] This 2D/3D passivation approach imparted an enriched n-type character to the 3D perovskite films and more efficient charge transfer due to the successful realignment of the energy band structure. The treated device exhibited a prolonged charge carrier lifetime and suppressed trap-assisted recombination at the perovskite/ETL interface, achieving an outstanding PCE of 24.3% (Figure 15a-c). The 3D/2D heterojunction at the absorber surface substantially improved the device stability under ageing conditions such as thermal, moisture, illumination, and electrical stress, meeting the mature industrial stability standards for photovoltaic

modules (Figure 15d). In the study by Chen et al., it was reported that adjusting the quantum size of the 2D/3D heterostructure using ligand-modified bulkier organics, such as 3-fluoro-phenethylammonium (3F-PEA), could reduce confinement within the 2D perovskite layer and lower the electron barrier between the 2D/3D perovskites (Figure 15e-f), resulting in an excellent quasi-steady-state certified PCE of 23.91%. When combined with a stable inorganic $NiO_x$ HTL, under ISOS-L3 accelerated ageing conditions, the quasi-2D-treated device maintained 92% of its initial performance after 500 hours of maximum power point (MPP) tracking.[67] Similarly, Vaynzof et al. incorporated PEAI, 4-chloro-phenylethylammonium iodide (Cl-PEAI), and 4-fluoro-phenylethylammonium iodide (F-PEAI) at both the top and bottom interfaces of the perovskite layer. By controlling the additive concentration, a higher-quality and more homogeneous film with low perovskite/ETL interfacial defect density was achieved. The devices displayed a significant and all-rounded increase in FF, $V_{OC,}$ $J_{SC}$, and PCE (1.184 V, 24.13 mA $cm^{-2}$, 84.6%, 23.7%, respectively).[70] Wu et al. employed a series of large alkylammonium interlayers (LAI) containing 1,4-butanediammonium iodide (BDAI), PEAI, and GAI, to modify the bottom interface between HTL and perovskites in the inverted PSCs.[205] These salts effectively improved the perovskite film crystallinity as evidenced by a stronger (001) diffraction peak and a narrower full width at half maximum (FWHM) of diffraction peaks compared to the control perovskite film. Moreover, the inserted LAI layer could reduce defect sites. When BDAI was used as the LAI, a high PCE exceeding 22% was obtained. In addition, an external quantum efficiency of the electroluminescence ($EQE_{EL}$) as high as 3.11% was observed when the BDAI-modified inverted PSC was operated as light-emitting diodes, demonstrating the reduced non-radiative recombination.

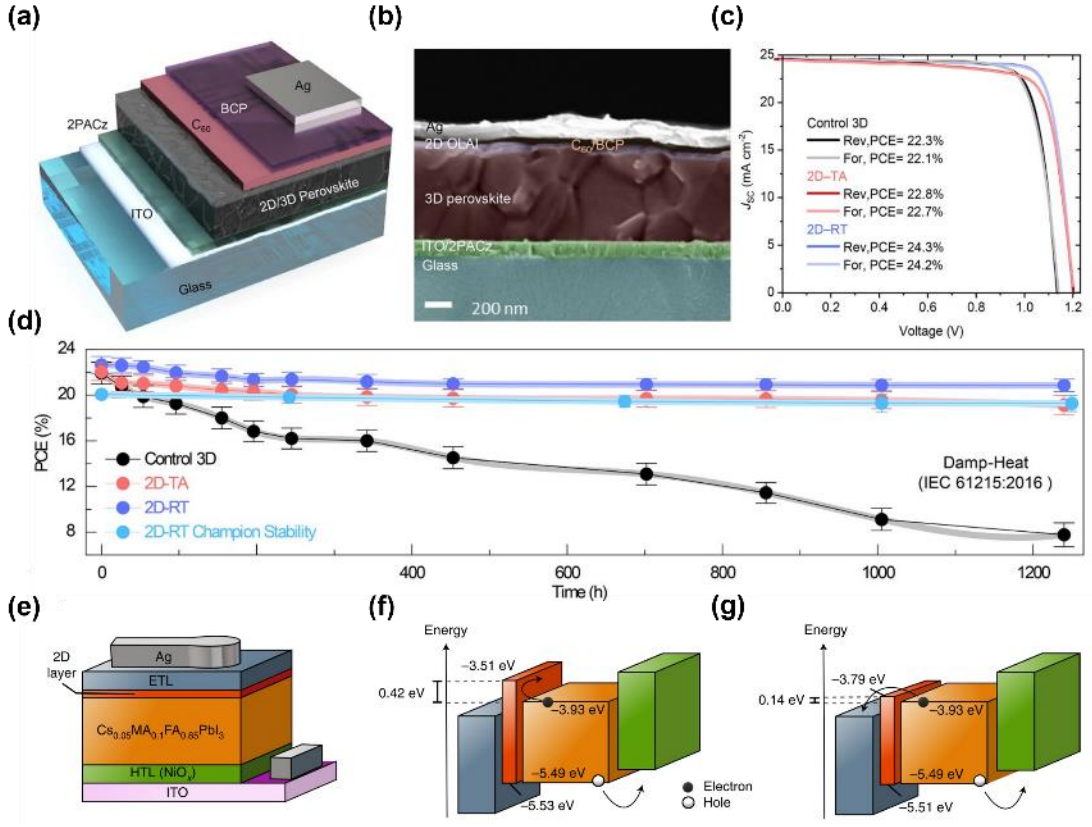


**Figure 17**. (a) A schematic diagram of the solar cell configuration used in this work. (b) Cross-sectional SEM images of the 2D OLAI treated PSCs. (c) *J–V* characteristics of control devices, 2D perovskite layer post-treatment at room temperature (2D-RT) and through thermal annealing (2D-TA). (d) PCEs evolution at damp-heat test of encapsulated devices. Reproduced with permission from ref [16]. Copyright 2021. American Association for the Advancement of Science. (e) Schematic of a typical 2D/3D heterostructure in inverted PSCs. The band alignment of the inverted PSCs with the 2D treatment (f) or the quasi-2D treatment (g). Reproduced with permission from ref [67]. Copyright 2022 Springer Nature.

To tackle the potential issue of 2D/3D interaction causing ammonium ligands to penetrate deeper into bulk perovskite and potentially leading to a drawback in device performance under extreme stress conditions, Sargent et al. explored an alternative approach using noninvasive surface-passivating ligands (Figure 16a), using 3,4,5-trifluoroanilinium (345FAn), which gave a promising PCE of 24.09%.[206] This 345FAn

has smaller binding energy to substitute perovskite A-site (Figure 16b,c) and higher interaction energy (Figure 16d,e), which together shows that this fluorinated anilinium less easily forms 2D perovskite while connecting tighter and stronger with perovskite at the surface and from the side, increasing the stability of the forming 2D layer.

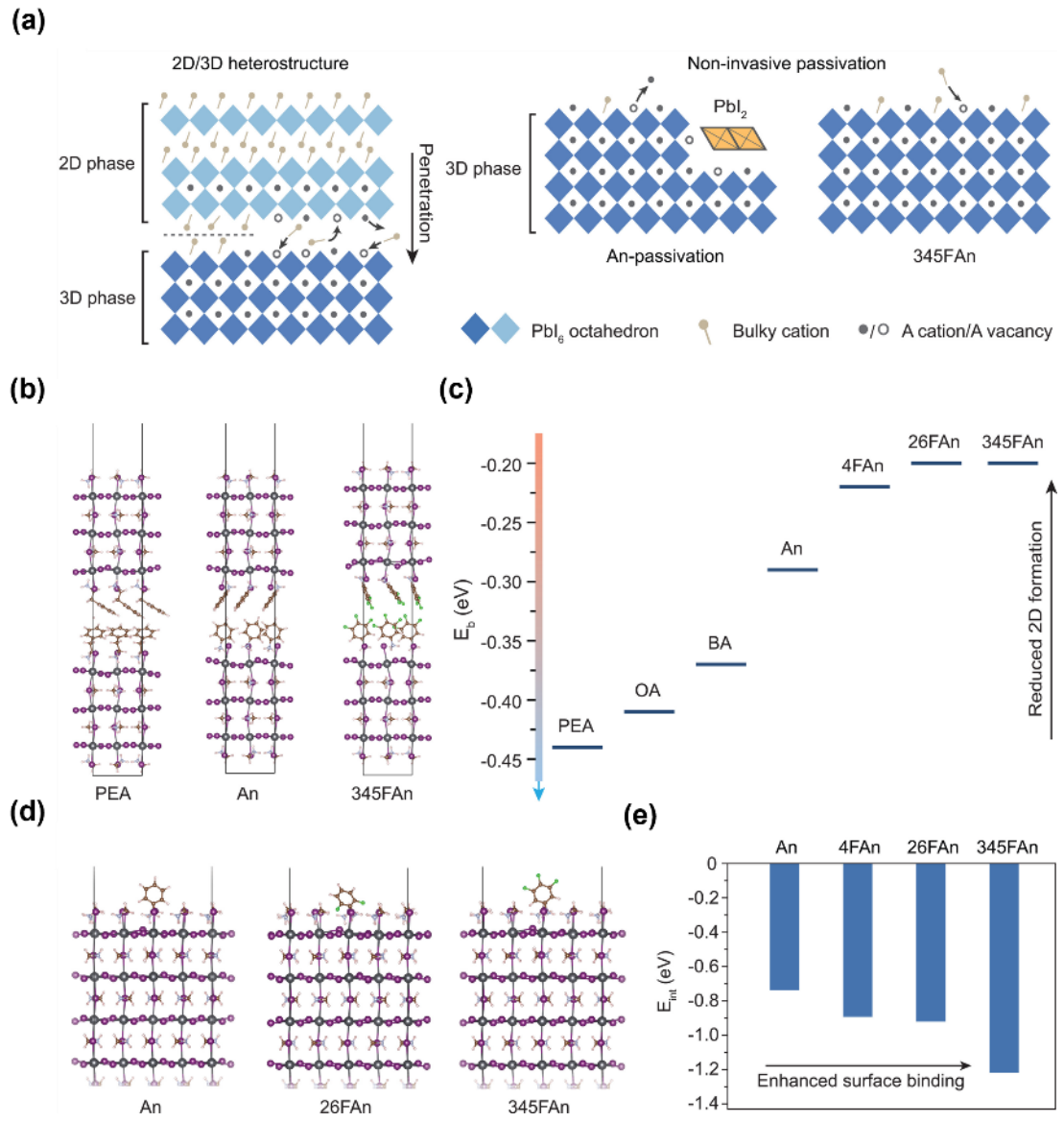


**Figure 18.** (a) A schematic representation showcasing how ammonium ligands interact with perovskite structures. (b) Theoretical models applied in Density Functional Theory (DFT) analyses to assess the binding energy ($E_b$) between closely positioned 2D perovskite segments. (c) Determined $E_b$ values for a set of seven distinct ammonium ligands incorporated within $MAPbI_3$ perovskite A-site. (d) Theoretical constructs used for calculating the interaction energy ($E_{int}$) between

various ammonium ligands and the surface of the $MAPbI_3$ perovskite. (e) Evaluation of $E_{int}$ values for a selection of four ammonium ligands interacting with the perovskite surface. Reproduced with permission from ref [206]. Copyright 2023 American Association for the Advancement of Science.

Lewis acids and bases, known for their ability to accept and donate electrons, effectively passivate both negatively and positively charged defects on absorber surfaces through coordinate or ionic bonding, reducing unwanted non-radiative recombination. For instance, Jen et al. improved the photovoltaic performance and stability of their device by applying 1H,1H,2H,2H-perfluorodecanethiol (PFDT) superhydrophobic SAMs to both the perovskite layer and the metal electrode. The thiol headgroup, a sulfur-donor Lewis base, stabilized uncoordinated Pb ions at the perovskite surface through metal-thiol interactions, while the rigid perfluorocarbon tail-chain granted the surface hydrophobic properties (Figure 17a) effectively blocking water and oxygen infiltration. This passivation method also prevented lead leakage in degraded PSCs.[211] In the same group, they employed the organometallic compound ferrocenyl-bis-thiophene-2-carboxylate ($FcTc_2$) to functionalize the perovskite surface (Figure 17b). The use of $FcTc_2$ introduced a strong Pb–O interaction to deplete surface trap states and enhanced interfacial charge transfer via the electron-rich ferrocene groups (Figure 17c,d). This additional interfacial bonding and the facilitated carrier dynamics induced by $FcTc_2$ suppressed unexpected ion migration, contributing to remarkable device stability under damp-heat testing conditions (85°C and 85% relative humidity), which successfully met the International Electrotechnical Commission (IEC) 61215 standard for mature photovoltaic technologies. The resulting devices achieved a milestone PCE of 25.0%. Later on, a diammonium-methylthio dual passivation (DMDP) strategy was developed.[51] This approach combined sulfur-modified methylthio molecules with diammonium molecules to passivate surface defects and reduce recombination through hydrogen bonding and strong coordination, while also achieving a decrease in

contact-induced interface recombination by repelling minority charge carriers through "field-effect passivation" (Figure 17e). Thiol-modified methanethiol molecules provide chemical passivation, and diammonium molecules act to repel minority charge carriers, thus reducing contact-induced recombination. The DMDP strategy led to a fivefold increase in charge carrier lifetime, one-third of the PLQE loss, and enabled a champion PCE of 26.4% with certified quasi-steady-state PCE of 25.1% (Figure 17f,g), and the optimized devices showed a stable operation at 65°C for more than 2000 hours in ambient air.

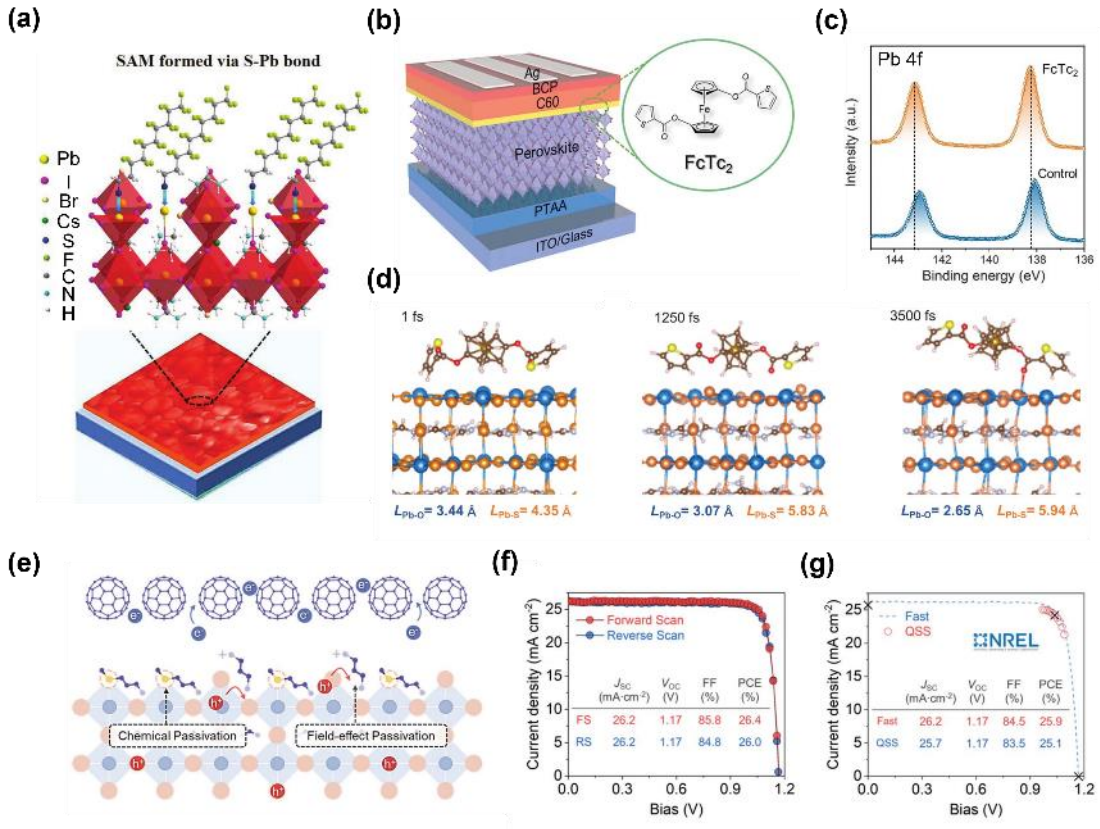


**Figure 19**. (a) Schematic of the interaction between PFDT and perovskite surface defects. Reproduced with permission from ref [31]. Copyright 2021 John Wiley and Sons. (b) Schematic illustrations of the device structure of inverted PSC passivated with $FcTc_2$. (c) XPS characterization of the Pb element. (d) The interaction between perovskite and FcTc2 investigated using molecular dynamics simulations. L, bond length. Reproduced with permission from ref [17, 87]. Copyright 2022. American

Association for the Advancement of Science. (e) Schematic of the perovskite surface with both chemical and field-effect passivation. (f) J-V curves of the champion DMDP-based inverted PSCs. (g) certified quasi-steady state J-V curve of one representative DMDP-based device at NREL. Reproduced with permission from ref [51, 87]. Copyright 2023. American Association for the Advancement of Science.

Although numerous passivation molecules have been developed, completely passivating all surface defects in perovskite films, due to their complexity and diversity, is still challenging. A pioneering approach to addressing this issue was reported by Zheng et al in 2017. They treated the $MAPbI_3$ perovskite films with quaternary ammonium halides (e.g. L-α-phosphatidylcholine, choline iodide, and choline chloride) containing both negative- and positive-charged components (Figure 18a). The choline group could fill the $MA^+$ vacancies, while additional halide ions were expected to passivate the $I^-$ vacancies due to the evaporation of MAI during annealing (Figure 18b). Such a synergistic effect greatly reduced trap density of states versus traditional PCBM passivation (Figure 18c). This research demonstrates the importance of completely passivating all defects in perovskite films and provides an avenue for improving the PCE and stability of perovskite photovoltaics.[84] Moreover, Jen et al. developed a bifunctional small organic molecule, piperazinium iodide (PI), which contains both electron-accepting ($R_2NH_2^+$) and electron-donating ($R_2NH$) groups within a 6-membered ring. This bifunctional passivation could regulate the surface termination by simultaneously using $R_2NH_2^+$ to insert A-site vacancy and $R_2NH$ to react with uncoordinated $Pb^{2+}$, reducing the defects such as Pb-I antisites, Pb clusters, and uncoordinated halides. This surface termination strategy alleviated the surface residual stress and facilitated the n-type characteristic of the perovskite layer for efficient charge transfer.[75] A similar strategy was adopted by Li's group.[212] They designed a fullerene electrolyte (PCBB-3N-3I) with high conductivity and a strong molecular electric dipole moment (Figure 17d). In PCBB-3N-3I, the Lewis acid, specifically the fullerene part, passivated negatively charged defects such as under-

coordinated $I^-$, while the iodide component interacted with positively charged under-coordinated $Pb^{2+}$ defects, leading to orderly packing and preferred orientation of PCBB-3N-3I on the perovskite surface. Reduced surface defects enhanced the build-in voltage, charge collection, and device ambient stability. Emerging small-band-gap non-fullerene small organic molecules like Y6 possess high mobility, suitable energy levels with perovskites, and electron-rich functional groups (e.g., C–S–C, C=O and C≡N.). When coated on the perovskite absorber surface, it was reported that this molecule played integrated roles in improving device performance including electron transportation, moisture resistance layer, near-infrared photocurrent intensification, surface trap passivation, and the containment of ion migration (Figure 17e).[87] The chloroform-processed Y6 (Y6-CF) treatment induced the face-on orientation and π-π stacking, which facilitated the extraction and transport efficiency of electrons from the perovskite layer. The boost in $J_{SC}$ (23.68 mA $cm^{-2}$) was attributed to the favorable surface energetic alignment between perovskite and ETL and the dissociation of the photoexcited exciton at the interface provided by this narrow band gap Y6. Additionally, the hydrophobicity nature of Y6 confined water penetration, thereby enhancing its ambient stability toward humidity.

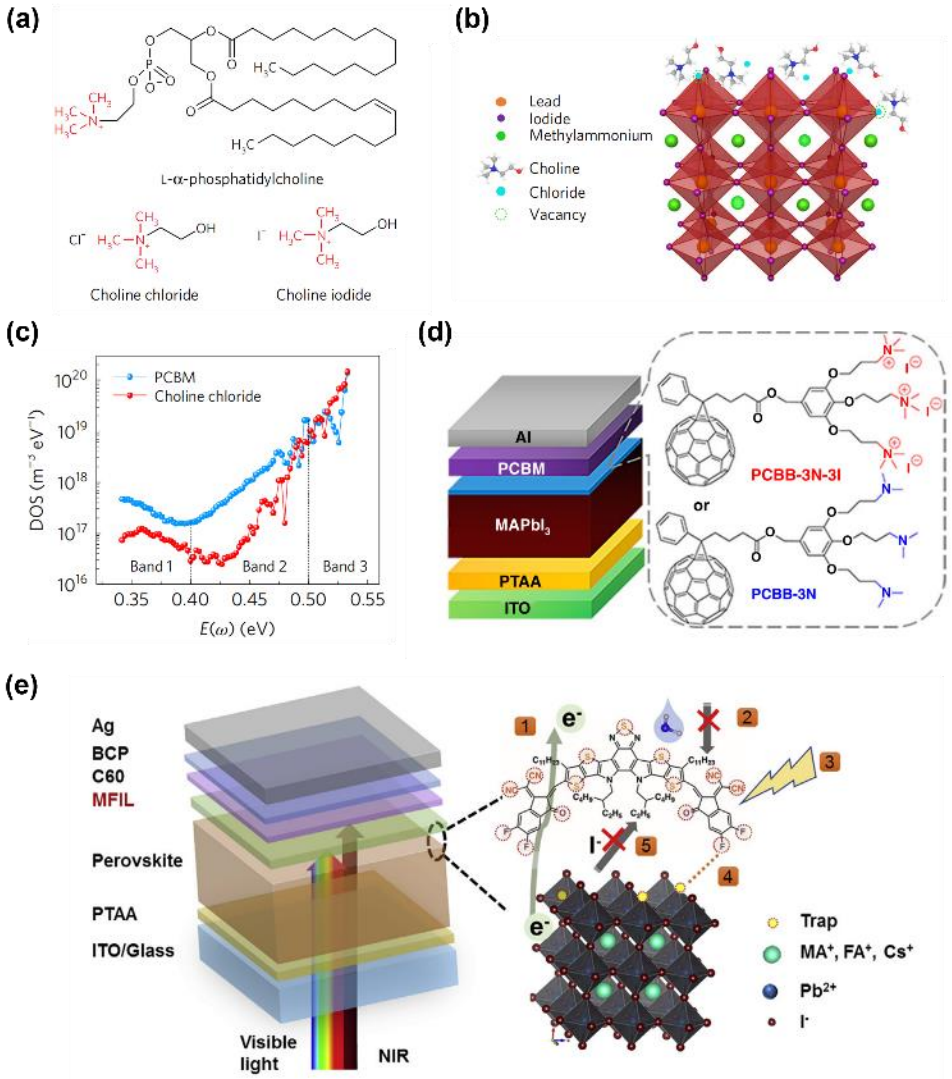


**Figure 20.** (a) Chemical structures of L-α-phosphatidylcholine, choline iodide, and choline chloride. (b) Schematic illustration of the passivating function of quaternary ammonium halides. (c) Trap density of states measured by thermal admittance spectroscopy for devices treated with PCBM and choline chloride. Reproduced with permission from ref [84]. Copyright 2017 Springer Nature. (d) Schematic illustration of the device architecture of PCBB-3N-3I/PCBB-3N-passivated inverted PSCs. Inserted with the chemical structures of PCBB-3N-3I/PCBB-3N. (e) Schematic illustration of an inverted PSC treated by Y6, and the use of Y6 shows multi-functions marked in the diagram (1) ETL, (2) moisture barrier, (3) near-infrared light absorption, (4) defect passivation, and (5) ion migration suppression. Reproduced with permission from ref [87]. Copyright 2020 Elsevier.

Inorganic molecules like LiF are also a popular type of surface engineering materials. Lu et al. employed a simple method to modify interfacial charge transport by adding a trace amount of indium bromide ($InBr_3$) atop $Cs_{0.07}FA_{0.70}MA_{0.23}PbI_3$ perovskites, which enabled a self-formed $n/n^+$ homojunction between the bulk and surface of a monolithic perovskite film by increasing the electron concentration. The passivated device exhibited an enlarged built-in electric field and an enhanced ability for charge carrier extraction and dynamics between the perovskite/ETL. The resulting blade-coated device showed a high PCE of 22.2%.[215] Similarly, Wu and co-workers regulated the top surface of perovskite film with cadmium iodide ($CdI_2$), which significantly reduced the iodine defect density and the ion migration.[214] A champion PCE of 21.9% with an impressively small voltage deficit of 0.31 V was obtained. Another illustrative example is that Jen and coworkers introduced fluoro-terminated $TiO_2$ nanosheets (F-$TiO_2$ NSs) between perovskite/$C_{60}$ ETL.[217] The high amount of exposed fluoro group induced interfacial interactions such as electronic coupling and hydrogen bonding with uncoordinated $Pb^{2+}$, and MA/FA cations, reducing the surface defect centers and inhibiting the ion migration. The treated device exhibited a PCE of 22.86% together with excellent operational stability.

As previously mentioned, various kinds of passivation agents have been introduced at the perovskite/fullerene based-ETL. Some perform chemical passivation functions by hydrogen bond, covalent bond, or coordination bond, others function as filed effect passivation.[223] Additionally, these passivation layers could serve to eliminate direct contact between the perovskite and the fullerene-based ETL, which is known to induce serious non-radiative recombination, leading to a decrease in $V_{OC}$ and PCE.[18, 224-225] For instance, Stolterfoht et al. denote that the majority of the recombination loss occurs within the initial monolayer of $C_{60}$ rather than in the bulk or at the perovskite surface, and the $C_{60}$ molecules act as deep trap states when directly contacting the perovskite, leading to significant recombination losses.[226] Janssen's group has also demonstrated that passivation agents like choline chloride and LiF, when employed at

the perovskite/$C_{60}$ interface, can suppress non-radiative recombination regardless of the perovskite layer's bandgap. This suppression is attributed to the increased spatial separation between perovskite and $C_{60}$, rather than an improvement in energy level alignment or surface as well as bulk passivation of perovskite films.[224]

### 4.2 Buried Interface Engineering

Due to the non-exposed nature and processing difficulties of the buried interface, most studies on interfacial engineering focus on the top interface of the perovskite film. In spite of the great advancement of top-interface engineering, the bottom interface should be treated with the same importance as the top interface, since the buried interface is also likely enriched with deep-level trap states from both HTLs and perovskite films inducing the unwanted charge combination. Additionally, band misalignment at the buried interface could adversely influence efficient charge transportation.[88, 227]. More importantly, the perovskite film coverage, nucleation, and growth are highly dependent on the substrate properties.[8, 162] Recently, we employed a facile lift-off method to expose the buried interface (Figure 18a). According to the SEM measurement, large flaky lead-halide grains were observed at the bottom surface, while the top surface exhibited more uniform morphology with smaller lead-halide grains (Figure 18b). Moreover, the confocal PL mapping measurement for the buried interface demonstrated that the accumulation of large lead-halide phases speeded up the annihilation of the photo-generated charge carriers (Figure 18c). Furthermore, it was found that the preferential orientation of the crystalline grains varied dramatically at the buried interface (Figure 18d). These results denote that the buried interface of the pristine perovskite films is accumulated with imperfection and pretty inhomogeneous, which adversely impacted the device performance. Therefore, the buried interface engineering, which has been largely neglected in perovskite photovoltaics, is essential. Through buried interface engineering, perovskite film morphology, charge-carrier extraction and transport, and crystal growth can be modulated, leading to the enhancement of device performance.

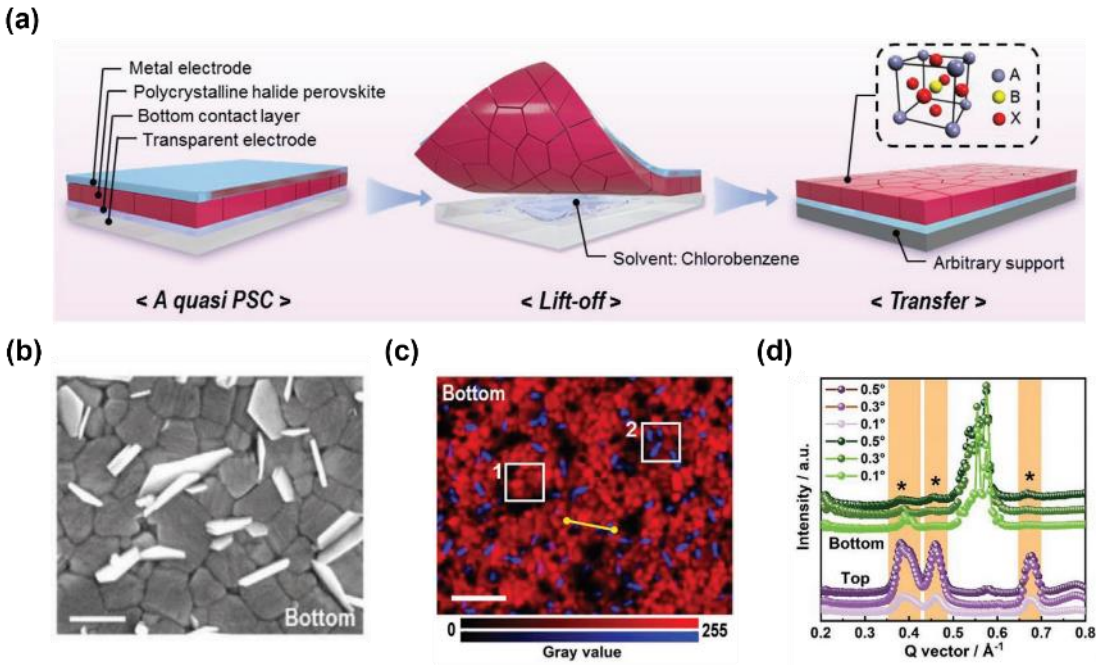


**Figure 21.** (a) Schematic of the lift-off process. A: monovalent organic or inorganic cations, B: $Pb^{2+}$, X: halogen anions. (b) Top-view SEM images of the bottom surface of the perovskite film. (c) Confocal PL mapping images of the bottom sides. Scale bar: 2 μm. The ranges of the detection are 700-790 nm (red bar) and 500-570 nm (blue bar), respectively. (d) Integral angle-dependent GIWAXS profiles for both top and bottom sides of the ammonium-halide-modified perovskite films. Reproduced with permission from ref [88]. Copyright 2021 John Wiley and Sons.

PTAA and poly-TPD, as well-known polymeric HTLs in the fabrication of inverted PSCs, exhibit hydrophobic surfaces, which makes it difficult to deposit pinhole-free and uniform perovskite films. It is typical to pre-treat the organic HTL with polar solvents or solutions with molecules dissolved in the polar solvent (e.g., IPA, DMF, methanol) before spin-coating the perovskite precursor. Apart from the surface-wetting effect mentioned before, these materials could also passivate defects at the buried interface. For example, in 2020, Li et al. modified the HTL/perovskite buried interface by fluorene-based conjugated polyelectrolytes including poly[(9,9-bis(3'-(N, N-dimethyl)-N-ethylammonium)-propyl)-2,7-flu-orene)-alt-2,7-(9,9-di-octylfluor-ene)] diiodide (PFN-I), PFN-Br, and PFN. The insertion of PFN-I at the underlying

interface between perovskite and polymeric HTLs eliminated the dewetting issue of poly-TPD as indicated by smaller contact angles of perovskite solutions on PFN-I treated HTL compared to the pristine HTL, thereby delivering full coverage of the perovskite film (Figure 19a,b). Additionally, it was discovered that the functional pendant groups of PFN-I were capable of passivating defects, e.g., ion vacancies in perovskite films, and the hydrophobic polymer chain could inhibit the ingress of moisture (Figure 19c).[207] This strategy was also applicable to the modification of PTAA/perovskite bottom interface in inverted PSCs. Through treating the buried interface with PFN-Br, the perovskite films based on the two-step sequential deposition method exhibited a remarkable Shockley−Read−Hall carrier lifetime of 18.2 μs, leading to a maximum PCE of 22.5% for the final inverted PSCs.[208] Alkylammonium salts dissolved in polar solvents are also effective in improving the wettability of the perovskite underlying substrate. For instance, Matteo's group treated HTL/perovskite interface by applying various alkylammonium salts with different halide anions, exploring their impact on the device performance. It was noted that, in contrast to studies on organic cations in post-treatment salts, the role of halide selection in the passivation effect has been largely underexplored.[228] They found that treating the interface with F-PEAI (in DMF) enhanced the wettability of PTAA, which helped obtain void-free contact at the HTL/perovskite interface and achieve better coverage of perovskite films compared to control films. Furthermore, when combined with top-interface modification using the same passivation salt, the F-PEAI-modified inverted PSCs delivered a champion PCE of 23.7%.[70]

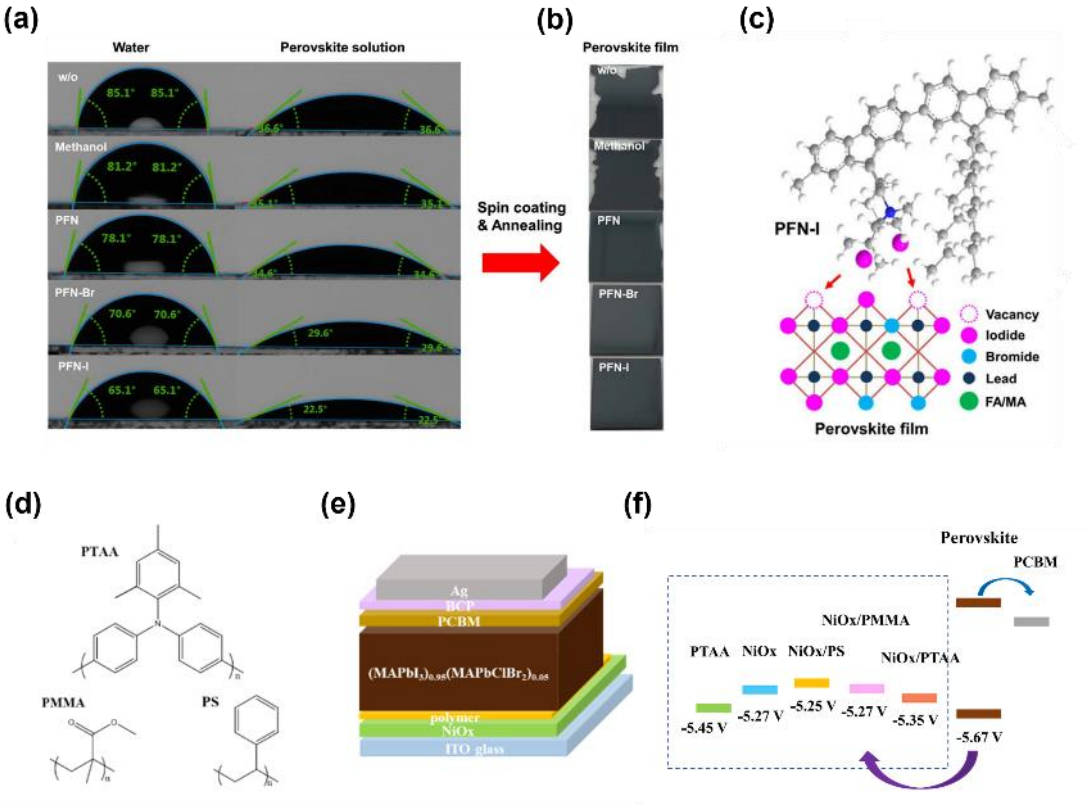


**Figure 22**. (a) The contact angle of water and perovskite precursor solution on the ITO-coated glass/poly-TPD substrate with various treatments for Ploy-TPD. (b) Images of corresponding formed perovskite film after spin-coating and annealing process. (c) Schematic illustration of the interaction between PFN-I with the perovskite. Reproduced with permission from ref [207]. Copyright 2020 John Wiley and Sons. (d) Chemical structures of the polymer materials PTAA, PMMA, and PS. (e) Scheme for the device architecture with the inverted structure. (f) Energy band structure of the perovskite films and different substrates. Reproduced with permission from ref [209]. Copyright 2020 American Chemical Society.

The deep-level trap states at the buried interface not only come from the bottom interface of the perovskite light-absorbing layer, but also from the HTLs, especially the inorganic HTLs typically $NiO_x$ in the fabrication of inverted PSCs. The $NiO_x$ film tends to have many types of defects on the surface like hydroxyl groups, oxygen vaccines, and unsaturated coordinated metal atoms, resulting in interface reaction and non-radiative recombination. Thereafter, treating the $NiO_x$/perovskite interface with

appropriate materials to realize the goal of passivating the perovskite films and HTLs surface is essential for obtaining highly efficient and stable inverted PSCs. Moreover, such treatment could help achieve improved energy level alignment. Polymers, small organic molecules, inorganic salts, and SAMs are found to be effective in modifying the buried interface of $NiO_x$/perovskite film.[147, 229] In 2020, Chen et al. introduced different polymers including polystyrene, poly(methyl methacrylate) (PMMA), and PTAA at the contact between $NiO_x$ and the perovskite layer (Figure 19d,e). The polymer barrier inhibited the direct interaction between $NiO_x$ and the perovskites, and the PMMA-containing carbonyl and methoxy groups could passivate defects at the buried interface, leading to a prominent $V_{OC}$ of 1.19 V. The use of PTAA delivered a deepened highest occupied molecular orbital (HOMO) level, endowing improved energy level alignment at the buried interface (Figure 19f). As a result, the inverted PSCs with PTAA-modified $NiO_x$ showed enhanced PCEs from 19.2% to 21.6%.[209]

Compared to organic interlayers that may degrade over time and compromise device stability, inorganic materials demonstrate superior charge carrier dynamics and thermal stability, also showing great potential as passivation layers to enhance the performance and stability of PSCs.[230] Xu et al. implemented an inorganic bilateral strategy by applying a potassium fluoride (KF) interlayer at both above and beneath the perovskite layer.[213] These bilateral KF "walls" provided chemical-anchoring functionality, inhibiting the formation of iodine-vacancy defects and suppressing trap-assisted recombination, while also physically impeding ion migration. The modified devices achieved a PCE of 22.02% and demonstrated outstanding thermal stability. Besides the abovementioned chemical passivation strategy, there are also some new approaches, such as the physical passivation method to undergo film treatment. For instance, Wang et al. in order to modify carrier distribution at the interface, they introduced an interlayer possessing fixed charges at the heterojunction.[218] This approach effectively lowered the density of charge carriers with identical charges near the heterojunction, while simultaneously increasing the density of charge carriers with

opposite charges. This led to an alteration in the capture cross-section, ultimately resulting in a reduced surface recombination rate ($U_s$). Moreover, they systematically incorporated metal oxides (MO), either aluminium oxide ($AlO_x$), which carried negative fixed charges, or silicon oxide ($SiO_x$), which carries positive fixed charges, at the perovskite/$NiO_x$ heterojunction (Figure 20a). Note that the ALD technique was employed to achieve accurate control of the layer thickness. This strategy contributed to a stabilization of negative and positive charges at the interfaces between the MO and perovskite, modifying the distribution of electrons and holes and thereby leading to improved passivation. The optimal device demonstrated superior efficiency and robust stability, even in stringent aging environments. Apart from depositing the $AlO_x$ by the ALD method, spin-coating a thick $Al_2O_3$ nanoplate layer (about 100 nm) with random nanoscale openings at the buried interface of the perovskite film was also effective in reducing the non-radiative recombination through contact area reduction and defect passivation (Figure 20b). This contact design at the buried interface was referred to as porous insulator contact (PIC). Through this design with optimized $Al_2O_3$ isolated islands coverage (~25%) and concentration (1.4 mg $ml^{-1}$) on the HTL (Figure 20c), a simultaneous maximization of $V_{OC}$ and FF of devices was realized, contributing to a remarkable PCE of 25.6% with a certified PCE of 24.7% (Figure 20d). In addition, the PIC devices with an active area of 1 $cm^2$ showed an impressive PCE of 23.3% (Figure 20e).[57]

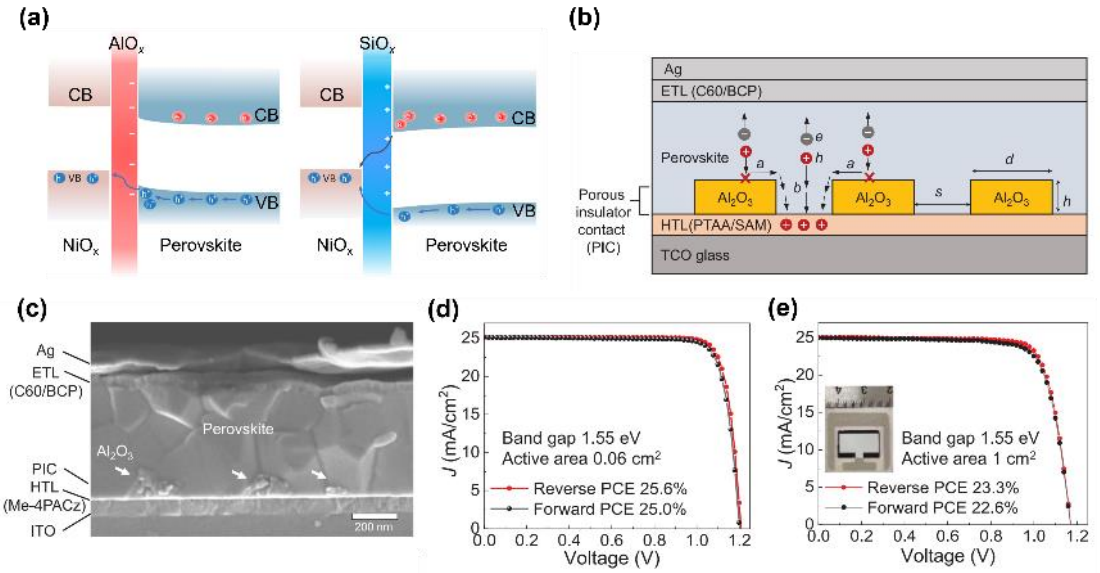


**Figure 23.** (a) Schematic diagrams of the electronic structures and charge carrier distribution in the conduction and valence bands (CB, VB) for perovskite/$NiO_x$ heterojunctions reveal that incorporating an $AlO_x$ interlayer (LHS) or adding a $SiO_x$ interlayer (RHS), would affect charge carried dynamics. Hole transport, represented by blue arrows, is present in both instances; however, the inherent negative charges in the $AlO_x$ interlayer led to a reduction in electron-hole recombination, as shown by the black arrow. Conversely, the inherent positive charges in the $SiO_x$ interlayer do not contribute to this reduction. Reproduced with permission from ref [218]. Copyright 2023 Springer Nature. (b) Schematic description of the porous insulator contact (PIC) device (not to scale). Local $Al_2O_3$ dielectric mask's height, width, and local opening width are represented by the parameters *h*, *d*, and *s*, respectively. Lateral transport of carriers that cannot electrically tunnel through the thick $Al_2O_3$ is denoted by process *a*. Carriers' "through-the-opening" transport through the channels formed by the perovskite infill is represented by process *b*. By reducing the perovskite/HTL contact area and suppressing interface recombination, the insertion of PIC reduces. The PIC coverage fraction is defined as $[d/(d + s)]^2$. The electron and hole charge carriers are represented by e and h, respectively. (c) Cross-sectional SEM image of the PIC device. J-V characteristics of the champion small-area (d) and large-area (e) PIC devices under reverse and forward scans. Reproduced with permission from ref [57]. Copyright

2023 American Association for the Advancement of Science.

To summarize, interface engineering of the perovskite active layer in the inverted architecture has become an indispensable part of constructing stable and efficient PSCs no matter the regular or inverted type. Numerous interface engineering strategies bloomed together, which served to: 1) Eliminate interface trap states; 2) Modify band alignment at the heterojunction interface; 3) Reduce the interface charge recombination; 4) Improve the perovskite film quality.

## 5. STABILITY OF INVERTED PSCS

Apart from the PCE, PSCs should also have excellent stability to meet the requirements of commercial applications. Prior to discussing the stability of inverted PSCs, it is essential to differentiate between stability, reliability, and durability, given that these terms are frequently misused within the field. Stability refers to the ability of a PSC to maintain its performance over an extended period of time, especially under various ageing conditions. It involves assessing the device's resistance to stresses like heat, light, oxygen, and other external factors that can impact its device performance.[231-232] For reliability, it goes beyond stability and encompasses the overall consistency and predictability of a PSC's performance. It involves evaluating the device's ability to consistently deliver the expected electrical output over its operational lifetime, without significant performance deviations or failures.[233] Durability is a broader concept that includes both stability and reliability. It refers to the overall capability of PSCs to maintain their performance over an extended period. It focuses on the device's ability to withstand mechanical stress, temperature cycles, and other operational conditions without degradation or failure. The durability assessment aims to ensure that the cell can maintain its performance and structural integrity for a specified period, typically the intended lifespan of the solar module.[234] Given the previous literature, the stability is mainly discussed here.

For perovskite photovoltaics to compete as commercial solar products, it is of critical

importance to enable a decent level of certainty that the fabricated PSCs will work for 25 years, which requires going beyond the industrial lifetime assessment standard issued by the IEC. Among the IEC standards, IEC 61215:2016 is the most-used standard for mature photovoltaic technologies.[235-236] For the regular-type PSCs, the use of $TiO_2$ ETL due to its photocatalytic properties would induce instability issues when exposed to ultraviolet (UV) illumination. Moreover, to improve the hole-transporting of 2,2′,7,7′-tetrakis(N,N-di-p-methoxyphenylamine)-9,9′spirobifluorene (Spiro-OMeTAD), introducing dopants like bis(trifluoromethanesulfonyl)imide (Li-TFSI) and 4-tert-butylpyridine (TBP) is essential. Whereas, the use of such hygroscopic dopants tends to trigger degradation of the perovskite films, hastening the drop of PCE.[237] In contrast, inverted PSCs are reported to exhibit outstanding long-term stability under various harsh ageing conditions such as damp-heat testing at 85°C and 85% relative humidity which is one of the main standard items for the mature IEC 61215:2016 standard, attracting enormous research attention.[16-17] The origin of the superior stability of inverted PSCs is as follows:

1) High-quality perovskite films. Stable PSCs regardless of inverted or regular configuration need compact, even, and ideally defect-free perovskite films, which are favorable to minimize trap-assisted recombination and inhibit ion migration. To achieve this goal, it is important to control perovskite crystallization and passivate defects in perovskite bulk films, which are mainly accumulated at surface and grain boundaries. In this regard, selecting proper deposition techniques, processing solvents, and additives could be effective in assisting the crystallization of perovskite and managing defects to obtain a high-quality perovskite layer. Additionally, composition tuning plays a decisive role in addressing the inherent instability problem of perovskites. MA- and Br- free perovskite composition may be a possible candidate for realizing stable inverted PSCs.[23, 26]

2) Stable and multifunctional CTLs. Differing from the regular PSCs largely relying

on Spiro-OMeTAD with hygroscopic dopants, dopant-free CTLs (e.g., PTAA, SAMs, $NiO_x$, fullerenes) are applicable to the inverted PSCs and exhibit good energy-level alignment with the perovskite layer. The ETLs atop the perovskite films like fullerene could protect the perovskite light absorber from the ingress of moisture due to its hydrophobic nature. Among the HTLs, SAM containing carbazole and phosphonic acid groups are emerging as an effective HTL, replacing the conventional HTL in inverted PSCs. It is reported that the SAM-HTL is beneficial for suppressing light-induced halide segregation due to both fast hole-extraction and efficient passivation at the buried interface.[177] Additionally, SAMs with super wetting properties can help form high-quality perovskite films and passivate the defects at the buried interface, endowing PSCs with improved stability under the damp-heat stability test compared to devices based on hydrophobic HTLs.[14] For inorganic $NiO_x$, the undercoordinated $Ni^{\geqslant 3+}$ defects which are detrimental to the device stability can be pre-treated by SAM layers or polymers to prevent the perovskite from reacting with defects in $NiO_x$ films.[158, 209, 238] A better coverage of the SAM layer by surface morphology regulation[189] or using binary SAM layers.[61, 76] is conducive to improving the device stability.

3) Perovskite-CTL interface engineering. For both regular and inverted PSCs, interfacial engineering has become an essential procedure for fabricating state-of-the-art PSCs with outstanding efficiencies and stability. As discussed before, extensive research efforts have been devoted to interfacial engineering for constructing stable inverted PSCs like constructing 2D/3D heterojunction interfaces,[16, 67, 70] perovskite secondary growth by large ammonium salts,[165] and surface sulfidation.[66] A notable illustration would be the surface treatment utilizing OLAI. The manipulation of the dimensionality (n) of the OLAI-based 2D-perovskite through adjustment of the annealing temperature significantly affects the stability of the device.[16] Another effective way of tuning the n of 2D perovskites is *via* choosing bulkier organic cations together with small

modifications to ligand, which is able to obtain preferential growth of n ⩾ 3 reduced dimensional perovskites (RDPs). Perovskite films coated with increased n ⩾ 3 RDPs exhibit more efficient charge extraction, leading to higher PCEs. More importantly, the modified devices displayed excellent stability under ISOS-L-3 ISOS-L-1I accelerated-ageing protocols.[67] Note that the interfacial engineering at the buried interface is equally important as the engineering at the top interface for improving the stability of inverted PSCs. For instance, constructing a bottom-up 2D/3D heterojunction at the buried interface through doping AICI into the perovskite precursor enabled excellent stability when subjected to a damp-heat test (85°C and 85% relative humidity).[23] Another notable example is depositing an $AlO_x$ layer by ALD at the $NiO_x$/perovskite interface. The optimized inverted PSCs maintained the initial performance after ageing at harsh conditions (85°C MPP tracking in the air) for 2000 h, which represents a breakthrough towards the real-life application of PSCs (Figure 21a,b).[218]

4) CTL-electrode interface engineering. The diffusion or migration of mobile ions from the perovskite absorber throughout the top ETL, followed by their accumulation at the metal electrode interface, has been shown to corrode the metal electrodes, posing a significant risk to the device stability.[239] Additionally, the migration of metal atoms from the electrode into the underlying electron-transporting and perovskite layers raises another crucial concern regarding long-term instability.[240-242] Pioneering research has demonstrated that incorporating a strategic barrier layer, such as ZnO nanoparticles[243] or a bilayered aluminum-doped zinc oxide (AZO)/$SnO_x$[244] between the ETL and the top electrode can significantly mitigate the issues related to the ingress and egress of mobile species. Afterwards, Jen and coworkers used a thiol-functionalized 2D conjugated metal–organic framework at the fullerene ETL/cathode interface, which could not only protect perovskites from the ingress of moisture and oxygen but also trapped mobile $Pb^{2+}$ ions (Figure 21c).[245] Alternatively, inserting a bilayer buffer

consisting of BCP/bismuth (Bi) between ETL and electrode could help prevent the perovskite from the invasion of moisture and protect the metal electrode from iodine corrosion (Figure 21d). Thereafter, Bi-devices maintain 95% and 97% of their initial PCEs after 500 h of ageing under thermal annealing at 85°C and light soaking in a nitrogen atmosphere, respectively.[240] Replacing the Ag electrode with Cr/Cu alloy is another effective way to prohibit electrode corrosion and diffusion. Whereas the improvement of device stability by this method may be at the expense of a slight drop in PCE.[65] Recently, a novel amorphous $ZrN_x$ buffer layer was developed to suppress ions/atoms diffusion and eliminate metal electrode corrosion (Figure 21e,f).[239] For inverted PSCs, the direct contact of metal electrodes with ETLs like PCBM or $C_{60}$ is prone to form Schottky contact, causing serious charge accumulation. It is often necessary to incorporate a BCP buffer layer to solve this problem. This buffer layer serves multiple purposes: it promotes an ohmic contact and reduces the accumulation of charges at the interface. Whereas, the organic BCP is relatively unstable compared to inorganic materials, posing a threat to the device stability. Replacing BCP with an inorganic buffer layer has shown great efficacy in improving the device stability.[16, 57] For instance, Wolf et al. substituted the organic buffer layer BCP with inorganic $SnO_2$/IZO to improve damp-heat (85°C/85% of relative humidity) stability.[16] Recently, we inserted an amorphous ytterbium oxide ($YbO_x$) layer between ETL and the electrode by simple thermal evaporation (Figure 21g). The $YbO_x$-based narrow-bandgap PSCs (1.53 eV) showed an outstanding certified PCE of 25.09%. Meanwhile, the wide-bandgap (1.77 eV) and mid-bandgap (1.61 eV) PSCs with $YbO_x$ realized state-of-the-art PCEs of 20.1% and 22.1%, respectively, indicating good universality of this buffer layer. We found that the charge transport follows a thermally activated hopping from one localized state to another. More importantly, compared to BCP devices, the $YbO_x$-based devices displayed enhanced stability under ISOS-L-3 ageing protocols. The XPS and Tof-SIMS testing results indicated

suppressed ion/atom migration by $YbO_x$ (Figure 21h). This work underscores the critical role of the buffer layer in inverted PSCs. Additionally, The success of amorphous-$YbO_x$ buffer layer indicates that amorphous metal oxides would be ideal buffer materials for inverted PSCs, paving a new avenue of developing multifunctional buffer layers for the construction of efficient and stable perovskite photovoltaics.[246]

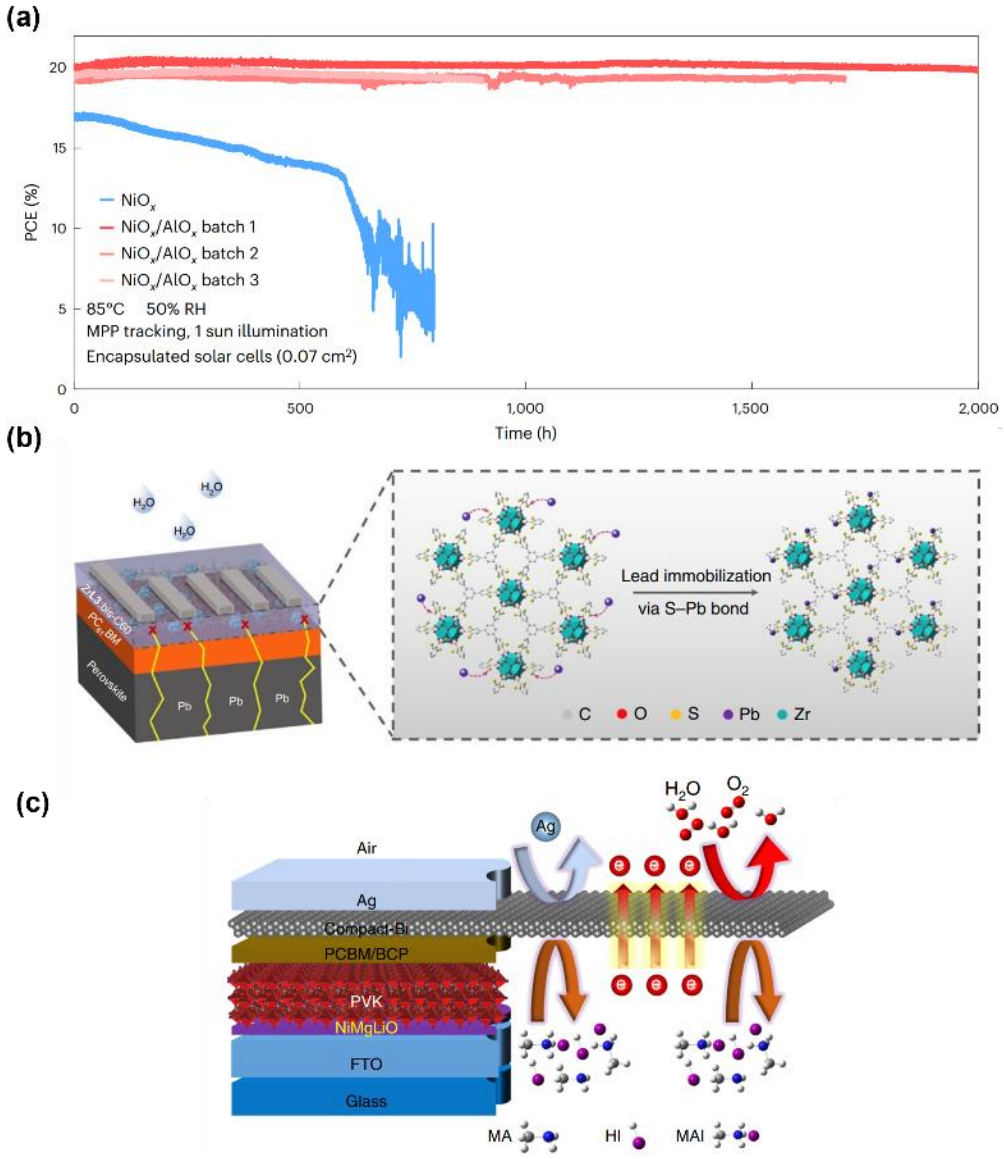


**Figure 24.** (a) MPP tracking of an unencapsulated device held at 85°C under 1-Sun illumination and 50% relative humidity. Reproduced with permission from ref [218]. Copyright 2023 Springer Nature. (b) Schematic illustration of the degradation process of PSCs and the immobilization function of ZrL3 on leaked $Pb^{2+}$. Reproduced with

permission from ref [245]. Copyright 2020 Springer Nature. (c) Schematic illustration of the blocking function of the bismuth interlayer. Reproduced with permission from ref [240]. Copyright 2019 Springer Nature.

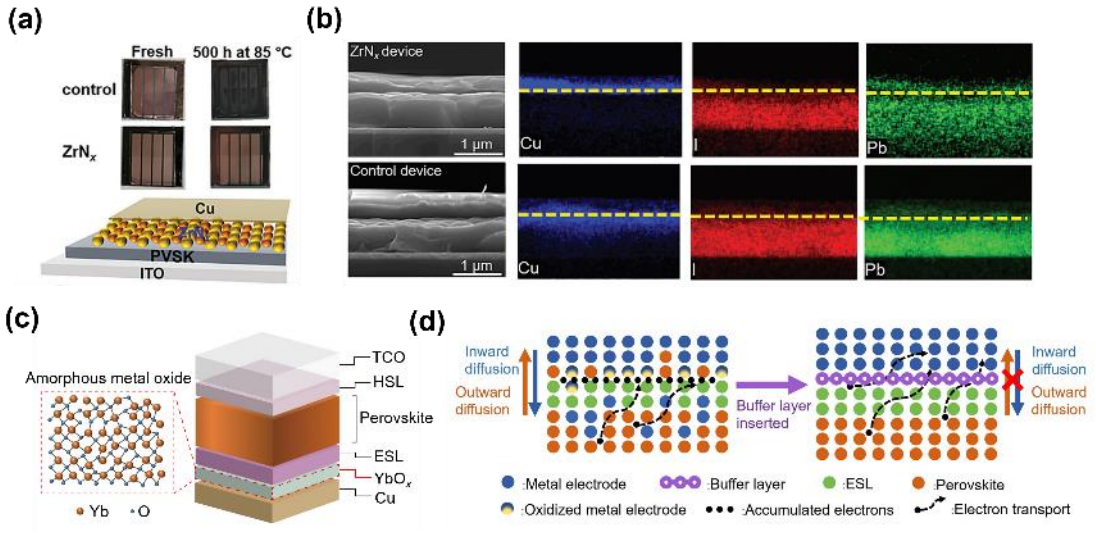


**Figure 25.** (a) Photographs of control and $ZrN_x$-based devices after thermal annealing at 85 °C for 100 h. (b) Cross-sectional energy dispersive spectrometer (EDS) images of the $ZrN_x$ devices and the control device after thermal aging at 85 °C for 1,000 h. Reproduced with permission from ref [239]. Copyright 2023 John Wiley and Sons. (c) Schematic illustration of the device configuration with the YbOx buffer layer. The magnified area illustrates the amorphous nature of the $YbO_x$ buffer layer. (d) Schematic illustration of the functions of an ideal buffer layer between the electron-selective layer (ESL) and the metal electrode, demonstrating its ability to prevent the movement of harmful species and non-radiative recombination.[246]

5) Effective encapsulation. Encapsulation is an important and widely used method to dramatically enhance the photovoltaic technology operational stability via preventing environmentally related performance degradation and improving the mechanical strength against external impact.[247] Chen et al. used low-cost paraffin as the encapsulant. It was found that in addition to preventing perovskite phase segregation by removing residual oxygen and moisture, the paraffin-based encapsulation strategy also impeded perovskite decomposition by suppressing

species volatilization.[248] Moreover, encapsulation with lead-absorbing materials (e.g., materials containing phosphonic acid groups) could reduce Pb leakage from PSCs.[249] Epoxy resin-based encapsulation could also effectively reduce the Pb leakage rate due to its great self-healing properties.[247] Similarly, very recently, Shao and coworkers reported a simple and economic shellac-based encapsulation strategy, which was effective in lead sequestration after mechanical shock damage. Moreover, the perovskite solar modules encapsulated by shellac had successfully passed various accelerated ageing testing according to IEC 61215 standards.[250] The encapsulation techniques in the silicon solar cells are also adaptable to the PSCs. In detail, commercial polymer encapsulants like polyolefin (POE) cohesively sandwiched the PSCs between two glass sheets, protecting the PSCs from the ingress of moisture and oxygen. For instance, Shi et al. reported a polymer/glass blanket encapsulation technique through the use of POE or polyisobutylene (PIB). Compared to the edge-sealed cells, PIB or POE blanket encapsulated cells showed greatly enhanced stability, passing the requirement set by the IEC 61215:2016 damp-heat and humidity freeze tests. Based on gas chromatography–mass spectrometry analysis, it was uncovered that by utilizing a polymer-glass blanket encapsulation method, a pressure-tight environment was created, inhibiting the escape of decomposition products (e.g., $CH_3I$, $CH_3Br$, and $NH_3$) and thus enhancing the device stability.[251] In general, the typical encapsulation techniques can be classified into two types. One is thin-film encapsulation, in which the encapsulation materials are directly deposited on the active layer; The other is edge seal, in which sealant is placed on the edge of the active area.[252]

IEC 61215:2016 and similar stability testing protocols typically focus on a single stressor or, at most, two stressors.[253] For instance, the damp-heat test assesses device stability under elevated temperature and humidity but does not consider exposure to light illumination. However, in real-life solar cell operating conditions, all aging

stressors, including sunlight intensity and spectrum, heat, and ambient humidity, are combined. Consequently, outdoor stability testing for solar cells is a complex undertaking. Despite the challenges, a comprehensive investigation of outdoor stability of PSCs is necessary for addressing the concerns about the stability of PSCs.

The ISOS protocols for outdoor stability testing can be divided into three types. First, in the ISOS-O-1 protocol, *J*–*V* curves are measured periodically using a solar simulator for illumination. For example, He et al. reported that by inserting a boron chloride subphthalocyanine ($Cl_6$SubPc) interlayer between the perovskite layer and $C_{60}$ (Figure 22a**)**, the interfacial defect density was reduced and ion migration was inhibited. The outdoor stability tests following ISOS-O1 protocol confirmed the excellent stability of $Cl_6$SubPc-based devices ($T_{95}$ of 1272 h) (Figure 22b**)**.[154] In the ISOS-O-2 protocol, the *J*–*V* measurements are periodically obtained under natural sunlight. Figure 22c shows an example of stability testing results under the ISOS-O-2 protocol. For outdoor testing, the devices were encapsulated by POE as an encapsulant and butyl rubber as the edge sealant, and this encapsulation method is also widely employed in silicon solar cells. The encapsulated devices maintained the initial PCE after outdoor stability testing for about 9 months. The performance recovery during the night contributes to such impressive stability. During the summer season (July–September, Berlin), the temperature of the device was increased, leading to a rapid performance drop. This means that the combination of illumination and thermal ageing stressors is likely to accelerate the degradation of PSCs.[254] As for ISOS-O-3, it necessitates both in situ MPPT under natural sunlight and periodic performance measurements using a solar simulator, which is the most demanding testing protocol for outdoor stability testing.[253, 255] For instance, following the ISOS-O-3 protocol, Khenkin et al. compared two common encapsulation techniques: glue-based encapsulation and lamination-based encapsulation. The former method has been widely used in the laboratory, while the latter one is generally used in the commercial field. As shown in Figure 22d, a sample with glue-based encapsulation failed after

only 4 days, while the other sample with the same encapsulation method failed after 6 weeks. The reason behind the quick drop in device performance when using glue-based encapsulation is probably the result of mechanical stress caused by an uneven encapsulation process. In comparison, devices with lamination-based encapsulation showed excellent stability with no performance loss after 10 months outdoor stability testing. A night-time performance recovery was also found after periodical indoor measurements.[256] The outdoor stability testing is complicated and has stringent requirements, making it hard to implement for most research groups. Indoor stability testing is more accessible. An investigation of the correlation between indoor tests and outdoor field operation can help many research groups better evaluate their device stability under real-world outdoor conditions. Zhu et al. found that the indoor operational stability testing at high temperatures (e.g., 85°C) under light illumination shows a significant correlation with outdoor stability testing(Figure 22e,f). [257]

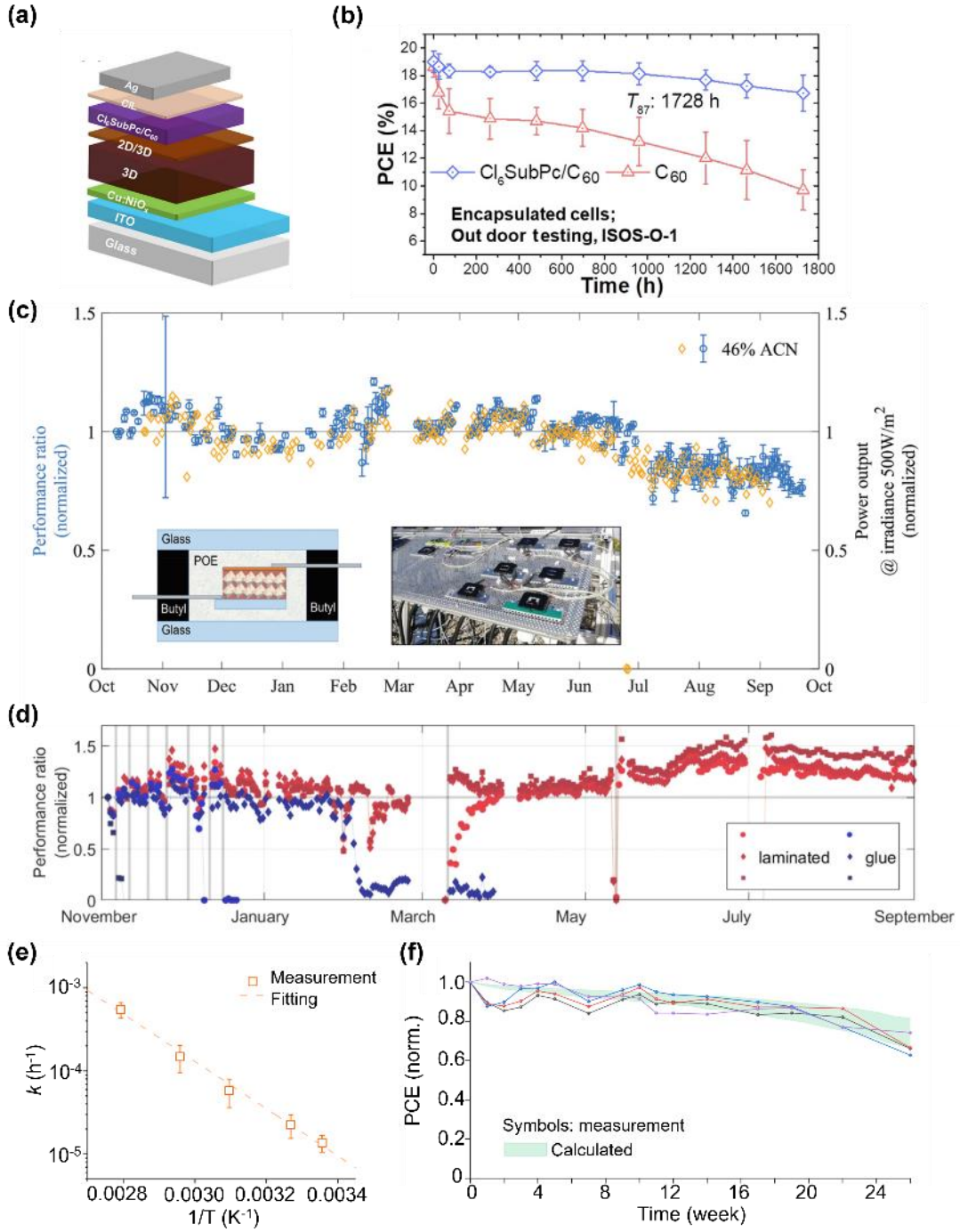


**Figure 26.** (a) Device architecture of the inverted PSCs with $Cl_6SubPc$. (b) Outdoor stability of the encapsulated control $C_{60}$ devices (five cells) and $Cl_6SubPc/C_{60}$ devices (nine cells) based on ISOS-O-1 protocol. Reproduced with permission from ref [154]. Copyright 2021 Elsevier. (b) Normalized PCE evolution (averaged over three PSCs) and cell MPP power at 500 W $m^{-2}$ based on ISOS-O-2 protocol. (c) Variations in the global irradiance in the plane of array and the power output of a PSC during one day.

(d) Device temperature and global irradiance throughout the entire exposure period. Reproduced with permission from ref [254]. Copyright 2023 John Wiley and Sons. (e) Normalized PCE evolution of glued and laminated cells based on ISOS-O-3 protocol. Gray lines indicate the days in which indoor control measurements were taken. Reproduced with permission from ref [256]. Copyright 2022 American Chemical Society. (f) The temperature-dependent hourly degradation rates ($k = 1/T80$). The error bars for each temperature are derived from 8–17 individual devices. (g) Normalized PCE evolution based on ISOS-O-1 protocol. The light green band demonstrates the calculated degradation range based on the temperature-dependent hourly degradation rates derived from Figure 22f. Reproduced with permission from ref [257]. Copyright 2023 Springer Nature.

## 6. TANDEM DEVICES WITH INVERTED PSCS

Nowadays, the PCE of single-junction solar cells is quite approaching their theoretical performance ceiling of ~33% PCE based on S–Q calculation.[30] To further increase the solar cell performance and break the S–Q limit of PCE, several absorber films with complementary absorption ranges can be stacked to fabricate the multijunction solar cells (tandem solar cells, TSCs). In one tandem solar cell, the front cell with a larger bandgap absorbs the high-energy photons, while the low-energy photons are captured by the smaller bandgap rear cell. By mitigating the losses of carrier thermalization, the TSCs can deliver an efficiency higher than either a single front or rear cell itself. Based on theoretical estimation, the ceiling PCE of two-junction TSCs could surpass 40%, and the ultimate efficiency achievable is 68% when infinite absorbers are stacked.[258-259] Note that triple-junction perovskite TSCs with higher theoretical PCE limit versus the two-junction TSCs have also been attracting more and mor research attentation and made significiant progresses. Sargent's group and Hou's group have realized champion certified PCEs of 23.87% for triple-junction all-perovskite TSCs and 27.10% for triple-junction perovskite/perovskite/Si TSCs, respectively.[260] [261] Considering that a TSC with two absorbers is cost superiority and sufficient for most

of the practical needs, therefore TSCs refer to two-junction solar cells specifically in the following text. The two absorbers of one TSC can be either stacked with a monolithic two-terminal configuration (2T) or stacked mechanically with a four-terminal configuration (4T). In the 2T configuration, two subcells are connected in series by an interconnecting layer (ICL) within one monolithic device. For the 4T configuration, the wide bandgap (WBG) subcell is only mechanically placed in front of the narrow bandgap (NBG) subcell, while both subcells have their own circuits and are electrically separated. Although the 4T configuration does not require the current matching between two subcells, this design would increase the fabrication process and cost. Over the past few years, the inverted PSC showing advantages of low-temperature processing, low parasitic absorption, and excellent operational stability has become a popular choice as the subcell for the construction of TSCs and achieved remarkable success.

Here we will mainly focus on the TSCs with 2T configuration. For a more comprehensive review of perovskite TSCs, we refer the readers to the previous works.[262-264] Figure 23 shows the efficiency evolution of three main types of 2T TSCs based on inverted PSCs, including perovskite-Si TSCs, all-perovskite TSCs, and perovskite-organic TSCs. In this section, we will review the development of all three types, with a focus on the optimization of subcells, manufacturing engineering, and the design of ICLs.

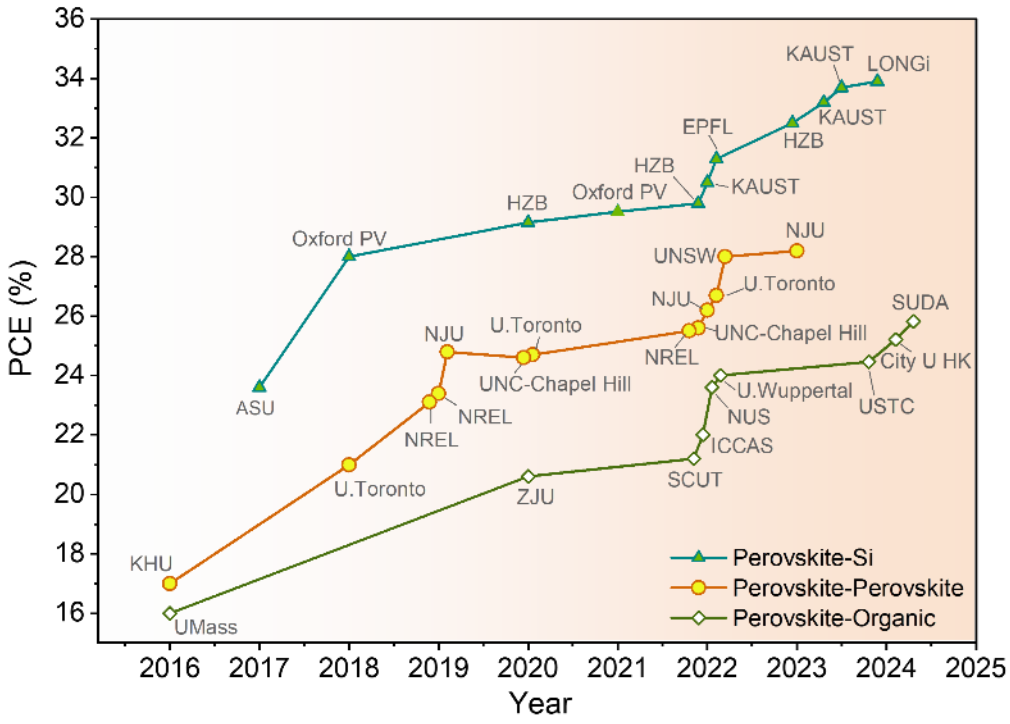


**Figure 27.** Chronological evolution of the PCE of inverted-structured TSCs.

### 6.1 2T Perovskite-Si TSCs

With the fast development in the past several decades, silicon solar cells have become the most mature photovoltaic technology and dominate the commercial photovoltaic market, which probably will last for another ten years or more. Since the champion PCE of silicon solar cells is 26.7%, which is quite approaching their S–Q limit, efficiency enhancement in silicon solar cells becomes very difficult with a small marginal benefit against vast research investment.[19] The low-cost perovskite materials with tunable bandgap have attracted communities' attention to fabricating perovskite-Si TSCs. The first perovskite-Si TSC was reported by Mailoa et al. in 2015.[265] Although the first perovskite-Si TSC delivered a moderate PCE of 13.7%, this seminal work demonstrates that the design of perovskite-Si TSC is feasible and the perovskite subcell is the efficiency-limiting part for further improvement. In the early years, most of the perovskite-Si TSCs employed the regular configuration due to the superior efficiency of n-i-p PSCs against their inverted counterparts.[266-269] However, these n-i-p devices employed the Spiro-OMeTAD as the HTL, which introduced

issues of material instability and low $J_{SC}$ due to its strong parasitic absorption in the short wavelength range.[237, 270] Owing to these issues of n-i-p structures and the raising of inverted PSCs, the perovskite-Si TSCs with inverted architecture have been attracting growing attention. To this end, McGehee et al. adopted the inverted structure in perovskite-Si TSCs for the first time in 2017.[271] To tackle the low $J_{SC}$ of n-i-p TSCs, this work used a functional bilayer consisting of $SnO_2$ and zinc tin oxide (ZTO) as the buffer layer, enabling the sputtering of the transparent ITO electrode. Through this design, parasitic absorption of window layers (i.e., layers that light passes through first before entering perovskite films) was minimized. Also, the bilayer was deposited by either ALD or pulsed chemical vapor deposition (CVD) that guaranteed a compact, conformal, and pinhole-free film, preventing shunt and damp-heat damage. For the WBG absorber, the recently developed perovskite with the composition of $Cs_{0.17}FA_{0.83}Pb(Br_{0.17}I_{0.83})_3$ was used due to its more complementary bandgap and much enhanced thermal stability compared with previous $MAPbI_3$. By integrating an infrared-tuned silicon heterojunction bottom cell (SHJ), this work lifted the $J_{SC}$ to 18.1 mA $cm^{-2}$ and achieved a record efficiency of 23.6% at that time.[271]

The efficient fabrication route for perovskite films atop Si substrate is another challenge. In previous works, the front sides of silicon cells were usually polished to be compatible with the crystallization features of perovskite precursor solutions. This inevitably leads to high reflection, low light trapping, and increased manufacturing costs. To solve this problem, Ballif's group et al. proposed a hybrid "evaporation + solution" (eva + sol) route to fabricate the perovskite films directly atop silicon pyramidal surfaces (Figure 24a-c).[272] In brief, the $PbI_2$ and CsBr were co-evaporated firstly, followed by the spin-coating of the FAI/FABr mixture, through which the perovskite films could maintain good conformal growth on the micrometer-sized silicon textured surfaces. Since as-fabricated TSCs made full use of the light management in silicon cells, a high $J_{SC}$ of 19.5 mA $cm^{-2}$ and consequentially a high PCE of 25.5% were yielded (Figure 24d,e). Liu et al employed the same method to

fabricate the WBG perovskite subcell on commercial silicon solar cells with an average pyramid size variation of ≈ 2–5 μm.[132] Combined with interface passivation, Ballif et al. realized an outstanding PCE of 31.25%.[273] Sargent et al. and Huang et al. successfully demonstrated that perovskite films could be solution-processed directly atop non-polished silicon pyramidal surfaces using either spin-coating or blading techniques, and achieved PCEs of 25.7% and 26.2%, respectively.[274-275] Inspired by the idea of making use of the texture, Becker et al. reported a gently designed nanotextured surface recently.[276] This nanotexture distinctly reduced the reflection loss while enabling excellent perovskite film formation. This design integrated the advantages of both polished surfaces and micrometer-sized textured surfaces and was responsible for minimizing $J_{SC}$ loss and increasing $V_{OC}$ respectively, finally leading to a certified PCE of 29.80%. These works indicate that the fabrication of perovskite films on textured substrates is no longer the most challenging factor.

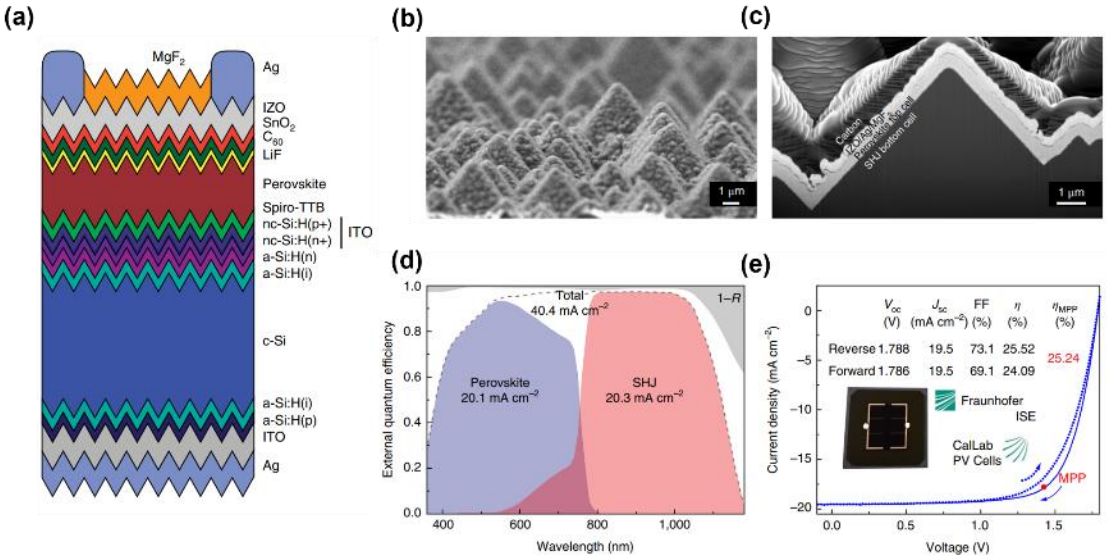


**Figure 28**. (a) Schematic of a fully textured monolithic perovskite/SHJ TSC. (b) Top-view SEM images of the perovskite film. (c) Cross-sectional SEM images of the full perovskite top cell prepared on the SHJ bottom cell. (d) External quantum efficiency (EQE) spectra and total absorptance (1 – R, where R is the reflectance) of the champion TSC. (e) Certified *J*–*V* curves of the champion device under reverse and forward scans with a scan rate of 100 mV $s^{-1}$. Reproduced with permission from ref

[272]. Copyright 2018 Springer Nature.

The optimization of perovskite-Si TSCs motivates increasing attention to another performance-limiting factor i.e., the WBG perovskite subcells. To be optically complementary with the silicon subcell, a WBG perovskite with a bandgap of 1.67–1.75 eV is desired.[263] Finely tuning perovskite bandgaps through compositional engineering without introducing stability issues is challenging. Instead of engineering the cation components, Kim et al. developed a 2D-3D mixed perovskite (1.68 eV) using an anion mixture of thiocyanate (SCN) with iodine.[277] Through careful anion engineering, optimal WBG perovskites treated by PEA($I_{0.25}SCN_{0.75}$) produced a PCE of 20.7% with a $V_{OC}$ larger than 1.2 V. Also, passivated by the 2D phase, as-prepared WBG PSCs can retain 80% of initial PCE after more than 1,000 h continuous illumination. Based on this treatment, the champion perovskite-Si TSC achieved 26.7% PCE with a $J_{SC}$ of 19.2 mA $cm^{-2}$, a $V_{OC}$ of 1.756 V, and an FF of 0.792 with negligible hysteresis. In the meantime, Xu et al. extended the traditional WBG perovskite double-halide composition using I and Br into a triple-halide composition including Cl.[40] Thanks to the ability of Cl to reduce defect density, it was observed the triple-halide WBG perovskite showed much enhancement in photocarrier lifetime and mobility by a factor of 2. The incorporation of Cl also suppressed the light-induced phase segregation at 100-sun illumination, ensuring long-term operational stability. By combining these WBG perovskites with silicon subcells, a PCE of 27.1% (stabilized PCE at the maximum power point of 27.04%) was obtained. Another notable example of reducing the bulk defects of WBG perovskite films is adding trimethylphenylammonium tribromide ($TPABr_3$). With the addition of $TPABr_3$, the best-performing WBG perovskite cell containing a thick perovskite absorber layer (about 1 μm) realized a PCE of 21.9% with an outstanding $V_{OC}$ of 1.25 V. The superior performance of WBG subcells contributed to an impressive PCE of 28.6% in monolithic perovskite–silicon tandem devices.[278]

In addition to the bulk perovskite materials, there are also massive imperfections that

exist at both surfaces and buried interfaces of perovskite films, rendering severe local non-radiative recombination and poor charge carrier extraction.[1] Using Me-4PACz as the HTL, Albrecht's group successfully minimized the non-radiative recombination while keeping efficient hole extraction simultaneously and a high FF of 84% was obtained in the WBG PSC (Figure 25a,b). By incorporating it into the silicon subcell, an outstanding PCE of 29.15% with an FF of 79.4% was achieved. Notably, Me-4PACz also provided excellent stability that 95.5% of the initial PCE was retained after 300 h operation under illumination.[177] Based on the same SAM, Ballif et al. managed to reduce $V_{OC}$ losses originating from the perovskite/HTL interface. After introducing the 2,3,4,5,6-pentafluorobenzylphosphonic acid (FBPAc) into the perovskite precursors, the top interface-related $V_{OC}$ losses were also suppressed due to favorable perovskite microstructures and reduced trap states. With the dual interfacial modification of the perovskite top cells, the PCE of final perovskite-Si TSCs reached 31.25%.[273] The substantial charge carrier recombination and mismatched energy level alignment at the perovskite/$C_{60}$ interface result in the loss of device performance, particularly a significant $V_{OC}$ deficit.[18, 225, 273] A feasible approach to address this issue is to introduce an interlayer between perovskite/$C_{60}$, and the lithium fluoride (LiF) interlayer prepared by thermal evaporation has been widely employed. Whereas, the deliquescent and high ion diffusivity of the Li salts exert an adverse impact on the device stability.[18] Wolf and colleagues found that a 1~ nm thick $MgF_x$ interlayer could not only improve the PCEs due to the reduced non-radiative recombination and facilitated charge transportation at the perovskite/$C_{60}$ interface (Figure 25c), but also greatly enhance the device stability. The perovskite-Si TSCs with $MgF_x$ retained 95.4% of the initial PCE after over 1,000 h ageing tests following IEC 61215:2021 standards (Figure 25d).[18] Recently, Albrecht et al. inserted PI, which was firstly reported by Jen's group,[75] into the perovskite/$C_{60}$ interface, a decreased conduction band offset was found originating from a positive dipole (Figure 25e). Different from the previous reports, the PI interlayer was only effective in forming better energy level alignment

rather than chemical passivation despite the fact that PI containing both electron acceptor and electron donor functional groups was capable of interacting with various kinds of defects at the perovskite surface. By combining the PI-modified perovskite top cell with the silicon cell, the TSCs realized a remarkable certified PCE of 32.5% (Figure 25f,g).[225] Note that SAMs were also employed in the former works using $MgF_x$ or PI interlayer, exerting a huge impact on the device performance. Although the development of SAMs has greatly enhanced both single and tandem inverted PSCs. Nevertheless, it is still challenging to obtain energetically homogenous SAM coverage, inducing the loss of device performance. As discussed in Section 3, one effective way to improve the SAM coverage is using mixed SAMs with relatively small and large SAMs.[76, 158] Another strategy is the rational design of SAMs. Developing new SAM molecules with weakened π-π intermolecular interaction was able to reduce the undesirable aggregation, thus improving the coverage of SAMs on the substrate. The favorable self-assembly of SAMs led to more uniform surface potential. When introduced into the fabrication of devices, a boosted PCE was observed due to improved charge transport and suppressed non-radiative recombination, contributing to a high PCE of 28.9% in monolithic perovskite-Si tandem devices.[195] Furthermore, the coverage of SAMs is also influenced by the anchored-substrate. Stefaan and coworkers found that SAMs showed better coverage on amorphous IZO compared to crystalline materials (i.e. ITO, IZrO) as evidenced by KPFM mapping and XPS spectra (Figure 25h). The optimal thickness of IZO was verified to be ~ 5 nm. Combining thinned front and rear IZO electrodes, an exceptionally certified PCE of 32.5% was realized. In addition, the encapsulated IZO-based tandem devices exhibited exceptional stability, maintaining 90% of their initial PCE after undergoing MPPT for 870 hours under approximately 1-sun illumination. This achievement represents one of the highest levels of stability observed in perovskite-Si tandem devices.[194]

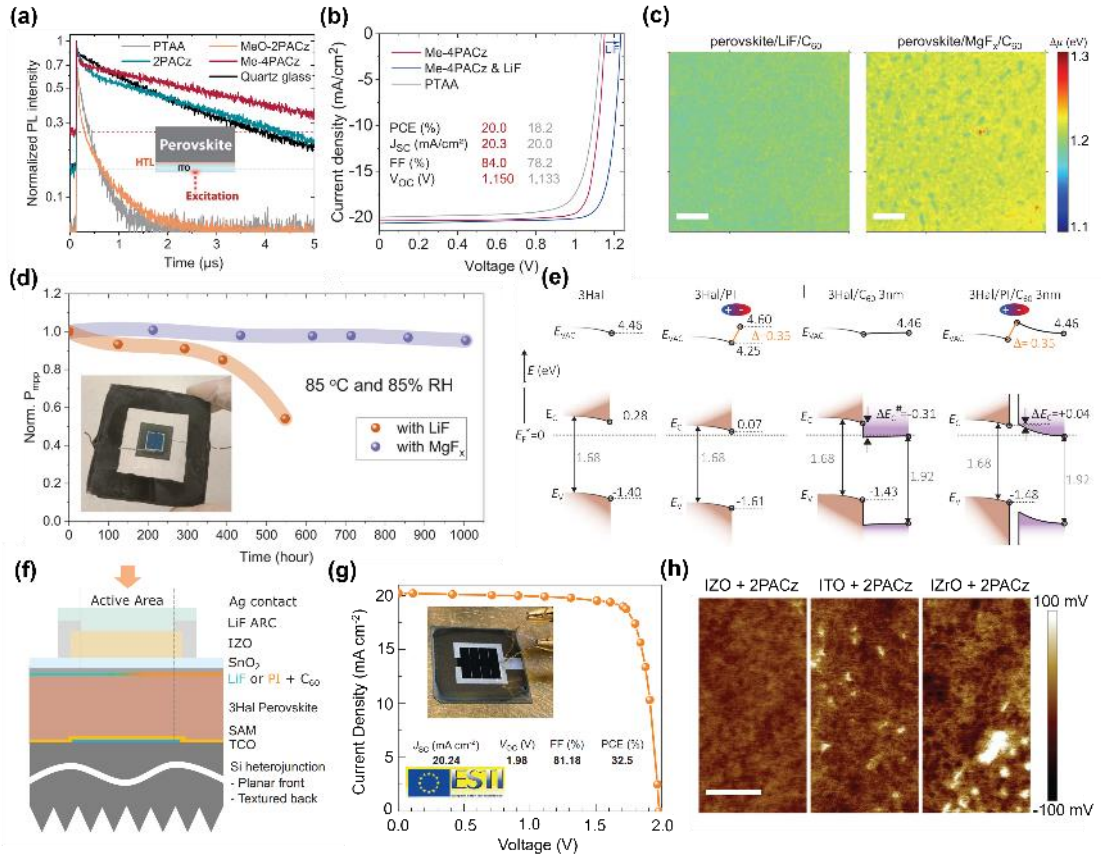


**Figure 29.** (a) Time-resolved photoluminescence (TRPL) of the perovskite film deposited on different ITO/HTL substrates. (b) *J*–*V* curves of the best single wide-bandgap PSCs based on various interfaces. Reproduced with permission from ref [177]. Copyright 2020 American Association for the Advancement of Science. (c) Quasi-Fermi level splitting mapping for perovskite/LiF/$C_{60}$ (left) and perovskite/$MgF_x$/$C_{60}$ (right) under 1-sun illumination (Scale bar: 50 μm). (d) Variation of the PCEs at damp-heat test of the encapsulated tandem devices. Reproduced with permission from ref [18]. Copyright 2022 American Association for the Advancement of Science. (e) Energy-level alignment of the pristine perovskite and perovskite/$C_{60}$ interface. (f) Schematic illustration of the device architecture. (g) *J*–*V* curve of the champion perovskite-Si TSC based on PI treatment. Insert: the performance parameters and a photograph of the encapsulated tandem cell. Reproduced with permission from ref [225]. Copyright 2023 American Association for the Advancement of Science. (h) KPFM images 2PACz-coated IZO (left), ITO (middle), and IZrO (right) substrates (Scale bar:

500 nm). Reproduced with permission from ref [194]. Copyright 2023 Springer Nature.

**Table 5. Summary of representative high-efficiency 2T perovskite-Si TSCs with inverted configuration.**

| WBG/front cell | ICL | NBG /rear cell | Front/rear surface | $V_{OC}$ (V) | $J_{SC}$ (mA cm$^{-2}$) | FF | PCE (%) | Year | Ref. |
|---|---|---|---|---|---|---|---|---|---|
| - | - | - | - | 1.97 | 20.8 | 0.83 | 33.9[a] | 2023 | 279 |
| $Cs_{0.05}FA_{0.8}MA_{0.15}Pb(I_{0.755}Br_{0.255})_3$ | IZO | SHJ | Textured | 1.95 | 20.9 | 0.81 | 32.8 (32.5)[a] | 2023 | 194 |
| $Cs_{0.05}(FA_{0.77}MA_{0.23})_{0.95}$ $Pb(I_{0.77}Br_{0.23})_3$ | IZO | SHJ | Polished/ textured | 2.00 | 20.0 | 0.81 | 32.4 (32.5)[a] | 2023 | 225 |
| $Cs_{0.18}FA_{0.82}Pb(IBr)_3$ | ITO | SHJ | Textured | 1.91 | 20.5 | 0.80 | 31.3[a] | 2023 | 273 |
| $Cs_{0.05}FA_{0.8}MA_{0.15}Pb(I_{0.755}Br_{0.255})_3$ | IZO | SHJ | Textured | 1.92 | 19.7 | 0.81 | 30.5 (29.3)[a] | 2022 | 18 |
| $Cs_{0.05}(FA_{0.77}MA_{0.23})_{0.95}Pb(I_{0.77}Br_{0.23})_3$ | ITO | SHJ | Textured | 1.90 | 19.5 | 0.81 | 29.8 | 2022 | 280 |
| $Cs_{0.05}(FA_{0.77}MA_{0.23})_{0.95}Pb(I_{0.77}Br_{0.23})_3$ | ITO | SHJ | Polished/ textured | 1.90 | 19.3 | 0.80 | 29.2[a] | 2020 | 177 |
| $Cs_{0.15}FA_{0.65}MA_{0.2}Pb(I_{0.8}Br_{0.2})_3$ | ITO | SHJ | Polished/ textured | 1.91 | 19.1 | 0.79 | 28.9 | 2023 | 195 |
| $Cs_xFA_yMA_{1-(x+y)}Pb(IBr)_3$ | ITO | SHJ | Textured | 1.79 | 20.1 | 0.80 | 28.8[a] | 2023 | 132 |
| $Cs_{0.1}FA_{0.2}MA_{0.7}Pb(I_{0.85}Br_{0.15})_3$ | ITO | SHJ | Textured | 1.92 | 18.9 | 0.79 | 28.6 | 2022 | 278 |
| $Cs_{0.22}FA_{0.78}Pb(Cl_{0.03}Br_{0.15}I_{0.85})_3$ | ITO | Topcon | Polished/ textured | 1.79 | 19.7 | 0.78 | 27.6 | 2022 | 281 |
| | Si:H(n+)/ Si:H(p+) | SHJ | Textured | 1.81 | 19.8 | 0.77 | 27.5 | 2021 | 282 |
| $Cs_{0.22}FA_{0.78}Pb(I_{0.85}Br_{0.15})_3$ | ITO | SHJ | Polished/ textured | 1.86 | 19.2 | 0.76 | 27.3 (27.2)[a] | 2022 | 283 |

| | | | | | | | | | |
|---|---|---|---|---|---|---|---|---|---|
| $FA_{0.78}Cs_{0.22}Pb(I_{0.85}Br_{0.15})_3$ + 3 mol% $MAPbI_3$ | ITO | SHJ | Polished/ textured | 1.89 | 19.1 | 0.75 | 27.1 | 2020 | 40 |
| $(FA_{0.65}MA_{0.2}Cs_{0.15})Pb(I_{0.8}Br_{0.2})_3$ | ITO | SHJ | Polished/ textured | 1.76 | 19.2 | 0.79 | 26.7 (26.2)[a] | 2020 | 277 |
| $Cs_{0.1}MA_{0.9}Pb(I_{0.9}Br_{0.1})_3$ | ITO | SHJ | Textured | 1.82 | 19.2 | 0.75 | 26.2 | 2020 | 275 |
| $Cs_{0.05}MA_{0.15}FA_{0.8}PbI_{2.25}Br_{0.75}$ | $InO_x$ | SHJ | Textured | 1.78 | 19.3 | 0.75 | 25.7[a] | 2020 | 274 |
| | SiCx(n) /Si:H(p+) | Topcon | Textured/ polished | 1.74 | 19.5 | 0.75 | 25.4 | 2019 | 284 |

[a]Certified values.

**Table 6. Summary of representative high-efficiency 2T perovskite-perovskite and perovskite-organic TSCs with inverted configuration**

| Front contacts | WBG/front cell | ICL | NBG/rear cell | Rear contacts | $V_{OC}$ (V) | $J_{SC}$ (mA $cm^{-2}$) | FF | PCE (%) | Year | Ref. |
|---|---|---|---|---|---|---|---|---|---|---|
| - | - | - | - | - | 2.16 | 16.6 | 0.79 | 28.2[a] | 2023 | 279 |
| ITO/$NiO_x$/2PACz:MeO-2PACz | $FA_{0.8}Cs_{0.2}Pb(I_{0.62}Br_{0.38})_3$ | $C_{60}$/$SnO_2$/Au/ PEDOT:PSS | $FA_{0.7}MA_{0.3}Pb_{0.5}Sn_{0.5}I_3$ | $C_{60}$/BCP /Cu | 2.11 | 16.5 | 0.82 | 28.5 (28.0)[a] | 2023 | 285 |
| FTO/$NiO_x$/ Me-4PACz | $Cs_{0.2}FA_{0.8}PbI_{1.9}Br_{1.1}$ | $C_{60}$/$SnO_2$/Au/ PEDOT:PSS | $Cs_{0.05}MA_{0.25}FA_{0.7}Pb_{0.5}Sn_{0.5}I_3$ | $C_{60}$/BCP /Ag | 2.14 | 15.6 | 0.84 | 28.1 | 2023 | 51 |
| ITO/2PACz | $FA_{0.8}Cs_{0.2}PbI_{1.8}Br_{1.2}$ | $C_{60}$/$SnO_2$/Au/ PEDOT:PSS | $FA_{0.7}MA_{0.3}Pb_{0.5}Sn_{0.5}I_3$ | $C_{60}$/BCP /Cu | 2.11 | 16.0 | 0.82 | 27.8 (27.3)[a] | 2023 | 36 |
| ITO/PTAA | $Cs_{0.2}FA_{0.8}Pb(I_{0.6}Br_{0.4})_3$ | $C_{60}$/$SnO_2$/IZO/ PEDOT:PSS | $FA_{0.6}MA_{0.3}Cs_{0.1}Pb_{0.5}Sn_{0.5}I_3$ | $C_{60}$/$SnO_2$ /Cu | 2.11 | 15.4 | 0.83 | 27.0[b] (26.6)[a] | 2023 | 286 |
| ITO/$NiO_x$/ Me-4PACz | $Cs_{0.2}FA_{0.8}Pb(I_{0.6}Br_{0.4})_3$ | $C_{60}$/$SnO_2$/Au /PEDOT:PSS | $Cs_{0.05}FA_{0.7}MA_{0.25}Pb_{0.5}Sn_{0.5}I_3$ | $C_{60}$/$SnO_x$ /Ag | 2.19 | 15.1 | 0.83 | 27.3 (26.3)[a] | 2022 | 287 |

| | | | | | | | | | | |
|---|---|---|---|---|---|---|---|---|---|---|
| ITO/2F | $Cs_{0.2}FA_{0.8}Pb(I_{0.6}Br_{0.4})_3$ | $C_{60}/SnO_2$/IZO/ PEDOT:PSS/2F | $FA_{0.6}MA_{0.3}Cs_{0.1}$ $Pb_{0.5}Sn_{0.5}I_3$ | $C_{60}/SnO_2$ /Cu | 2.13 | 15.5 | 0.82 | 27.2 (26.3)[a] | 2023 | 288 |
| ITO/SAMs | $Cs_{0.3}FA_{0.6}DMA_{0.1}$ $Pb(I_{0.7}Br_{0.3})_3$ | $C_{60}/SnO_2$/Au /PEDOT:PSS | $FA_{0.6}MA_{0.4}Sn_{0.6}$ $Pb_{0.4}I_3$ | $C_{60}$/BCP /Ag | 2.20 | 15.1 | 0.82 | 27.2 | 2023 | 289 |
| ITO/$NiO_x$/ VNPB | $FA_{0.8}Cs_{0.2}Pb(I_{0.62}Br_{0.38})_3$ | $C_{60}/SnO_2$/Au /PEDOT:PSS | $FA_{0.7}MA_{0.3}Pb_{0.5}$ $Sn_{0.5}I_3$ | $C_{60}$/BCP /Cu | 2.03 | 16.5 | 0.80 | 26.7 (26.4)[a] | 2022 | 290 |
| ITO/$NiO_x$/ VNPB | $DMA_{0.1}FA_{0.5}Cs_{0.4}Pb$ $(I_{0.75}Br_{0.25})_{2.95}Cl_{0.05}$ | $C_{60}/SnO_2$/Au /PEDOT:PSS | $MA_{0.3}FA_{0.7}Pb_{0.5}$ $Sn_{0.5}I_3$ | $C_{60}$/BCP /Cu | 2.05 | 16.0 | 0.80 | 26.2 | 2022 | 291 |
| ITO/PTAA | $FA_{0.6}Cs_{0.4}PbI_2Br$ | $C_{60}/SnO_2$/ graphene oxide /PEDOT:PSS | $Cs_{0.2}FA_{0.8}Pb_{0.5}Sn_{0.5}I_3$ | $C_{60}$/BCP /Cu | 2.03 | 15.8 | 0.79 | 25.6 | 2022 | 292 |
| ITO/MeO-2PACz | $FA_{0.7}Cs_{0.3}PbI_{2.1}Br_{0.9}$ | LiF/$C_{60}$/$SnO_x$/ Au/PEDOT:PSS | $(FASnI_3)_{0.6}(MA$ $PbI_3)_{0.4}$ | $C_{60}$/BCP /Ag | 2.12 | 15.0 | 0.80 | 25.5 (24.3)[a] | 2022 | 293 |
| ITO/PTAA | $FA_{0.8}Cs_{0.2}Pb(I_{0.6}Br_{0.4})_3$ | $C_{60}/SnO_2$/Au /PEDOT:PSS | $FA_{0.7}MA_{0.3}Pb_{0.5}$ $Sn_{0.5}I_3$ | $C_{60}$/BCP /Cu | 1.97 | 15.6 | 0.81 | 24.8[a] | 2019 | 34 |
| ITO/$NiO_x$ | $FA_{0.8}Cs_{0.2}Pb(I_{0.6}Br_{0.4})_3$ | $C_{60}/SnO_2$/Au /PEDOT:PSS | $FA_{0.7}MA_{0.3}Pb_{0.5}$ $Sn_{0.5}I_3$ | $C_{60}/SnO_2$ /Cu | 2.01 | 15.5 | 0.79 | 24.7 (24.2)[a] | 2020 | 294 |
| ITO/PTAA | $FA_{0.6}Cs_{0.4}Pb(I_{0.65}Br_{0.35})_3$ | $C_{60}/SnO_{1.76}$ | $FA_{0.5}MA_{0.45}Cs_{0.05}$ $Pb_{0.5}Sn_{0.5}I_3$ | $C_{60}$/BCP /Cu | 2.03 | 15.2 | 0.80 | 24.6 | 2020 | 295 |
| ITO/PTAA | $FA_{0.8}MA_{0.15}Cs_{0.05}Pb$ $(I_{0.85}Br_{0.15})_3$ | $C_{60}$/BCP/Ag/ $MoO_x$/ITO/ PEDOT:PSS | $(FASnI_3)_{0.6}(MA$ $PbI_3)_{0.4}$ | $C_{60}$/BCP /Ag | 1.94 | 15.0 | 0.80 | 23.4 | 2019 | 296 |
| ITO/poly-TPD | $FA_{0.6}DMA_{0.1}Cs_{0.3}Pb$ $(I_{0.8}Br_{0.2})_3$ | LiF/$C_{60}$/PEIE /AZO/IZO/ PEDOT:PSS | $FA_{0.75}Cs_{0.25}Sn_{0.5}$ $Pb_{0.5}I_3$ | $C_{60}$/BCP /Ag | 1.88 | 16.0 | 0.77 | 23.1 | 2019 | 297 |
| ITO/$NiO_x$/ 2PACz | $FA_{0.8}Cs_{0.2}PbI_{1.6}Br_{1.4}$ | $C_{60}$/BCP/Ag/ $MoO_3$/2PACz | D18-Cl:N3:PCBM | $C_{60}$/BCP /Ag | 2.12 | 14.7 | 0.83 | 25.8 (25.1)[a] | 2024 | 298 |
| ITO/DC-PA | $Cs_{0.2}FA_{0.8}Pb(I_{0.6}Br_{0.4})_3$ | $C_{60}$/BCP /Au/$MoO_3$ | PM6:Y6:$PC_{71}BM$ | PNDIT-F3N/Ag | 2.15 | 14.4 | 0.82 | 25.2 (24.3)[a] | 2024 | 299 |
| ITO/$NiO_x$/ 2PACz | $FA_{0.8}Cs_{0.2}Pb(I_{0.5}Br_{0.5})_3$ | $C_{60}$/BCP /Au/$MoO_3$ | PM6:PM7:Y6: $PC_{71}BM$ | $C_{60}$/BCP /Ag | 2.14 | 14.2 | 0.81 | 24.5 | 2023 | 300 |

| | | | | | | | | | | |
|---|---|---|---|---|---|---|---|---|---|---|
| ITO/MeO-2PACz | $FA_{0.8}MA_{0.2}Pb(I_{0.6}Br_{0.4})_3$ | $C_{60}$/C-C1-P/Ag/$MoO_3$ | PM6:BTP-eC9:$PC_{71}BM$ | TPMA/Ag | 2.09 | 14.6 | 0.79 | 24.1 | 2023 | 301 |
| ITO/MeO-2PACz | $FA_{0.8}Cs_{0.2}Pb(I_{0.5}Br_{0.5})_3$ | PCBM/AZO-NP/$SnO_x$/$InO_x$/$MoO_x$ | PM6:Y6:PCBM | $C_{60}$/BCP/Ag | 2.15 | 14.1 | 0.78 | 24.0 (23.1)[a] | 2022 | 302 |
| ITO/$NiO_x$/BPA | $FA_{0.75}Cs_{0.25}Pb(I_{0.6}Br_{0.4})_3$ | $C_{60}$/BCP/IZO/$MoO_x$ | PM6:Y6:PCBM | PNDIT-F3N/Ag | 2.06 | 14.8 | 0.77 | 23.6 (23.0)[a] | 2022 | 159 |
| ITO/2PACz | $FA_{0.6}MA_{0.4}Pb(I_{0.6}Br_{0.4})_3$ | $C_{60}$/BCP/Ag/$MoO_x$ | PTB7-Th:BTPV-4CleC9 | PDINN/Ag | 1.88 | 15.7 | 0.75 | 22.0 | 2022 | 303 |
| ITO/poly-TPD | $MA_{0.96}FA_{0.1}PbI_2Br(SCN)_{0.12}$ | PCBM/BCP/Ag/$MoO_x$ | PM6:CH1007 | PFN-Br/Ag | 1.96 | 13.8 | 0.78 | 21.2 | 2022 | 304 |
| ITO/$NiO_x$ | $FA_{0.8}MA_{0.02}Cs_{0.18}PbI_{(0.6}Br_{0.4)_3}$ | $C_{60}$/BCP/Ag/$MoO_x$ | PM6:Y6:$PC_{71}BM$ | TPBi/Ag | 1.90 | 13.1 | 0.83 | 20.6 (19.5)[a] | 2020 | 305 |
| ITO/PEDOT:PSS | $MAPbI_3$ | PCBM/$C_{60}$-SB/Ag/$MoO_3$ | PTB7-Th:$PC_{71}BM$ | $C_{60}$-N/Ag | 1.63 | 13.1 | 0.75 | 16.0 | 2016 | 306 |

[a]Certified values. [b]Note that the active area is 1.044 $cm^2$.

### 6.2 2T All-Perovskite TSCs

Due to the nature of tunable bandgaps, different perovskites with complementary absorption ranges can be combined to fabricate all-perovskite TSCs. Compared with other perovskite-based TSCs, all-perovskite TSCs can retain and make full use of the merits of perovskites e.g., high efficiency, low cost, solution-processability, and good flexibility. Although the early all-perovskite TSCs were designed with the n-i-p configuration,[307-308] at present, most of the high-efficiency all-perovskite TSCs have been fabricated in the inverted geometry, mainly due to two reasons: 1) efficient NBG perovskite cells are mainly in inverted type; 2) inverted perovskite devices are catching up with the n-i-p counterparts.[12, 309] In this section, we will briefly review the representative efforts related to the construction of high-performance all-perovskite TSCs including the optimization of NBG and WBG subcells and the design of ICLs.

Different from perovskite-Si TSCs where the NBG silicon absorber has a fixed bandgap of ~1.1 eV, the compositions and bandgaps of WBG and NBG absorbers in all-perovskites TSCs can be engineered to cater to each other, which provides a wide range of material combinations. The optimal bandgap combinations between WBG (1.7~1.8 eV) and NBG (1.0~1.2 eV) perovskites have been estimated elsewhere to guide the TSC design.[258] Due to the fact that the classic Pb-based perovskite cannot be tuned to below 1.48 eV while the Sn-based materials are notoriously air-sensitive, the fabrication of stable and efficient NBG perovskites becomes the main challenge. With the ideal 1.2 eV NBG $FA_{0.75}Cs_{0.25}Sn_{0.5}Pb_{0.5}I_3$, the first representative inverted all-perovskite TSCs was fabricated by Snaith et al. in 2016.[310] Through a precursor-phase antisolvent immersion technique, the precursor complex was firstly formed due to retarded crystallization in a DMF/DMSO mixture solvent, followed by an antisolvent bath and gentle annealing for complete crystallization. As-prepared materials were highly crystalline, uniform, smooth, and dark, delivering a PCE of 14.8% and a $V_{OC}$ of 0.74 V (with bandgap ~1.2 eV). Combining with a 1.8 eV perovskite in the construction of WBG perovskite top cell, the TSC delivered a notable PCE of 17.0%

with a $J_{SC}$ of 14.5 mA $cm^{-2}$, a $V_{OC}$ of 1.66 V, and an FF of 0.70, exceeding either individual subcells. To meet the requirement of current matching between two subcells, the NBG perovskite should be thick enough to absorb sufficient infrared light. However, limited by the suitable fabrication and consequential bulk material imperfections, it is difficult to grow thick NBG perovskite without sacrificing FF or $V_{OC}$. To tackle this issue, Yan et al. developed a strategy of incorporating chlorine into $(FASnI_3)_{0.6}(MAPbI_3)_{0.4}$ and successfully fabricated 750 nm thick perovskite films with good quality.[311] The 2.5% chlorine incorporation was found to segregate onto and passivate grain boundaries, resulting in enlarged grain with good crystallinity and reduced trap densities. These enabled fewer charge carrier scattering at grain boundaries and ionized defects, and therefore charge carrier transportation and extraction were facilitated. The reduced electronic disorder and suppressed non-radiative recombination guaranteed a good perovskite film and the NBG PSCs obtained a high PCE of 18.1% with a $V_{OC}$ of 0.841 V. Based on this efficient NBG subcell, the TSCs obtained a PCE of 21.0% with a $V_{OC}$ of 1.922 V. Following the idea of improving Sn-based perovskites, Zhu et al. proposed the incorporation of another additive i.e., guanidinium thiocyanate (GuaSCN) into $(FASnI_3)_{0.6}(MAPbI_3)_{0.4}$, which presented a strong passivation ability.[296] The treated perovskite showed reduced defect densities by a factor of 10, resulting in a long carrier lifetime > 1 microsecond and diffusion length > 2.5 micrometers. Such a treatment ensured the perovskite film with superior quality up to 1 micrometer thickness (Figure 26a-c), providing sufficient infrared absorption and achieving a high $J_{SC}$ of 30.5 mA $cm^{-2}$ and the PCE exceeded the threshold of 20% for the first time to 20.2%. The final all-perovskite TSC also achieved a high PCE of 23.1%. Later, reductive zwitterionic antioxidant[294] and metallic Sn power[34] have been separately used by Tan's group. to inhibit $Sn^{2+}$ oxidation. The PCEs of as-treated NBG cell and all-perovskite TSC were successfully enhanced to 21.7% and 24.8% respectively. Since the widely used surface passivators like PEA are partially adsorbed on the surface defective sites at perovskite

crystallization temperatures, leading to the fact that a certain amount of grain surfaces was left un-passivated. To enhance the passivator adsorption on perovskite surfaces, Tan et al. reported a new ammonium cation, 4-trifluoromethyl-phenylammonium (CF3-PA), to passivate the NBG Pb-Sn perovskite.[290] The theoretical calculation and experiments confirmed that CF3-PA noticeably suppressed the defects owing to the strongest binding energy with acceptor-type defects on the perovskite grain surface and increased Sn vacancy formation energy (Figure 26d-f). This effective passivator enabled much enhanced $J_{SC}$ of 33 mA $cm^{-2}$ due to the sufficient infrared light absorption from 1.2 micrometers thick absorber and a high PCE of 22.2% was measured. The final TSC hit an outstanding PCE of 26.7%, which, for the first time, surpassed the best PCE of single-junction PSCs.

One step further beyond the single molecular passivation, a bimolecular passivation strategy has been demonstrated on multiple perovskite compositions.[51] Specifically, the diammonium molecule was paired with the methylthio molecule as one combination. Through this approach, the field-effect passivation and chemical bonding passivation could be achieved simultaneously. By comparing a set of combinations, the $PDAI_2$/3MTPAI combination generated the best efficiency of 28.1% for all-perovskite TSCs. This work successfully combined the merits of several types of molecules, providing a new idea in designing the passivation route. Different from the molecular passivation, a 3D/3D bilayer heterojunction has also been constructed on the NBG perovskite surfaces for both suppressing non-radiative recombination and facilitating carrier extraction.[285] By taking a two-step evaporation-solution route, a ~50 nm layer of lead-halide WBG perovskite was deposited on the NBG perovskite surface. The formed type II band alignment at the interface could effectively drive holes away and accelerate the drift of electrons, thus minimizing the non-radiative recombination at the NBG perovskite-ETL interface (Figure 26g,h). Such an exquisite design increased the PCE of NBG perovskite to 23.8% with a remarkably high $V_{OC}$ of 0.873 V. Thereby, the champion all-perovskite TSC reached a record-high PCE of

28.5% (certified 28.0%) (Figure 26i).

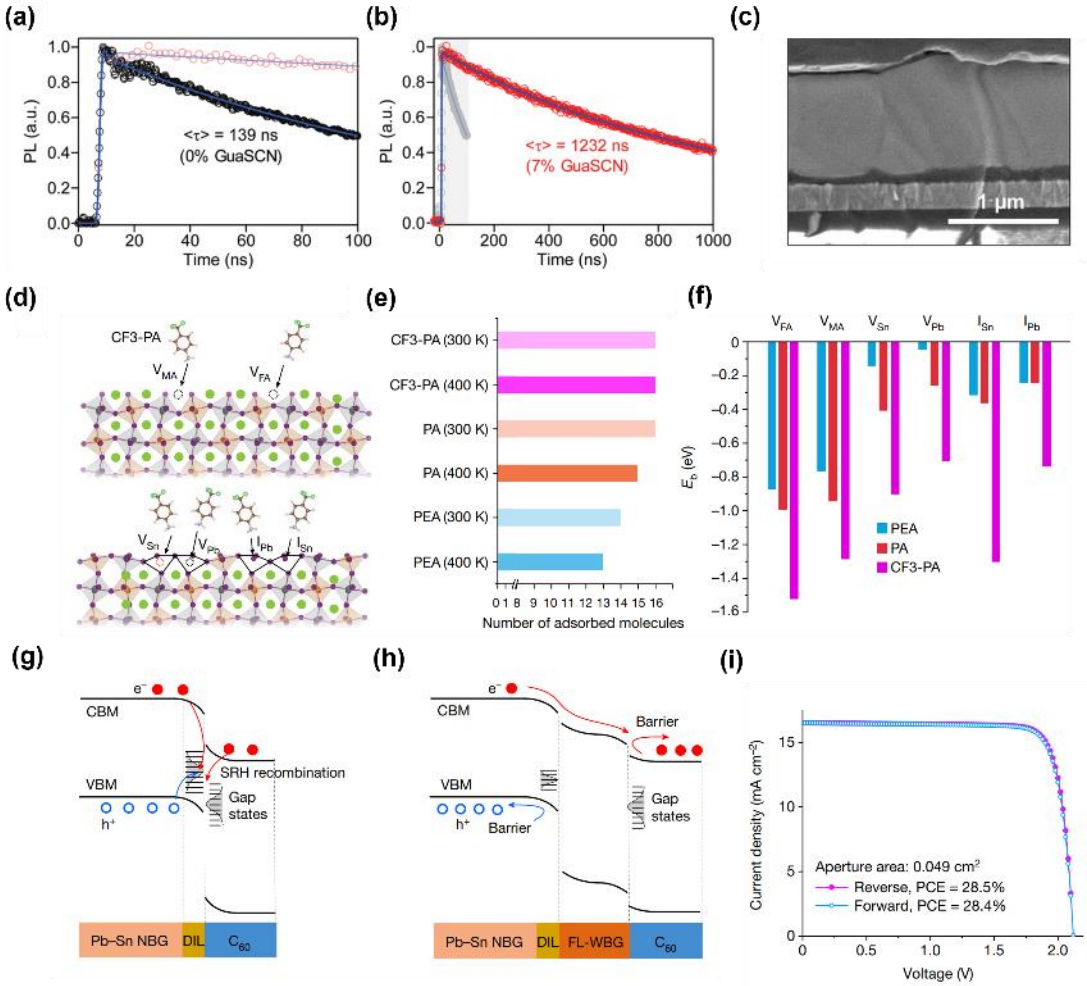


**Figure 30**. TRPL spectra of the control perovskite film without adding GuaSCN (a) and with adding 7% GuaSCN (b). (c) Cross-sectional SEM image of the NBG PSC using the GuaSCN-treated $(FASnI_3)_{0.6}(MAPbI_3)_{0.4}$ perovskite film. Reproduced with permission from ref [296]. Copyright 2019 American Association for the Advancement of Science. (d) Schematic diagram of the interaction between CF3-PA with the defects in the perovskite film. (e) The number of adsorbed molecules for CF3-PA, phenylammonium (PA), and PEA at 300 and 400 K. (f) The binding energy ($E_b$) between passivators and different acceptor-like defects. Reproduced with permission from ref [290]. Copyright 2022 Springer Nature. Energy diagram for the control (g) and perovskite heterojunction (h) Pb–Sn PSCs. Note that the abbreviations DIL and FL in the figure are referred to as defective interface layer and full-lead, respectively. (i) J-V curves of the champion devices under reverse and forward scans. Reproduced with

permission from ref [285]. Copyright 2023 Springer Nature.

To enhance the performance of subcells, the buried interface between HTL and the perovskite absorber layer is of significant importance since these interfaces usually act as the starting point for the perovskite crystallization process. Therefore, it is necessary to regulate the crystal growth for better film quality. As introduced in Section 3, SAM has been increasingly explored for wider applications in solar cells. However, current SAMs are still nonideal in terms of regulating crystallization, full substrate coverage, band alignment, charge selection, and extraction, etc. Thus, rational design in new SAMs may provide innovative breakthroughs. For instance, a SAM of (4-(7H-dibenzo[c,g]carbazol-7-yl)butyl)phosphonic acid (4PADCB) was designed as the HTL for WBG PSCs.[286] Here two benzene rings were introduced into the carbazole groups of the commonly used 4PACz. The partial distortion in the backbone could modulate the self-aggregation of the unfused-ring electron acceptor, improve the solubility, and generate uniform-coating of SAMs. Also, the larger conjugation range of the building block helped the charge transport. Ultimately, the cell based on this new SAM achieved a high $V_{OC}$ of 1.31 V in a 1.77-eV PSC and achieved a PCE of 27.0% (26.4% certified stabilized). Later, a donor-acceptor type SAM, 4-(7-(4-(bis(4-methoxyphenyl) amino)-2,5-difluorophenyl)benzo[c][1,2,5]thiadiazol-4-yl) benzoic acid (MPA2FPh-BT-BA, denoted as 2F), was synthesized as the hole selective contact.[288] In addition to the good functionalities as the HTL, the synthesis process of 2F only contained four steps, implying a moderate synthetic yield. It is also worth mentioning that 2F could be applied for both wide and narrow bandgap subcells, exerting different functions. As a result, the WBG and NBG subcells yielded PCEs of 19.33% and 23.24%, respectively. As a result, the PCE of as-prepared TSC reached 27.22% (certified 26.3%).

In addition to the improvement in the absorbers, copious efforts have also been put into the ICLs. A typical ICL consists of several parts: ETL, HTL, and recombination layer (RL)/tunnelling layer in most cases, which makes the design of ICLs an

interactive and sophisticated engineering. Generally, the ICLs should meet the constraints from three aspects, e.g., electrics, optics, and mechanics, plus practical processing compatibility. The main role of ICLs in 2T TSCs is to electrically connect both subcells in series, which requires the annihilation of opposite charge carriers that occurs at ICLs. However, ETLs usually possess low work function while HTLs possess high work function, leading to an energy barrier for direct carrier transport and a parasitic p-n junction formed to ruin the TSCs' $V_{OC}$. To address this issue, there are two concepts of solutions: a) forming a tunnelling junction; b) forming an RL. In the former case, both sides of the small p-n junction are heavily doped, for narrowing the width of the depletion region thin enough to enable tunnelling through. This strategy has been widely applied in III-V group TSCs as the ease realization of degenerate doping in corresponding materials, which however is not applied to perovskite-based TSCs. Then perovskite researchers looked into the second strategy where an ICL was constructed using an RL and a sandwiched structure of ETL/RL/HTL has been widely adopted in perovskite- and organic-based TSCs. Another requirement of ICLs is to be highly optically transparent, especially in the near-infrared region (NIR) region, to enable sufficient low-energy photons to pass through and arrive at the rear absorbers. Thirdly, ICLs should provide outstanding mechanical connections between two subcells. For example, ICLs should be compact enough to be physical barriers to solvent permeation and ion migration from the rear cells into the front cells. In particular, due to that both subcells in all-perovskite TSCs use similar strong polar solvents, it sets a higher standard of compactness to prevent solvent from dissolving the underlying layers. Therefore, the quality of ICLs impacts, and even determines, the performance and long-term stability of TSCs. To date, TCO and metals are the two dominant options for RLs in inverted TSCs, as summarized in Tables 5 and 6.

TCOs e.g., indium tin oxide (ITO), IZO, and AZO, have inherent high transparency and conductivity, making them very compatible being the RLs. To produce a dense

and compact film, the target TCO material will be magnetically sputtered with high energy, which may damage the underlying layers. Therefore, a dense and compact buffer layer is needed in advance to shield the sputtering damage. As the buffer layer also needs to meet the three constraints applied to the ICLs, this inevitably introduces further complexity and uncertainty. In the first representative all-perovskite TSC, Snaith's group demonstrated a sophisticated TCO-based ICL consisting of PCBM/$SnO_2$/zinc-tin-oxide (ZTO)/ITO/PEDOT:PSS. In this stack, $SnO_2$ (4 nm)/ZTO(2 nm) was deposited using the ALD technique as the buffer layer, followed by the sputtering of ITO with 100 nm.[310] The dense ICL allowed for direct spin-coating of aqueous PEDOT:PSS on top. No distinct hysteresis was observed in the *J*–*V* curves of TSC, while the mismatched $J_{SC}$ from two subcells meant there was plenty of room to further optimize. The small voltage loss of the TSC (defined as the difference between $V_{OC\_tandem}$ and the sum of $V_{OC\_front}$ and $V_{OC\_rear}$) of 0.2 V and the FF of 0.70 demonstrated the effectiveness of carrier transportation and recombination within this ICL. Generally, this ICL fulfilled the basic duties and provided a good example of ICL design. Replacing the ALD-grown $SnO_2$, Yan's group demonstrated the role of $MoO_x$ used in ICLs. The multilayer Ag (1 nm)/$MoO_x$(3 nm)/ITO(120 nm) was sandwiched between the ETL and HTL. In this stack, both ultrathin Ag and sputtered ITO were used together as the recombination sites, while $MoO_x$ had a dual role of a buffer layer for preventing sputtering damage and a spacer to separate Ag from ITO (otherwise the silver oxide may form). With this ICL, the TSC voltage loss was reduced to a negligible value of ~0.07 V, and the FF reached 78.1%, proving it was an effective design.[311] Due to the concern of rear cell solvent permeation, the sputtered TCOs have to be thick enough (~100 nm), which inevitably increases the parasitic absorption and probably leads to shunting between subcells. Reducing the thickness of TCOs can be realized by sharing their responsibility of preventing solvent permeation e.g., by strengthening the ALD-grown dense films. In another work, Snaith's group used the dense ALD-grown AZO film (25 nm) as the buffer

layer followed by sputtering a thin layer of IZO with only 5 nm as the RL.[309] This thin bilayer combined the merits of strong resistance to solvent permeation and high transparency. It is worth mentioning that the thin TCO made the ICL much less brittle and therefore flexible devices can be made. In fact, the ALD-grown film can be further thinned to ~10 nm while still being an effective solvent barrier.[312]

Although TCOs can almost meet the requirements from electrical and optical considerations, the high energy sputtering processing to some extent limits the wider applications. In contrast, ultrathin metal layers can be deposited through thermal evaporation at low temperatures, guaranteeing a less damaging fabrication process. The ultrathin metal layers (~1 nm) e.g., gold, have both good conductivity and transparency. Combined with the ALD-grown dense films, the metal-based RLs are expected to construct the qualified ICLs. Since $SnO_2$ has excellent electron extraction ability and is also ALD-grown friendly, $SnO_2$/Au becomes a competitive candidate for ICLs of all-perovskite TSCs. Note that a layer of $C_{60}$ or PCBM is usually needed in advance of $SnO_2$ for two reasons: 1) ALD process starts with nucleation at substrates where PCBM surfaces have more suitable nucleation sites than bare perovskite surfaces; 2) water is widely used as oxidant during ALD process which is harmful to perovskite. The concept of $SnO_2$/Au-based ICL was realized by Tan's group in 2019.[34] Using the $C_{60}$/$SnO_2$/Au/PEDOT:PSS as the ICL, the TSC generated a high PCE of 24.8%, a high FF of 81.0%, and a negligible voltage loss of 0.06 V, demonstrating the huge success of this ICL. In the following years, a number of all-perovskite TSCs have adopted this concept as the ICLs and achieved high PCEs, proving its wide applicability.[290-291, 294, 296]

Despite the success of ETL/RL/HTL sandwiched ICL concept, the TSC community is constantly pursuing simplifying the ICL structures to shorten the manufacturing time and lower the cost. In this regard, a pioneer work by Huang et al. on $C_{60}$/$SnO_{1.76}$ set a good example.[295] In this work, through the precise control over the ALD process parameters e.g., pulse time, reaction time, and temperature, the $SnO_{1.76}$ was

intentionally left incomplete oxide and therefore possessed the ambipolar transport property (Figure 27a). Owing to the incomplete oxidation status, a high density of $Sn^{2+}$ existed in $SnO_{1.76}$ formed mid-gap states, enabling the extraction ability of holes from the rear cells. Also, the $C_{60}$ layer was unintentionally n-doped by the iodine ions from adjacent perovskite materials, thereby forming the Ohmic contact with $SnO_{1.76}$ (Figure 27b). This ingenious ICL obtained a PCE of 24.6% with a high FF of ~80% and a small $V_{OC}$ loss of ~0.1 V, indicating that the bilayer ICLs, and even monolayer ICLs, become feasible in the future and point the direction of enhancing ICL fabrication efficiency (Figure 27c).

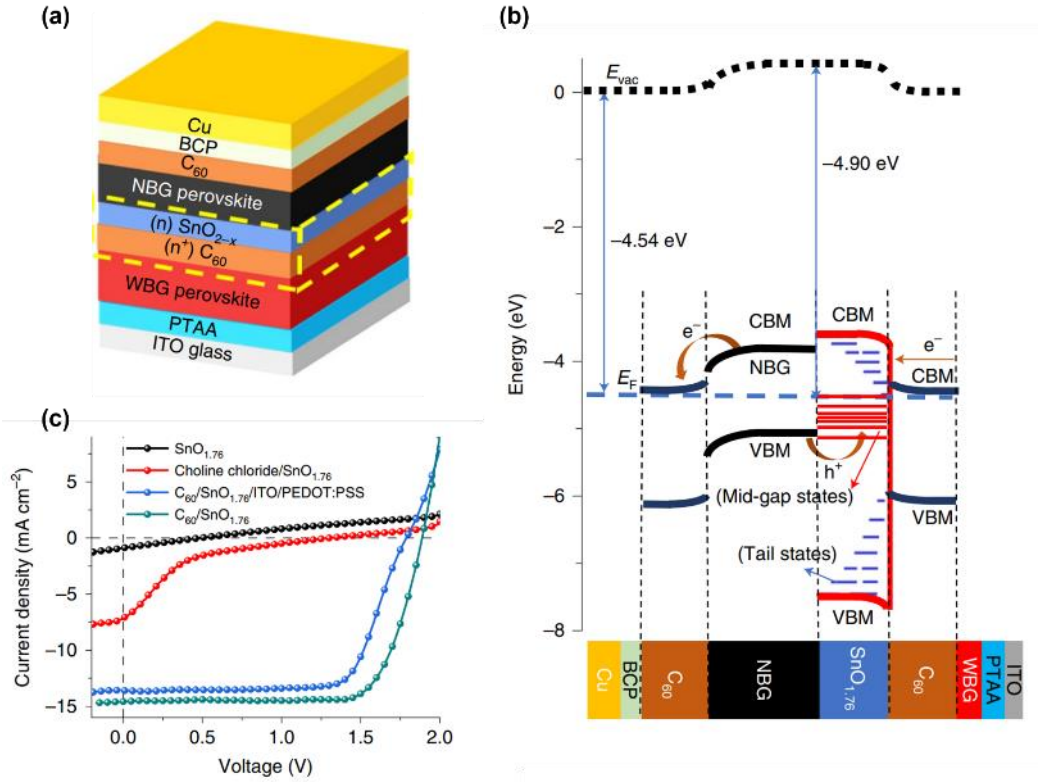


**Figure 31**. (a) Schematic of the device architecture with simplified ICL highlighted by the yellow-dash rectangle. (b) *J*–*V* characteristics of the TSCs with various ICLs. (c) Energy-level scheme for the $C_{60}/SnO_{1.76}/NBG/C_{60}$ layers in all-perovskite TSCs. Reproduced with permission from ref [295]. Copyright 2020 Springer Nature.

### 6.3 2T Perovskite-Organic TSCs

Benefiting from the progress of non-fullerene acceptors (NFA), the past several years

have witnessed rapid advances in high-efficiency monolithic perovskite-organic TSCs.[313-314] This type of TSC shares a high similarity in device structure with the all-perovskite TSC, only replacing the NBG perovskite rear cell with the NBG organic rear cell. This replacement provides the design of TSCs with more freedom and flexibility, as the orthogonal solvents are used in two subcells which relieves the concerns about solvent permeation in all-perovskite TSCs. Furthermore, the issue of unwanted transformation of $Sn^{2+}$ in NBG PSCs would be inhibited by substituting the NBG PSCs with NBG organic solar cells (OSCs).[313] By taking advantage of this unique feature, the WBG perovskite and NBG organic bulk heterojunction (BHJ) can be even contacted directly without the ICLs inserted thus forming the so-called perovskite-organic bilayer integrated cells. This type of hybrid cell is another promising topic in recent years but it is beyond the scope of this review. Interested readers are advised to read the information elsewhere.[315] Table 6 summarizes the high-efficiency inverted perovskite-organic TSCs reported in recent years. Compared with the perovskite/Si and all-perovskite TSCs, it is clear that perovskite-organic TSCs show generally inferior PCEs, which mainly result from the lower $J_{SC}$ and FF.

In 2015, Yang's group reported a pioneer work where an organic BHJ of PBSeDTEG8:PCBM was used as the infrared absorber and worked with $MAPbI_3$ to construct the TSC.[316] The mismatched bandgap combination between two subcells led to the distinct absorption overlap. Also, since the absorption coefficient of organics was lower than that of perovskites, the NBG organic subcell was placed in front of the WBG perovskite subcell to absorb more light and match the current. This stack order however obstructed the sufficient absorption of high-energy photons by the WBG perovskite subcell and therefore further decreased the total $J_{SC}$ attainable. Although the final TSC obtained a PCE of 10.23% with a $J_{SC}$ of 10.05 mA $cm^{-2}$, this work paves an avenue that perovskite-organic TSC can deliver further high PCEs with more reasonable structures if efficient NBG organic absorbers are synthesized. Given that the organic subcell is the performance-limiting factor, Russell's group optimized it in

both the BHJ composition and the stack order.[306] Interestingly, despite that the PCE of the organic subcell had a small increment (from Yang's work 7.03% to this work 9.7%) while the same perovskite was used, the PCE of TSC saw a large increment (from Yang's work 10.23% to this work 16.0%), together with the enhancement of $J_{SC}$ to 13.1 mA cm$^{-2}$, implying the contribution and importance of organic subcells on TSC performance. Since then, the efficiency gap between all-perovskite TSCs and perovskite-organic TSCs has been increasingly widened due to the skyrocketing development of NBG Pb-Sn perovskites.

The development of perovskite-organic TSCs waited for more efficient NBG organic absorbers, and the successful application of NFA in OSCs has brought a new round of breakthroughs. In 2020, the PM6:Y6:$PC_{71}BM$, a star NFA-based BHJ, was used as the NBG absorber in the perovskite-organic TSC by Yang's group.[305] Thanks to the NBG absorber's strong light-harvesting ability, the inter-subcell current matching was easily fulfilled through thickness optimization guided by the device simulation. More importantly, both the FF and $V_{OC}$ of NFA-based organic subcell were enhanced benefited from much-improved film morphology and reduced non-radiative recombination. The big breakthrough in organic subcells led to the enhancement in $V_{OC}$ and FF of TSC to 1.902 V and 83.1%, respectively, and the final PCE exceeded the 20% milestone for the first time. Based on this star NFA-based BHJ as the NBG absorber, the further optimization of WBG subcells successively lifted the PCE of perovskite-organic TSCs. Note that the majority of efficient perovskite-organic TSCs rely on the PM6:Y6 BHJ system with a bandgap of 1.33 eV. To pair with this organic NBG light absorber, the ideal bandgap for the WBG perovskites is determined to be around 1.85 eV, which is larger than those of the WBG perovskites in perovskite-silicon (1.65-1.75 eV) and all-perovskite TSCs (~ 1.8 eV).[262, 286, 317] A wider bandgap in typical perovskites generally means higher Br amount, which induces severe phase segeration under illumination and greatly impairs the performance of perovskite-organic TSCs. To solve this problem, Riedl's group replaced traditional PTAA HTL

with a SAM layer, and modified the perovskite surface with PEAI to form a 2D capping layer. The resulting WBG PSCs with a bandgap of 1.85 eV delivered a high $V_{OC}$ of 1.34 V. More importantly, the increase in $V_{OC}$ is not accompanied by the loss of FF. A champion FF of 82% was obtained. These led to an outstanding PCE of 24.0% (certified 23.1%) in the TSCs.[302] Considering the oxidation of iodine and the formation of metallic $Pb^0$ under illumination in WBG solar cells severely deteriorate the device performance, recently, a redox mediator-stabilized strategy was developed by Jen's group. The anthraquinone-based mediator could not only reduce iodine and oxidize metallic $Pb^0$, but also passivated perovskite film defects. As a result, the 1.85-eV WBG PSCs achieved a PCE of 19.58% with a $V_{OC}$ of 1.35 V. When employed into the fabrication of perovskite-organic TSCs, the final optimized devices provided an impressive of PCE of 25.22% (certified 24.27%).[299] Subsequently, pseudo-halogen thiocyanate (SCN) ions, in the form of $Pb(SCN)_2$, were added to the WBG perovskite presursor by Li and coworkers. It was discovered that the addition of $Pb(SCN)_2$ enhanced crystallization and reduced grain boundaries of perovskite films. Morevover, a atrace amont of SCN- entered the perovskite lattice, passivating the halide vacancies and thus inhibiting the nontorious ion migration. The resulting single-junction WBG PSCs delievered a high PCE of 18.96% with a $V_{OC}$ of 1.32 V, and a chanpion PCE of 25.82% (certified 25.06%) was achieved in the TSCs. This work further reduces the PCE gap between perovskite-organic TSCs and other type of perovskite-based TSCs.[298]

Despite the success achieved by the PM6:Y6:$PC_{71}BM$, the NFA in this BHJ absorber i.e. Y6 possesses a bandgap of ~1.4 eV, which is larger than the optimal 1.15 eV to pair with the typical WBG perovskite with bandgaps around 1.75 eV.[303] The nonideal bandgap combination between WBG and NBG leads to the inefficient absorption of incident light and therefore lower $J_{SC}$. To tackle the issue, another NFA, BTPV-4Cl-eC9, with 1.22 eV bandgap was synthesized by Meng's group.[303] As a result, the NBG single cell delivered an ultrahigh $J_{SC}$ of 28.6 mA $cm^{-2}$. Based on this efficient NFA

organic cell, the TSC eventually achieved a PCE of 22.0% with an outstanding $J_{SC}$ of 15.7 mA cm$^{-2}$, which is also comparable with that of all-perovskite TSCs. The main PCE deficit resulted from the low $V_{OC}$ of this new NFA-based NGB subcell which provided room for future enhancement. Since the debut of NFA, the perovskite-organic TSCs have seen rapid development in the past several years and are still in the close running after their all-perovskite counterparts. In the near future, the advance of perovskite-organic TSCs will still rely on the progress of NBG OSCs as they are the limiting subcells. Specifically, the organic absorbers with more suitable (narrow) bandgaps with strong abilities of light absorption, exciton dissociation, and carrier transportation are expected. With the understanding deepening into the working mechanism of NFA-based absorbers, device engineering, and material innovation, the PCE of single-junction OSCs is expected to surpass 20% or even higher soon. And the competitiveness between all-perovskite and perovskite-organic TSCs will continues.

In addition to the absorber materials, the design of ICL for perovskite-organic TSCs also plays a decisive role in device performance. Recently, a dual-functional molecule, 4,7-bis((4-vinylbenzyl)oxy)-1,10-phenanthroline (C1), was introduced in the ICL to act as both the transport and protective layer.[301] The conjugated phenanthroline skeleton in C1 provided high electron mobility and hole-blocking capability, making it a qualified candidate for ETL in the ICL. Also, C1 possesses styryl groups which could be thermally crosslinked and thereby strong enough to protect the underlying layers from the sputtering damage. By using C1-based ICL, the perovskite-organic TSC reached an eminent PCE of 24.07%. This work points out the new route for ICL design. In the ICL, the commonly used charge recombination layer (CRL) is thin metal (1 nm Ag or Au) prepared by thermal evaporation. Nevertheless, these CRLs cannot meet requirements of an ideal ICL including efficient carrier recombination, minimum current leakage, and minimum optical losses.[159] It was found that when metal CRLs were replaced by 4-nm-thick IZO or 1.5-nm-thick $InO_x$, such issues can be addressed, contributing to the enhancment of PCEs.[159, 302]

## 7. SCALING UP INVERTED PSCS

At present, most high-performance PSCs are fabricated on substrates with small active areas by the spin-coating method (typically < 0.1 $cm^2$), which is far from the requirement of large-scale application.[20, 39] For the commercial application of perovskite photovoltaics, it is necessary to scale up the size of PSCs and fabricate perovskite solar modules. Depending on the area of the solar module, the perovskite solar modules can be classified into minimodule (< 200 $cm^2$), submodule (200–800 $cm^2$), small module (800–6500 $cm^2$), standard module (6500–14,000 $cm^2$), and large module (> 14,000 $cm^2$).[129, 318] To reduce the resistive loss and limit the current generated from a perovskite solar module, dividing the large cell into small subcells with series interaction is the most frequently applied technique. The general fabrication procedures of perovskite solar modules in this way are demonstrated in Figure 28a. To divide the subcells, a scribing process is employed, which can be done mechanically or through laser ablation. The scribing process typically involves three steps referred to as P1, P2, and P3. During P1, the transparent conductive oxide electrode is patterned to create conducting stripes. In P2, the ETL, perovskite, and HTL are removed before depositing the top-electrode material. This top-electrode material serves to connect the top contact of one cell to the bottom contact of the next cell. Lastly, P3 is performed to separate one subcell from another.[319-320] The photograph of the final perovskite module is shown in Figure 28b. The scribing regions, also known as dead areas, are inactive for photocurrent generation in perovskite solar modules. These regions are necessary to physically separate the subcells, however, they contribute to power loss in the module. The presence of dead areas reduces the overall active area available for light absorption and conversion to electrical energy, thus decreasing the power output of the solar module. Therefore, it is important to develop strategies to minimize the impact of dead areas and improve the power output of perovskite solar modules.

Both inverted- and regular-structured perovskite solar modules have been reported.

The inverted perovskite solar modules have some attractive advantages for large-scale deployment. Firstly, fabricating inverted perovskite solar modules is cost-effective, since cheap metal electrodes (e.g., Cu, Ag) are used without the need to use noble metals (e.g., Au).[321] Secondly, the manufacturing process of inverted perovskite solar modules does not need high-temperature thermal annealing, greatly reducing energy consumption and making it a suitable candidate for constructing flexible as well as perovskite-silicon tandem devices.[264, 322]

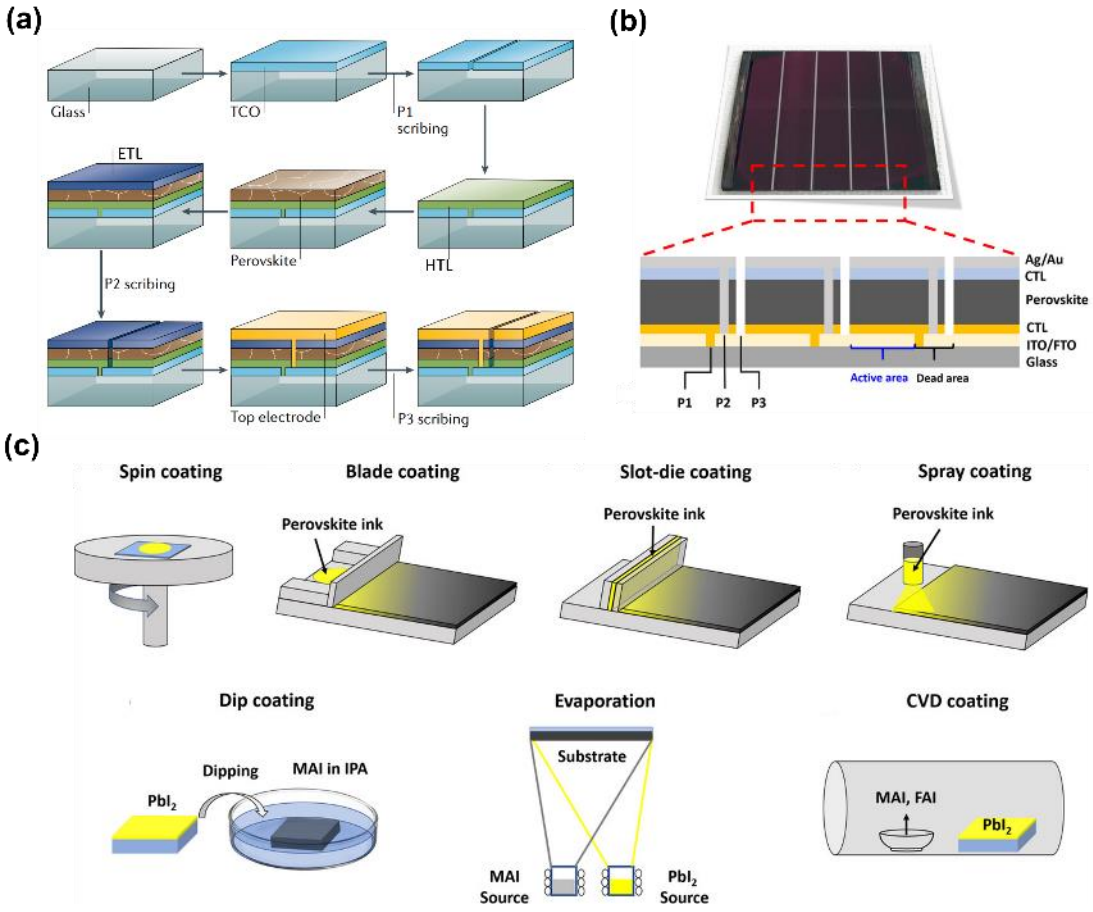


**Figure 32**. (a) Schematic illustration of the fabrication procedure of an inverted perovskite solar module. Reproduced with permission from ref [319]. Copyright 2020 Springer Nature. (b) Schematic of the final module structure. (c) Schematic of different methods to prepare perovskite films for perovskite solar modules. Reproduced with permission from ref [323]. Copyright 2022 John Wiley and Sons.

The lab-scale PSCs with a substrate size < 2.5 cm × 2.5 cm is generally fabricated by

the spin-coating method. While, this method is not adaptable for fabricating perovskite solar modules due to the unpleasant film uniformity in a large area especially with the antisolvent-dropping method. Additionally, approximately 90% of the precursor ink would be wasted during this method, increasing the device fabrication cost.[323] In comparison, blade coating, slot-die coating, spray coating, dip coating, evaporation, and CVD coating are more suitable for fabricating large-sized solar modules (Figure 28c). Among the various scalable methods for perovskite deposition, blade coating and slot-die coating are the most widely used. Blade coating is a relatively simple and cost-effective method where a blade is used to spread the perovskite precursor solution onto a substrate. The thickness of the resulting film can be controlled by adjusting the blade height or tilt angle. Slot-die coating, on the other hand, offers more precise control over film thickness. It involves the use of a slot die, which uniformly dispenses the perovskite solution onto the substrate in a continuous manner. The film thickness can be adjusted by controlling parameters such as solution flow rate, substrate speed, and slot-die geometry. Slot-die coating is frequently employed in manufacturing processes where high-quality and uniform films are required.

Achieving high-quality perovskite coatings on a large-area substrate is the prerequisite for constructing efficient and stable perovskite solar modules. The solvent volatilization time of the wet precursor film directly impacts the perovskite film morphology. Adding diphenyl sulfoxide, a nonvolatile Lewis base solvent with strong coordination capability, was effective in enlarging the nucleation energy barrier, modulating the nucleation of perovskite, and stabilizing the wet precursor film (Figure 29a).[324] The thickness inhomogeneities in the wet perovskite film due to the inhomogeneous flow (also referred to as ribbing effects) would induce perovskite film inhomogeneity after thermal annealing. To solve this problem, an effective way is to adjust the perovskite ink. Through the addition of the low-viscosity solvent ACN, the dynamic viscosity (μ) of the perovskite ink was reduced. In the meantime, surface

tension (σ) was increased, contributing to eliminating the ribbing effects (Figure 29b). Furthermore, the film porosity and thickness variation were reduced by this method. When adding 46 vol% ACN into the precursor solution, the slot-die-coated perovskite solar mini-modules obtained a champion PCE of 17.1% with an active area of 12.7 $cm^2$.[254] Huang et al. reported that the addition of a trace amount of surfactant additive could suppress microscale fluid flows and helped obtain uniform perovskite film over large area at a high coating speed of 180 m $h^{-1}$ using a blade coating method (Figure 29c). Afterward, in the same group, they combined the advantages of volatile noncoordinating solvents (e.g., 2-ME, ACN) and low-volatile coordinating solvents (e.g., DMF, DMSO), achieving both fast deposition and large perovskite grains. The inverted perovskite modules with an aperture area of over 63.7 $cm^2$ showed a champion-certified PCE of 16.4%. Furthermore, they found that compared to commercial CIGSe and silicon solar cells, the perovskite modules exhibited a smaller temperature coefficient.[118]

It is reported that the crystallization of perovskite films is from the top surface to the bottom interface.[325] During film formation, the evaporation of initially trapped DMSO could result in the generation of amorphous regions and voids at the bottom of perovskite films on a scale of tens of nanometers.[68] Although the voids at the buried interface can be eliminated by additive engineering, the amorphous regions with nonuniform distribution may still presented, reducing the device efficiency and performance reproducibility, especially for large-area devices. To address this problem, Huang et al. demonstrated a lead chelation molecule (LCM) strategy by incorporating a commonly used electron-transporting material, BCP, into the interface between the HTL and perovskite which could significantly diminish the amorphous area at the buried interface of perovskite films. The BCP is considered as LCM to effectively compete with DMSO for binding with lead ions via strong chelation interaction, leading to a reduction in DMSO residue and, consequently, increasing the crystallinity of the buried perovskite interface and giving a better film quality. The treated films

displayed fewer pinholes at the grain boundary during light soaking and gave rise to an enhanced crystallinity. The resulting small-area device delivered a champion PCE of 24.6%. More importantly, the champion minimodules (aperture area of 26.9 $cm^2$) achieved a certified PCE of 21.8% with a notable FF of 0.803, which was the highest FF reported for perovskite minimodules.[62]

The interface properties like band alignment and wettability are also closely relevant to the perovskite film quality at a large substrate. A hydrophobic surface poses challenges to depositing pinhole-free large-area perovskite films. It is known that most vacuum-processed $NiO_x$ films exhibit relatively hydrophobic surfaces, which would reduce the adhesion of perovskite inks. Liu and coworkers report a surface redox engineering (SRE) strategy, which could effectively solve this problem. In detail, the SRE process combined an Ar-plasma-initiated oxidation process and a Brønsted acid-mediated reduction process, which is desirable for increasing the surface energy and diminishing the pinholes (Figure 29d). Additionally, SRE improved the band alignment and reduced trap-assisted recombination, thus leading to an outstanding PCE of 18.6% on a 156 × 156 $mm^2$ substrate (Figure 29e).[119] We summarize the representative research on inverted perovskite mini-modules in Table 7.

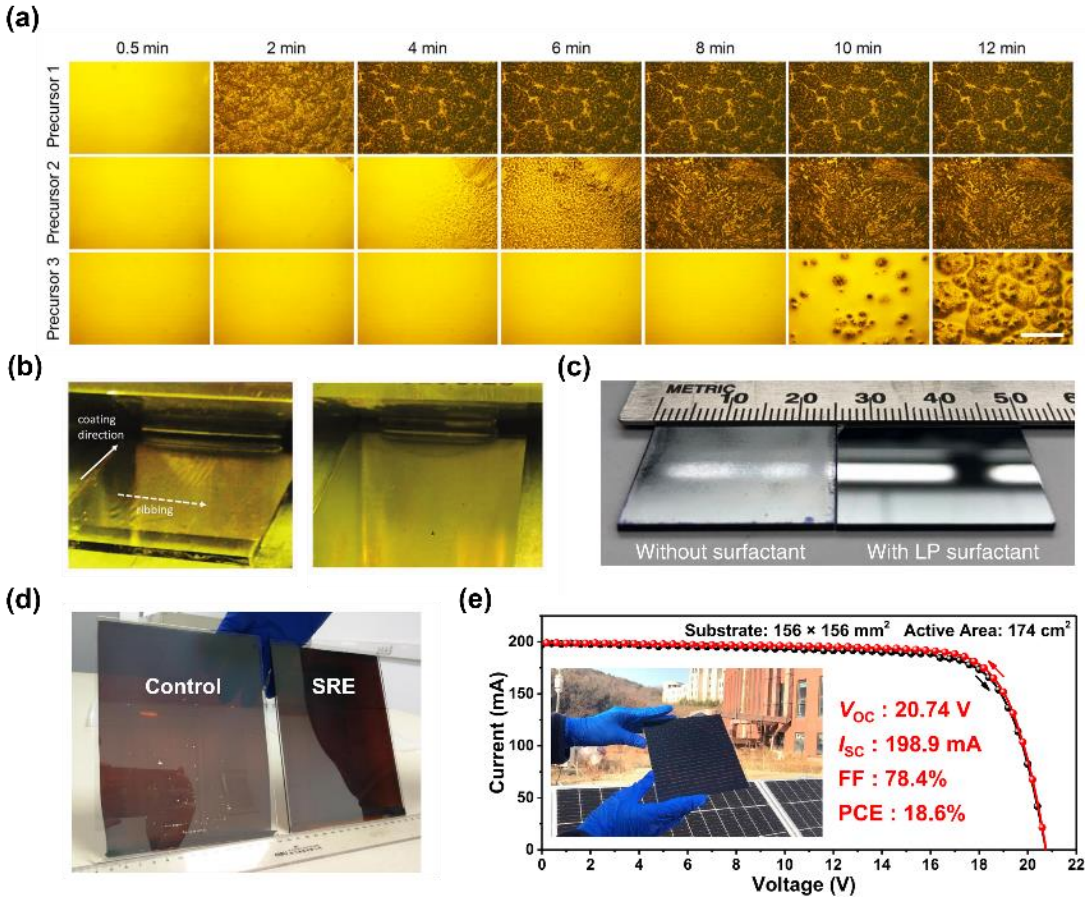


**Figure 33**. (a) Semi–in situ observation of morphology evolutions of the perovskite precursor film (scale bar, 100 μm). The perovskite precursors dissolved in DMF, DMF-NMP, and DMF-NMP-DPSO are labeled as precursors 1, 2, and 3, respectively. Reproduced with permission from ref [324]. Copyright 2021 Springer Nature. (b) Photographs of wet perovskite films without ACN (left) and 46% ACN. Reproduced with permission from ref [254]. Copyright 2023 John Wiley and Sons. (c) Photographs of perovskite films with and without surfactant. Reproduced with permission from ref [326]. Copyright 2018 Springer Nature. (d) Photographs of the perovskite films coated on control and SRE $NiO_x$ films (156 × 200 $mm^2$). (e) I-V curves of the module measured in the reverse and forward scan modes. Reproduced with permission from ref [119]. Copyright 2022 Elsevier.

In the industrial field, perovskite solar modules with an inverted structure have also gained significant research interest due to their low cost and superior stability. In China, several companies have been actively involved in the production of inverted

perovskite solar modules, with module sizes reaching up to 1 m × 2 m (Table 8 and Figure 30a). This highlights the scalability of the technology for larger module sizes suitable for commercial applications. Additionally, the construction of a perovskite demonstration station has been undertaken to evaluate the field performance of these modules (Figure 30b). This station serves as a platform to assess the long-term stability and overall performance of perovskite solar modules under real-world conditions. Recently, a company announced a certified steady-state PCE of 20.7% with a module size of 810 $cm^2$ (Figure 30c). Despite the significant advancements in inverted perovskite solar modules, their stability is generally poorer compared to small-area modules. This suggests that the performance degradation of these modules is more complex and challenging to mitigate.[241] For instance, in perovskite solar modules with series-interconnected subcells, the metal electrodes are in direct contact with the perovskite at the P2 scribe channels. This direct contact raises concerns about the long-term stability of perovskite solar modules, as there is a possibility of reaction between the perovskite material and the metals.[241, 319] Introducing an additional barrier layer like 2D graphitic carbon nitride nanosheets and ALD-$SnO_x$ at the interconnection regions can effectively protect the exposed perovskite material from lateral ion diffusion, contributing to the enhanced stability of the perovskite solar modules.[229, 241] Recently, a novel and effective method, through the ozone treatment of laser scribing grooves, was reported by Mai and coworkers, leading to in situ construction of lead oxide ($PbO_x$) blocking barriers at the edge of the sub-cells. The resulting perovskite solar modules showed a certified PCE of 21.37% (aperture area of the perovskite solar module is 12.84 $cm^2$) together with excellent long-term stability.[327] Apart from the aforementioned approaches, an ingenious solution is to fabricate parallel interconnected modules, which do not require the scribing process.[324, 328] In parallel-connected modules, a metallic grid is needed to reduce resistive losses at the substrate. Recently, we developed TCOs with buried-metal-grid to enhance the conductivity of the substrate so as to reduce the substrate-related power

loss. By modulating the thickness and shaded area of buried-metal-grids, a balance between high transmittance and low sheet resistance was realized. When upscaling the device size, the PSCs with buried-metal-grid showed lower PCE drop in comparison to the devices with pristine ITO.[328] It is worth noting that apart from progresses of upscaling the single-junction inverted PSCs, the PCEs perovskite-silicon tandem solar modules have also achieved huge achievements recently. Oxford PV announced that a certified PCE of 28.6% was achieved on a commercial-sized 'M4' (258.15 $cm^2$) solar cell.[329] Very recently, another company named Golden Concord Holdings Limited demonstrated a 4T 1.71 $m^2$ perovskite-silicon tandem solar module with a certified PCE of 26.36%.[330] Nevertheless, no experimental details can be found about these progresses, and the report on the commercial scale of perovskite-silicon tandem solar modules is still rare versus the single-junction solar modules.

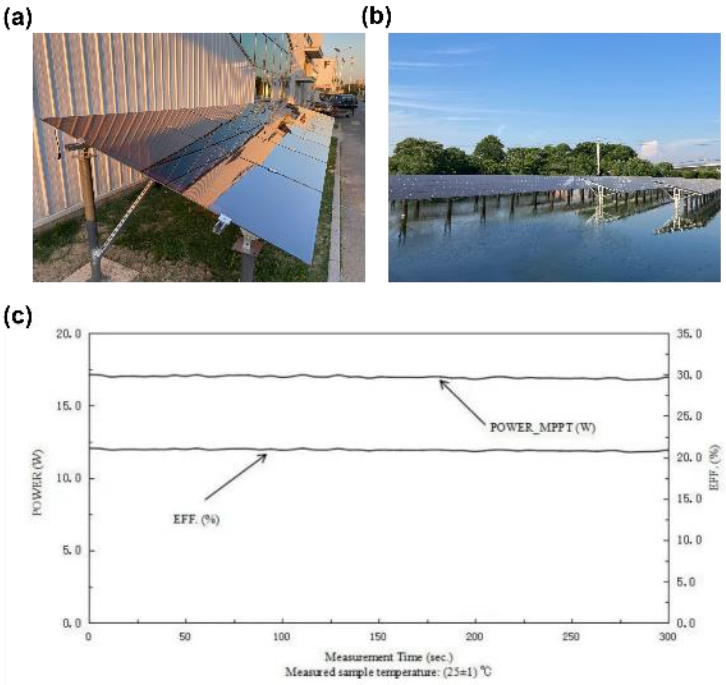


**Figure 34**. (a) Photograph of a perovskite demonstration power station (The module size is 1 m × 2 m). Reproduced with permission from ref [331]. Copyright Pandaily. (b) Photograph of a perovskite fish-light complementary power station. Reproduced with permission from ref [332]. Copyright Microquanta Semiconductor. (c) Certification report of a perovskite module with a size of 810 $cm^2$. Reproduced with permission

from ref [333]. Copyright UtmoLight.

**Table 7. Summary of representative high-efficiency inverted perovskite solar minimodules.**

| Device structure | Coating method | Solvent | Module size (cm × cm) | Aperture area ($cm^2$) | PCE (%) | Year | Ref. |
|---|---|---|---|---|---|---|---|
| ITO/$NiO_x$/Me-4PACz/Perovskite/ETL/BCP/Ag | Blade coating | DMF:DMSO (4:1/v:v) | 5 × 5 | 11.19[a] | 20.30 | 2023 | 334 |
| ITO/PTAA/$MA_{0.7}FA_{0.3}PbI_3$/$C_{60}$/$SnO_2$/ITO | Blade coating | 2-ME:DMSO | - | ~22.0[b] | 19.2 | 2023 | 335 |
| ITO/Poly-4PACz/$MA_{0.7}FA_{0.3}PbI_3$/$C_{60}$/BCP/Cu | Blade coating | 2-ME:DMSO | - | 25[b] | 20.7 (aa) | 2023 | 197 |
| ITO/PTAA:BCP/$FA_{0.9}Cs_{0.1}PbI_3$/$C_{60}$/BCP/Cu | Blade coating | 2-ME:DMSO | 15 × 12 | ~26.9[b] | 21.8 | 2023 | 62 |
| ITO/PTAA/$MA_{0.6}FA_{0.4}PbI_3$/$C_{60}$/BCP/Cu | Blade coating | 2-ME:DMSO | 13.0 × 8.5 | 50[b] | 19.2 | 2021 | 68 |
| ITO/PTAA/$FA_{0.83}Cs_{0.17}PbI_3$/$C_{60}$/BCP/Ag | Spin-coating | DMF:NMP | 6.5 × 6.5 | 23.25[b] | 20.91 | 2023 | 60 |
| FTO/$NiO_x$/Me-4PACz/$FAPbI_3$/PCBM/$SnO_2$/Cu | Spin-coating | DMF:DMSO (4:1/v:v) | 5 × 5 | 14.65[b] | 21.0 | 2023 | 58 |
| ITO/PTAA/$Al_2O_3$/$Cs_{0.05}(FA_{0.9}MA_{0.1})_{0.95}Pb(I_{0.9}Br_{0.1})_3$ /$C_{60}$/$SnO_2$/Ag | Spin-coating | DMF:DMSO (4:1/v:v) | 5 × 5.6 | 12.84[b] | 21.37 | 2024 | 327 |
| FTO/Urea-$NiO_x$/$Cs_{0.05}(FA_{0.95}MA_{0.05})_{0.95}Pb(I_{0.95}Br_{0.05})_3$ /BzMIMBr/$C_{60}$/BCP/Cu | Slot-die coating | DMF:DMSO:NMP (5.5:0.9:1/v:v:v) | 14 × 14 | 178.4[a] | 17.18 | 2023 | 336 |
| ITO/$NiO_x$/PTAA/$Cs_{0.05}(FA_{0.95}MA_{0.05})_{0.95}Pb(I_{0.95}Br_{0.05})_3$ /PCBM/BCP/Ag | Slot-die coating | DMF:DMSO (4:1/v:v) | 6 × 6 | 19.30[b] | 21.2 | 2023 | 337 |
| Glass/ITO/MeO-2PACz/$FAPbI_3$/LiF/$C_{60}$/BCP/Cu | Slot-die coating | 2-ME:NMP:ACN (46:8:46/v:v:v) | 5 × 5 | 12.7[a] | 17.1 | 2023 | 254 |
| ITO/$NiO_x$/Perovskite/PCBM/BCP/Ag | Slot-die coating | DMF:NMP (6:1/v:v) | 15.6 × 15.6 | 174[a] | 18.6 | 2022 | 119 |
| FTO/NiMgLiO/$FA_{0.83}Cs_{0.17}PbI_{2.83}Br_{0.17}$/ LiF/$C_{60}$/BCP/Bi/Ag | Slot-die coating | DMF:NMP:DPSO | - | 20.77[a] | 16.63 | 2021 | 324 |

[a]active area, [b]aperture area.

**Table 8. Examples of companies or organizations working on the upscaling of inverted PSCs.**

| Company | Country | Module type/area | Latest progress | Date of news release | Ref. |
|---|---|---|---|---|---|
| Golden Concord Holdings Limited | China | Single-junction PSCs/ 1 m × 2 m | 19.04% | 06 Mar 2024 | 338 |
| UtmoLight | China | Single-junction PSCs/ 810 $cm^2$ | 20.7% | 29 Feb 2024 | 333 |
| Mellow Energy | China | Single-junction PSCs/ 30 cm × 30 cm | 22.86% | 30 Aug 2023 | 339 |
| China Huaneng Group Co., Ltd. | China | Single-junction PSCs/ 3500 $cm^2$ | 18.5% | 10 Oct 2022 | 340 |
| Renshine Solar | China | Single-junction PSCs/ 30 cm × 40 cm | 20.86% | 20 Sep 2023 | 341 |
| Oxford PV | UK | Perovskite-Si TSCs/ 258.15 $cm^2$ | 28.6% | 24 May 2023 | 329 |
| Golden Concord Holdings Limited | China | Perovskite-Si TSCs/ 1.71 $m^2$ | 26.36% | 08 Apr 2023 | 330 |

## 8. ECONOMIC ASSESSMENT OF INVERTED PSCS

Inverted PSCs have been gaining attention for their potential cost advantages compared to traditional silicon solar cells and regular PSCs. This is due to several factors: 1) Material cost: Inverted PSCs can be made using low-cost CTL materials like $NiO_x$ and simple manufacturing processes, which can potentially reduce the overall production cost; 2) Efficiency: Inverted PSCs have demonstrated significant success in producing top-of-the-line single-junction and tandem PSCs. Currently, the highest recorded PCEs for both single-junction and tandem PSCs are achieved using the inverted structure. This can lead to higher energy yield and cost savings in the long run; 3) Stability: As discussed in Section 5, the optimized inverted PSCs have passed stringent ageing tests following ISOS or IEC protocols. The outstanding stability of inverted PSCs would help reduce the levelized cost of energy (LCOE), enhancing their market competitiveness; 4) Flexibility: Inverted PSCs with the advantages of low-temperature processing can be made into flexible and lightweight modules, which can reduce installation costs and open up new applications, such as building-integrated photovoltaics, wearable applications, high-

altitude ballons and airship;[342-343] 5) Manufacturing process: The manufacturing process for inverted PSCs is less energy-intensive compared to silicon solar cells and regular PSCs using mesoporous $TiO_2$, which can lead to lower production costs and a smaller carbon footprint.

Since the small-area high-efficiency PSCs are generally based on spin-coating technique, which is not compatible with high-throughput fabrication. It is more reasonable to evaluate the costs of perovskite solar modules. As for the cost of fabricating inverted perovskite solar modules, there is no consensus because no standard process sequence can be employed for the estimations of manufacturing cost.[344] The development period of PSCs is relatively shorter in comparison to silicon solar cells. The CTLs, perovskite compositions, deposition methods for perovskite films, passivating materials, and electrodes remain undetermined for the ultimate commercial deployment. This uncertainty is further reflected in the range of published manufacturing cost data. Early in 2017, the cost of single-junction inverted perovskite solar modules using inorganic metal oxide CTLs was estimated to be 31.7 $/m$^2$.[321] Park et al. noted that PSCs with cheap carrier-transport and conductive layers (e.g., $NiO_x$) as well as a high-throughput solution process could further reduce the module fabrication cost. They assumed that the fabrication cost for perovskite solar modules is half the cost of silicon solar cells (40 $/m$^2$ for perovskite solar cells and 80 $/m$^2$ for silicon solar cells, respectively).[345] The glass substrate coated with TCO is universally recognized as the priciest component in perovskite solar modules, constituting more than half of the overall expenses, as illustrated in Figure 30a.[145, 346] In the case of inverted PSCs, cost-effective metals such as Cu are employed for the rear contact, while CTLs like $C_{60}$ represent the second most significant cost factor. Grancini et al. summarized the calculated manufacturing costs for perovskite modules from 2016 to 2022 (Figure 30b). The solar cells with the gold electrode or very expensive CTLs (e.g., Spiro-MeOTAD) would result in manufacturing

costs > 150 $/m$^2$ and these devices were excluded in Figure 30b. It is clear that perovskite solar modules with the inverted configuration have an average lower cost compared to their regular counterparts.[347]

The assessment of the economic competitiveness of photovoltaic technology often involves the utilization of LCOE. The LCOE is a key metric in the energy industry used to assess the cost of generating electricity from a particular energy source over the lifetime of a system. It takes into account that the total cost of building, operating, and maintaining a power plant, as well as the amount of electricity it can produce over its lifetime. The LCOE provides a standardized way to compare different energy technologies and is a crucial tool for policymakers, investors, and energy planners when making decisions about energy investments and policy. It enables a direct comparison of the cost of different energy sources and helps in understanding the long-term economic viability of different energy generation methods.[344, 347] The reported LCOE values for perovskite photovoltaics vary depending on the calculation and assumption approaches employed.[347] Grancini et al. summarized the calculated LCOE values for perovskite solar modules reported from 2016 to 2022 (Figure 30c). Clearly, the increasing number of reports indicates a growing interest in the assessment of LCOE values. And the majority of LCOE calculations assumed perovskite module efficiency between 16 and 20%. Based on the 95% confidence interval for the remaining values, the LCOE values are shown to fall between 4.52 and 6.11 c$ per kW h with 95% probability, as highlighted by the green-shaded area in Figure 30c. Despite the surge in PCEs of PSCs, compared with silicon solar cells, PSCs still show a higher LCOE due to their high capital expenditure.[348] Furthermore, silicon solar cells exhibit a long lifespan of more than 25 years, while whether the PSCs can maintain stable long-term field performance is still obscure. Figure 30d shows the differences $\Delta LCOE = LCOE_{Pero,min} - LCOE_{Si.min}$ and $\Delta_{LCOE} = LCOE_{Tandem,min} - LCOE_{Si.min}$, respectively. With decreasing the lifetime of PSCs,

there is a dramatic increase in the LCOE. For perovskite single-junction solar modules with PCEs ~ 20% ($\Delta_{efficiency}$ = −2%) or perovskite solar modules with PCEs approaching 30% ($\Delta_{efficiency}$ = 8%), approximately 2–5 years shorter lifetimes could be tolerated. Due to the low perovskite processing cost, perovskite-based TSCs show similar cost projections. It is predicted by Holman et al. that tandem technology is favorable over single-junction modules for further reducing the LCOEs when system costs are higher than the cell cost.[349] However, at present, compared to the single-junction perovskite solar modules, the perovskite-based TSCs, especially for all-perovskite TSCs, show unpleasant device stability largely due to the unstable perovskite absorber layers with NBGs and WGBs. Given the high efficiency of PSCs, it is crucial to focus on addressing the short lifetime of PSCs in future research. Additionally, the low-cost processing of perovskite modules is important for commercial applications. Employing cost-effective raw materials is key to lowering the LCOE. In a recent breakthrough, Xu and colleagues introduced an aqueous synthesis technique for crafting high-purity $FAPbI_3$ perovskite microcrystals. This method utilizes inexpensive, low-grade starting materials and achieves a material cost significantly reduced—by two orders of magnitude—compared to the commercial prices of $PbI_2$ and FAI.[350] Additionally, streamlining the manufacturing process and minimizing equipment investment are promising strategies for reducing the LCOE) of PSCs.

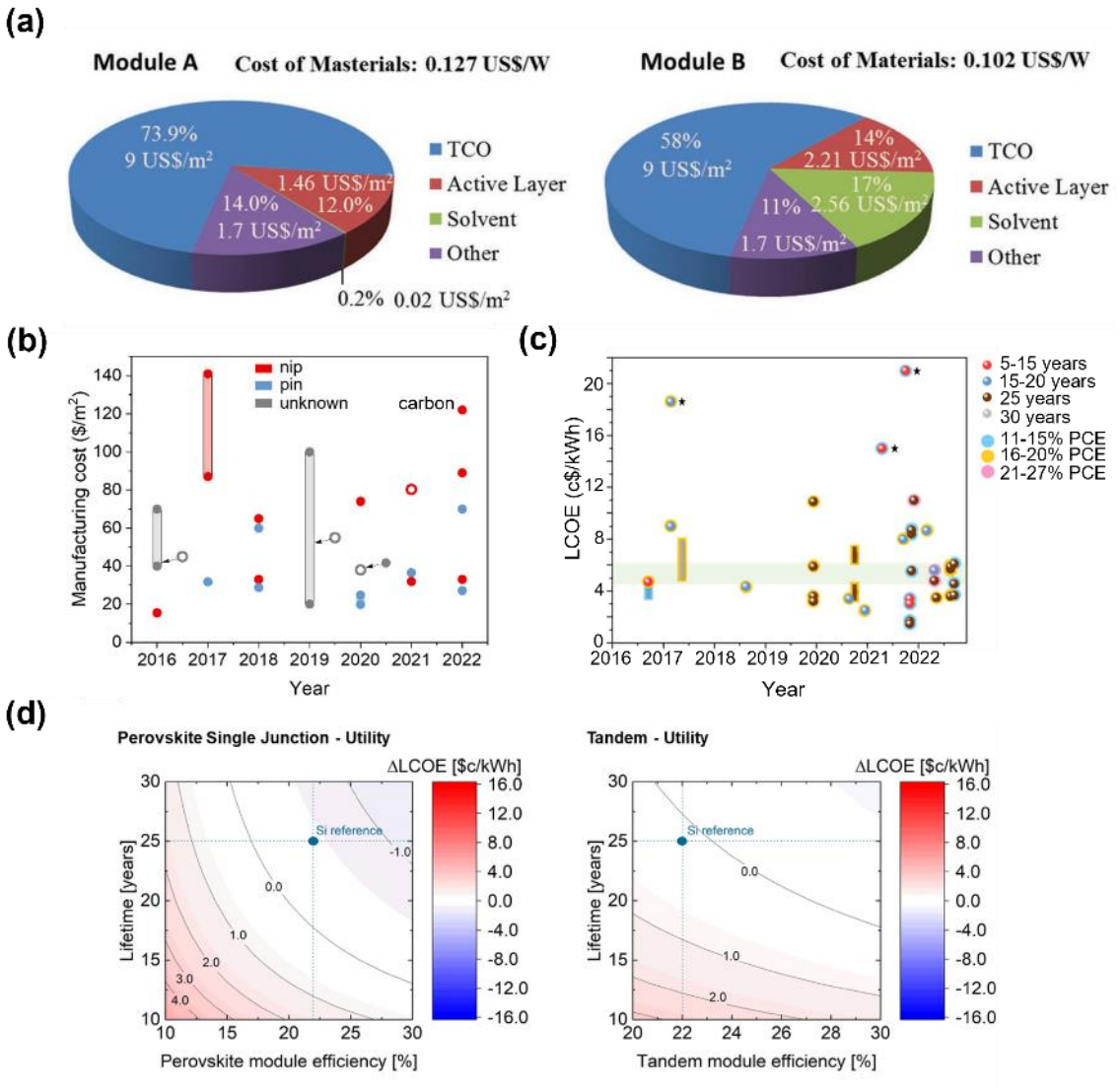


**Figure 35**. (a) Material cost analysis for two representative examples. Reproduced with permission from ref [346]. Copyright 2017 John Wiley and Sons. (b) Manufacturing cost for n-i-p (regular) and p-i-n (inverted) perovskite solar modules from 2016 to 2022. (c) The reported LCOE predictions for perovskite photovoltaic. The data is sorted based on the stability of the perovskite modules (represented by red, blue, brown, and grey dots, with lifespans ranging from 5 to 30 years) and their efficiencies (illustrated by pink, yellow, and light blue contours). The rectangular shapes indicate the range of the LCOE when specific values are not provided. Outlier values are denoted by a star. The green-shaded area displays the 95% confidence interval for the true LCOE value for perovskite devices,

which falls between 4.53 and 6.12 c$ per kW h. Reproduced with permission from ref [347], Copyright 2023 Royal Society of Chemistry. (d) Comparing the LCOE impact of lifetime and efficiency to a silicon module reference with a 25-year lifespan and 22% efficiency in a future scenario for perovskite single junction modules (left) and perovskite silicon tandem modules (right) for utility scale. Reproduced with permission from ref [344]. Copyright 2020 IEEE.

## 9. SUMMARY AND PERSPECTIVES

With the excellent features, e.g., high stability, excellent PCEs, low-temperature processing for all functional layers, and tandem structure compatibility, inverted PSCs have experienced a skyrocketing development in recent years with single-junction inverted PSCs and perovskite-based inverted TSCs achieving outstanding PCEs of 26.1% and 33.9%, respectively. We expect the trend of performance enhancement for inverted PSCs will continue in the near future. Despite the tremendous success of inverted PSCs, to bring this new technology into commercialization, substantial efforts are still needed to further improve the device efficiencies and stability, reduce the cell-to-module PCE gap, and reduce the cost of perovskite solar modules.

**Perovskite films**. It is known that the quality of perovskite films is a critical factor for the performance of PSCs, and tremendous efforts have been put into improving the film quality from the initial composition engineering through the crystal growth process. Furthermore, the composition of the perovskites is closely related to the device's intrinsic stability. In the current state-of-the-art inverted PSCs, mixed-cation perovskites (FA-MA-Cs) are the most popular choice. Whereas, the organic MA cation with a volatile nature is likely to lead to irreversible degeneration of perovskite structures, especially under

elevated temperatures, thereby impairing the device long-term stability.[104, 120, 351] Therefore, the utilization of MA-free perovskites could further boost the thermal and operational stability of PSCs. However, some reports show that inverted PSCs based on MA-containing compositions also demonstrated excellent stability and passed the stringent ageing tests protocol.[16, 67, 218] These controversial results denote that a deeper understanding of composition-film quality-device performance relationship is needed. Moreover, all-inorganic perovskites (e.g., $CsPbI_3$, $CsPbI_2Br$, $CsPbBr_3$) have recently attracted increasing attention due to their outstanding thermal stability up to 400°C. Moreover, all-inorganic perovskites with suitable WBG are good candidates for fabricating TSCs with NBG solar cells.[352] Despite the eye-catching advantages, the all-inorganic perovskites exhibit poor structural stability induced by the small ionic size of the Cs cation.[352-353] Taking typical $CsPbI_3$ as an example, the perovskite-to-nonperovskite polymorphic transition would perform under ambient conditions and this process would be accelerated when exposed to moisture. Several challenges need to be overcome to fully tap the potential of inverted all-inorganic PSCs. Firstly, the exact degradation mechanisms of all-inorganic PSCs should be investigated by operando/in-situ characterization techniques. Furthermore, by learning from other types of high-performance perovskites, developing effective stabilization methods (e.g., composition tuning, dimensional engineering, additive engineering) is a promising research direction.[353-354] Recently, Zhao et al. coated a 2D $Cs_2PbI_2Cl_2$ perovskite atop the 3D all-inorganic perovskite light absorber. The existence of a 2D/3D interface layer greatly suppressed the ion migration and effectively passivates the surface defects, demonstrating an excellent intrinsic lifetime of 51,000 ± 7,000 hours at 35℃ with the regular architecture and all-inorganic CTLs.[355] Given the water-repelling nature of 2D perovskites, this feature makes them a perfect candidate to protect the all-inorganic perovskites from the attack of moisture. Note that most all-inorganic PSCs use the n-i-p

architecture. We believe that the inverted all-inorganic PSCs with the elimination of hydroscopic Spiro-OMeTAD could further improve the stability of all-inorganic PSCs, meeting the mature industrial standard. Moreover, the discovery of stable and high-performance perovskite compositions could be facilitated by employing the high-throughput screening or machine learning method. For instance, Brabec et al. utilized a self-constructed high-throughput screening platform to select a stable perovskite with a composition of $MA_{0.1}Cs_{0.05}FA_{0.85}Pb(I_{0.95}Br_{0.05})_3$. When employed in the fabrication of PSCs, the final device retained its initial PCE after 1,450 h of continuous operation at 65°C.[356] In the long run, to absorb more sunlight and achieve the theoretical record efficiency limit for solar cells, lowering the bandgap to approach the ideal bandgap (1.34 eV) by using the mixed Pb-Sn perovskites is welcomed while this may raise stability issues due to the readily oxidizable $Sn^{2+}$. To address this issue, additives like $SnF_2$, $SnI_2$, $SnCl_2$, and metallic Sn have been added to the precursor solvents.[357-358] Despite the recent breakthroughs in Sn-containing perovskite, Sn-related inverted PSCs are still demonstrating unpleasant PCEs, which are far from the theoretical performance limit. More importantly, the Sn-related inverted PSCs show inferior long-term stability compared to the Pb-based PSCs, which hinders the development of all-perovskite TSCs. We reason that the origin of unpleasant stability of Sn-related PSCs is still related to the $Sn^{2+}$ oxidation and the use of unstable CTLs (i.e., acid PEDOT:PSS). To obtain efficient and stable inverted Pb-Sn PSCs, selecting high-purity Sn(II) halides salts as the Sn source, preparing the perovskite films at highly inert atmospheres, further developing effective reductants for $Sn^{4+}$, using stable inorganic CTLs, and encapsulation are promising solutions to solve these problems.[358] With these approaches, all-perovskite TSCs containing Pb-Sn NBG PSCs are likely to realize a higher PCE and improved stability.

The deposition methods for the perovskite light absorbers should also be given enough consideration in the future, as the perovskite film quality (e.g., crystallinity, defect

densities, and morphology) is strongly dependent on the fabrication process. The one-step method with the assistance of antisolvent treatment has shown great success in attaining highly efficient PSCs. While the two-step method exhibiting advantages of good performance reproducibility and ease of processing has attracted rarely less research attention, especially in the inverted PSCs compared to their regular counterparts. If selecting suitable HTLs and treating the bottom interface before coating the lead halide layers in the two-step fabrication process, the performance of the inverted PSCs based on the two-step method could be enhanced due to the modification of the perovskite nucleation and growth. Solution-processed polycrystalline perovskite films inevitably have larger amount defect densities than single-crystal perovskites. Note that commercial photovoltaic technologies such as silicon and GaAs solar cells largely rely on single-crystalline absorbers, which demonstrate a small $V_{OC}$ deficit and remarkable FFs of over 86% owing to the very low defect state density. Moreover, the use of single-crystal absorbers is beneficial for reducing the bandgap to approach the ideal band gap for single-junction solar cells without alloying the $Sn^{2+}$. Despite the huge potential, research on single-crystal PSCs is still rarely seen, which calls for more efforts (e.g., further reducing the band gap, interfacial defects passivation, CTLs modification, scaling up the device). To narrow the cell-to-module PCE gap and bring the perovskite photovoltaics close to commercialization, the commonly used solution-based spin-coating technique may not be the ideal choice. It was known that the vacuum evaporation method is more compatible with large-scale production compared to solution-based fabrication techniques. Additionally, the vacuum evaporation method does not need to use toxic solvents such as DMF and GBL, which is more environmentally friendly,[359-360] and this mature technique in the semiconductor industry is capable of obtaining highly even and uniform films on both planar and textured surfaces. Given the fact that most perovskite-Si TSCs utilize textured bottom cells with high surface roughness, it is difficult to get

uniform perovskite films atop the highly rough substrate by conventional solution-based techniques. Thereafter, the vacuum-deposited PSCs could be a potential alternative strategy to solve this problem. It was reported that the performance of PSCs based on the vacuum evaporation method is highly sensitive to the processing conditions (e.g., vacuum chamber pressures, precursor rates and rate stability, post-annealing temperatures, precursor suppliers).[360] We envision that the vacuum deposition method will be a hot research topic in the future and greatly help commercialize PSCs.

**Charge transporting layers**. The CTLs are vital to the device performance, which is also the most significant difference between the inverted and regular configurations. For ETL, the majority of inverted PSCs use fullerene and their derivatives (e.g., $C_{60}$, PCBM) as the ETL prepared by thermal evaporation, less frequent $SnO_2$ prepared by ALD. For HTL, there are a certain number of outstanding HTLs for inverted structures e.g., PTAA, $NiO_x$, and SAMs which are compatible with low-temperature processing and possess enhanced stability, These HTLs endow the fabricated inverted PSCs with remarkable long-term stability. It is worth noting that the recently-emerging SAMs HTLs have shown great hole selectivity and the great ability to reduce interfacial recombination, which are suitable for the fabrication of both high-performance single-junction and tandem inverted PSCs.[72, 76, 177, 194, 225] Nevertheless, modulating the molecular structures of SAMs is still needed to improve the coverage of SAMs, tune the interfacial interactions and energy level alignment between SAMs and perovskite, and modify wettability of perovskite inks on SAMs. In the future, there is a possibility of introducing more novel units for synthesizing new SAM molecules. If the functional groups on the tail of the SAM molecule are intentionally designed to further passivate the various defects of perovskite that arise at the buried interface, such as uncoordinated ions and antisite atoms, it has the potential to lead to notable improvements in the photovoltaic performance of inverted PSCs. However, this process involves a trial-and-error approach, necessitating further

theoretical research and device validation. Another popular HTL for inverted PSCs is the inorganic $NiO_x$ HTL, which presents some unique advantages such as high charge mobility and intrinsic stability. At present, the chemically synthesized $NiO_x$ nanoparticle ink due to high crystallinity has been widely used to obtain high-quality $NiO_x$ HTLs, and corresponding inverted PSCs delivered high PCEs over 25%. Nonetheless, this solution-based technique may hamper scalable applications. Sputtering and ALD as alternative deposition routes for $NiO_x$ films could guarantee scalability over large areas. Moreover, through extinct doping treatment (e.g., Cu-doping, Cs-doping), the conductivity of $NiO_x$ film can be further improved. It is noteworthy that the high defect densities at the $NiO_x$ film surface and misalignment of energy at the $NiO_x$/perovskite interface are detrimental to the device efficiency and stability.[147, 172, 227] Surface passivation seems to be of vital importance for the deposited $NiO_x$ films. We believe that SAM layers with excellent hole selectivity and functional anchoring groups are ideal candidates for the modification of both $NiO_x$ HTL and buried perovskite interface. The $NiO_x$/SAM bilayer HTL would also be applicable to various perovskite compositions. However, employing such bilayer HTLs tends to increase the fabrication procedures of PSCs, which is undesirable for commercial applications.

Although the CTLs especially the HTLs in inverted PSCs have widened the range of choices, this is far from good enough to realize the full potential of inverted PSCs. Therefore, more CTLs should be developed in the future. We believe that by building a CTL database based on reported work and using machine learning technology can we deeply understand the structure-performance relationship and shorten the time of new CTLs innovation.[1, 361] The development of new CTLs should consider the following aspects: 1) proper energy level alignment with the perovskite layer for efficient photo-carrier extraction and reduced charge recombination at the interface; 2) high electron or hole mobility to guarantee efficient charge carrier transport within the CTL; 3) high

transmittance to reduce the optical energy loss; 4) excellent stability against ambient environment to eliminate the risks of CTL degradation earlier than perovskite films during the device operation period; 5) a moderate deposition method to avoid further introducing damages or imperfections.

**Interface engineering**. Since interface defects of perovskite films are the main origin of non-radiative recombination, it is critical to suppress these imperfections scattered at both the top and buried surfaces of perovskite films. In addition to these intrinsic surface defects of perovskite materials, the contact between perovskite and adjacent CTLs may further introduce interfacial defects. Until now, most of the studies on interfacial engineering have focused on the top interface due to the exposed nature which makes it easy to characterize and modify, while the unexposed buried interface is rarely investigated, inducing the properties (e.g., microstructure, defect types) of the buried interface largely unexplored.[88, 94, 227] The lack of in-depth understanding of the buried interface in perovskite photovoltaics is impeding the further enhancement of device performance.[227] Therefore, the buried interface of perovskite light-absorber should be paid equal attention to the top surface and more work is needed. The massive significance of interface engineering has been growingly recognized. The wide range of passivation materials explored in recent years, including inorganic salts and organic molecules, load the toolbox of defect passivation and pave the way to minimize the non-radiative recombination and realize the theoretical limits of $V_{OC}$ and FF. However, an in-depth understanding of perovskite defects and passivation mechanisms for the defects in perovskite films is still urgently needed. For example, it is still hard to explicitly attain the distribution, type, and density of certain defects in perovskite films with various compositions or grown on different substrates, which makes it challenging to develop target passivation materials. Moreover, we need to investigate the key passivation group in multifunctional passivation molecules. High-throughput screening and machine

learning methods could be a reliable solution to selecting proper passivation materials and developing new passivation materials. For example, Sargent and coworkers developed a machine learning workflow trained by density functional theory. Through this method, 15 potential bifunctional desirable pseudo-halide anion-based passivating molecules were found. The further experiment verified that sodium thioglycolate was the most effective passivant, leading to a certified quasi-steady-state PCE of 24.04%.[362]

**Perovskite-based tandem solar cells**. Beyond the high-efficiency single-junction solar cells, TSCs are also the future direction for inverted PSCs. In contrast to the requirement of high-temperature annealing in n-i-p structures, most inverted PSCs are manufactured under 100°C, which enables the direct deposition of perovskite subcells atop silicon heterojunction cell to construct the TSCs. The feature of low-temperature processibility and consequential saved energy cost make inverted PSCs a warm welcome in the industry. By taking advantage of established success in silicon cells, the 2T perovskite-Si TSC has achieved a remarkable certified PCE of approaching 34%, representing the highest efficiency among perovskite-based TSCs. Meanwhile, by virtue of the tunability of perovskite composition, all-perovskite TSCs with potentials of ultralight-weight and flexibility have been seen as the strong game-changer against perovskite-Si TSCs. Similarly, thanks to the breakthrough of NFA-based organic materials, perovskite-organic TSCs have become another promising competitor among various TSC technologies.[313] For perovskite-based TSCs, reducing the $V_{OC}$ deficit of WBG subcells is an urgent requirement.[264] It is generally acknowledged that the origin of the large $V_{OC}$ deficit in Br-rich WBG PSCs is photo-induced halide segregation. Contrary to popular belief, Snaith and coworkers claimed that the dominant $V_{OC}$ loss mechanism was imperfections located at both the perovskite light absorber and the perovskite/CTLs interfaces.[363] Albrecht et al. have found similar results. SAMs with fast hole extraction and reduced nonradiative recombination at the HTL interface, when working as the HTLs for WBG PSCs, could

significantly increase the $V_{OC}$ and inhibit phase segregation under illumination.[177] Such controversial results indicate that the exact origin of $V_{OC}$ loss for the WBG PSCs is still unclear and should be carefully investigated in future research. Common methods to enhance the PCE of PSCs include effectively reducing bulk and surface defects, implementing precise bandgap tuning strategies, and utilizing robust and reliable charge carrier extraction materials. For WBG PSCs, the phase segregation under illumination leads to a loss of device performance, thereby affecting the stability of perovskite-based TSCs. Shen et al. have suggested potential solutions to this issue, such as using wide-bandgap perovskite quantum dots or inorganic $CsPbI_3$ perovskites. Additionally, they proposed a bifacial design strategy incorporating a narrower perovskite light absorber (i.e., lower Br content) to mitigate halide segregation concerns.[262] Another pressing issue related to the unpleasant device stability in all-perovskite TSCs is the easy $Sn^{2+}$ oxidation, and possible approaches to address this issue have been discussed before. In perovskite-silicon TSCs, a designed silicon textured surface for the 'trade-off' requirements of reducing reflection and fabricating efficient perovskite top cells is needed. Developing conformal coating techniques for perovskite films is a possible solution to reduce the limitations imposed by the texturing size. In perovskite-organic TSCs, the OSCs based on the small-molecule nonfullerene acceptors (e.g., Y6) are the most popular choice in perovskite-organic TSCs. Recently, Liu et al. reported a highly efficient single-junction OSC with a certified PCE of over 19% through modulating network morphology in the active layer, which offers the possibility of exceeding 20% for single-junction OSCs in the near future.[364] We envision that the future development of perovskite-organic TSCs is largely dependent on the advancement of OSCs, and there are several possible strategies for this pressing issue: 1) inventing novel donors and acceptors materials with good stability and optoelectronic properties;[365-368] 2) manipulating active-layer morphology;[364] 3) interfacial modification;[369] 4) device architecture engineering.[370-371]

In addition to the enhancement of $V_{OC}$ and FF in the WBG PSCs and NBG PSCs/OSCs, suitable ICLs are also waiting to be designed to cater to perovskite-based TSCs. Meeting the requirement of optics (i.e. minimized parasitic light absorption,[302] mechanics and electrics (i.e., low electric loss[305]) simultaneously represents one of the important research directions. Zhang et al. predicted that using dense, crack-free, and amorphous ICLs was likely to reduce the optical losses.[264] Additionally, the removal of recombination layers/tunneling junction layers in the ICLs is also a promising research direction to reduce the cost and processing complexity.[264] The ICLs are also expected to be fabricated feasible and scalable. Spatial-ALD is one possible direction to speed up the time-consuming ALD process. The research into monolayer ICL using ambipolar materials would be the goal. Note that recently the integrated perovskite/OSCs without employing the ICLs have received wide attention.[315, 372] This type of device contains both perovskites and organic near-infrared light absorbers, which can significantly enhance the $J_{SC}$ by additional light harvesting of OSCs in the near-infrared region while keeping the high $V_{OC}$ of PSCs.[373-375] However, first and foremost, the research on the fundamental working mechanism for this kind of device is scarce (e.g., the carrier transportation path at the perovskites/organic BHJs interface), and a deeper understanding of the operational mechanism is of critical importance for further increasing the PCEs of this kind devices. Moreover, most high-performance integrated perovskite/OSCs are based on comparably narrow bandgap perovskites, inducing a comparable low $V_{OC}$. We believe that combining WBG perovskites and the organic BHJ layer with decent energy level alignment is the future direction.

**Stability, scaling up, and cost**. For the field application and commercialization of perovskite photovoltaics, the stability, scaling up, and cost are dominant factors. Stability as a dominant factor for the commercial application of photovoltaic technologies is presently known as the main obstacle for PSCs. Even though several lab-scale inverted

PSCs have shown excellent stability under industrial damp-heat conditions, based on the research experience from silicon solar cells, such results are insufficient to guarantee long-term stable operation of the PSCs under real-world exposure. Therefore, more research attention should be paid to long-term field testing of PSCs. To further enhance the stability of PSCs, first and foremost, uncovering the fundamental degradation mechanisms and the factors that influence perovskite degradation are needed to construct PSCs with enhanced stability. Subsequently, more work is required to develop holistic defect passivation strategies,[235, 376-377] stable CTLs,[237, 378] effective encapsulation,[248, 252] and stable perovskite compositions[26, 355-356] with the aim of better withstanding external stress (e.g., moisture, oxygen, heat, applied electric bias, light illumination) for inverted PSCs.

The industrial development of PSCs greatly relies on the large-scale fabrication of perovskite solar modules with high PCEs, high stability, and high performance reproducibility. Differing from the fabrication of lab-scale PSCs with < 1 $cm^2$ active area, upscaling this to modules necessitates different technologies and instruments. Making homogeneous large-area perovskite films is a critical step. We expect that for single-junction perovskite solar modules, slot-die coating will provide more accurate control over film thickness compared to other coating methods, making it a preferred choice for preparing perovskite films on larger surfaces. For perovskite-silicon TSCs, hybrid sequential deposition, using vacuum deposition of a porous inorganic template followed by solution deposition of organic salts, combines the benefits of vacuum and solution-based deposition techniques, making it ideal for conformal coating perovskite films on textured surfaces. From technical and economic points of view, it is impractical to expand the space of nitrogen-filled gloveboxes to meet the requirements of depositing large-area perovskite films (e.g., 1 m × 2 m) so preparing these films in ambient air is more realistic. However, the moisture in ambient air can trigger the decomposition of the perovskite

layer, resulting in a reduction of device efficiency. Additive engineering[379] and solvent engineering[380] have proven to be effective in enabling the crystallization of high-quality films in ambient air. To realize practical application, performance reproducibility of the solar modules is another important consideration. Since in the pilot line, the perovskite films are generally deposited in ambient air, the humidity and temperature should be strictly controlled. In addition, to ensure the high yield of perovskite solar modules, according to the experience of silicon technology, electroluminescence measurements should be performed during the fabrication of perovskite solar modules. Currently, laser scribing is the most commonly employed method for dividing a large-area device into smaller subcells and creating a series-connected solar module. However, challenges remain in terms of precisely controlling scribing lines (e.g., depth, width, straightness accuracy), minimizing thermal damage to the perovskite layer near scribe channel edges, and preventing direct contact of metal electrodes with perovskite within the P2 scribe channels. These challenges present a significant risk to the PCE of the final perovskite solar modules. To address these challenges, the following strategies can be considered in future research: 1) substituting the gauss light beam with the flat-topped light beam; 2) depositing a protection layer to prevent the direct contact of metal with the perovskite within the P2 scribe channels; 3) avoiding the use of laser scribing by making parallel-connected modules.

Lastly, in order to penetrate the solar market, a sufficient level of market competitiveness, which can be assessed through LCOE, is essential. The initial step is choosing an appropriate production route for the PSCs, a key determinant. Due to silicon solar cells representing over 92% of the solar market, substantial financial investment has been directed towards silicon technology.[262] Considering economic and feasibility factors, the fabrication of perovskite-silicon TSCs may serve as a shortcut for the entry of perovskite photovoltaics into the solar market in the immediate future. Additionally, in perovskite-

silicon TSCs, the module size is smaller compared to large-area single-junction perovskite solar modules (e.g., 1 m × 2 m), likely resulting in decreased capital expenditure. It was reported that for commercial systems made from perovskite-Si TSCs to be competitive, they would need to achieve an efficiency exceeding 26% and maintain module fabrication costs in the range of US$90 to US$150 $m^{-2}$, with the assumption that the TSC stability matches that of c-Si cells.[262] Whereas, most perovskite-based TSCs show inferior device stability versus their single-junction counterparts due to the higher Br content in WBG perovskites, leading to a reduced LCOE. This means that the most pressing issue is to increase the device stability of perovskite-silicon TSCs. As mentioned before, employing bifacial TSCs strategy could lower the bandgap of the perovskite subcells so as to increase the device stability. We envision that this would be a promising direction in future research. It is predicted that in order for an 1 TWp cumulative PV installation around 2025 to become a reality, the perovskite technology must advance to a stage where single junction modules efficiencies above 22% or tandem solar modules efficiencies surpassing 30% are realizable, while ensuring that system lifetimes are akin to silicon, all through cost-effective industrial scale production.[344] Note that single-junction perovskite solar modules offer distinct advantages in certain application scenarios, such as building-integrated photovoltaics[381] and high-altitude balloons[342, 382], thanks to their thin films, lightweight design, and flexibility. Traditional silicon photovoltaics face challenges in being used in these fields. To enter the market with a competitive edge in the initial stages of perovskite photovoltaic development, employing a differentiated competitive strategy by targeting perovskite products specifically for these applications could be a wise move. Furthermore, we speculate that the effective approaches to further decrease the cost and LCOE of inverted perovskite solar modules are (1) Further improving the PCEs and stability, especially the stability; (2) Reducing the cost of raw materials for devices; (3) Developing more efficient, cost-effective or simple

manufacturing processes for devices; (4) Increasing the installed power-generating capacity to GW level.

The past few years have witnessed rapid development in both single-junction and tandem inverted PSCs. The champion-certified PCE of single-junction inverted PSCs has surpassed that of regular PSCs for the first time in 2023. While for inverted TSCs, the optimal PCE is approaching 34%. The tremendous experience and strategies accumulated during this period have paved the way for the systematic exploration of perovskite-based device physics and the optimization of device performance. This enables us to have a reasonable expectation for the commercialization of PSCs in the next decade.

## AUTHOR INFORMATION

### Corresponding Authors

**Wei Zhang** − *Advanced Technology Institute, University of Surrey, Guildford, Surrey GU2 7XH, UK; State Centre for International Cooperation on Designer Low-carbon & Environmental Materials (CDLCEM), School of Materials Science and Engineering, Zhengzhou University, Zhengzhou 450001, P. R. China;* orcid.org/0000-0002-2678-8372; Email: wz0003@surrey.ac.uk

**Henry J. Snaith** − *Clarendon Laboratory, Department of Physics, University of Oxford, Oxford OX1 3PU, UK;* orcid.org/0000-0001-8511-790X; E-mail: henry.snaith@physics.ox.ac.uk

**Qihuang Gong** − *State Key Laboratory for Artificial Microstructure and Mesoscopic Physics, School of Physics, Frontiers Science Center for Nano-optoelectronics & Collaborative Innovation Center of Quantum Matter, Peking University, Beijing 100871, China; Peking University Yangtze Delta Institute of Optoelectronics, Nantong, Jiangsu 226010, China; Collaborative Innovation Center of Extreme Optics, Shanxi University, Taiyuan, Shanxi 030006, China*; orcid.org/0000-0003-4974-6244; E-mail: qhgong@pku.edu.cn

**Rui Zhu** − *State Key Laboratory for Artificial Microstructure and Mesoscopic Physics, School of Physics, Frontiers Science Center for Nano-optoelectronics & Collaborative Innovation Center of Quantum Matter, Peking University, Beijing 100871, China; Peking University Yangtze Delta Institute of Optoelectronics, Nantong, Jiangsu 226010, China; Collaborative Innovation Center of Extreme Optics, Shanxi University, Taiyuan, Shanxi 030006, China*; orcid.org/0000-0001-7631-3589; E-mail: zhurui3@pku.edu.cn

### Authors

**Peng Chen** − *State Key Laboratory for Artificial Microstructure and Mesoscopic*

*Physics, School of Physics, Frontiers Science Center for Nano-optoelectronics & Collaborative Innovation Center of Quantum Matter, Peking University, Beijing 100871, China*

**Yun Xiao** − *Clarendon Laboratory, Department of Physics, University of Oxford, Oxford OX1 3PU, UK; State Key Laboratory for Artificial Microstructure and Mesoscopic Physics, School of Physics, Frontiers Science Center for Nano-optoelectronics & Collaborative Innovation Center of Quantum Matter, Peking University, Beijing 100871, China.*

**Shunde Li** − *State Key Laboratory for Artificial Microstructure and Mesoscopic Physics, School of Physics, Frontiers Science Center for Nano-optoelectronics & Collaborative Innovation Center of Quantum Matter, Peking University, Beijing 100871, China.*

**Xiaohan Jia** − *State Key Laboratory for Artificial Microstructure and Mesoscopic Physics, School of Physics, Frontiers Science Center for Nano-optoelectronics & Collaborative Innovation Center of Quantum Matter, Peking University, Beijing 100871, China. Present address: Cavendish Laboratory, Department of Physics, University of Cambridge, Cambridge, CB3 0HE, United Kingdom.*

**Deying Luo** − *Department of Materials Science and Engineering, University of Toronto, Toronto, M5G 3E4, Canada.*

Complete contact information is available at: XXXX.

## Author Contributions

P. C., Y. X., S. L., and X. J. contributed equally to this work.

## Notes

Henry J. Snaith is the founder and Chief Scientific Officer of Oxford Photovoltaics, a company commercializing perovskite photovoltaics.

## Biographies

Peng Chen is a postdoctoral researcher at Department of Physics, Peking University; He obtained his Ph.D. at the same place in 2023, supervised by Prof. Rui Zhu. His current research interests focus on fabricating high-performance p-i-n perovskite solar cells and understanding the interface physics in perovskite optoelectronics.

Yun Xiao obtained his Ph.D. at University of Oxford, U.K., under the supervision of Prof. Henry J. Snaith. His research focuses on fabricating well-performing p-i-n perovskite solar cells with a particular interest in wide bandgap perovskite solar cells as well as perovskite-based tandem devices.

Shunde Li is a Ph.D. student in the Department of Physics at Peking University. He obtained his Master's degree from the School of Physical Science and Technology at Shanghai Tech University in 2021. His research focuses on material physics of perovskite solar cells and perovskite photovoltaic applications. Currently, he is primarily engaged in exploring systematic control over the optoelectronic properties of perovskite films through crystallization engineering, aiming to develop high-performance single-junction p-i-n perovskite solar cells.

Xiaohan Jia received her MSci degree in Chemistry from the University College London (UCL) in 2021. She joined Prof. Rui Zhu's research group as a research assistant in the Department of Physics at Peking University between 2021 and 2023. She is currently a Ph.D. student in the Cavendish Laboratory at the University of Cambridge, supervised by Dr. Ibrahim Dar. Her current research focuses on wide bandgap perovskite solar cells.

Deying Luo is a Future Assistant Professor at Peking University in China, with an appointment in the School of Integrated Circuits. He received a B.Eng. degree in Electronic Science and Technology from Yunnan University in 2011 and a Ph.D. degree in Atomic and Molecular Physics from Peking University in 2019. He pursued postdoctoral training at the University of Toronto in Canada (under the supervision of

Prof. Zheng-Hong Lu) and the University of California, San Diego in the USA (under the supervision of Prof. Sheng Xu). His current research focuses on developing and understanding new materials and device concepts for solar energy conversion, Si-CMOS-based heterointegration micro-display, and TFT-based heterointegration infrared imaging.

Wei Zhang is an Associate Professor in Energy Technology at the Advanced Technology Institute, University of Surrey. His current research interest includes halide perovskites for photovoltaic and light-emission applications, and low-dimensional nanomaterials (semiconductors, plasmonic metal nanoparticles, photonic crystals, etc.) for energy conversion and storage.

Henry J. Snaith is the Binks Professor of Renewable Energy in the Department of Physics, University of Oxford, U.K. His research focuses on developing and understanding new materials and device concepts for photovoltaic solar energy conversion. His research group works with organic, metal oxide, and metal halide perovskite semiconductors, processed via solution or vapor phase deposition methods. His interdisciplinary work ranges from new material synthesis and discovery, device fabrication and development, advanced characterization methodologies, and theoretical modeling. Beyond his academic appointment, Henry J. Snaith is also a cofounder and CSO of two spin-out companies, Oxford PV, Ltd., and Helio Display Materials, Ltd., commercializing metal halide perovskites for PV and light-emitting applications, respectively.

Qihuang Gong is Member of the Chinese Academy of Sciences, Cheung Kong professor of physics at Peking University, China, where he is also the founding director of the Institute of Modern Optics and the President of Peking University. His research interests include optelectronic materials and devices, ultrafast optics, nonlinear optics, and mesoscopic optic.

Rui Zhu is a professor in the State Key Laboratory of Artificial Microstructure and

Mesoscopic Physics, Department of Physics, Peking University. He received his Bachelor's degree from Nanjing University in 2003 and Ph.D. degree from Fudan University in 2007. He joined the Department of Physics at Peking University in 2013. His research focuses on the development of advanced photovoltaic materials and device.

## ACKNOWLEDGMENTS

This work was financially supported by National Natural Science Foundation of China (52325310), Beijing Natural Science Foundation (JQ21005), the National Key R&D Program of China (2021YFB3800100 and 2021YFB3800101), Yunnan Provincial Science and Technology Project at Southwest United Graduate School (202302AO370013), the open research fund of Songshan Lake Materials Laboratory (2022SLABFK07), the China Postdoctoral Science Foundation (2023TQ0009, 2023M740116), the State-sponsored Postdoctoral Researcher Program (GZB20230030), and the R&D Fruit Fund (20210001). W.Z. thanks EPSRC standard research (EP/V027131/1) for financial support. H.S. acknowledges funding from the Engineering and Physical Science Council (EPSRC). Y.X. acknowledges China Oxford Scholarship Fund.

## GLOSSARY

2F = 4-(7-(4-(bis(4-methoxyphenyl) amino)-2,5- difluorophenyl)benzo[c][1,2,5]thiadi

2ME = 2-methoxy-ethanol

2PACz = 2-(9H-carbazol-9-yl)ethyl)phosphonic acid

2T = two-terminal

345FAn = 3,4,5-trifluoroanilinium

3-APy = 3-(Aminomethyl)pyridine

3F-PEA = 3-fluoro-phenethylammonium

3-MPA = 3-mercaptopropionic acid

3MTPAI = 3(methylthio) propylamine hydroiodide

4PADCB = (4-(7H-dibenzo[c,g]carbazol-7-yl)butyl)phosphonic acid

4T = four-terminal

ACN = acetonitrile

AFM = atomic force microscopy

AICI = 2-aminoindan hydrochloride

ALD = atomic layer deposition

$AlO_x$ = aluminium oxide

ANS = anisole;

ATO = antimony-doped tin oxides

AZO = aluminum-doped zinc oxide

-azol-4-yl) benzoic acid

BA = n-butylamine

BAI = butylammonium iodide

$BAMA^+$ = (butylamino)methaniminium

BCP = bathocuproine

BDAI = butanediammonium iodide

BHJ = bulk heterojunction

Bi = bismuth

$BMIMBF_4$ = 1-Butyl-3-methylimidazolium tetrafluoroborate

BPA = benzylphosphonic acid

Bphen = bathophenanthroline

Br-2EPT = (2-(3,7-dibromo-10H-phenothiazin-10-yl)ethyl)phosphonic acid

C1 = 4,7-bis((4-vinylbenzyl)oxy)-1,10-phenanthroline

CB = chlorobenzene

CF3-PA = 4-trifluoromethyl-phenylammonium

CIGSe = copper indium gallium selenide

$Cl_6$SubPc = boron chloride subphthalocyanine

Cl-PEAI = 4-chloro-phenylethylammonium iodide

Cl-PEAI = 4-chloro-phenylethylammonium iodide

CSBA = p-chlorobenzenesulfonic acid

CTLs = charge transporting layers

CVD = chemical vapor deposition

DC-PA = (2,7-dimethoxy-9H-carbazol-9-yl) methyl) phosphonic acid

DE = diethyl ether;

DMAc = dimethylacetamide;

DMAcPA = (4-(2,7-dibromo-9,9-dimethylacridin-10(9H)yl)butyl)phosphonic acid

DMDP = diammonium-methylthio dual passivation

DMF = dimethyl formamide

DMSO = dimethyl sulfoxide

$D_N$ = Gutmann donor number

DPPP = 1,3-Bis(diphenylphosphino)propane

DSSCs = dye-sensitized solar cells

EA = ethyl acetate

$EDAI_2$= ethylenediammonium diiodide

$EQE_{EL}$ = external quantum efficiency of the electroluminescence

ETL = electron transporting layer

FBPAc = 2,3,4,5,6-pentafluorobenzylphosphonic acid

$FcTc_2$ = ferrocenyl-bis-thiophene-2-carboxylate

FEAI = 2-(2,3,4,5,6-pentafluorophenyl) ethylammonium iodide

FF = fill factor

F-PEAI = 4-fluoro-phenylethylammonium iodide

F-PEAI = 4-fluoro-phenylethylammonium iodide

FTIR = fourier transform infrared

FWHM = full width at half maximum

GABr = guanidinium bromide

GAI = guanidinium iodide

GBL = γ-butyrolactone

GIWAXS = grazing-incidence wide-angle X-ray scattering

GlyHCl = glycine hydrochloride

GuaSCN = guanidinium thiocyanate

GYL = γ-valerolactone

HAADF = high-angle annular dark-field

HRTEM = high-resolution transmission electron microscopy

HTL = hole transporting layer

IAHA = 6-(iodo-λ5-azanyl) hexanoic acid

ICBA = indene-$C_{60}$ bisadduct

ICL = interconnecting layer

IEC = International Electrotechnical Commission

$InBr_3$ = indium bromide

IPA = isopropanol

ISOS = international summit on organic photovoltaic stability

ITO = indium tin oxide

IZO = indium zinc oxide

$J_{SC}$ = short-circuit current density

KF = potassium fluoride

KPFM = kelvin probe force microscopy

LAI = large alkylammonium interlayers

LCM = lead chelation molecule

LCOE = levelized cost of energy

LiF = lithium fluoride

Li-TFSI = bis(trifluoromethanesulfonyl)imide

MACl = methylammonium chloride

MAFa = methylammonium formate

Me-4PACz = 4-(3,6-dimethyl-9H-carbazol-9-yl)butyl)phosphonic acid

MeO-2PACz = 2-(3,6-dimethoxy-9H-carbazol-9-yl)ethyl)phosphonic acid

MeO-4PADBC = (4-(3,11-dimethoxy-7H-dibenzo[c,g]carbazol-7-yl)butyl)phosphonic acid

$MoO_x$ = molybdenum oxide

MPA = methyl phosphonic acid

MPA-CPA = (2-(4-(bis(4-methoxyphenyl)amino)phenyl)-1-cyanovinyl)phosphonic acid

MPP = maximum power point

MPyFA+ = N-(3-methylpyridine)formamidinium

NBG = narrow bandgap

NFA = non-fullerene acceptors

$NiO_x$ = nickel oxide

NMP = N-methyl-2-pyrrolidone;

NPs = nanoparticles

OA = octylamine

OAm = oleylamine

OLAI = olaylammonium iodide

OSCs = organic solar cells

P3HT = poly(3-hexylthiophene)

PBAI = benzenebutanammonium iodide

$PbPyA_2$ = pyridine-2-carboxylic lead

PC = propylene carbonate

PCBM = [6,6]-phenyl-C61-butyric acid methyl ester

PCE = power conversion efficiency

$PDAI_2$ = 3-propane diammonium iodide

PEA = phenethylamine

PEABr = phenethylammonium bromide

PEACl = phenethylammonium chlorine

PEAI = phenethylammonium iodide

$PEAMA^+$ = phenethylamino)methaniminium

PEDOT:PSS = poly(3,4-ethylenedioxythiophene)−poly(styrenesulfonate)

PEIE = polyethyleneimine ethoxylated

PEN = polyethylene naphthalate

PFDT = 1H,1H,2H,2H-perfluorodecanethiol

PFN-Br = poly[(9,9-bis(3'-(N, N-dimethyl)-N-ethylammonium)-propyl)-2,7-flu-orene)-alt-2,7-(9,9-di-octylfluor-ene)] dibromide

PFN-I = poly[(9,9-bis(3'-(N, N-dimethyl)-N-ethylammonium)-propyl)-2,7-flu-orene)-alt-2,7-(9,9-di-octylfluor-ene)] diiodide

PI = piperazinium iodide

PIB = polyisobutylene

PIC = porous insulator contact

PL = photoluminescence

PLEDs = perovskite light-emitting diodes

PMMA = poly(methyl methacrylate)

POE = polyolefin

poly-TPD = poly(N,N'-bis-4-butylphenyl-N,N'-bisphenyl)benzidine

PPP = polyhedral oligomeric silsesquioxane-poly(trifluoroethyl methacrylate)-b-poly(methyl methacrylate)

PPS =

PS = polystyrene

PSCs = perovskite solar cells

PSP= =(phenylsulfonyl)pyrrole

PTAA = poly[bis(4-phenyl)(2,4,6-trimethylphenyl)amine]

RDPs = reduced dimensional perovskites

RP = Ruddlesden-Popper

SAM = self-assembled monolayers

SC = single-crystal

SCN = thiocyanate

SEM = secondary electron microscopy

$SiO_x$ = silicon oxide

$SnO_2$ = tin(IV) dioxide

Spiro-OMeTAD = 2,2′,7,7′-tetrakis(N,N-di-p-methoxyphenylamine)-9,9′spirobifluorene

S-Q = Shockley–Queisser

SRE = surface redox engineering

SST = surface sulfidation treatment

STEM = scanning transmission electron microscopy

TCO = transparent conductive oxides

$TiO_2$ = titanium dioxide

TL = toluene

ToF-SIMS = time-of-flight secondary ions mass spectroscopy

$TPABr_3$ = trimethylphenylammonium tribromide

TPB = 4-tert-butylpyridine

TPBi = 1,3,5-Tris(1-phenyl-1H-benzimidazol-2-yl)benzene

TRPL = time-resolved photoluminescence

TSCs = tandem solar cells

$V_{OC}$ = open-circuit voltage

$VO_x$ = vanadium oxide

WBG = wide bandgap

XPS = X-ray photoelectron spectroscopy

$YbO_x$ = ytterbium oxide

ZTO = zinc tin oxide

β-pV2F = β-poly(1,1-difluoroethylene)

## REFERENCES


1. Luo, D.; Su, R.; Zhang, W.; Gong, Q.; Zhu, R., Minimizing Non-Radiative Recombination Losses in Perovskite Solar Cells. *Nat. Rev. Mater.* **2019,** *5*, 44-60.
2. Liu, X. K.; Xu, W.; Bai, S.; Jin, Y.; Wang, J.; Friend, R. H.; Gao, F., Metal Halide Perovskites for Light-Emitting Diodes. *Nat. Mater.* **2021,** *20*, 10-21.
3. Ren, A.; Wang, H.; Zhang, W.; Wu, J.; Wang, Z.; Penty, R. V.; White, I. H., Emerging Light-Emitting Diodes for Next-Generation Data Communications. *Nature Electronics* **2021,** *4*, 559-572.
4. Kim, J. Y.; Lee, J. W.; Jung, H. S.; Shin, H.; Park, N. G., High-Efficiency Perovskite Solar Cells. *Chem. Rev.* **2020,** *120*, 7867-7918.
5. Kojima, A.; Teshima, K.; Shirai, Y.; Miyasaka, T., Organometal Halide Perovskites as Visible-Light Sensitizers for Photovoltaic Cells. *J. Am. Chem. Soc.* **2009,** *131*, 6050-6051.
6. Im, J. H.; Lee, C. R.; Lee, J. W.; Park, S. W.; Park, N. G., 6.5% Efficient Perovskite Quantum-Dot-Sensitized Solar Cell. *Nanoscale* **2011,** *3*, 4088-4093.
7. Kim, H. S.; Lee, C. R.; Im, J. H.; Lee, K. B.; Moehl, T.; Marchioro, A.; Moon, S. J.; Humphry-Baker, R.; Yum, J. H.; Moser, J. E., et al., Lead Iodide Perovskite Sensitized All-Solid-State Submicron Thin Film Mesoscopic Solar Cell with Efficiency Exceeding 9%. *Sci. Rep.* **2012,** *2*, 591.
8. Liu, T. H.; Chen, K.; Hu, Q.; Zhu, R.; Gong, Q. H., Inverted Perovskite Solar Cells: Progresses and Perspectives. *Adv. Energy Mater.* **2016,** *6*, 1600457.
9. Wu, J.; Chen, P.; Xu, H.; Yu, M.; Li, L.; Yan, H.; Huangfu, Y.; Xiao, Y.; Yang, X.; Zhao, L., et al., Ultralight Flexible Perovskite Solar Cells. *Sci. China Mater.* **2022,** *65*, 2319-2324.
10. Príncipe, J.; Duarte, V. C. M.; Andrade, L., Inverted Perovskite Solar Cells: The Emergence of a Highly Stable and Efficient Architecture. *Energy Technology* **2022,** *10*, 2100952.
11. Lin, X.; Cui, D.; Luo, X.; Zhang, C.; Han, Q.; Wang, Y.; Han, L., Efficiency Progress of Inverted Perovskite Solar Cells. *Energy Environ. Sci.* **2020,** *13*, 3823-3847.
12. Zhu, R., Inverted Devices Are Catching Up. *Nat. Energy* **2020,** *5*, 123–124.
13. Tan, Q.; Li, Z.; Luo, G.; Zhang, X.; Che, B.; Chen, G.; Gao, H.; He, D.; Ma, G.; Wang, J., et al., Inverted Perovskite Solar Cells Using Dimethylacridine-Based Dopants. *Nature* **2023,** *620*, 545-551.
14. Zhang, S.; Ye, F.; Wang, X.; Chen, R.; Zhang, H.; Zhan, L.; Jiang, X.; Li, Y.; Ji, X.; Liu, S., et al., Minimizing Buried Interfacial Defects for Efficient Inverted Perovskite Solar Cells. *Science* **2023,** *380*, 404-409.
15. Park, J.; Kim, J.; Yun, H.-S.; Paik, M. J.; Noh, E.; Mun, H. J.; Kim, M. G.; Shin, T. J.; Seok, S. I., Controlled Growth of Perovskite Layers with Volatile Alkylammonium Chlorides. *Nature* **2023,** *616*, 724-730.
16. Azmi, R.; Ugur, E.; Seitkhan, A.; Aljamaan, F.; Subbiah, A. S.; Liu, J.; Harrison, G. T.; Nugraha, M. I.; Eswaran, M. K.; Babics, M., Damp Heat–Stable Perovskite

Solar Cells with Tailored-Dimensionality 2D/3D Heterojunctions. *Science* **2022,** *376*, 73-77.
17. Li, Z.; Li, B.; Wu, X.; Sheppard, S. A.; Zhang, S.; Gao, D.; Long, N. J.; Zhu, Z., Organometallic-Functionalized Interfaces for Highly Efficient Inverted Perovskite Solar Cells. *Science* **2022,** *376*, 416-420.
18. Liu, J.; Bastiani, M. D.; Aydin, E.; Harrison, G. T.; Gao, Y.; Pradhan, R. R.; Eswaran, M. K.; Mandal, M.; Yan, W.; Seitkhan, A., et al., Efficient and Stable Perovskite-Silicon Tandem Solar Cells through Contact Displacement by $MgF_x$. *Science* **2022,** *377*, 302-306.
19. NREL PV Research Cell Record Efficiency Chart; 2023. https://www.nrel.gov/pv/assets/pdfs/best-research-cell-efficiencies.pdf (accessed 11-29-2023).
20. Green, M. A.; Dunlop, E. D.; Yoshita, M.; Kopidakis, N.; Bothe, K.; Siefer, G.; Hao, X., Solar Cell Efficiency Tables (Version 62). *Prog. Photovolt. Res. Appl.* **2023,** *31*, 651-663.
21. Lee, J. W.; Tan, S.; Seok, S. I.; Yang, Y.; Park, N. G., Rethinking the a Cation in Halide Perovskites. *Science* **2022,** *375*, eabj1186.
22. Jeon, N. J.; Noh, J. H.; Yang, W. S.; Kim, Y. C.; Ryu, S.; Seo, J.; Seok, S. I., Compositional Engineering of Perovskite Materials for High-Performance Solar Cells. *Nature* **2015,** *517*, 476-480.
23. Li, H.; Zhang, C.; Gong, C.; Zhang, D.; Zhang, H.; Zhuang, Q.; Yu, X.; Gong, S.; Chen, X.; Yang, J., et al., 2D/3D Heterojunction Engineering at the Buried Interface Towards High-Performance Inverted Methylammonium-Free Perovskite Solar Cells. *Nat. Energy* **2023,** *8*, 946-955.
24. Saliba, M.; Matsui, T.; Seo, J. Y.; Domanski, K.; Correa-Baena, J. P.; Nazeeruddin, M. K.; Zakeeruddin, S. M.; Tress, W.; Abate, A.; Hagfeldt, A., et al., Cesium-Containing Triple Cation Perovskite Solar Cells: Improved Stability, Reproducibility and High Efficiency. *Energy Environ Sci* **2016,** *9*, 1989-1997.
25. Saliba, M.; Matsui, T.; Domanski, K.; Seo, J.-Y.; Ummadisingu, A.; Zakeeruddin, S. M.; Correa-Baena, J.-P.; Tress, W. R.; Abate, A.; Hagfeldt, A., Incorporation of Rubidium Cations into Perovskite Solar Cells Improves Photovoltaic Performance. *Science* **2016,** *354*, 206-209.
26. Turren-Cruz, S. H.; Hagfeldt, A.; Saliba, M., Methylammonium-Free, High-Performance, and Stable Perovskite Solar Cells on a Planar Architecture. *Science* **2018,** *362*, 449-453.
27. Wang, Z.; Zeng, L.; Zhu, T.; Chen, H.; Chen, B.; Kubicki, D. J.; Balvanz, A.; Li, C.; Maxwell, A.; Ugur, E., et al., Suppressed Phase Segregation for Triple-Junction Perovskite Solar Cells. *Nature* **2023**, DOI:10.1038/s41586-023-06006-7.
28. Nasti, G.; Abate, A., Tin Halide Perovskite ($ASnX_3$) Solar Cells: A Comprehensive Guide toward the Highest Power Conversion Efficiency. *Adv. Energy Mater.* **2019,** *10*, 1902467.
29. Chen, P.; Zhu, R., Overcoming the Performance Deadlock by Ideal-Bandgap

Perovskites. *Matter* **2021,** *4*, 1445-1447.
30. Shockley, W.; Queisser, H. J., Detailed Balance Limit of Efficiency of p-n Junction Solar Cells. *J. Appl. Phys.* **1961,** *32*, 510-519.
31. Zong, Y.; Wang, N.; Zhang, L.; Ju, M. G.; Zeng, X. C.; Sun, X. W.; Zhou, Y.; Padture, N. P., Homogenous Alloys of Formamidinium Lead Triiodide and Cesium Tin Triiodide for Efficient Ideal-Bandgap Perovskite Solar Cells. *Angew. Chem. Int. Ed.* **2017,** *56*, 12658-12662.
32. Gu, S.; Lin, R.; Han, Q.; Gao, Y.; Tan, H.; Zhu, J., Tin and Mixed Lead-Tin Halide Perovskite Solar Cells: Progress and Their Application in Tandem Solar Cells. *Adv. Mater.* **2020,** *32*, 1907392.
33. Jiang, T.; Chen, Z.; Chen, X.; Liu, T.; Chen, X.; Sha, W. E. I.; Zhu, H.; Yang, Y., Realizing High Efficiency over 20% of Low-Bandgap Pb–Sn-Alloyed Perovskite Solar Cells by in Situ Reduction of $Sn^{4+}$. *Solar RRL* **2019,** *4*, 1900467.
34. Lin, R. X.; Xiao, K.; Qin, Z. Y.; Han, Q. L.; Zhang, C. F.; Wei, M. Y.; Saidaminov, M. I.; Gao, Y.; Xu, J.; Xiao, M., et al., Monolithic All-Perovskite Tandem Solar Cells with 24.8% Efficiency Exploiting Comproportionation to Suppress Sn(II) Oxidation in Precursor Ink. *Nat. Energy* **2019,** *4*, 864-873.
35. Nakamura, T.; Yakumaru, S.; Truong, M. A.; Kim, K.; Liu, J.; Hu, S.; Otsuka, K.; Hashimoto, R.; Murdey, R.; Sasamori, T., et al., Sn(IV)-Free Tin Perovskite Films Realized by in Situ Sn(0) Nanoparticle Treatment of the Precursor Solution. *Nat. Commun.* **2020,** *11*, 3008.
36. Zhou, S.; Fu, S.; Wang, C.; Meng, W.; Zhou, J.; Zou, Y.; Lin, Q.; Huang, L.; Zhang, W.; Zeng, G., et al., Aspartate All-in-One Doping Strategy Enables Efficient All-Perovskite Tandems. *Nature* **2023**, DOI:10.1038/s41586-023-06707-z.
37. Zhou, X.; Zhang, L.; Wang, X.; Liu, C.; Chen, S.; Zhang, M.; Li, X.; Yi, W.; Xu, B., Highly Efficient and Stable GABr-Modified Ideal-Bandgap (1.35 eV) Sn/Pb Perovskite Solar Cells Achieve 20.63% Efficiency with a Record Small Voc Deficit of 0.33 V. *Adv. Mater.* **2020,** *32*, 1908107.
38. McMeekin, D. P.; Sadoughi, G.; Rehman, W.; Eperon, G. E.; Saliba, M.; Hörantner, M. T.; Haghighirad, A.; Sakai, N.; Korte, L.; Rech, B., A Mixed-Cation Lead Mixed-Halide Perovskite Absorber for Tandem Solar Cells. *Science* **2016,** *351*, 151-155.
39. Almora, O.; Baran, D.; Bazan, G. C.; Cabrera, C. I.; Erten-Ela, S.; Forberich, K.; Guo, F.; Hauch, J.; Ho-Baillie, A. W. Y.; Jacobsson, T. J., et al., Device Performance of Emerging Photovoltaic Materials (Version 3). *Adv. Energy Mater.* **2022,** *13*, 2203313.
40. Xu, J.; Boyd, C. C.; Yu, Z. J.; Palmstrom, A. F.; Witter, D. J.; Larson, B. W.; France, R. M.; Werner, J.; Harvey, S. P.; Wolf, E. J., et al., Triple-Halide Wide–Band Gap Perovskites with Suppressed Phase Segregation for Efficient Tandems. *Science* **2020,** *367*, 1097-1104.
41. Liu, X.; Luo, D.; Lu, Z. H.; Yun, J. S.; Saliba, M.; Seok, S. I.; Zhang, W., Stabilization of Photoactive Phases for Perovskite Photovoltaics. *Nat Rev Chem* **2023,**

*7*, 462-479.
42. Balakrishna, R. G.; Kobosko, S. M.; Kamat, P. V., Mixed Halide Perovskite Solar Cells. Consequence of Iodide Treatment on Phase Segregation Recovery. *ACS Energy Lett.* **2018,** *3*, 2267-2272.
43. Jiang, Q.; Chu, Z.; Wang, P.; Yang, X.; Liu, H.; Wang, Y.; Yin, Z.; Wu, J.; Zhang, X.; You, J., Planar-Structure Perovskite Solar Cells with Efficiency Beyond 21%. *Adv. Mater.* **2017,** *29*, 1703852.
44. Jacobsson, T. J.; Correa-Baena, J.-P.; Halvani Anaraki, E.; Philippe, B.; Stranks, S. D.; Bouduban, M. E. F.; Tress, W.; Schenk, K.; Teuscher, J.; Moser, J.-E., et al., Unreacted $PbI_2$ as a Double-Edged Sword for Enhancing the Performance of Perovskite Solar Cells. *J. Am. Chem. Soc.* **2016,** *138*, 10331-10343.
45. Roldán-Carmona, C.; Gratia, P.; Zimmermann, I.; Grancini, G.; Gao, P.; Graetzel, M.; Nazeeruddin, M. K., High Efficiency Methylammonium Lead Triiodide Perovskite Solar Cells: The Relevance of Non-Stoichiometric Precursors. *Energy Environ. Sci.* **2015,** *8*, 3550-3556.
46. Zhang, D.; Zhang, H.; Guo, H.; Ye, F.; Liu, S.; Wu, Y., Stable α-$FAPbI_3$ in Inverted Perovskite Solar Cells with Efficiency Exceeding 22% Via a Self-Passivation Strategy. *Adv. Funct. Mater.* **2022,** *32*, 2200174.
47. Roose, B.; Dey, K.; Chiang, Y. H.; Friend, R. H.; Stranks, S. D., Critical Assessment of the Use of Excess Lead Iodide in Lead Halide Perovskite Solar Cells. *J. Phys. Chem. Lett.* **2020,** *11*, 6505-6512.
48. Guo, R.; Han, D.; Chen, W.; Dai, L.; Ji, K.; Xiong, Q.; Li, S.; Reb, L. K.; Scheel, M. A.; Pratap, S., et al., Degradation Mechanisms of Perovskite Solar Cells under Vacuum and One Atmosphere of Nitrogen. *Nat. Energy* **2021,** *6*, 977-986.
49. Zhao, L.; Li, Q.; Hou, C.-H.; Li, S.; Yang, X.; Wu, J.; Zhang, S.; Hu, Q.; Wang, Y.; Zhang, Y., et al., Chemical Polishing of Perovskite Surface Enhances Photovoltaic Performances. *J. Am. Chem. Soc.* **2022,** *144*, 1700-1708.
50. Chen, H.; Liu, C.; Xu, J.; Maxwell, A.; Zhou, W.; Yang, Y.; Zhou, Q.; Bati, A. S. R.; Wan, H.; Wang, Z., et al., Improved Charge Extraction in Inverted Perovskite Solar Cells with Dual-Site-Binding Ligands. *Science* **2024,** *384*, 189-193.
51. Liu, C.; Yang, Y.; Chen, H.; Xu, J.; Liu, A.; Bati, A. S. R.; Zhu, H.; Grater, L.; Hadke, S. S.; Huang, C., et al., Bimolecularly Passivated Interface Enables Efficient and Stable Inverted Perovskite Solar Cells. *Science* **2023,** *382*, 810-815.
52. Zheng, Y.; Li, Y.; Zhuang, R.; Wu, X.; Tian, C.; Sun, A.; Chen, C.; Guo, Y.; Hua, Y.; Meng, K., et al., Towards 26% Efficiency in Inverted Perovskite Solar Cells Via Interfacial Flipped Band Bending and Suppressed Deep-Level Traps. *Energy Environ. Sci.* **2024**, DOI: 0.1039/d3ee03435f.
53. Li, B.; Gao, D.; Sheppard, S. A.; Tremlett, W. D. J.; Liu, Q.; Li, Z.; White, A. J. P.; Brown, R. K.; Sun, X.; Gong, J., et al., Highly Efficient and Scalable p-i-n Perovskite Solar Cells Enabled by Poly-Metallocene Interfaces. *J. Am. Chem. Soc.* **2024**, DOI:10.1021/jacs.4c02220.
54. Liang, Z.; Zhang, Y.; Xu, H.; Chen, W.; Liu, B.; Zhang, J.; Zhang, H.; Wang, Z.;

Kang, D.-H.; Zeng, J., et al., Homogenizing out-of-Plane Cation Composition in Perovskite Solar Cells. *Nature* **2023,** *624*, 557-563.
55. Li, J.; Liang, H.; Xiao, C.; Jia, X.; Guo, R.; Chen, J.; Guo, X.; Luo, R.; Wang, X.; Li, M., et al., Enhancing the Efficiency and Longevity of Inverted Perovskite Solar Cells with Antimony-Doped Tin Oxides. *Nat. Energy* **2024,** *9*, 308-315.
56. Li, Z.; Sun, X.; Zheng, X.; Li, B.; Gao, D.; Zhang, S.; Wu, X.; Li, S.; Gong, J.; Luther, J. M., et al., Stabilized Hole-Selective Layer for High-Performance Inverted p-i-n Perovskite Solar Cells. *Science* **2023,** *382*, 284-289.
57. Peng, W.; Mao, K.; Cai, F.; Meng, H.; Zhu, Z.; Li, T.; Yuan, S.; Xu, Z.; Feng, X.; Xu, J., et al., Reducing Nonradiative Recombination in Perovskite Solar Cells with a Porous Insulator Contact. *Science* **2023,** *379*, 683-690.
58. Yu, S.; Xiong, Z.; Zhou, H.; Zhang, Q.; Wang, Z.; Ma, F.; Qu, Z.; Zhao, Y.; Chu, X.; Zhang, X., et al., Homogenized NiOx Nanoparticles for Improved Hole Transport in Inverted Perovskite Solar Cells. *Science* **2023,** *382*, 1399-1404.
59. Jiang, Q.; Tong, J.; Xian, Y.; Kerner, R. A.; Dunfield, S. P.; Xiao, C.; Scheidt, R. A.; Kuciauskas, D.; Wang, X.; Hautzinger, M. P., et al., Surface Reaction for Efficient and Stable Inverted Perovskite Solar Cells. *Nature* **2022,** *611*, 278-283.
60. Pan, X.; Xu, H.; Liang, Z.; Ye, J.; Zhang, Y.; Wang, Z.; Zhang, H.; Wan, C.; Xu, G.; Zeng, J., et al., Constructing Robust Heterointerface for Carrier Viaduct Via Interfacial Molecular Bridge Enables Efficient and Stable Inverted Perovskite Solar Cell. *Energy Environ. Sci.* **2023**, DOI:10.1039/d3ee02591h.
61. Park, S. M.; Wei, M.; Lempesis, N.; Yu, W.; Hossain, T.; Agosta, L.; Carnevali, V.; Atapattu, H. R.; Serles, P.; Eickemeyer, F. T., et al., Low-Loss Contacts on Textured Substrates for Inverted Perovskite Solar Cells. *Nature* **2023,** *624*, 289-294.
62. Fei, C.; Li, N.; Wang, M.; Wang, X.; Gu, H.; Chen, B.; Zhang, Z.; Ni, Z.; Jiao, H.; Xu, W., et al., Lead-Chelating Hole-Transport Layers for Efficient and Stable Perovskite Minimodules. *Science* **2023,** *380*, 823-829.
63. Li, G.; Su, Z.; Canil, L.; Hughes, D.; Aldamasy, M. H.; Dagar, J.; Trofimov, S.; Wang, L.; Zuo, W.; Jerónimo-Rendon, J. J., et al., Highly Efficient p-i-n Perovskite Solar Cells That Endure Temperature Variations. *Science* **2023,** *379*, 399-403.
64. Zheng, X. P.; Li, Z.; Zhang, Y.; Chen, M.; Liu, T.; Xiao, C. X.; Gao, D. P.; Patel, J. B.; Kuciauskas, D.; Magomedov, A., et al., Co-Deposition of Hole-Selective Contact and Absorber for Improving the Processability of Perovskite Solar Cells. *Nat. Energy* **2023,** *8*, 462.
65. Li, C.; Wang, X.; Bi, E.; Jiang, F.; Park, S. M.; Li, Y.; Chen, L.; Wang, Z.; Zeng, L.; Chen, H., et al., Rational Design of Lewis Base Molecules for Stable and Efficient Inverted Perovskite Solar Cells. *Science* **2023,** *379*, 690-694.
66. Li, X.; Zhang, W.; Guo, X.; Lu, C.; Wei, J.; Fang, J., Constructing Heterojunctions by Surface Sulfidation for Efficient Inverted Perovskite Solar Cells. *Science* **2022,** *375*, 434-437.
67. Chen, H.; Teale, S.; Chen, B.; Hou, Y.; Grater, L.; Zhu, T.; Bertens, K.; Park, S. M.; Atapattu, H. R.; Gao, Y. J., et al., Quantum-Size-Tuned Heterostructures Enable

Efficient and Stable Inverted Perovskite Solar Cells. *Nat. Photonics* **2022,** *16*, 352.
68. Chen, S.; Dai, X.; Xu, S.; Jiao, H.; Zhao, L.; Huang, J., Stabilizing Perovskite-Substrate Interfaces for High-Performance Perovskite Modules. *Science* **2021,** *373*, 902-907.
69. Luo, X.; Shen, Z.; Shen, Y.; Su, Z.; Gao, X.; Wang, Y.; Han, Q.; Han, L., Effective Passivation with Self-Organized Molecules for Perovskite Photovoltaics. *Adv. Mater.* **2022,** *34*, 2202100.
70. Degani, M.; An, Q.; Albaladejo-Siguan, M.; Hofstetter, Y. J.; Cho, C.; Paulus, F.; Grancini, G.; Vaynzof, Y., 23.7% Efficient Inverted Perovskite Solar Cells by Dual Interfacial Modification. *Sci. Adv.* **2021,** *7*, eabj7930.
71. Hu, S.; Otsuka, K.; Murdey, R.; Nakamura, T.; Truong, M. A.; Yamada, T.; Handa, T.; Matsuda, K.; Nakano, K.; Sato, A., et al., Optimized Carrier Extraction at Interfaces for 23.6% Efficient Tin–Lead Perovskite Solar Cells. *Energy Environ. Sci.* **2022,** *15*, 2096-2107.
72. Deng, X.; Qi, F.; Li, F.; Wu, S.; Lin, F. R.; Zhang, Z.; Guan, Z.; Yang, Z.; Lee, C. S.; Jen, A. K., Co-Assembled Monolayers as Hole-Selective Contact for High-Performance Inverted Perovskite Solar Cells with Optimized Recombination Loss and Long-Term Sstability. *Angew. Chem. Int. Ed.* **2022,** *61*, 202203088.
73. Li, M.; Li, H.; Zhuang, Q.; He, D.; Liu, B.; Chen, C.; Zhang, B.; Pauporté, T.; Zang, Z.; Chen, J., Stabilizing Perovskite Precursor by Synergy of Functional Groups for $NiO_x$-Based Inverted Solar Cells with 23.5% Efficiency. *Angew. Chem. Int. Ed.* **2022,** *61*, e202206914.
74. Cao, Q.; Li, Y.; Zhang, Y.; Zhao, J.; Wang, T.; Yang, B.; Pu, X.; Yang, J.; Chen, H.; Chen, X., et al., N‐Type Conductive Small Molecule Assisted 23.5% Efficient Inverted Perovskite Solar Cells. *Adv. Energy Mater.* **2022,** *12*, 2201435.
75. Li, F.; Deng, X.; Qi, F.; Li, Z.; Liu, D.; Shen, D.; Qin, M.; Wu, S.; Lin, F.; Jang, S. H., et al., Regulating Surface Termination for Efficient Inverted Perovskite Solar Cells with Greater Than 23% Efficiency. *J. Am. Chem. Soc.* **2020,** *142*, 20134-20142.
76. Kapil, G.; Bessho, T.; Sanehira, Y.; Sahamir, S. R.; Chen, M.; Baranwal, A. K.; Liu, D.; Sono, Y.; Hirotani, D.; Nomura, D., et al., Tin–Lead Perovskite Solar Cells Fabricated on Hole Selective Monolayers. *ACS Energy Lett.* **2022,** *7*, 966-974.
77. Zheng, X. P.; Hou, Y.; Bao, C. X.; Yin, J.; Yuan, F. L.; Huang, Z. R.; Song, K. P.; Liu, J. K.; Troughton, J.; Gasparini, N., et al., Managing Grains and Interfaces Via Ligand Anchoring Enables 22.3%-Efficiency Inverted Perovskite Solar Cells. *Nat. Energy* **2020,** *5*, 131-140.
78. Siekmann, J.; Ravishankar, S.; Kirchartz, T., Apparent Defect Densities in Halide Perovskite Thin Films and Single Crystals. *ACS Energy Lett.* **2021,** *6*, 3244-3251.
79. Zhang, F.; Zhu, K., Additive Engineering for Efficient and Stable Perovskite Solar Cells. *Adv. Energy Mater.* **2019,** *10*, 1902579.
80. Yin, W.-J.; Shi, T.; Yan, Y., Unusual Defect Physics in $CH_3NH_3PbI_3$ Perovskite Solar Cell Absorber. *Appl. Phys. Lett.* **2014,** *104*, 063903.
81. Ma, Y.; Zhang, S.; Yi, Y.; Zhang, L.; Hu, R.; Liu, W.; Du, M.; Chu, L.; Zhang, J.;

Li, X. a., et al., Deep Level Defects Passivated by Small Molecules for the Enhanced Efficiency and Stability of Inverted Perovskite Solar Cells. *J. Mater. Chem. C* **2022,** *10*, 5922-5928.
82. Ran, C.; Xu, J.; Gao, W.; Huang, C.; Dou, S., Defects in Metal Triiodide Perovskite Materials Towards High-Performance Solar Cells: Origin, Impact, Characterization, and Engineering. *Chem Soc Rev* **2018,** *47*, 4581–4610.
83. Zhang, H.; Pfeifer, L.; Zakeeruddin, S. M.; Chu, J.; Grätzel, M., Tailoring Passivators for Highly Efficient and Stable Perovskite Solar Cells. *Nat. Rev. Chem.* **2023,** *7*, 632–652.
84. Zheng, X.; Chen, B.; Dai, J.; Fang, Y.; Bai, Y.; Lin, Y.; Wei, H.; Zeng, Xiao C.; Huang, J., Defect Passivation in Hybrid Perovskite Solar Cells Using Quaternary Ammonium Halide Anions And cations. *Nat. Energy* **2017,** *2*, 17102.
85. Han, T. H.; Lee, J. W.; Choi, C.; Tan, S.; Lee, C.; Zhao, Y. P.; Dai, Z. H.; De Marco, N.; Lee, S. J.; Bae, S. H., et al., Perovskite-Polymer Composite Cross-Linker Approach for Highly-Stable and Efficient Perovskite Solar Cells. *Nat. Commun.* **2019,** *10*, 520.
86. Bi, D.; Yi, C.; Luo, J.; Décoppet, J.-D.; Zhang, F.; Zakeeruddin, Shaik M.; Li, X.; Hagfeldt, A.; Grätzel, M., Polymer-Templated Nucleation and Crystal Growth of Perovskite Films for Solar Cells with Efficiency Greater Than 21%. *Nat. Energy* **2016,** *1*, 16142.
87. Hu, Q.; Chen, W.; Yang, W.; Li, Y.; Zhou, Y.; Larson, B. W.; Johnson, J. C.; Lu, Y.-H.; Zhong, W.; Xu, J., et al., Improving Efficiency and Stability of Perovskite Solar Cells Enabled by a near-Infrared-Absorbing Moisture Barrier. *Joule* **2020,** *4*, 1575-1593.
88. Yang, X.; Luo, D.; Xiang, Y.; Zhao, L.; Anaya, M.; Shen, Y.; Wu, J.; Yang, W.; Chiang, Y. H.; Tu, Y., et al., Buried Interfaces in Halide Perovskite Photovoltaics. *Adv. Mater.* **2021,** *33*, 2006435.
89. Son, D. Y.; Kim, S. G.; Seo, J. Y.; Lee, S. H.; Shin, H.; Lee, D.; Park, N. G., Universal Approach toward Hysteresis-Free Perovskite Solar Cell Via Defect Engineering. *J. Am. Chem. Soc.* **2018,** *140*, 1358-1364.
90. Su, R.; Xu, Z.; Wu, J.; Luo, D.; Hu, Q.; Yang, W.; Yang, X.; Zhang, R.; Yu, H.; Russell, T. P., et al., Dielectric Screening in Perovskite Photovoltaics. *Nat. Commun.* **2021,** *12*, 2479.
91. Zhu, H.; Teale, S.; Lintangpradipto, M. N.; Mahesh, S.; Chen, B.; McGehee, M. D.; Sargent, E. H.; Bakr, O. M., Long-Term Operating Stability in Perovskite Photovoltaics. *Nat. Rev. Mater.* **2023,** *8*, 569-586.
92. Wang, S.; Zhang, Z.; Tang, Z.; Su, C.; Huang, W.; Li, Y.; Xing, G., Polymer Strategies for High-Efficiency and Stable Perovskite Solar Cells. *Nano Energy* **2021,** *82*, 105712.
93. Cao, Q.; Li, Y. J.; Zhang, H.; Yang, J. B.; Han, J.; Xu, T.; Wang, S. J.; Wang, Z. S.; Gao, B. Y.; Zhao, J. S., et al., Efficient and Stable Inverted Perovskite Solar Cells with Very High Fill Factors Via Incorporation of Star-Shaped Polymer. *Sci. Adv.* **2021,** *7*,

eabg0633.
94. Park, K.; Lee, J. H.; Lee, J. W., Surface Defect Engineering of Metal Halide Perovskites for Photovoltaic Applications. *ACS Energy Lett.* **2022,** *7*, 1230-1239.
95. Krishna, A.; Gottis, S.; Nazeeruddin, M. K.; Sauvage, F., Mixed Dimensional 2D/3D Hybrid Perovskite Absorbers: The Future of Perovskite Solar Cells? *Adv. Funct. Mater.* **2019,** *29*, 1806482.
96. Mao, L.; Stoumpos, C. C.; Kanatzidis, M. G., Two-Dimensional Hybrid Halide Perovskites: Principles and Promises. *J. Am. Chem. Soc.* **2019,** *141*, 1171-1190.
97. Wang, X.; Rakstys, K.; Jack, K.; Jin, H.; Lai, J.; Li, H.; Ranasinghe, C. S. K.; Saghaei, J.; Zhang, G.; Burn, P. L., et al., Engineering Fluorinated-Cation Containing Inverted Perovskite Solar Cells with an Efficiency of >21% and Improved Stability Towards Humidity. *Nat. Commun.* **2021,** *12*, 52.
98. Odysseas Kosmatos, K.; Theofylaktos, L.; Giannakaki, E.; Deligiannis, D.; Konstantakou, M.; Stergiopoulos, T., Methylammonium Chloride: A Key Additive for Highly Efficient, Stable, and up‐Scalable Perovskite Solar Cells. *Energy Environ. Mater.* **2019,** *2*, 79-92.
99. Kim, M.; Kim, G. H.; Lee, T. K.; Choi, I. W.; Choi, H. W.; Jo, Y.; Yoon, Y. J.; Kim, J. W.; Lee, J.; Huh, D., et al., Methylammonium Chloride Induces Intermediate Phase Stabilization for Efficient Perovskite Solar Cells. *Joule* **2019,** *3*, 2179-2192.
100. Wang, M.; Shi, Z.; Fei, C.; Deng, Z. J. D.; Yang, G.; Dunfield, S. P.; Fenning, D. P.; Huang, J., Ammonium Cations with High Pka in Perovskite Solar Cells for Improved High-Temperature Photostability. *Nat. Energy* **2023,** *8*, 1229-1239.
101. Bai, S.; Da, P.; Li, C.; Wang, Z.; Yuan, Z.; Fu, F.; Kawecki, M.; Liu, X.; Sakai, N.; Wang, J. T., et al., Planar Perovskite Solar Cells with Long-Term Stability Using Ionic Liquid Additives. *Nature* **2019,** *571*, 245-250.
102. Wang, Y.; Chao, L.; Niu, T.; Li, D.; Wei, Q.; Wu, H.; Qiu, J.; Lu, H.; Ran, C.; Zhong, Q., et al., Efficient and Stable Perovskite Solar Cells by Fluorinated Ionic Lquid–Induced Component Interaction. *Solar RRL* **2020,** *5*, 2000582.
103. Caprioglio, P.; Cruz, D. S.; Caicedo-Davila, S.; Zu, F. S.; Sutanto, A. A.; Pena-Camargo, F.; Kegelmann, L.; Meggiolaro, D.; Gregori, L.; Wolff, C. M., et al., Bi-Functional Interfaces by Poly(Ionic Liquid) Treatment in Efficient pin and nip Perovskite Solar Cells. *Energy Environ. Sci.* **2021,** *14*, 4508-4522.
104. Li, D.; Huang, Y.; Wang, G.; Lian, Q.; Shi, R.; Zhang, L.; Wang, X.; Gao, F.; Kong, W.; Xu, B., et al., Boosting the Performance of MA-Free Inverted Perovskite Solar Cells Via Multifunctional Ion Liquid. *J. Mater. Chem. A* **2021,** *9*, 12746-12754.
105. Rezaee, E.; Zhang, W.; Silva, S. R. P., Solvent Engineering as a Vehicle for High Quality Thin Films of Perovskites and Their Device Fabrication. *Small* **2021,** *17*, 2008145.
106. Yang, W. S.; Noh, J. H.; Jeon, N. J.; Kim, Y. C.; Ryu, S.; Seo, J.; Seok, S. I., High-Performance Photovoltaic Perovskite Layers Fabricated through Intramolecular Exchange. *Science* **2015,** *348*, 1234-1237.
107. Lee, J. W.; Kim, H. S.; Park, N. G., Lewis Acid-Base Adduct Approach for

High Efficiency Perovskite Solar Cells. *Acc. Chem. Res.* **2016,** *49*, 311-319.
108. Lee, S. H.; Hong, S.; Kim, H. J., Selection of a Suitable Solvent Additive for 2-Methoxyethanol-Based Antisolvent-Free Perovskite Film Fabrication. *ACS Appl. Mater. Interfaces* **2022,** *14*, 39132-39140.
109. Park, N.-G., Green Solvent for Perovskite Solar Cell Production. *Nat. Sustain.* **2020,** *4*, 192-193.
110. Vidal, R.; Alberola-Borràs, J.-A.; Habisreutinger, S. N.; Gimeno-Molina, J.-L.; Moore, D. T.; Schloemer, T. H.; Mora-Seró, I.; Berry, J. J.; Luther, J. M., Assessing Health and Environmental Impacts of Solvents for Producing Perovskite Solar Cells. *Nat. Sustain.* **2020,** *4*, 277-285.
111. Miao, Y.; Ren, M.; Chen, Y.; Wang, H.; Chen, H.; Liu, X.; Wang, T.; Zhao, Y., Green Solvent Enabled Scalable Processing of Perovskite Solar Cells with High Efficiency. *Nat. Sustain.* **2023**, DOI:10.1038/s41893-023-01196-4.
112. Yun, H.-S.; Kwon, H. W.; Paik, M. J.; Hong, S.; Kim, J.; Noh, E.; Park, J.; Lee, Y.; Il Seok, S., Ethanol-Based Green-Solution Processing of A-Formamidinium Lead Triiodide Perovskite Layers. *Nat. Energy* **2022,** *7*, 828-834.
113. Wang, F.; Duan, D.; Singh, M.; Sutter‐Fella, C. M.; Lin, H.; Li, L.; Naumov, P.; Hu, H., Ionic Liquid Engineering in Perovskite Photovoltaics. *Energy & Environmental Materials* **2023,** *6*, e12435.
114. Moore, D. T.; Tan, K. W.; Sai, H.; Barteau, K. P.; Wiesner, U.; Estroff, L. A., Direct Crystallization Route to Methylammonium Lead Iodide Perovskite from an Ionic Liquid. *Chem. Mater.* **2015,** *27*, 3197-3199.
115. Hui, W.; Chao, L.; Lu, H.; Xia, F.; Huang, W., Stabilizing Black-Phase Formamidinium Perovskite Formation at Room Temperature and High Humidity. *Science* **2021,** *371*, 1359-1364.
116. Liang, C.; Gu, H.; Xia, Y.; Wang, Z.; Liu, X.; Xia, J.; Zuo, S.; Hu, Y.; Gao, X.; Hui, W., et al., Two-Dimensional Ruddlesden–Popper Layered Perovskite Solar Cells Based on Phase-Pure Thin Films. *Nat. Energy* **2020,** *6*, 38-45.
117. Xu, W.; Gao, Y.; Ming, W.; He, F.; Li, J.; Zhu, X. H.; Kang, F.; Li, J.; Wei, G., Suppressing Defects-Induced Nonradiative Recombination for Efficient Perovskite Solar Cells through Green Antisolvent Engineering. *Adv. Mater.* **2020,** *32*, e2003965.
118. Deng, Y.; Van Brackle, C. H.; Dai, X.; Zhao, J.; Chen, B.; Huang, J., Tailoring Solvent Coordination for High-Speed, Room-Temperature Blading of Perovskite Photovoltaic Films. *Sci. Adv.* **2019,** *5*, eaax7537.
119. Du, M.; Zhao, S.; Duan, L.; Cao, Y.; Wang, H.; Sun, Y.; Wang, L.; Zhu, X.; Feng, J.; Liu, L., et al., Surface Redox Engineering of Vacuum-Deposited $NiO_x$ for Top-Performance Perovskite Solar Cells and Modules. *Joule* **2022,** *6*, 1931-1943.
120. Bu, T.; Li, J.; Li, H.; Tian, C.; Huang, F., Lead Halide–Templated Crystallization of Methylamine-Free Perovskite for Efficient Photovoltaic Modules. *Science* **2021,** *372*, 1327-1332.
121. Hamill, J. C.; Schwartz, J.; Loo, Y.-L., Influence of Solvent Coordination on Hybrid Organic–Inorganic Perovskite Formation. *ACS Energy Lett.* **2017,** *3*, 92-97.

122. Sidhik, S.; Wang, Y.; De Siena, M.; Asadpour, R.; Torma, A. J.; Terlier, T.; Ho, K.; Li, W.; Puthirath, A. B.; Shuai, X., et al., Deterministic Fabrication of 3D/2D Perovskite Bilayer Stacks for Durable and Efficient Solar Cells. *Science* **2022,** *377*, 1425-1430.
123. Bautista-Quijano, J. R.; Telschow, O.; Paulus, F.; Vaynzof, Y., Solvent–Antisolvent Interactions in Metal Halide Perovskites. *Chem. Commun.* **2023,** *59*, 10588-10603.
124. Jeon, N. J.; Noh, J. H.; Kim, Y. C.; Yang, W. S.; Ryu, S.; Seok, S. I., Solvent Engineering for High-Performance Inorganic-Organic Hybrid Perovskite Solar Cells. *Nat. Mater.* **2014,** *13*, 897-903.
125. Nie, W.; Tsai, H.; Asadpour, R.; Blancon, J. C.; Neukirch, A. J.; Gupta, G.; Crochet, J. J.; Chhowalla, M.; Tretiak, S.; Alam, M. A., et al., High-Efficiency Solution-Processed Perovskite Solar Cells with Millimeter-Scale Grains. *Science* **2015,** *347*, 522-525.
126. Brinkmann, K. O.; He, J.; Schubert, F.; Malerczyk, J.; Kreusel, C.; van gen Hassend, F.; Weber, S.; Song, J.; Qu, J.; Riedl, T., Extremely Robust Gas-Quenching Deposition of Halide Perovskites on Top of Hydrophobic Hole Transport Materials for Inverted (P–I–N) Solar Cells by Targeting the Precursor Wetting Issue. *ACS Appl. Mater. Interfaces* **2019,** *11*, 40172-40179.
127. Babayigit, A.; D'Haen, J.; Boyen, H.-G.; Conings, B., Gas Quenching for Perovskite Thin Film Deposition. *Joule* **2018,** *2*, 1205-1209.
128. Li, X.; Bi, D.; Yi, C.; Décoppet, J.-D.; Luo, J.; Zakeeruddin, S. M.; Hagfeldt, A.; Grätzel, M., A Vacuum Flash–Assisted Solution Process for High-Efficiency Large-Area Perovskite Solar Cells. *Science* **2016,** *353*, 58-62.
129. Le, T. H.; Driscoll, H.; Hou, C. H.; Montgomery, A.; Li, W.; Stein, J. S.; Nie, W., Perovskite Solar Module: Promise and Challenges in Efficiency, Meta‐Stability, and Operational Lifetime. *Adv. Electron. Mater.* **2023,** *9*.
130. Han, Y.; Xie, H.; Lim, E. L.; Bi, D., Review of Two‐Step Method for Lead Halide Perovskite Solar Cells. *Solar RRL* **2022,** *6*, 2101007.
131. Tan, L.; Zhou, J.; Zhao, X.; Wang, S.; Li, M.; Jiang, C.; Li, H.; Zhang, Y.; Ye, Y.; Tress, W., et al., Combined Vacuum Evaporation and Solution Process for High Efficiency Large‐Area Perovskite Solar Cells with Exceptional Reproducibility. *Adv. Mater.* **2023**, 2205027.
132. Mao, L.; Yang, T.; Zhang, H.; Shi, J.; Hu, Y.; Zeng, P.; Li, F.; Gong, J.; Fang, X.; Sun, Y., et al., Fully Textured, Production‐Line Compatible Monolithic Perovskite/Silicon Tandem Solar Cells Approaching 29% Efficiency. *Adv. Mater.* **2022,** *34*, 2206193.
133. Huang, Z.; Bai, Y.; Huang, X.; Li, J.; Wu, Y.; Chen, Y.; Li, K.; Niu, X.; Li, N.; Liu, G., et al., Anion–Π Interactions Suppress Phase Impurities in $FAPbI_3$ Solar Cells. *Nature* **2023,** *623*, 531-537.
134. Chen, P.; Xiao, Y.; Li, L.; Zhao, L.; Yu, M.; Li, S.; Hu, J.; Liu, B.; Yang, Y.; Luo, D., et al., Efficient Inverted Perovskite Solar Cells Via Improved Sequential

Deposition. *Adv. Mater.* **2022,** *35*, 2206345.
135. Alsalloum, A. Y.; Turedi, B.; Almasabi, K.; Zheng, X.; Naphade, R.; Stranks, S. D.; Mohammed, O. F.; Bakr, O. M., 22.8%-Efficient Single-Crystal Mixed-Cation Inverted Perovskite Solar Cells with a near-Optimal Bandgap. *Energy Environ. Sci.* **2021,** *14*, 2263-2268.
136. Alsalloum, A. Y.; Turedi, B.; Zheng, X.; Mitra, S.; Zhumekenov, A. A.; Lee, K. J.; Maity, P.; Gereige, I.; AlSaggaf, A.; Roqan, I. S., et al., Low-Temperature Crystallization Enables 21.9% Efficient Single-Crystal $MAPbI_3$ Inverted Perovskite Solar Cells. *ACS Energy Lett.* **2020,** *5*, 657-662.
137. Li, N.; Feng, A.; Guo, X.; Wu, J.; Xie, S.; Lin, Q.; Jiang, X.; Liu, Y.; Chen, Z.; Tao, X., Engineering the Hole Extraction Interface Enables Single-Crystal $MAPbI_3$ Perovskite Solar Cells with Efficiency Exceeding 22% and Superior Indoor Response. *Adv. Energy Mater.* **2022,** *12*, 2103241.
138. Lintangpradipto, M. N.; Zhu, H.; Shao, B.; Mir, W. J.; Gutiérrez-Arzaluz, L.; Turedi, B.; Abulikemu, M.; Mohammed, O. F.; Bakr, O. M., Single-Crystal Methylammonium-Free Perovskite Solar Cells with Efficiencies Exceeding 24% and High Thermal Stability. *ACS Energy Lett.* **2023,** *8*, 4915-4922.
139. Zhang, J.; McGettrick, J.; Ji, K.; Bi, J.; Webb, T.; Liu, X.; Liu, D.; Ren, A.; Xiang, Y.; Li, B., et al., Fast and Balanced Charge Transport Enabled by Solution-Processed Metal Oxide Layers for Efficient And stable Inverted Perovskite Solar Cells. *Energy & Environmental Materials* **2023,** *0*, e12595.
140. Pham, H. D.; Li, X. Q.; Li, W. H.; Manzhos, S.; Kyaw, A. K. K.; Sonar, P., Organic Interfacial Materials for Perovskite-Based Optoelectronic Devices. *Energy Environ. Sci.* **2019,** *12*, 1177-1209.
141. Wu, Y.; Yang, X.; Chen, W.; Yue, Y.; Cai, M.; Xie, F.; Bi, E.; Islam, A.; Han, L., Perovskite Solar Cells with 18.21% Efficiency and Area over 1 $cm^2$ Fabricated by Heterojunction Engineering. *Nat. Energy* **2016,** *1*, 16148.
142. Jiang, X.; Wang, F.; Wei, Q.; Li, H.; Shang, Y.; Zhou, W.; Wang, C.; Cheng, P.; Chen, Q.; Chen, L., et al., Ultra-High Open-Circuit Voltage of Tin Perovskite Solar Cells Via an Electron Transporting Layer Design. *Nat. Commun.* **2020,** *11*, 1245.
143. Yu, B. B.; Chen, Z.; Zhu, Y.; Wang, Y.; Han, B.; Chen, G.; Zhang, X.; Du, Z.; He, Z., Heterogeneous 2D/3D Tin-Halides Perovskite Solar Cells with Certified Conversion Efficiency Breaking 14%. *Adv. Mater.* **2021,** *33*, 2102055.
144. Zheng, X.; Jiang, T.; Bai, L.; Chen, X.; Chen, Z.; Xu, X.; Song, D.; Xu, X.; Li, B.; Yang, Y. M., Enhanced Thermal Stability of Inverted Perovskite Solar Cells by Interface Modification and Additive Strategy. *RSC Adv.* **2020,** *10*, 18400-18406.
145. Li, Z.; Zhao, Y.; Wang, X.; Sun, Y.; Zhao, Z.; Li, Y.; Zhou, H.; Chen, Q., Cost Analysis of Perovskite Tandem Photovoltaics. *Joule* **2018,** *2*, 1559-1572.
146. Meyer, J.; Hamwi, S.; Kröger, M.; Kowalsky, W.; Riedl, T.; Kahn, A., Transition Metal Oxides for Organic Electronics: Energetics, Device Physics and Applications. *Adv. Mater.* **2012,** *24*, 5408-5427.
147. Ma, F.; Zhao, Y.; Li, J.; Zhang, X.; Gu, H.; You, J., Nickel Oxide for Inverted

Structure Perovskite Solar Cells. *J. Energy Chem.* **2021,** *52*, 393-411.
148. Tiwari, N.; Arianita Dewi, H.; Erdenebileg, E.; Narayan Chauhan, R.; Mathews, N.; Mhaisalkar, S.; Bruno, A., Advances and Potentials of $NiO_x$ Surface Teatments for p-i-n Perovskite Solar Cells. *Solar RRL* **2021,** *6*, 2100700.
149. Wang, R.; Dong, X.; Liu, Y., Recent Progress of Inorganic Hole‐Transport Materials for Perovskite Solar Cells†. *Chin. J. Chem* . **2023,** *41*, 3373-3387.
150. Chen, W.; Wu, Y.; Yue, Y.; Liu, J.; Zhang, W.; Yang, X.; Chen, H.; Bi, E.; Ashraful, I.; Gratzel, M., et al., Efficient and Stable Large-Area Perovskite Solar Cells with Inorganic Charge Extraction Layers. *Science* **2015,** *350*, 944-948.
151. Chen, W.; Liu, F. Z.; Feng, X. Y.; Djurisic, A. B.; Chan, W. K.; He, Z. B., Cesium Doped NiOx as an Efficient Hole Extraction Layer for Inverted Planar Perovskite Solar Cells. *Adv. Energy Mater.* **2017,** *7*, 1700722.
152. Kim, J. H.; Liang, P. W.; Williams, S. T.; Cho, N.; Chueh, C. C.; Glaz, M. S.; Ginger, D. S.; Jen, A. K., High-Performance and Environmentally Stable Planar Heterojunction Perovskite Solar Cells Based on a Solution-Processed Copper-Doped Nickel Oxide Hole-Transporting Layer. *Adv. Mater.* **2015,** *27*, 695-701.
153. Chen, W.; Wu, Y. H.; Fan, J.; Djurisic, A. B.; Liu, F. Z.; Tam, H. W.; Ng, A.; Surya, C.; Chan, W. K.; Wang, D., et al., Understanding the Doping Effect on Nio: Toward High-Performance Inverted Perovskite Solar Cells. *Adv. Energy Mater.* **2018,** *8*, 1703519.
154. Chen, W.; Han, B.; Hu, Q.; Gu, M.; Zhu, Y.; Yang, W.; Zhou, Y.; Luo, D.; Liu, F.-Z.; Cheng, R., et al., Interfacial Stabilization for Inverted Perovskite Solar Cells with Long-Term Stability. *Sci. Bull.* **2021,** *66*, 991-1002.
155. Islam, R.; Chen, G.; Ramesh, P.; Suh, J.; Fuchigami, N.; Lee, D.; Littau, K. A.; Weiner, K.; Collins, R. T.; Saraswat, K. C., Investigation of the Changes in Electronic Properties of Nickel Oxide (NiOx) Due to Uv/Ozone Treatment. *ACS Appl. Mater. Interfaces* **2017,** *9*, 17201-17207.
156. Zhai, Z.; Huang, X.; Xu, M.; Yuan, J.; Peng, J.; Ma, W., Greatly Reduced Processing Temperature for a Solution‐Processed NiOx Buffer Layer in Polymer Solar Cells. *Adv. Energy Mater.* **2013,** *3*, 1614-1622.
157. Boyd, C. C.; Shallcross, R. C.; Moot, T.; Kerner, R.; Bertoluzzi, L.; Onno, A.; Kavadiya, S.; Chosy, C.; Wolf, E. J.; Werner, J., et al., Overcoming Redox Reactions at Perovskite-Nickel Oxide Interfaces to Boost Voltages in Perovskite Solar Cells. *Joule* **2020,** *4*, 1759-1775.
158. Li, L.; Wang, Y.; Wang, X.; Lin, R.; Luo, X.; Liu, Z.; Zhou, K.; Xiong, S.; Bao, Q.; Chen, G., et al., Flexible All-Perovskite Tandem Solar Cells Approaching 25% Efficiency with Molecule-Bridged Hole-Selective Contact. *Nat. Energy* **2022,** *7*, 708-717.
159. Chen, W.; Zhu, Y.; Xiu, J.; Chen, G.; Liang, H.; Liu, S.; Xue, H.; Birgersson, E.; Ho, J. W.; Qin, X., et al., Monolithic Perovskite/Organic Tandem Solar Cells with 23.6% Efficiency Enabled by Reduced Voltage Losses and Optimized Interconnecting Layer. *Nat. Energy* **2022,** *7*, 229-237.

160. Li, Z.; Sun, X.; Zheng, X.; Li, B.; Gao, D.; Zhang, S.; Wu, X.; Li, S.; Gong, J.; Luther, J. M., Stabilized Hole-Selective Layer for High-Performance Inverted pin Perovskite Solar Cells. *Science* **2023,** *382*, 284-289.
161. Hu, S. F.; Thiesbrummel, J.; Pascual, J.; Stolterfoht, M.; Wakamiya, A.; Snaith, H. J., Narrow Bandgap Metal Halide Perovskites for All-Perovskite Tandem Photovoltaics. *Chem. Rev.* **2024,** *124*, 4079-4123.
162. Bi, C.; Wang, Q.; Shao, Y.; Yuan, Y.; Xiao, Z.; Huang, J., Non-Wetting Surface-Driven High-Aspect-Ratio Crystalline Grain Growth for Efficient Hybrid Perovskite Solar Cells. *Nat. Commun.* **2015,** *6*, 7747.
163. Liu, J.; Ozaki, M.; Yakumaru, S.; Handa, T.; Nishikubo, R.; Kanemitsu, Y.; Saeki, A.; Murata, Y.; Murdey, R.; Wakamiya, A., Lead-Free Solar Cells Based on Tin Halide Perovskite Films with High Coverage and Improved Aggregation. *Angew. Chem. Int. Ed.* **2018,** *57*, 13221-13225.
164. Zhang, S.; Stolterfoht, M.; Armin, A.; Lin, Q.; Zu, F.; Sobus, J.; Jin, H.; Koch, N.; Meredith, P.; Burn, P. L., et al., Interface Engineering of Solution-Processed Hybrid Organohalide Perovskite Solar Cells. *ACS Appl. Mater. Interfaces* **2018,** *10*, 21681-21687.
165. Luo, D.; Yang, W.; Wang, Z.; Sadhanala, A.; Hu, Q.; Su, R.; Shivanna, R.; Trindade, G. F.; Watts, J. F.; Xu, Z., et al., Enhanced Photovoltage for Inverted Planar Heterojunction Perovskite Solar Cells. *Science* **2018,** *360*, 1442-1446.
166. You, J.; Guo, F.; Qiu, S.; He, W.; Wang, C.; Liu, X.; Xu, W.; Mai, Y., The Fabrication of Homogeneous Perovskite Films on Non-Wetting Interfaces Enabled by Physical Modification. *J. Energy Chem.* **2019,** *38*, 192-198.
167. Wang, Y.; Duan, L.; Hameiri, Z.; Zhang, M.; Liu, X.; Bai, Y.; Hao, X., PTAA as Efficient Hole Hransport Materials in Perovskite Solar Cells: A Review. *Solar RRL* **2022,** *6*, 2200234.
168. Zhang, J.; Sun, Q.; Chen, Q.; Wang, Y.; Zhou, Y.; Song, B.; Yuan, N.; Ding, J.; Li, Y., High Efficiency Planar P-I-N Perovskite Solar Cells Using Low-Cost Fluorene-Based Hole Transporting Material. *Adv. Funct. Mater.* **2019,** *29*, 1900484.
169. Wang, Y.; Chen, W.; Wang, L.; Tu, B.; Chen, T.; Liu, B.; Yang, K.; Koh, C. W.; Zhang, X.; Sun, H., et al., Dopant-Free Small-Molecule Hole-Transporting Material for Inverted Perovskite Solar Cells with Efficiency Exceeding 21%. *Adv. Mater.* **2019,** *31*, 1902781.
170. Chen, W.; Wang, Y.; Liu, B.; Gao, Y. J.; Wu, Z.; Shi, Y. Q.; Tang, Y. M.; Yang, K.; Zhang, Y. J.; Sun, W. P., et al., Engineering of Dendritic Dopant-Free Hole Transport Molecules: Enabling Ultrahigh Fill Factor in Perovskite Solar Cells with Optimized Dendron Construction. *Sci. China Chem.* **2021,** *64*, 41-51.
171. Li, M.; Liu, M.; Qi, F.; Lin, F. R.; Jen, A. K., Self-Assembled Monolayers for Interfacial Engineering in Solution-Processed Thin-Film Electronic Devices: Design, Fabrication, and Applications. *Chem Rev* **2024,** *124*, 2138-2204.
172. Yao, Y.; Cheng, C.; Zhang, C.; Hu, H.; Wang, K.; De Wolf, S., Organic Hole Transport Layers for Efficient, Stable and Scalable Inverted Perovskite Solar Cells.

*Adv. Mater.* **2022**, 2203794.
173. Kim, S. Y.; Cho, S. J.; Byeon, S. E.; He, X.; Yoon, H. J., Self-Assembled Monolayers as Interface Engineering Nanomaterials in Perovskite Solar Cells. *Adv. Energy Mater.* **2020,** *10*, 2002606.
174. Isikgor, F. H.; Zhumagali, S.; Merino, L. V. T.; De Bastiani, M.; McCulloch, I.; De Wolf, S., Molecular Engineering of Contact Interfaces for High-Performance Perovskite Solar Cells. *Nat. Rev. Mater.* **2023,** *8*, 89-108.
175. Bauer, T.; Schmaltz, T.; Lenz, T.; Halik, M.; Meyer, B.; Clark, T., Phosphonate- and Carboxylate-Based Self-Assembled Monolayers for Organic Devices: A Theoretical Study of Surface Binding on Aluminum Oxide with Experimental Support. *ACS Appl. Mater. Interfaces* **2013,** *5*, 6073-80.
176. Al-Ashouri, A.; Kohnen, E.; Li, B.; Magomedov, A.; Hempel, H.; Caprioglio, P.; Marquez, J. A.; Morales Vilches, A. B.; Kasparavicius, E.; Smith, J. A., et al., Monolithic Perovskite/Silicon Tandem Solar Cell with >29% Efficiency by Enhanced Hole Extraction. *Science* **2020,** *370*, 1300-1309.
177. Al-Ashouri, A.; Köhnen, E.; Li, B.; Magomedov, A.; Hempel, H.; Caprioglio, P.; Márquez, J. A.; Morales Vilches, A. B.; Kasparavicius, E.; Smith, J. A., et al., Monolithic Perovskite/Silicon Tandem Solar Cell with >29% Efficiency by Enhanced Hole Extraction. *Science* **2020,** *370*, 1300-1309.
178. Al-Ashouri, A.; Magomedov, A.; Ross, M.; Jost, M.; Talaikis, M.; Chistiakova, G.; Bertram, T.; Marquez, J. A.; Kohnen, E.; Kasparavicius, E., et al., Conformal Monolayer Contacts with Lossless Interfaces for Perovskite Single Junction and Monolithic Tandem Solar Cells. *Energy Environ. Sci.* **2019,** *12*, 3356-3369.
179. Magomedov, A.; Al-Ashouri, A.; Kasparavicius, E.; Strazdaite, S.; Niaura, G.; Jost, M.; Malinauskas, T.; Albrecht, S.; Getautis, V., Self-Assembled Hole Transporting Monolayer for Highly Efficient Perovskite Solar Cells. *Adv. Energy Mater.* **2018,** *8*, 1801892.
180. Azmi, R.; Ugur, E.; Seitkhan, A.; Aljamaan, F.; Subbiah, A. S.; Liu, J.; Harrison, G. T.; Nugraha, M. I.; Eswaran, M. K.; Babics, M., et al., Damp Heat-Stable Perovskite Solar Cells with Tailored-Dimensionality 2D/3D Heterojunctions. *Science* **2022,** *376*, 73-77.
181. Choi, K.; Choi, H.; Min, J.; Kim, T.; Kim, D.; Son, S. Y.; Kim, G.-W.; Choi, J.; Park, T., A Short Review on Interface Engineering of Perovskite Solar Cells: A Self‐Assembled Monolayer and Its Roles. *Solar RRL* **2019,** *4*, 1900251.
182. Tang, H.; Shen, Z.; Shen, Y.; Yan, G.; Wang, Y.; Han, Q.; Han, L., Reinforcing Self-Assembly of Hole Transport Molecules for Stable Inverted Perovskite Solar Cells. *Science* **2024,** *383*, 1236-1240.
183. Song, D.; Narra, S.; Li, M.-Y.; Lin, J.-S.; Diau, E. W.-G., Interfacial Engineering with a Hole-Selective Self-Assembled Monolayer for Tin Perovskite Solar Cells Via a Two-Step Fabrication. *ACS Energy Lett.* **2021,** *6*, 4179-4186.
184. Gu, Z.; Zuo, L.; Larsen-Olsen, T. T.; Ye, T.; Wu, G.; Krebs, F. C.; Chen, H.,

Interfacial Engineering of Self-Assembled Monolayer Modified Semi-Roll-to-Roll Planar Heterojunction Perovskite Solar Cells on Flexible Substrates. *J. Mater. Chem. A* **2015,** *3*, 24254-24260.
185. Wang, Q.; Chueh, C. C.; Zhao, T.; Cheng, J.; Eslamian, M.; Choy, W. C. H.; Jen, A. K., Effects of Self-Assembled Monolayer Modification of Nickel Oxide Nanoparticles Layer on the Performance and Application of Inverted Perovskite Solar Cells. *ChemSusChem* **2017,** *10*, 3794-3803.
186. Yalcin, E.; Can, M.; Rodriguez-Seco, C.; Aktas, E.; Pudi, R.; Cambarau, W.; Demic, S.; Palomares, E., Semiconductor Self-Assembled Monolayers as Selective Contacts for Efficient PiN Perovskite Solar Cells. *Energy Environ. Sci* **2019,** *12*, 230-237.
187. Wang, Y.; Liao, Q. G.; Chen, J. H.; Huang, W.; Zhuang, X. M.; Tang, Y. M.; Li, B. L.; Yao, X. Y.; Feng, X. Y.; Zhang, X. H., et al., Teaching an Old Anchoring Group New Tricks: Enabling Low-Cost, Eco-Friendly Hole-Transporting Materials for Efficient and Stable Perovskite Solar Cells. *J. Am. Chem. Soc.* **2020,** *142*, 16632-16643.
188. Gharibzadeh, S.; Fassl, P.; Hossain, I. M.; Rohrbeck, P.; Frericks, M.; Schmidt, M.; Duong, T.; Khan, M. R.; Abzieher, T.; Nejand, B. A., et al., Two Birds with One Stone: Dual Grain-Boundary and Interface Passivation Enables >22% Efficient Inverted Methylammonium-Free Perovskite Solar Cells. *Energy Environ. Sci.* **2021,** *14*, 5875-5893.
189. Guo, R.; Wang, X.; Jia, X.; Guo, X.; Li, J.; Li, Z.; Sun, K.; Jiang, X.; Alvianto, E.; Shi, Z., et al., Refining the Substrate Surface Morphology for Achieving Efficient Inverted Perovskite Solar Cells. *Adv. Energy Mater.* **2023,** *1*, 2302280.
190. Aktas, E.; Phung, N.; Köbler, H.; González, D. A.; Méndez, M.; Kafedjiska, I.; Turren-Cruz, S.-H.; Wenisch, R.; Lauermann, I.; Abate, A., et al., Understanding the Perovskite/Self-Assembled Selective Contact Interface for Ultra-Stable and Highly Efficient p-i-n Perovskite Solar Cells. *Energy Environ. Sci.* **2021,** *14*, 3976-3985.
191. Ullah, A.; Park, K. H.; Nguyen, H. D.; Siddique, Y.; Shah, S. F. A.; Tran, H.; Park, S.; Lee, S. I.; Lee, K. K.; Han, C. H., et al., Novel Phenothiazine-Based Self-Assembled Monolayer as a Hole Selective Contact for Highly Efficient and Stable P-I-N Perovskite Solar Cells. *Adv. Energy Mater.* **2021,** *12*, 2103175.
192. Zhang, J.; Yang, J.; Dai, R.; Sheng, W.; Su, Y.; Zhong, Y.; Li, X.; Tan, L.; Chen, Y., Elimination of Interfacial Lattice Mismatch and Detrimental Reaction by Self-Assembled Layer Dual-Passivation for Efficient and Stable Inverted Perovskite Solar Cells. *Adv. Energy Mater.* **2022,** *12*, 2103674.
193. Li, Z.; Tan, Q.; Chen, G.; Gao, H.; Wang, J.; Zhang, X.; Xiu, J.; Chen, W.; He, Z., Simple and Robust Phenoxazine Phosphonic Acid Molecules as Self-Assembled Hole Selective Contacts for High-Performance Inverted Perovskite Solar Cells. *Nanoscale* **2023,** *15*, 1676-1686.
194. Aydin, E.; Ugur, E.; Yildirim, B. K.; Allen, T. G.; Dally, P.; Razzaq, A.; Cao,

F.; Xu, L.; Vishal, B.; Yazmaciyan, A., et al., Enhanced Optoelectronic Coupling for Perovskite-Silicon Tandem Solar Cells. *Nature* **2023**, DOI:10.1038/s41586-023-06667-4.
195. Wang, G.; Zheng, J.; Duan, W.; Yang, J.; Mahmud, M. A.; Lian, Q.; Tang, S.; Liao, C.; Bing, J.; Yi, J., et al., Molecular Engineering of Hole-Selective Layer for High Band Gap Perovskites for Highly Efficient and Stable Perovskite-Silicon Tandem Solar Cells. *Joule* **2023,** *7*, 2583-2594.
196. Luo, D.; Li, X.; Dumont, A.; Yu, H.; Lu, Z. H., Recent Progress on Perovskite Surfaces and Interfaces in Optoelectronic Devices. *Adv. Mater.* **2021,** *33*, 2006004.
197. Ren, Z.; Cui, Z.; Shi, X.; Wang, L.; Dou, Y.; Wang, F.; Lin, H.; Yan, H.; Chen, S., Poly(Carbazole Phosphonic Acid) as a Versatile Hole-Transporting Material for p-i-n Perovskite Solar Cells and Modules. *Joule* **2023,** *7*, 2894-2904.
198. Farag, A.; Feeney, T.; Hossain, I. M.; Schackmar, F.; Fassl, P.; Küster, K.; Bäuerle, R.; Ruiz-Preciado, M. A.; Hentschel, M.; Ritzer, D. B., et al., Evaporated Self-Assembled Monolayer Hole Transport Layers: Lossless Interfaces in P-I-N Perovskite Solar Cells. *Adv. Energy Mater.* **2023,** *13*, 2203982.
199. Hotchkiss, P. J.; Jones, S. C.; Paniagua, S. A.; Sharma, A.; Kippelen, B.; Armstrong, N. R.; Marder, S. R., The Modification of Indium Tin Oxide with Phosphonic Acids: Mechanism of Binding, Tuning of Surface Properties, and Potential for Use in Organic Electronic Applications. *Acc. Chem. Res.* **2012,** *45*, 337-346.
200. Chen, B.; Rudd, P. N.; Yang, S.; Yuan, Y.; Huang, J., Imperfections and Their Passivation in Halide Perovskite Solar Cells. *Chem Soc Rev* **2019,** *48*, 3842-3867.
201. Ni, Z.; Bao, C.; Liu, Y.; Jiang, Q.; Wu, W.-Q.; Chen, S.; Dai, X.; Chen, B.; Hartweg, B.; Yu, Z., et al., Resolving Spatial and Energetic Distributions of Trap States in Metal Halide Perovskite Solar Cells. *Science* **2020,** *367*, 1352-1358.
202. Chen, P.; Hu, J.; Yu, M.; Li, P.; Su, R.; Wang, Z.; Zhao, L.; Li, S.; Yang, Y.; Zhang, Y., et al., Refining Perovskite Heterojunctions for Effective Light-Emitting Solar Cells. *Adv Mater* **2023,** *35*, e2208178.
203. Schulz, P.; Cahen, D.; Kahn, A., Halide Perovskites: Is It All About the Interfaces? *Chem. Rev.* **2019,** *119*, 3349-3417.
204. Zhang, F.; Ye, S.; Zhang, H.; Zhou, F.; Hao, Y.; Cai, H.; Song, J.; Qu, J., Comprehensive Passivation Strategy for Achieving Inverted Perovskite Solar Cells with Efficiency Exceeding 23% by Trap Passivation and Ion Constraint. *Nano Energy* **2021,** *89*, 106370.
205. Wu, S.; Zhang, J.; Li, Z.; Liu, D.; Qin, M.; Cheung, S. H.; Lu, X.; Lei, D.; So, S. K.; Zhu, Z., et al., Modulation of Defects and Interfaces through Alkylammonium Interlayer for Efficient Inverted Perovskite Solar Cells. *Joule* **2020,** *4*, 1248-1262.
206. Park, S. M.; Wei, M.; Xu, J.; Atapattu, H. R.; Eickemeyer, F. T.; Darabi, K.; Grater, L.; Yang, Y.; Liu, C.; Teale, S., et al., Engineering Ligand Reactivity Enables High-Temperature Operation of Stable Perovskite Solar Cells. *Science* **2023,** *381*,

209-215.
207. Li, B.; Xiang, Y.; Jayawardena, K. D. G. I.; Luo, D.; Watts, J. F.; Hinder, S.; Li, H.; Ferguson, V.; Luo, H.; Zhu, R., et al., Tailoring Perovskite Adjacent Interfaces by Conjugated Polyelectrolyte for Stable and Efficient Solar Cells. *Solar RRL* **2020,** *4*, 2000060.
208. Gutierrez-Partida, E.; Hempel, H.; Caicedo-Dávila, S.; Raoufi, M.; Peña-Camargo, F.; Grischek, M.; Gunder, R.; Diekmann, J.; Caprioglio, P.; Brinkmann, K. O., et al., Large-Grain Double Cation Perovskites with 18 μs Lifetime and High Luminescence Yield for Efficient Inverted Perovskite Solar Cells. *ACS Energy Lett.* **2021,** *6*, 1045-1054.
209. Lian, X.; Chen, J.; Shan, S.; Wu, G.; Chen, H., Polymer Modification on the $NiO_x$ Hole Transport Layer Boosts Open-Circuit Voltage to 1.19 V for Perovskite Solar Cells. *ACS Appl. Mater. Interfaces* **2020,** *12*, 46340-46347.
210. Li, B.; Xiang, Y.; Jayawardena, K. D. G. I.; Luo, D.; Wang, Z.; Yang, X.; Watts, J. F.; Hinder, S.; Sajjad, M. T.; Webb, T., et al., Reduced Bilateral Recombination by Functional Molecular Interface Engineering for Efficient Inverted Perovskite Solar Cells. *Nano Energy* **2020,** *78*, 105249.
211.Zhang, H.; Li, K.; Sun, M.; Wang, F. L.; Wang, H.; Jen, A. K. Y., Design of Superhydrophobic Surfaces for Stable Perovskite Solar Cells with Reducing Lead Leakage. *Adv. Energy Mater.* **2021,** *11*, 2102281.
212. Zhang, M.; Chen, Q.; Xue, R.; Zhan, Y.; Wang, C.; Lai, J.; Yang, J.; Lin, H.; Yao, J.; Li, Y., et al., Reconfiguration of Interfacial Energy Band Structure for High-Performance Inverted Structure Perovskite Solar Cells. *Nat. Commun.* **2019,** *10*, 4593.
213. Xu, J.; Xi, J.; Dong, H.; Ahn, N.; Zhu, Z.; Chen, J.; Li, P.; Zhu, X.; Dai, J.; Hu, Z., et al., Impermeable Inorganic “Walls” Sandwiching Perovskite Layer toward Inverted and Indoor Photovoltaic Devices. *Nano Energy* **2021,** *88*, 106286.
214. Wu, W. Q.; Rudd, P. N.; Ni, Z.; Van Brackle, C. H.; Wei, H.; Wang, Q.; Ecker, B. R.; Gao, Y.; Huang, J., Reducing Surface Halide Deficiency for Efficient and Stable Iodide-Bsed Perovskite Solar Cells. *J. Am. Chem. Soc.* **2020,** *142*, 3989-3996.
215. Lu, Y. N.; Zhong, J. X.; Yu, Y. Y.; Chen, X.; Yao, C. Y.; Zhang, C. X.; Yang, M. F.; Feng, W. H.; Jiang, Y.; Tan, Y., et al., Constructing an $n/n^+$ Homojunction in a Monolithic Perovskite Film for Boosting Charge Collection in Inverted Perovskite Photovoltaics. *Energy Environ. Sci.* **2021,** *14*, 4048-4058.
216. Gao, Z. W.; Wang, Y.; Ouyang, D.; Liu, H.; Huang, Z.; Kim, J.; Choy, W. C. H., Triple Interface Passivation Strategy‐Enabled Efficient and Stable Inverted Perovskite Solar Cells. *Small Methods* **2020,** *4*, 2000478.
217. Deng, X.; Li, F.; Wang, Q.; Liu, D.; Lin, F.; Shen, D.; Lei, D.; Peng, Y.-K.; Zhu, Z.; Jen, A. K.-Y., Highly Efficient and Stable Perovskite Solar Cells Enabled by a Fluoro-Functionalized $TiO_2$ Inorganic Interlayer. *Matter* **2021,** *4*, 3301-3312.
218. Yang, Y.; Cheng, S.; Zhu, X.; Li, S.; Zheng, Z.; Zhao, K.; Ji, L.; Li, R.; Liu, Y.; Liu, C., et al., Inverted Perovskite Solar Cells with over 2,000 h Operational Stability at 85 °C Using Fixed Charge Passivation. *Nat. Energy* **2023**,

DOI:10.1038/s41560-023-01377-7.
219. Bai, Y.; Meng, X.; Yang, S., Interface Engineering for Highly Efficient and Stable Planar p-i-n Perovskite Solar Cells. *Adv. Energy Mater.* **2018,** *8*, 1701883.
220. Fu, L.; Li, H.; Wang, L.; Yin, R. Y.; Li, B.; Yin, L. W., Defect Passivation Strategies in Perovskites for an Enhanced Photovoltaic Performance. *Energy Environ. Sci.* **2020,** *13*, 4017-4056.
221. McGott, D. L.; Muzzillo, C. P.; Perkins, C. L.; Berry, J. J.; Zhu, K.; Duenow, J. N.; Colegrove, E.; Wolden, C. A.; Reese, M. O., 3D/2D Passivation as a Secret to Success for Polycrystalline Thin-Film Solar Cells. *Joule* **2021,** *5*, 1057-1073.
222. Sutanto, A. A.; Caprioglio, P.; Drigo, N.; Hofstetter, Y. J.; Garcia-Benito, I.; Queloz, V. I. E.; Neher, D.; Nazeeruddin, M. K.; Stolterfoht, M.; Vaynzof, Y., et al., 2D/3D Perovskite Engineering Eliminates Interfacial Recombination Losses in Hybrid Perovskite Solar Cells. *Chem* **2021,** *7*, 1903-1916.
223. Zhang, Z.; Qiao, L.; Meng, K.; Long, R.; Chen, G.; Gao, P., Rationalization of Passivation Strategies toward High-Performance Perovskite Solar Cells. *Chem Soc Rev* **2022**.
224. Remmerswaal, W. H. M.; van Gorkom, B. T.; Zhang, D.; Wienk, M. M.; Janssen, R. A. J., Quantifying Non-Radiative Recombination in Passivated Wide-Bandgap Metal Halide Perovskites Using Absolute Photoluminescence Spectroscopy. *Adv. Energy Mater.* **2024,** *14*, 2303664.
225. Mariotti, S.; Köhnen, E.; Scheler, F.; Sveinbjörnsson, K.; Zimmermann, L.; Piot, M.; Yang, F.; Li, B.; Warby, J.; Musiienko, A., et al., Interface Engineering for High-Performance, Triple-Halide Perovskite–Silicon Tandem Solar Cells. *Science* **2023,** *381*, 63-69.
226. Warby, J.; Zu, F.; Zeiske, S.; Gutierrez-Partida, E.; Frohloff, L.; Kahmann, S.; Frohna, K.; Mosconi, E.; Radicchi, E.; Lang, F., et al., Understanding Performance Limiting Interfacial Recombination in pin Perovskite Solar Cells. *Adv. Energy Mater.* **2022,** *12*.
227. Gao, Z. W.; Wang, Y.; Choy, W. C. H., Buried Interface Modification in Perovskite Solar Cells: A Materials Perspective. *Adv. Energy Mater.* **2022,** *12*, 2104030.
228. Liu, X.; Webb, T.; Dai, L.; Ji, K.; Smith, J. A.; Kilbride, R. C.; Yavari, M.; Bi, J.; Ren, A.; Huang, Y., et al., Influence of Halide Choice on Formation of Low-Dimensional Perovskite Interlayer in Efficient Perovskite Solar Cells. *Energy Environ. Mater.* **2022,** *5*, 670-682.
229. Xiao, K.; Lin, Y.-H.; Zhang, M.; Oliver, R. D. J.; Wang, X.; Liu, Z.; Luo, X.; Li, J.; Lai, D.; Luo, H., et al., Scalable Processing for Realizing 21.7%-Efficient All-Perovskite Tandem Solar Modules. *Science* **2022,** *376*, 762-767.
230. Yang, S.; Chen, S.; Mosconi, E.; Fang, Y.; Xiao, X.; Wang, C.; Zhou, Y.; Yu, Z.; Zhao, J.; Gao, Y., et al., Stabilizing Halide Perovskite Surfaces for Solar Cell Operation with Wide-Bandgap Lead Oxysalts. *Science* **2019,** *365*, 473-478.
231. Li, B.; Zhang, W., Improving the Stability of Inverted Perovskite Solar Cells

Towards Commercialization. *Commun. Mater.* **2022,** *3*, 65.
232. Leijtens, T.; Eperon, G. E.; Noel, N. K.; Habisreutinger, S. N.; Petrozza, A.; Snaith, H. J., Stability of Metal Halide Perovskite Solar Cells. *Adv. Energy Mater.* **2015,** *5*, 1500963.
233. Dai, Z.; Yadavalli, S. K.; Chen, M.; Abbaspourtamijani, A.; Qi, Y.; Padture, N. P., Interfacial Toughening with Self-Assembled Monolayers Enhances Perovskite Solar Cell Reliability. *Science* **2021,** *372*, 618-622.
234. Kitamura, T.; Okada, K.; Matsui, H.; Tanabe, N., Durability of Dye-Sensitized Solar Cells and Modules. *J. Sol. Energy Eng.* **2010,** *132*, 021105.
235. Mei, A.; Sheng, Y.; Ming, Y.; Hu, Y.; Rong, Y.; Zhang, W.; Luo, S.; Na, G.; Tian, C.; Hou, X., et al., Stabilizing Perovskite Solar Cells to IEC61215:2016 Standards with over 9,000-h Operational Ttracking. *Joule* **2020,** *4*, 2646-2660.
236. Snaith, H. J., Present Status and Future Prospects of Perovskite Photovoltaics. *Nat. Mater.* **2018,** *17*, 372-376.
237. Jung, E. H.; Jeon, N. J.; Park, E. Y.; Moon, C. S.; Shin, T. J.; Yang, T. Y.; Noh, J. H.; Seo, J., Efficient, Stable and Scalable Perovskite Solar Cells Using Poly(3-Hexylthiophene). *Nature* **2019,** *567*, 511-515.
238. Li, B.; Zhang, C.; Gao, D.; Sun, X.; Zhang, S.; Li, Z.; Gong, J.; Li, S.; Zhu, Z., Suppressing Oxidation at Perovskite-NiOx Interface for Efficient and Stable Tin Perovskite Solar Cells. *Adv. Mater.* **2023**, e2309768.
239. Xiao, M.; Yuan, G.; Lu, Z.; Xia, J.; Li, D.; Chen, Y.; Zhang, Y.; Pei, F.; Chen, C.; Bai, Y., et al., Engineering Amorphous-Crystallized Interface of ZrNx Barriers for Stable Perovskite Solar Cells. *Adv. Mater.* **2023,** *35*, 2301684.
240. Wu, S.; Chen, R.; Zhang, S.; Babu, B. H.; Yue, Y.; Zhu, H.; Yang, Z.; Chen, C.; Chen, W.; Huang, Y., et al., A Chemically Inert Bismuth Interlayer Enhances Long-Term Stability of Inverted Perovskite Solar Cells. *Nat. Commun.* **2019,** *10*, 1-10.
241. Bi, E.; Tang, W.; Chen, H.; Wang, Y.; Barbaud, J.; Wu, T.; Kong, W.; Tu, P.; Zhu, H.; Zeng, X., et al., Efficient Perovskite Solar Cell Modules with High Stability Enabled by Iodide Diffusion Barriers. *Joule* **2019,** *3*, 2748-2760.
242. Zhang, S.; Liu, Z.; Zhang, W.; Jiang, Z.; Chen, W.; Chen, R.; Huang, Y.; Yang, Z.; Zhang, Y.; Han, L., et al., Barrier Designs in Perovskite Solar Cells for Long-Term Stability. *Adv. Energy Mater.* **2020,** *10*, 2001610.
243. Bush, K. A.; Bailie, C. D.; Chen, Y.; Bowring, A. R.; Wang, W.; Ma, W.; Leijtens, T.; Moghadam, F.; McGehee, M. D., Thermal and Environmental Stability of Semi-Transparent Perovskite Solar Cells for Tandems Enabled by a Solution-Processed Nanoparticle Buffer Layer and Sputtered Ito Electrode. *Adv. Mater.* **2016,** *28*, 3937-3943.
244. Brinkmann, K. O.; Zhao, J.; Pourdavoud, N.; Becker, T.; Hu, T.; Olthof, S.; Meerholz, K.; Hoffmann, L.; Gahlmann, T.; Heiderhoff, R., et al., Suppressed Decomposition of Organometal Halide Perovskites by Impermeable Electron-Extraction Layers in Inverted Solar Cells. *Nat Commun* **2017,** *8*, 13938.
245. Wu, S.; Li, Z.; Li, M. Q.; Diao, Y.; Lin, F.; Liu, T.; Zhang, J.; Tieu, P.; Gao,

W.; Qi, F., et al., 2D Metal-Organic Framework for Stable Perovskite Solar Cells with Minimized Lead Leakage. *Nature Nanotechnolgy* **2020,** *15*, 934-940.
246. Chen, P.; Xiao, Y.; Hu, J.; Li, S.; Luo, D.; Su, R.; Caprioglio, P.; Kaienburg, P.; Jia, X.; Chen, N., et al., Multifunctional Ytterbium Oxide Buffer for Perovskite Solar Cells. *Nature* **2024,** *625*, 516–522.
247. Jiang, Y.; Qiu, L.; Juarez-Perez, E. J.; Ono, L. K.; Hu, Z.; Liu, Z.; Wu, Z.; Meng, L.; Wang, Q.; Qi, Y., Reduction of Lead Leakage from Damaged Lead Halide Perovskite Solar Modules Using Self-Healing Polymer-Based Encapsulation. *Nat. Energy* **2019,** *4*, 585-593.
248. Ma, S.; Bai, Y.; Wang, H.; Zai, H. C.; Wu, J. F.; Li, L.; Xiang, S. S.; Liu, N.; Liu, L.; Zhu, C., et al., 1000 h Operational Lifetime Perovskite Solar Cells by Ambient Melting Encapsulation. *Adv. Energy Mater.* **2020,** *10*, 1902472.
249. Li, X.; Zhang, F.; He, H.; Berry, J. J.; Zhu, K.; Xu, T., On-Device Lead Sequestration for Perovskite Solar Cells. *Nature* **2020,** *578*, 555-558.
250. Zhang, G.; Zheng, Y.; Wang, H.; Ding, G.; Yang, F.; Xu, Y.; Yu, J.; Shao, Y., Shellac Protects Perovskite Solar Cell Modules under Real-World Conditions. *Joule* **2024**, DOI: 10.1016/j.joule.2023.12.008.
251. Shi, L.; Bucknall, M. P.; Young, T. L.; Zhang, M.; Hu, L.; Bing, J.; Lee, D. S.; Kim, J.; Wu, T.; Takamure, N., Gas Chromatography–Mass Spectrometry Analyses of Encapsulated Stable Perovskite Solar Cells. *Science* **2020,** *368*, eaba2412.
252. Li, J.; Xia, R.; Qi, W.; Zhou, X.; Cheng, J.; Chen, Y.; Hou, G.; Ding, Y.; Li, Y.; Zhao, Y., et al., Encapsulation of Perovskite Solar Cells for Enhanced Stability: Structures, Materials and Characterization. *J Power Sources* **2021,** *485*, 229313.
253. Khenkin, M. V.; Katz, E. A.; Abate, A.; Bardizza, G.; Berry, J. J.; Brabec, C.; Brunetti, F.; Bulović, V.; Burlingame, Q.; Di Carlo, A., et al., Consensus Statement for Stability Assessment and Reporting for Perovskite Photovoltaics Based on Isos Procedures. *Nat. Energy* **2020,** *5*, 35-49.
254. Li, J.; Dagar, J.; Shargaieva, O.; Maus, O.; Remec, M.; Emery, Q.; Khenkin, M.; Ulbrich, C.; Akhundova, F.; Márquez, J. A., et al., Ink Design Enabling Slot-Die Coated Perovskite Solar Cells with >22% Power Conversion Efficiency, Micro-Modules, and 1 Year of Outdoor Performance Evaluation. *Adv. Energy Mater.* **2023,** *13*, 2203898.
255. Ali, M. U.; Mo, H.; Li, Y.; Djurišić, A. B., Outdoor Stability Testing of Perovskite Solar Cells: Necessary Step toward Real-Life Applications. *APL Energy* **2023,** *1*, 020903.
256. Emery, Q.; Remec, M.; Paramasivam, G.; Janke, S.; Dagar, J.; Ulbrich, C.; Schlatmann, R.; Stannowski, B.; Unger, E.; Khenkin, M., Encapsulation and Outdoor Testing of Perovskite Solar Cells: Comparing Industrially Relevant Process with a Simplified Lab Procedure. *ACS Appl. Mater. Interfaces* **2022,** *14*, 5159-5167.
257. Jiang, Q.; Tirawat, R.; Kerner, R. A.; Gaulding, E. A.; Xian, Y.; Wang, X.; Newkirk, J. M.; Yan, Y.; Berry, J. J.; Zhu, K., Towards Linking Lab and Field Lifetimes of Perovskite Solar Cells. *Nature* **2023**, DOI:10.1038/s41586-023-06610-7.

258. Hörantner, M. T.; Leijtens, T.; Ziffer, M. E.; Eperon, G. E.; Christoforo, M. G.; McGehee, M. D.; Snaith, H. J., The Potential of Multijunction Perovskite Solar Cells. *ACS Energy Lett.* **2017,** *2*, 2506-2513.
259. Hossain, M. I.; Qarony, W.; Ma, S.; Zeng, L.; Knipp, D.; Tsang, Y. H., Perovskite/Silicon Tandem Solar Cells: From Detailed Balance Limit Calculations to Photon Management. *Nano-Micro Lett.* **2019,** *11*, 58.
260. Wang, J.; Zeng, L.; Zhang, D.; Maxwell, A.; Chen, H.; Datta, K.; Caiazzo, A.; Remmerswaal, W. H. M.; Schipper, N. R. M.; Chen, Z., et al., Halide Homogenization for Low Energy Loss in 2-eV-Bandgap Perovskites and Increased Efficiency in All-Perovskite Triple-Junction Solar Cells. *Nat. Energy* **2023**, DOI: 10.1038/s41560-023-01406-5.
261. Liu, S.; Lu, Y.; Yu, C.; Li, J.; Luo, R.; Guo, R.; Liang, H.; Jia, X.; Guo, X.; Wang, Y.-D., et al., Triple-Junction Solar Cells with Cyanate in Ultrawide-Bandgap Perovskites. *Nature* **2024,** *628*, 306-312.
262. Duan, L.; Walter, D.; Chang, N.; Bullock, J.; Kang, D.; Phang, S. P.; Weber, K.; White, T.; Macdonald, D.; Catchpole, K., et al., Stability Challenges for the Commercialization of Perovskite–Silicon Tandem Solar Cells. *Nat. Rev. Mater.* **2023,** *8*, 261-281.
263. Leijtens, T.; Bush, K. A.; Prasanna, R.; McGehee, M. D., Opportunities and Challenges for Tandem Solar Cells Using Metal Halide Perovskite Semiconductors. *Nat. Energy* **2018,** *3*, 828-838.
264. Li, H.; Zhang, W., Perovskite Tandem Solar Cells: From Fundamentals to Commercial Deployment. *Chem. Rev.* **2020,** *120*, 9835-9950.
265. Mailoa, J. P.; Bailie, C. D.; Johlin, E. C.; Hoke, E. T.; Akey, A. J.; Nguyen, W. H.; McGehee, M. D.; Buonassisi, T., A 2-Terminal Perovskite/Silicon Multijunction Solar Cell Enabled by a Silicon Tunnel Junction. *Appl. Phys. Lett.* **2015,** *106*, 121105.
266. Werner, J.; Weng, C. H.; Walter, A.; Fesquet, L.; Seif, J. P.; De Wolf, S.; Niesen, B.; Ballif, C., Efficient Monolithic Perovskite/Silicon Tandem Solar Cell with Cell Area >1 $cm^2$. *J. Phys. Chem. Lett.* **2016,** *7*, 161-166.
267. Werner, J.; Walter, A.; Rucavado, E.; Moon, S. J.; Sacchetto, D.; Rienaecker, M.; Peibst, R.; Brendel, R.; Niquille, X.; De Wolf, S., et al., Zinc Tin Oxide as High-Temperature Stable Recombination Layer for Mesoscopic Perovskite/Silicon Monolithic Tandem Solar Cells. *Appl. Phys. Lett.* **2016,** *109*, 233902.
268. Albrecht, S.; Saliba, M.; Correa Baena, J. P.; Lang, F.; Kegelmann, L.; Mews, M.; Steier, L.; Abate, A.; Rappich, J.; Korte, L., et al., Monolithic Perovskite/Silicon-Heterojunction Tandem Solar Cells Processed at Low Temperature. *Energy Environ. Sci.* **2016,** *9*, 81-88.
269. Zheng, J.; Mehrvarz, H.; Ma, F.-J.; Lau, C. F. J.; Green, M. A.; Huang, S.; Ho-Baillie, A. W. Y., 21.8% Efficient Monolithic Perovskite/Homo-Junction-Silicon Tandem Solar Cell on 16 $cm^2$. *ACS Energy Lett.* **2018,** *3*, 2299-2300.
270. Jena, A. K.; Numata, Y.; Ikegami, M.; Miyasaka, T., Role of Spiro-OMeTAD in Performance Deterioration of Perovskite Solar Cells at High Temperature and

Reuse of the Perovskite Films to Avoid Pb-Waste. *J. Mater. Chem. A* **2018,** *6*, 2219-2230.
271. Bush, K. A.; Palmstrom, A. F.; Yu, Z. J.; Boccard, M.; Cheacharoen, R.; Mailoa, J. P.; McMeekin, D. P.; Hoye, R. L. Z.; Bailie, C. D.; Leijtens, T., et al., 23.6%-Efficient Monolithic Perovskite/Silicon Tandem Solar Cells with Improved Stability. *Nat. Energy* **2017,** *2*, 17009.
272. Sahli, F.; Werner, J.; Kamino, B. A.; Brauninger, M.; Monnard, R.; Paviet-Salomon, B.; Barraud, L.; Ding, L.; Diaz Leon, J. J.; Sacchetto, D., et al., Fully Textured Monolithic Perovskite/Silicon Tandem Solar Cells with 25.2% Power Conversion Efficiency. *Nat. Mater.* **2018,** *17*, 820-826.
273. Chin, X. Y.; Turkay, D.; Steele, J. A.; Tabean, S.; Eswara, S.; Mensi, M.; Fiala, P.; Wolff, C. M.; Paracchino, A.; Artuk, K., et al., Interface Passivation for 31.25%-Efficient Perovskite/Silicon Tandem Solar Cells. *Science* **2023,** *381*, 59-63.
274. Hou, Y.; Aydin, E.; De Bastiani, M.; Xiao, C.; Isikgor, F. H.; Xue, D.-J.; Chen, B.; Chen, H.; Bahrami, B.; Chowdhury, A. H., et al., Efficient Tandem Solar Cells with Solution-Processed Perovskite on Textured Crystalline Silicon. *Science* **2020,** *367*, 1135-1140.
275. Chen, B.; Yu, Z. J.; Manzoor, S.; Wang, S.; Weigand, W.; Yu, Z.; Yang, G.; Ni, Z.; Dai, X.; Holman, Z. C., et al., Blade-Coated Perovskites on Textured Silicon for 26%-Efficient Monolithic Perovskite/Silicon Tandem Solar Cells. *Joule* **2020,** *4*, 850-864.
276. Tockhorn, P.; Sutter, J.; Cruz, A.; Wagner, P.; Jäger, K.; Yoo, D.; Lang, F.; Grischek, M.; Li, B.; Al-Ashouri, A., et al., Nano-Optical Designs Enhance Monolithic Perovskite/Silicon Tandem Solar Cells toward 29.8% Efficiency. *Nat. Nanotechnol.* **2022,** *17*, 1214-1221.
277. Kim, D.; Jung, H. J.; Park, I. J.; Larson, B. W.; Dunfield, S. P.; Xiao, C.; Kim, J.; Tong, J.; Boonmongkolras, P.; Ji, S. G., et al., Efficient, Stable Silicon Tandem Cells Enabled by Anion-Engineered Wide-Bandgap Perovskites. *Science* **2020,** *368*, 155-160.
278. Yang, G.; Ni, Z.; Yu, Z. J.; Larson, B. W.; Yu, Z.; Chen, B.; Alasfour, A.; Xiao, X.; Luther, J. M.; Holman, Z. C., et al., Defect Engineering in Wide-Bandgap Perovskites for Efficient Perovskite–Silicon Tandem Solar Cells. *Nat. Photonics* **2022,** *16*, 588-594.
279. Green, M. A.; Dunlop, E. D.; Yoshita, M.; Kopidakis, N.; Bothe, K.; Siefer, G.; Hao, X., Solar Cell Efficiency Tables (Version 63). *Progress in photovoltaics: research and applications* **2023,** *32*, 3-13.
280. Tockhorn, P.; Sutter, J.; Cruz, A.; Wagner, P.; Jäger, K.; Yoo, D.; Lang, F.; Grischek, M.; Li, B.; Li, J., et al., Nano-Optical Designs for High-Efficiency Monolithic Perovskite–Silicon Tandem Solar Cells. *Nat. Nanotechnol.* **2022,** *17*, 1214-1221.
281. Wu, Y.; Zheng, P.; Peng, J.; Xu, M.; Chen, Y.; Surve, S.; Lu, T.; Bui, A. D.; Li, N.; Liang, W., et al., 27.6% Perovskite/c‐Si Tandem Solar Cells Using Industrial

Fabricated TOPCon Device. *Adv. Energy Mater.* **2022,** *12*, 2200821.
282. Li, Y. C.; Shi, B. A.; Xu, Q. J.; Yan, L. L.; Ren, N. Y.; Chen, Y. L.; Han, W.; Huang, Q.; Zhao, Y.; Zhang, X. D., Wide Bandgap Interface Layer Induced Stabilized Perovskite/Silicon Tandem Solar Cells with Stability over Ten Thousand Hours. *Adv. Energy Mater.* **2021,** *11*, 2102046.
283. Li, R.; Chen, B.; Ren, N.; Wang, P.; Shi, B.; Xu, Q.; Zhao, H.; Han, W.; Zhu, Z.; Liu, J., et al., $CsPbCl_3$-Cluster-Widened Bandgap and Inhibited Phase Segregation in a Wide-Bandgap Perovskite and Its Application to $NiO_x$-Based Perovskite/Silicon Tandem Solar Cells. *Adv. Mater.* **2022,** *34*, 201451.
284. Nogay, G.; Sahli, F.; Werner, J.; Monnard, R.; Boccard, M.; Despeisse, M.; Haug, F. J.; Jeangros, Q.; Ingenito, A.; Ballif, C., 25.1%-Efficient Monolithic Perovskite/Silicon Tandem Solar Cell Based on a p-type Monocrystalline Textured Silicon Wafer and High-Temperature Passivating Contacts. *ACS Energy Lett.* **2019,** *4*, 844-845.
285. Lin, R.; Wang, Y.; Lu, Q.; Tang, B.; Li, J.; Gao, H.; Gao, Y.; Li, H.; Ding, C.; Wen, J., et al., All-Perovskite Tandem Solar Cells with 3D/3D Bilayer Perovskite Heterojunction. *Nature* **2023,** *620*, 994-1000.
286. He, R.; Wang, W.; Yi, Z.; Lang, F.; Chen, C.; Luo, J.; Zhu, J.; Thiesbrummel, J.; Shah, S.; Wei, K., et al., Improving Interface Quality for 1-$cm^2$ All-Perovskite Tandem Solar Cells. *Nature* **2023,** *618*, 80-86.
287. Chen, H.; Maxwell, A.; Li, C.; Teale, S.; Chen, B.; Zhu, T.; Ugur, E.; Harrison, G.; Grater, L.; Wang, J., et al., Regulating Surface Potential Maximizes Voltage in All-Perovskite Tandems. *Nature* **2022,** *613*, 676-681.
288. Zhu, J.; Luo, Y.; He, R.; Chen, C.; Wang, Y.; Luo, J.; Yi, Z.; Thiesbrummel, J.; Wang, C.; Lang, F., et al., A Donor–Acceptor-Type Hole-Selective Contact Reducing Non-Radiative Recombination Losses in Both Subcells Towards Efficient All-Perovskite Tandems. *Nat. Energy* **2023,** *8*, 714-724.
289. Jiang, Q.; Tong, J.; Scheidt, R. A.; Wang, X.; Louks, A. E.; Xian, Y.; Tirawat, R.; Palmstrom, A. F.; Hautzinger, M. P.; Harvey, S. P., et al., Compositional Texture Engineering for Highly Stable Wide-Bandgap Perovskite Solar Cells. *Science* **2022,** *378*, 1295-1300.
290. Lin, R.; Xu, J.; Wei, M.; Wang, Y.; Qin, Z.; Liu, Z.; Wu, J.; Xiao, K.; Chen, B.; Park, S. M., et al., All-Perovskite Tandem Solar Cells with Improved Grain Surface Passivation. *Nature* **2022,** *603*, 73-78.
291. Wen, J.; Zhao, Y.; Liu, Z.; Gao, H.; Lin, R.; Wan, S.; Ji, C.; Xiao, K.; Gao, Y.; Tian, Y., et al., Steric Engineering Enables Efficient and Photostable Wide-Bandgap Perovskites for All-Perovskite Tandem Solar Cells. *Adv. Mater.* **2022,** *34*, 2110356.
292. Yu, Z.; Chen, X.; Harvey, S. P.; Ni, Z.; Chen, B.; Chen, S.; Yao, C.; Xiao, X.; Xu, S.; Yang, G., et al., Gradient Doping in Sn-Pb Perovskites by Barium Ions for Efficient Single-Junction and Tandem Solar Cells. *Adv. Mater.* **2022,** *34*, 2110351.
293. Tong, J.; Jiang, Q.; Ferguson, A. J.; Palmstrom, A. F.; Wang, X.; Hao, J.; Dunfield, S. P.; Louks, A. E.; Harvey, S. P.; Li, C., et al., Carrier Control in Sn–Pb

Perovskites Via 2D Cation Engineering for All-Perovskite Tandem Solar Cells with Improved Efficiency and Stability. *Nat. Energy* **2022,** *7*, 642-651.
294. Xiao, K.; Lin, R.; Han, Q.; Hou, Y.; Qin, Z.; Nguyen, H. T.; Wen, J.; Wei, M.; Yeddu, V.; Saidaminov, M. I., et al., All-Perovskite Tandem Solar Cells with 24.2% Certified Efficiency and Area over 1 $cm^2$ Using Surface-Anchoring Zwitterionic Antioxidant. *Nat. Energy* **2020,** *5*, 870-880.
295. Yu, Z.; Yang, Z.; Ni, Z.; Shao, Y.; Chen, B.; Lin, Y.; Wei, H.; Yu, Z. J.; Holman, Z.; Huang, J., Simplified Interconnection Structure Based on $C_{60}/SnO_{2-X}$ for All-Perovskite Tandem Solar Cells. *Nat. Energy* **2020,** *5*, 657-665.
296. Tong, J.; Song, Z.; Kim, D. H.; Chen, X.; Chen, C.; Palmstrom, A. F.; Ndione, P. F.; Reese, M. O.; Dunfield, S. P.; Reid, O. G., Carrier Lifetimes of> 1 μs in Sn-Pb Perovskites Enable Efficient All-Perovskite Tandem Solar Cells. *Science* **2019,** *364*, 475-479.
297. Palmstrom, A. F.; Eperon, G. E.; Leijtens, T.; Prasanna, R.; Habisreutinger, S. N.; Nemeth, W.; Gaulding, E. A.; Dunfield, S. P.; Reese, M.; Nanayakkara, S., et al., Enabling Flexible All-Perovskite Tandem Solar Cells. *Joule* **2019,** *3*, 2193-2204.
298. Zhang, Z.; Chen, W.; Jiang, X.; Cao, J.; Yang, H.; Chen, H.; Yang, F.; Shen, Y.; Yang, H.; Cheng, Q., et al., Suppression of Phase Segregation in Wide-Bandgap Perovskites with Thiocyanate Ions for Perovskite/Organic Tandems with 25.06% Efficiency. *Nat. Energy* **2024,** *9*, 592–601.
299. Wu, S.; Yan, Y.; Yin, J.; Jiang, K.; Li, F.; Zeng, Z.; Tsang, S.-W.; Jen, A. K. Y., Redox Mediator-Stabilized Wide-Bandgap Perovskites for Monolithic Perovskite-Organic Tandem Solar Cells. *Nat. Energy* **2024,** *9*, 411-421.
300. Wang, X.; Zhang, D.; Liu, B.; Wu, X.; Jiang, X.; Zhang, S.; Wang, Y.; Gao, D.; Wang, L.; Wang, H., et al., Highly Efficient Perovskite/Organic Tandem Solar Cells Enabled by Mixed-Cation Surface Modulation. *Adv Mater* **2023,** *35*, e2305946.
301. Ma, Z.; Dong, Y.; Wang, R.; Xu, Z.; Li, M.; Tan, Z. a., Transparent Recombination Electrode with Dual‐Functional Transport and Protective Layer for Efficient and Stable Monolithic Perovskite/Organic Tandem Solar Cells. *Adv. Mater.* **2023,** *35*, 2307502.
302. Brinkmann, K. O.; Becker, T.; Zimmermann, F.; Kreusel, C.; Gahlmann, T.; Theisen, M.; Haeger, T.; Olthof, S.; Tückmantel, C.; Günster, M., et al., Perovskite–Organic Tandem Solar Cells with Indium Oxide Interconnect. *Nature* **2022,** *604*, 280-286.
303. Qin, S.; Lu, C.; Jia, Z.; Wang, Y.; Li, S.; Lai, W.; Shi, P.; Wang, R.; Zhu, C.; Du, J., et al., Constructing Monolithic Perovskite/Organic Tandem Solar Cell with Efficiency of 22.0% Via Reduced Open-Circuit Voltage Loss and Broadened Absorption Spectra. *Adv. Mater.* **2022,** *34*, 2108829.
304. Xie, Y. M.; Yao, Q.; Zeng, Z.; Xue, Q.; Niu, T.; Xia, R.; Cheng, Y.; Lin, F.; Tsang, S. W.; Jen, A. K. Y., et al., Homogeneous Grain Boundary Passivation in Wide‐Bandgap Perovskite Films Enables Fabrication of Monolithic Perovskite/Organic Tandem Solar Cells with over 21% Efficiency. *Adv. Funct. Mater.* **2022,** *32*, 2112126.

305. Chen, X.; Jia, Z.; Chen, Z.; Jiang, T.; Bai, L.; Tao, F.; Chen, J.; Chen, X.; Liu, T.; Xu, X., et al., Efficient and Reproducible Monolithic Perovskite/Organic Tandem Solar Cells with Low-Loss Interconnecting Layers. *Joule* **2020,** *4*, 1594-1606.
306. Liu, Y.; Renna, L. A.; Bag, M.; Page, Z. A.; Kim, P.; Choi, J.; Emrick, T.; Venkataraman, D.; Russell, T. P., High Efficiency Tandem Thin-Perovskite/Polymer Solar Cells with a Graded Recombination Layer. *ACS Appl. Mater. Interfaces* **2016,** *8*, 7070-7076.
307. Jiang, F.; Liu, T.; Luo, B.; Tong, J.; Qin, F.; Xiong, S.; Li, Z.; Zhou, Y., A Two-Terminal Perovskite/Perovskite Tandem Solar Cell. *J. Mater. Chem. A* **2016,** *4*, 1208-1213.
308. Heo, J. H.; Im, S. H., $CH_3NH_3PbBr_3$-$CH_3NH_3PbI_3$ Perovskite-Perovskite Tandem Solar Cells with Exceeding 2.2 V Open Circuit Voltage. *Adv. Mater.* **2016,** *28*, 5121-5125.
309. McMeekin, D. P.; Mahesh, S.; Noel, N. K.; Klug, M. T.; Lim, J.; Warby, J. H.; Ball, J. M.; Herz, L. M.; Johnston, M. B.; Snaith, H. J., Solution-Processed All-Perovskite Multi-Junction Solar Cells. *Joule* **2019,** *3*, 387-401.
310. Eperon, G. E.; Leijtens, T.; Bush, K. A.; Prasanna, R.; Green, T.; Wang, J. T.; McMeekin, D. P.; Volonakis, G.; Milot, R. L.; May, R., et al., Perovskite-Perovskite Tandem Photovoltaics with Optimized Band Gaps. *Science* **2016,** *354*, 861-865.
311.Dewei, Z.; Cong, C.; Guojia, F.; Changlei, W.; Junda, M. M.; Kai, Z.; Yanfa, Y.; Zhaoning, S.; Grice, C. R.; Yue, Y., et al., Efficient Two-Terminal All-Perovskite Tandem Solar Cells Enabled by High-Quality Low-Bandgap Absorber Layers. *Nat. Energy* **2018,** *3*, 1093-1100.
312. Yang, Z.; Yu, Z.; Wei, H.; Xiao, X.; Ni, Z.; Chen, B.; Deng, Y.; Habisreutinger, S. N.; Chen, X.; Wang, K., et al., Enhancing Electron Diffusion Length in Narrow-Bandgap Perovskites for Efficient Monolithic Perovskite Tandem Solar Cells. *Nat. Commun.* **2019,** *10*, 4498.
313. Wu, S.; Liu, M.; Jen, A. K. Y., Prospects and Challenges for Perovskite-Organic Tandem Solar Cells. *Joule* **2023,** *7*, 484-502.
314. Liu, Y.; Liu, B.; Ma, C.-Q.; Huang, F.; Feng, G.; Chen, H.; Hou, J.; Yan, L.; Wei, Q.; Luo, Q., et al., Recent Pogress in Organic Solar Cells (Part I Material Science). *Sci. China Chem.* **2021,** *65*, 224-268.
315. Liu, Y.; Chen, Y., Integrated Perovskite/Bulk-Heterojunction Organic Solar Cells. *Adv. Mater.* **2020,** *32*, 1805843.
316. Chen, C.-C.; Bae, S.-H.; Chang, W.-H.; Hong, Z.; Li, G.; Chen, Q.; Zhou, H.; Yang, Y., Perovskite/Polymer Monolithic Hybrid Tandem Solar Cells Utilizing a Low-Temperature, Full Solution Process. *Mater. Horiz.* **2015,** *2*, 203-211.
317. Brinkmann, K. O.; Wang, P.; Lang, F.; Li, W.; Guo, X.; Zimmermann, F.; Olthof, S.; Neher, D.; Hou, Y.; Stolterfoht, M., et al., Perovskite–Organic Tandem Solar Cells. *Nat. Rev. Mater.* **2024,** *9*, 202-217.
318. Wang, H.; Qin, Z.; Miao, Y.; Zhao, Y., Recent Progress in Large-Area Perovskite Photovoltaic Modules. *Transactions of Tianjin University* **2022,** *28*, 323-

340.
319. Park, N.-G.; Zhu, K., Scalable Fabrication and Coating Methods for Perovskite Solar Cells and Solar Modules. *Nat. Rev. Mater.* **2020,** *5*, 333-350.
320. Li, Z.; Klein, T. R.; Kim, D. H.; Yang, M.; Berry, J. J.; van Hest, M. F. A. M.; Zhu, K., Scalable Fabrication of Perovskite Solar Cells. *Nat. Rev. Mater.* **2018,** *3*, 1-20.
321. Song, Z.; McElvany, C. L.; Phillips, A. B.; Celik, I.; Krantz, P. W.; Watthage, S. C.; Liyanage, G. K.; Apul, D.; Heben, M. J., A Technoeconomic Analysis of Perovskite Solar Module Manufacturing with Low-Cost Materials and Techniques. *Energy Environ. Sci.* **2017,** *10*, 1297-1305.
322. Li, X.; Li, P.; Wu, Z.; Luo, D.; Yu, H.-Y.; Lu, Z.-H., Review and Perspective of Materials for Flexible Solar Cells. *Materials Reports: Energy* **2021,** *1*, 100001.
323. Cheng, Y.; Peng, Y.; Jen, A. K. Y.; Yip, H.-L., Development and Challenges of Metal Halide Perovskite Solar Modules. *Solar RRL* **2021,** *6*, 2100545.
324. Yang, Z.; Zhang, W.; Wu, S.; Zhu, H.; Liu, Z.; Liu, Z.; Jiang, Z.; Chen, R.; Zhou, J.; Lu, Q., Slot-Die Coating Large-Area Formamidinium-Cesium Perovskite Film for Efficient and Stable Parallel Solar Module. *Sci. Adv.* **2021,** *7*, eabg3749.
325. Chen, S.; Xiao, X.; Chen, B.; Kelly, L. L.; Zhao, J.; Lin, Y.; Toney, M. F.; Huang, J., Crystallization in One-Step Solution Deposition of Perovskite Films: Upward or Downward? *Sci. Adv.* **2021,** *7*, eabb2412.
326. Deng, Y.; Zheng, X.; Bai, Y.; Wang, Q.; Zhao, J.; Huang, J., Surfactant-Controlled Ink Drying Enables High-Speed Deposition of Perovskite Films for Efficient Photovoltaic Modules. *Nat. Energy* **2018,** *3*, 560-566.
327. Gao, Y.; Liu, C.; He, M.; Zhang, C.; Liu, L.; Luo, Q.; Wu, Y.; Zhang, H.; Zhong, X.; Guo, R., et al., Efficient and Stable Perovskite Solar Modules Enabled by Inhibited Escape of Volatile Species. *Adv. Mater.* **2024,** *36*, e2309310.
328. Li, L.; Chen, P.; Su, R.; Xu, H.; Li, Q.; Zhong, Q.; Yan, H.; Yang, X.; Hu, J.; Li, S., et al., Buried - Metal - Grid Electrodes for Efficient Parallel - Connected Perovskite Solar Cells. *Adv. Mater.* **2023,** *36*, 2305238.
329. Oxford PV Sets New Solar Cell World Record; PV, O., 2023. https://www.oxfordpv.com/news/oxford-pv-sets-new-solar-cell-world-record (accessed 05-24-2023).
330. 26.36% @ 1.71m²! GCL Perovskite Module Breaks World Record Again.; abPv, 2024. https://www.perovskite-info.com/gcl-achieves-conversion-efficiency-2617-its-perovskite-tandem-module (accessed 04-08-2024).
331. GCL Perovskite Bags B+ Round of Financing Worth $72m; Pandaily, 2022. https://pandaily.com/gcl-perovskite-bags-b-round-of-financing-worth-72m/ (accessed 12-14-2022).
332. The World First Perovskite Fish-Light Complementary Power Station Has Successfully Been Connected to Grid; Semiconductor, M., 2023. https://www.microquanta.com/en/newsinfo/4812255D9A185CF0/ (accessed 07-13-2023).
333. 20.7%! The Steady-State Efficiency of the Large-Sized Perovskite Module

from Utmolight Is Breaking the World Record Again; UtmoLight, 2024. http://www.utmolight.com/20492/140698.html (accessed 29-29-2024).
334. Sun, X.; Li, Y.; Liu, D.; Liu, R.; Zhang, B.; Tian, Q.; Fan, B.; Wang, X.; Li, Z.; Shao, Z., et al., $V_{oc}$ of Inverted Perovskite Solar Cells Based on N-Doped Pcbm Exceeds 1.2 V: Interface Energy Alignment and Synergistic Passivation. *Adv. Energy Mater.* **2023**, DOI:10.1002/aenm.202302191.
335. Gu, H.; Fei, C.; Yang, G.; Chen, B.; Uddin, M. A.; Zhang, H.; Ni, Z.; Jiao, H.; Xu, W.; Yan, Z., et al., Design Optimization of Bifacial Perovskite Minimodules for Improved Efficiency and Stability. *Nat. Energy* **2023,** *8*, 675-684.
336. Li, C.; Zhang, Y.; Zhang, X.; Zhang, P.; Yang, X.; Chen, H., Efficient Inverted Perovskite Solar Cells with a Fill Factor over 86% Via Surface Modification of the Nickel Oxide Hole Contact. *Adv. Funct. Mater.* **2023**, 2214774.
337. Huang, Y. C.; Yan, K. R.; Niu, B. F.; Chen, Z.; Gu, E. M. Y.; Liu, H. R.; Yan, B. Y.; Yao, J. Z.; Zhu, H. M.; Chen, H. Z., et al., Finite Perovskite Hierarchical Structures Via Ligand Confinement Leading to Efficient Inverted Perovskite Solar Cells. *Energy Environ. Sci.* **2023,** *16*, 557-564.
338. GCL Perovskite Reaches 18.04% Efficiency with Its Perovskite Single-Junction Solar Module; Network, C. N. E., 2023. https://www.ne21.com/news/show-191049.html (accessed 03-06-2024).
339. 22.86%! The Power Conversion Efficiency of the 30 cm*30 cm Perovskite Photovoltaic Module from Mellow Energy Reached a New High.; energy, M., 2023. https://www.mellow-energy.cn/official/journalism/details/0/0/109.html (accessed 12-29-2023).
340. China Huaneng Group Co., Ltd.: 18.5% Efficiency! Perovskite PV Modules Exceeding 3500 cm2; PVTECH, 2023. https://www.pv-tech.cn/news/Huaneng_Qingneng_Institute_more_than_3500_cm2_perovskite_modules (accessed 02-09-2023).
341. New World Record: 20.86%! Steady-State Efficiency of Large-Area Perovskite Modules; Solar, R., 2024. https://www.renshinesolar.com/page99?article_id=120 (accessed 05-05-2024).
342. Tu, Y.; Wu, J.; Xu, G.; Yang, X.; Cai, R.; Gong, Q.; Zhu, R.; Huang, W., Perovskite Solar Cells for Space Applications: Progress and Challenges. *Adv. Mater.* **2021,** *33*, 2006545.
343. Hu, Y.; Niu, T.; Liu, Y.; Zhou, Y.; Xia, Y.; Ran, C.; Wu, Z.; Song, L.; Müller-Buschbaum, P.; Chen, Y., et al., Flexible Perovskite Solar Cells with High Power-Per-Weight: Progress, Application, and Perspectives. *ACS Energy Lett.* **2021,** *6*, 2917-2943.
344. Zafoschnig, L. A.; Nold, S.; Goldschmidt, J. C., The Race for Lowest Costs of Electricity Production: Techno-Economic Analysis of Silicon, Perovskite and Tandem Solar Cells. *IEEE Journal of Photovoltaics* **2020,** *10*, 1632-1641.
345. Park, N.-G.; Grätzel, M.; Miyasaka, T.; Zhu, K.; Emery, K., Towards Stable and Commercially Available Perovskite Solar Cells. *Nat. Energy* **2016,** *1*, 16152.

346. Cai, M.; Wu, Y.; Chen, H.; Yang, X.; Qiang, Y.; Han, L., Cost-Performance Analysis of Perovskite Solar Modules. *Adv. Sci.* **2017,** *4*, 1600269.
347. De Bastiani, M.; Larini, V.; Montecucco, R.; Grancini, G., The Levelized Cost of Electricity from Perovskite Photovoltaics. *Energy Environ. Sci.* **2023,** *16*, 421-429.
348. Yan, J.; Savenije, T. J.; Mazzarella, L.; Isabella, O., Progress and Challenges on Scaling up of Perovskite Solar Cell Technology. *Sustainable Energy & Fuels* **2022,** *6*, 243-266.
349. Yu, Z. J.; Carpenter, J. V.; Holman, Z. C., Techno-Economic Viability of Silicon-Based Tandem Photovoltaic Modules in the United States. *Nat. Energy* **2018,** *3*, 747-753.
350. Zhu, P.; Wang, D.; Zhang, Y.; Liang, Z.; Li, J.; Zeng, J.; Zhang, J.; Xu, Y.; Wu, S.; Liu, Z., et al., Aqueous Synthesis of Perovskite Precursors for Highly Efficient Perovskite Solar Cells. *Science* **2024,** *383*, 524-531.
351. Gao, X. X.; Luo, W.; Zhang, Y.; Hu, R.; Zhang, B.; Zuttel, A.; Feng, Y.; Nazeeruddin, M. K., Stable and High-Efficiency Methylammonium-Free Perovskite Solar Cells. *Adv. Mater.* **2020,** *32*, 1905502.
352. Tian, J. J.; Xue, Q. F.; Yao, Q.; Li, N.; Brabec, C. J.; Yip, H. L., Inorganic Halide Perovskite Solar Cells: Progress and Challenges. *Adv. Energy Mater.* **2020,** *10*, 2000183.
353. Tai, Q. D.; Tang, K. C.; Yan, F., Recent Progress of Inorganic Perovskite Solar Cells. *Energy Environ. Sci.* **2019,** *12*, 2375.
354. Zhou, Y. Y.; Zhao, Y. X., Chemical Stability and Instability of Inorganic Halide Perovskites. *Energy Environ. Sci.* **2019,** *12*, 1495-1511.
355. Zhao, X.; Liu, T.; Burlingame, Q. C.; Liu, T.; Holley, R., 3rd; Cheng, G.; Yao, N.; Gao, F.; Loo, Y. L., Accelerated Aging of All-Inorganic, Interface-Stabilized Perovskite Solar Cells. *Science* **2022,** *377*, 307-310.
356. Zhao, Y.; Heumueller, T.; Zhang, J.; Luo, J.; Kasian, O.; Langner, S.; Kupfer, C.; Liu, B.; Zhong, Y.; Elia, J., et al., A Bilayer Conducting Polymer Structure for Planar Perovskite Solar Cells with over 1,400 Hours Operational Stability at Elevated Temperatures. *Nat. Energy* **2021,** *7*, 144-152.
357. Hasan, S. A. U.; Lee, D. S.; Im, S. H.; Hong, K.-H., Present Status and Research Prospects of Tin-Based Perovskite Solar Cells. *Solar RRL* **2019,** *4*, 1900310.
358. Li, B.; Chang, B. H.; Pan, L.; Li, Z. H.; Fu, L.; He, Z. B.; Yin, L. W., Tin-Based Defects and Passivation Strategies in Tin-Related Perovskite Solar Cells. *ACS Energy Lett.* **2020,** *5*, 3752-3772.
359. Li, H.; Zhou, J.; Tan, L.; Li, M.; Jiang, C.; Wang, S.; Zhao, X.; Liu, Y.; Zhang, Y.; Ye, Y., et al., Sequential Vacuum-Evaporated Perovskite Solar Cells with More Than 24% Efficiency. *Sci. Adv.* **2022,** *8*, eabo7422.
360. Chiang, Y. H.; Anaya, M.; Stranks, S. D., Multisource Vacuum Deposition of Methylammonium-Free Perovskite Solar Cells. *ACS Energy Lett.* **2020,** *5*, 2498-2504.
361. Zhang, L.; He, M.; Shao, S., Machine Learning for Halide Perovskite

Materials. *Nano Energy* **2020,** *78*, 105380.
362. Xu, J.; Chen, H.; Grater, L.; Liu, C.; Yang, Y.; Teale, S.; Maxwell, A.; Mahesh, S.; Wan, H.; Chang, Y., et al., Anion Optimization for Bifunctional Surface Passivation in Perovskite Solar Cells. *Nat. Mater.* **2023,** *22*, 1507-1514.
363. Mahesh, S.; Ball, J. M.; Oliver, R. D. J.; Mcmeekin, D. P.; Nayak, P. K.; Johnston, M. B.; Snaith, H. J., Revealing the Origin of Voltage Loss in Mixed-Halide Perovskite Solar Cells. *Energy Environ. Sci.* **2020,** *13*, 258-267.
364. Zhu, L.; Zhang, M.; Xu, J.; Li, C.; Yan, J.; Zhou, G.; Zhong, W.; Hao, T.; Song, J.; Xue, X., et al., Single-Junction Organic Solar Cells with over 19% Efficiency Enabled by a Refined Double-Fibril Network Morphology. *Nat. Mater.* **2022,** *21*, 656-663.
365. Tong, Y.; Xiao, Z.; Du, X. Y.; Zuo, C. T.; Li, Y. L.; Lv, M. L.; Yuan, Y. B.; Yi, C. Y.; Hao, F.; Hua, Y., et al., Progress of the Key Materials for Organic Solar Cells. *Sci. China Chem.* **2020,** *63*, 758-765.
366. Feng, K.; Huang, J.; Zhang, X.; Wu, Z.; Shi, S.; Thomsen, L.; Tian, Y.; Woo, H. Y.; McNeill, C. R.; Guo, X., High-Performance All-Polymer Solar Cells Enabled by N-Type Polymers with an Ultranarrow Bandgap Down to 1.28 eV. *Adv. Mater.* **2020,** *32*, 2001476.
367. Shi, S.; Chen, P.; Chen, Y.; Feng, K.; Liu, B.; Chen, J.; Liao, Q.; Tu, B.; Luo, J.; Su, M., et al., A Narrow-Bandgap N-Type Polymer Semiconductor Enabling Efficient All-Polymer Solar Cells. *Adv. Mater.* **2019,** *31*, 1905161.
368. Yu, J.; Chen, P.; Koh, C. W.; Wang, H.; Yang, K.; Zhou, X.; Liu, B.; Liao, Q.; Chen, J.; Sun, H., et al., Phthalimide-Based High Mobility Polymer Semiconductors for Efficient Nonfullerene Solar Cells with Power Conversion Efficiencies over 13%. *Adv. Sci.* **2019,** *6*, 1801743.
369. Bi, S.; Leng, X.; Li, Y.; Zheng, Z.; Zhang, X.; Zhang, Y.; Zhou, H., Interfacial Modification in Organic and Perovskite Solar Cells. *Adv. Mater.* **2019,** *31*, 1805708.
370. Yin, Z.; Wei, J.; Zheng, Q., Interfacial Materials for Organic Solar Cells: Recent Advances and Perspectives. *Adv. Sci.* **2016,** *3*, 1500362.
371. Liu, Y.; Liu, B.; Ma, C.-Q.; Huang, F.; Feng, G.; Chen, H.; Hou, J.; Yan, L.; Wei, Q.; Luo, Q., et al., Recent Progress in Organic Solar Cells (Part II Device Engineering). *Sci. China Chem.* **2022,** *65*, 1457-1495.
372. Wang, P.; Zhao, Y.; Wang, T., Recent Progress and Prospects of Integrated Perovskite/Organic Solar Cells. *Appl. Phys. Rev.* **2020,** *7*, 031303.
373. Chen, W.; Sun, H.; Hu, Q.; Djurišić, A. B.; Russell, T. P.; Guo, X.; He, Z., High Short-Circuit Current Density Via Integrating the Perovskite and Ternary Organic Bulk Heterojunction. *ACS Energy Lett.* **2019,** *4*, 2535-2536.
374. Liao, Q.; Sun, H.; Li, B.; Guo, X., 26 mA $cm^{-2}$ Jsc Achieved in the Integrated Solar Cells. *Sci. Bull.* **2019,** *64*, 1747-1749.
375. Wu, S.; Li, Z.; Zhang, J.; Wu, X.; Deng, X.; Liu, Y.; Zhou, J.; Zhi, C.; Yu, X.; Choy, W. C. H., et al., Low-Bandgap Organic Bulk-Heterojunction Enabled Efficient

and Flexible Perovskite Solar Cells. *Adv. Mater.* **2021,** *33*, 2105539.
376. Liu, Z.; Qiu, L.; Ono, L. K.; He, S.; Hu, Z.; Jiang, M.; Tong, G.; Wu, Z.; Jiang, Y.; Son, D.-Y., et al., A Holistic Approach to Interface Stabilization for Efficient Perovskite Solar Modules with over 2,000-hour Operational Stability. *Nat. Energy* **2020,** *5*, 596-604.
377. He, X.; Chen, J.; Ren, X.; Zhang, L.; Liu, Y.; Feng, J.; Fang, J.; Zhao, K.; Liu, S. F., 40.1% Record Low-Light Solar-Cell Efficiency by Holistic Trap-Passivation Using Micrometer-Thick Perovskite Film. *Adv. Mater.* **2021,** *33*, 2100770.
378. Lin, X.; Su, H.; He, S.; Song, Y.; Wang, Y.; Qin, Z.; Wu, Y.; Yang, X.; Han, Q.; Fang, J., et al., In Situ Growth of Graphene on Both Sides of a Cu–Ni Alloy Electrode for Perovskite Solar Cells with Improved Stability. *Nat. Energy* **2022,** *7*, 520-527.
379. Yan, L.; Huang, H.; Cui, P.; Du, S.; Lan, Z.; Yang, Y.; Qu, S.; Wang, X.; Zhang, Q.; Liu, B., et al., Fabrication of Perovskite Solar Cells in Ambient Air by Blocking Perovskite Hydration with Guanabenz Acetate Salt. *Nat. Energy* **2023,** *8*, 1158-1167.
380. Chao, L.; Xia, Y.; Li, B.; Xing, G.; Chen, Y.; Huang, W., Room-Temperature Molten Salt for Facile Fabrication of Efficient and Stable Perovskite Solar Cells in Ambient Air. *Chem* **2019,** *5*, 995-1006.
381. Batmunkh, M.; Zhong, Y. L.; Zhao, H., Recent Advances in Perovskite-Based Building-Integrated Photovoltaics. *Adv. Mater.* **2020,** *32*, 2000631.
382. Tu, Y. G.; Xu, G. N.; Yang, X. Y.; Zhang, Y. F.; Li, Z. J.; Su, R.; Luo, D. Y.; Yang, W. Q.; Miao, Y.; Cai, R., et al., Mixed-Cation Perovskite Solar Cells in Space. *Sci China Phys Mech* **2019,** *62*, 974221.